A STUDY OF PHYSICAL MECHANISMS FOR FILAMENT ERUPTION AND CORONAL MASS EJECTION VIA NUMERICAL SIMULATION

FINAL REPORT FOR NAGW-9

Period of Performance: October 1, 1979 - March 31, 1994

by

S. T. Wu
Center for Space Plasma and Aeronomic Research
and Department of Mechanical and Aerospace Engineering
The University of Alabama in Huntsville
Huntsville, AL 35899
(205) 895-6268
(205) 895-6382 [fax]

for

National Aeronautics and Space Administration
Headquarters
Washington, DC 20546

June 1994

During the fifteen year period of performance of this grant (October 1, 1979 - March 31, 1994) we have significant contribution. The contribution for the period October 1, 1979 - December 30, 1993 were submitted in earlier reports and will not be repeated here. During the period January 1, 1993 - March 31, 1994 contributions have been made in the following areas:

I. Flare Physics

In this area, we have published three papers in theory and numerical modeling and one paper utilizing a non-linear-force-free (NLFF) model to interpret the magnetic structures and energy of the 1989 March flares. These papers are:

- Magnetic Structures and Energy of 1989 March Flares, S. T. Wu, F. S. Weng, H. M. Wang, H. Zirin and G. X. Ai, *Adv. Space Res.* **13**, 9, (9)127-(9)130, 1993
- Magnetic Diffusion and Flare Energy Buildup, S. T. Wu, C. L. Yin, W.-H. Yang, *Solar Physics*, **142**, 313-325,1992.
- Numerical Modeling of the Energy Storage and Release in Solar Flares, S. T. Wu and F. S. Weng, *J. of Atmospheric and Terrestrial Phys.*, **55**, 7, 939-945, 1993.
- Magnetohydrodynamic Simulation of the Evolution of Bipolar Magnetic Regions, S. T. Wu, C. L. Yin, P. McIntosh, and E. Hildner, *Astronomical Society of the Pacific Conference Series* The Magnetic and Velocity Fields of Solar Active Regions (H. Zirin, G. Ai, and H. M. Wang, eds.) **46**, 98-107, 1993

II. Coronal Dynamics

Eleven papers have been published in this area. We have achieved partial construction of a two-dimensional and three-dimensional quantitative coronal model, studied the physical mechanisms of rising prominence loops, shear-induced instability and arch filament eruptions, and the fundamentals of MHD wave generation and propagation in the corona to understand the coronal heating processes. These published results are:

- On Generation and Propagation of MHD Body and Surface Waves: Single Magnetic Interface and Magnetic Slab, S. T. Wu, Y. C. Xiao, Z. E. Musielak, and S. T. Suess, *Physics of Fluids B: Plasma Physics*, 1994 (submitted).
- Model Calculations of the Rising Motion of a Prominence Loop, T. Yeh and S. T. Wu, *Solar Physics*, **132**, 335-351, 1991.
- Shear-Induced Instability and Arch Filament Eruption: A Magnetohydrodynamic (MHD) Numerical Simulation, S. T. Wu, M. T. Song, P. C. H. Martens, and M. Dryer, *Solar Physics*, **134**, 353-377, 1991.
- Numerical Simulation of Extended Corona, S. T. Wu, A. H. Wang, *Adv. Space Res.* **11**, 1, (1)187-(2)195, 1991.
- A Two-Dimensional MHD Global Coronal Model: Steady-State Streamers, A. H. Wang, S. T. Wu, S. T. Suess, and G. Poletto, Solar Wind VII., Proceedings of the 3rd COSPAR

Colloquium held in Goslar, Germany, 16-20 September 1991, E. Marsch and R. Schwenn (eds.) Pergamon Press, Oxford, 311-314.

- Predicting Ly-α Intensities in Coronal Streamers, G. Noci, G. Poletto, S. T. Suess, A. H. Wang, S. T. Wu, Proceedings of the First SOHO Workshop, Annapolis, Maryland, USA 25-28 August 1992, (EAS SP-348), November 1992.
- A Two-Dimensional MHD Global Coronal Model: Steady State Streamers, A. H. Wang, S. T. Wu, S. T. Suess, and G. Poletto, *Solar Physics*, **147**, 51-71, 1993.
- Lα Intensity in Coronal Streamers, G. Noci, G. Poletto, S. T. Suess, A. H. Wang, and S. T. Wu, *Solar Physics*, **147**, 73-96, 1993.
- Numerical Simulation of CME Propagation in a Helmet Streamer: Emerging Magnetic Flux Mechanism, J. H. Zhang, S. T. Wu, M. Dryer, F. S. Wei, IAU Colloquium 144, Solar Coronal Structures, V. Rusin, P. Heinzel and J. C. Vial (eds.), 7-11, 1993.
- Magnetohydrodynamic Simulation of a Streamer Beside a Realistic Coronal Hole, S. T. Suess, S. T. Wu, A. H. Wang, G. Poletto, Proceedings of SOHO Workshop, Elba, Italy, September 27 - October, 1993.
- Coronal Heating Due to the Emergence of Magnetic Flux, S. T. Wu, M. T. Song, C. C. Cheng, and M. Dryer, *Space Sci. Reviews*, 1994 (in press).

III. Interplanetary Dynamics

In this area, we present a three-dimensional, time-dependent, MHD model for the understanding of the solar-interplanetary-magnetosphere (SIM) coupling. Three papers were published:

- Three-Dimensional Numerical Simulation of Interplanetary Magnetic Field Changes at 1 AU as a consequence of Simulated Solar Flares, Study of the Solar-Terrestrial System, Proceedings of the 26th ESLAB Symposium, Killarney, Ireland, 16 - 19 June 1992, ESA-SP346, September, 1992.
- Heliospheric Current Sheet Effects on the Propagation of Solar-Generated Shock Waves, M. Dryer, S. T. Wu, C. C. Wu and S. M. Han, Study of the Solar-Terrestrial System, Proceedings of the 25th ESLAB Symposium, June 16-19, 1992, Killarney, Ireland, R. Reinhard, (ed.), 77-79, 1993
- Forecasting the Arrival of Fast Coronal Mass Ejecta at Earth by the Detection of 2- 20 keV Neutral Atoms, K. C. Hsieh, K. L. Shih, D. J. McComas, S. T. Wu, and C. C. Wu, SPIE Conference Paper, 1992.

IV. Numerical Methods

In order to assure the accuracy and efficiency of the numerical simulation we have developed new numerical techniques for solving nonlinear MHD systems resulting from the physics we try to understand. Three papers are published/submitted for publication which include:

- Modified ICED-ALE Method for Astrogeophysical Plasma Flows, S, T. Wu, M. T. Song, M. Dryer, AIAA 91-1470, presented at the AIAA 22nd Fluid Dynamics, Plasma Dynamics and

Lasers Conference, June 24-26, 1991, Honolulu, Hawaii.

- Extension of Rezoned Eulerian-Lagrangian Method to Astrophysical Plasma Applications, M. T. Song, S. T. Wu and M. Dryer, AIAA 93-3177, presented at the AIAA 24nd Plasma Dynamics and Lasers Conference, July 6-9, 1993, Orlando, Florida.
- On the Time-Dependent Numerical Boundary Conditions of Magnetohydrodynamic Flows, M. T. Sun, S. T. Wu, and M. Dryer, *J. Computational Physics*, 1993 (submitted).

In summary, accomplishments resulting from this grant are reported in the publication of twenty-one papers in four areas. All the reprints/preprints are enclosed with this final report.

Adv. Space Res. Vol. 13, No. 9, pp. (9)127–(9)130, 1993
Printed in Great Britain. All rights reserved.

0273–1177/93 $24.00
Copyright © 1993 COSPAR

MAGNETIC STRUCTURES AND ENERGY OF 1989 MARCH FLARES

S. T. Wu,* F. S. Weng,* H. M. Wang,** H. Zirin** and G. X. Ai***

* *Center for Space Plasma and Aeronomic Research, and Department of Mechanical Engineering, University of Alabama in Huntsville, Huntsville, AL 35899, U.S.A.*
** *California Institute of Technology, Pasadena, CA 91125, U.S.A.*
*** *Beijing Astronomical Observatory, Beijing, People's Republic of China*

ABSTRACT

We use a recently developed non-linear force-free model to analyze the magnetic structures and energy for 1989 March flares. In this analysis, we extrapolated the magnetic structure using the vector magnetograms obtained at Huairou Solar Observatory. In order to validate our extrapolated magnetic field topology, we compared our computed magnetic field results with H_α pictures obtained at Big Bear Solar Observatory. The results are presented for the evolution of the magnetic field structure (i.e. potential and non-linear force-free field), magnetic energy, and current distribution. It shows that the location of the occurrences of the flares are approximately related to the location of the high intensity of the currents. Further, we demonstrate that the amount of energy in force-free fields is more than adequate to power the flares.

1. INTRODUCTION

It has been recognized that the active region of 1989 March (NOAA AR 5395) was the most prolific flare-producing region in recent history. This region produced some 200 flares, of which fifty were class M flares and ten were class X. The data analysis on the basis of the observations of this region from Big Bear and Huairou Solar Observatories for the spots motions, magnetic field morphology and flare locations is presented by Wang *et al.* /1/. In this paper, we present an analysis on the magnetic structures, current distributions and available energy of the active region 1989 March. To achieve these goals, we employed a recently developed non-linear force-free (NLFF) model /2/ to extrapolate the magnetic field configuration up to coronal heights (~30,000 km) using the vector magnetograms obtained at Huairou Solar Observatory. Using these computed magnetic field configuration, we deduced the current systems and available energy of this active region. The procedures for the extrapolation of magnetic field on the basis of observed vector magnetograms are briefly outlined in Section 2. The results and physical interpretations are presented in Section 3 and discussed in Section 4.

2. MAGNETIC FIELD EXTRAPOLATION PROCEDURES

To understand the physics of an active region, the storage and release of flare energy, and the formation of hot plasma loops, it is imperative that we study and determine the structure of the solar magnetic field. Up to date, the technique used to study and determine the solar magnetic field structures is the potential field model given by Schmidt /3/ which represents the minimum energy and zero electric current state. This approximation is far from a realistic representation of the solar magnetic field in an active region. Recently, Wu *et al.* /2/ proposed a NLFF field model which is an order of magnitude better than the potential field model. This model gives a description of the current system which could resemble the realistic solar atmosphere under the force-free condition (i.e. $\beta = \frac{16\pi nkT}{B^2} << 1$). The detailed description and accuracy of the nonlinear force-free model are presented in reference 2, we shall not repeat them here. However, we summarize briefly the procedures to operate this method as follows: we take as boundaries the

PRECEDING PAGE BLANK NOT FILMED

six planes of the computational domain as the physical observed domain. The values of the field on the lower surface at discrete points are taken from measurements of the vector magnetograms at the photospheric level. The specific computational procedures are described in ref. 2.

3. RESULTS AND PHYSICAL INTERPRETATIONS

We have analyzed vector magnetograms from Huairou Solar Observatory and Hα filtergrams from Big Bear Observatory. These vector magnetograms covered a period of seven days (from 9 - 15 March 1989). These data have a domain of 512 × 512 pixel with 0.8 arc sec for each pixel. In the present study, we only employ a 64 × 64 grid domain by taking the average of every four pixel to save the computer memories. In order to demonstrate the reliability of the present nonlinear

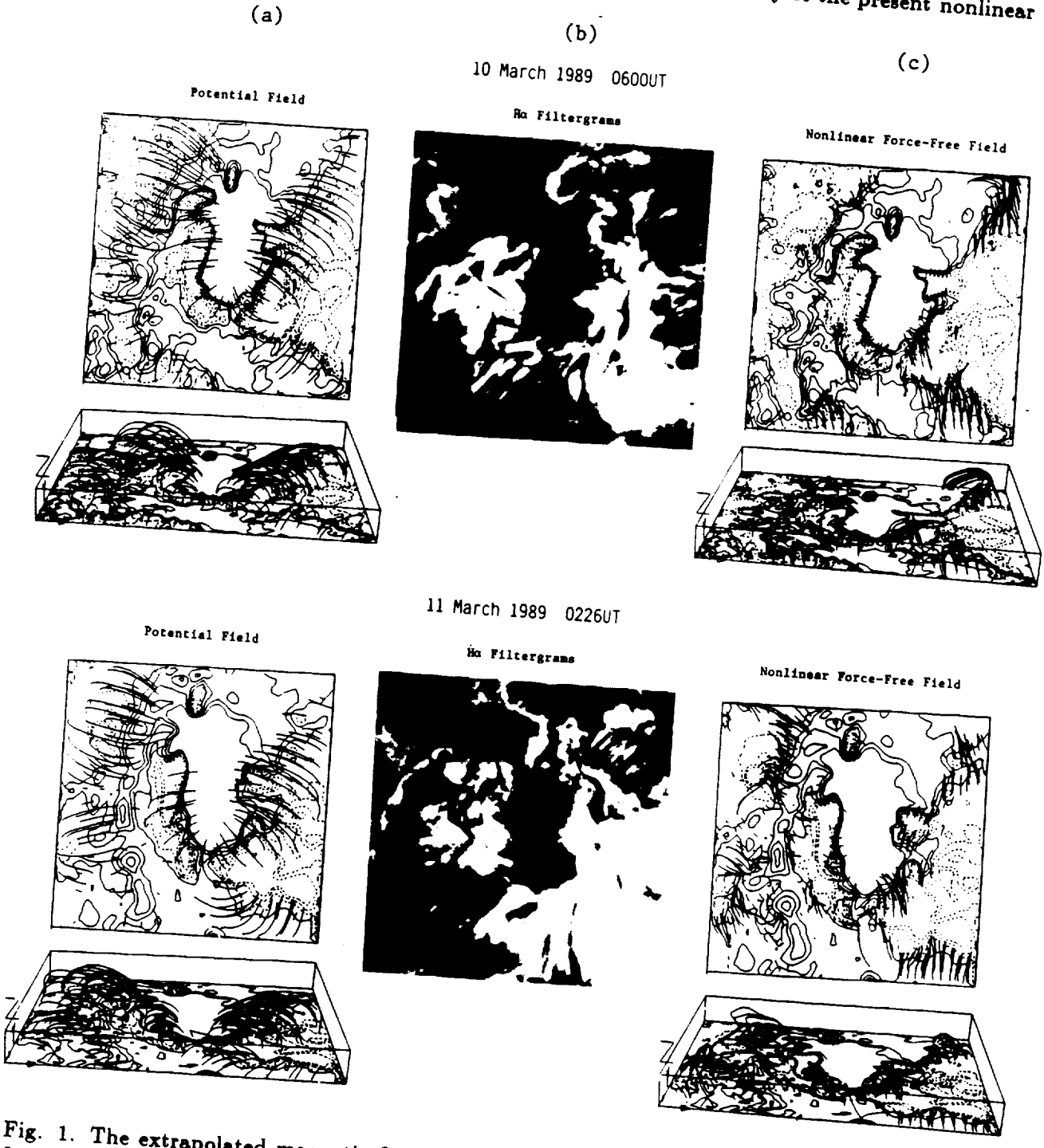

Fig. 1. The extrapolated magnetic field configuration for (a) potential and (c) nonlinear force-free fields in comparison with (b) Hα filtergrams for 10 and 11 March 1989, respectively using the NLFF model (ref. 2).

force-free field (NLFF) model, we have used it to compute the potential field configuration in comparison with Schmidt method /3/. These results clearly indicate that the magnetic field configuration in the potential field approximation derived from NLFF and Schmidt models give identical results which we have not shown here.

As soon as we verified the numerical code for NLFF model, we used this code to extrapolate the magnetic field configuration and deduced physical parameters such as total available energy and currents for NOAA AR 5395 during the period 9 - 15 March 1989. However, we only selected the most important results to present in this short paper. More detailed results will be presented elsewhere. Figure 1 shows the evolution of the three-dimensional magnetic field configuration from 10 - 11 March 1989. In this figure, the left panel is the potential field representation of the extrapolated field, the middle panel is the Hα filtergram and right panel is the nonlinear force-free representation of the extrapolated field. From these results, we note the following:

i. The potential field representation does not resemble any of the fibril and loop structures observed in the Hα filtergrams. In addition, we notice that there is no significant change in field configuration during this period. This is because in the potential field representation only the observed line-of-sight of field component is used, any the change in the transvers field is not included. In fact, it is known that the variation of transverse field is significant. This is shown in the nonlinear force-free field representation.

ii. The nonlinear force-free field representation resembles some of the fibril and loop structures observed in Hα filtergrams. For example, if we compare the results shown by Hα filtergrams and nonlinear force- free field for 10 March 1989 0600 UT, we immediately notice that the features on the right upper and lower corner resemble each other. Similar loop structures are also shown in the upper right and left corner and lower right corner of Hα filtergrams and nonlinear force-free representation on 11 March 1989 0226 UT in Figure 1.

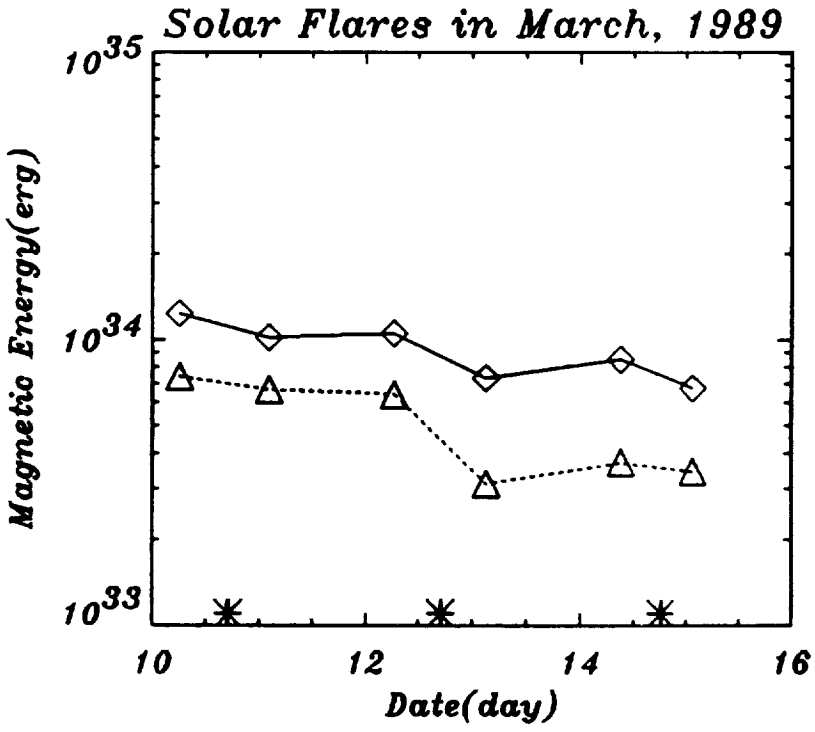

Fig. 2. Computed total available energy for the NOAA AR 5395 during the period 10 - 15 March 1989, where the solid line respresents the total energy computed from NLFF model and the dotted line represents the total energy computed from the potential field model. The difference of these two is the total available energy. The * indicates the occurrance of the flare.

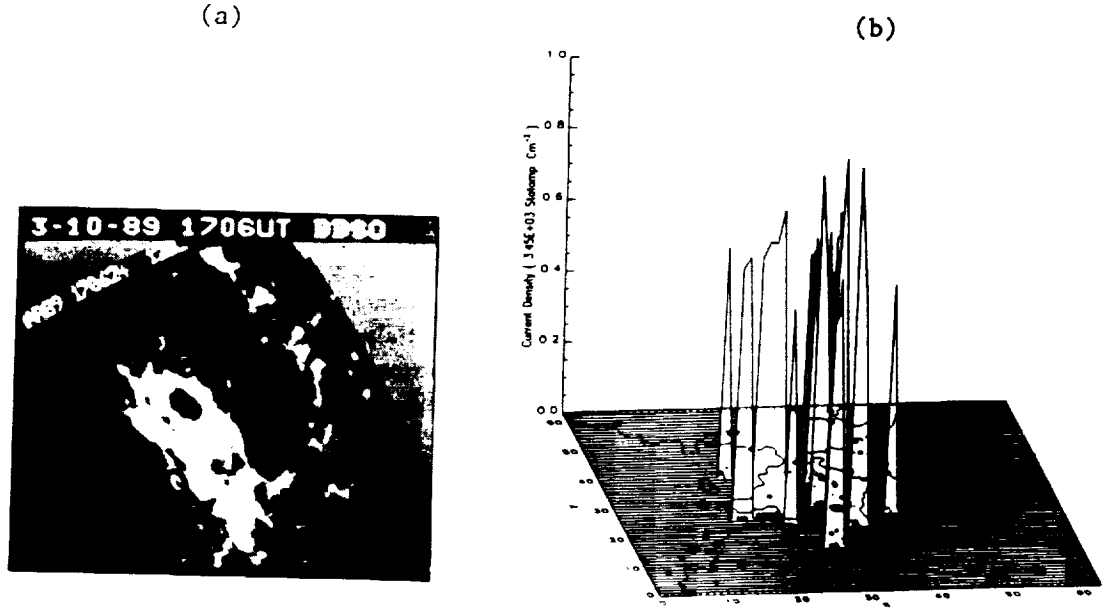

Fig. 3. (a) The location of the 10 March 1989 flare (indicated by (0)) and (b) the computed total current intensity.

iii. Using the nonlinear force-free representation, we reveal the change of the loop structures from 10 to 11 March 1989. For example, on the upper right corner, the large loop system seen on 10 March has been replaced by a rather small loop system on 11 March. On the upper left corner not much loop is seen on 10 March, but a huge loop system appeared on 11 March. To understand the geometric size of these loops, we should refer to the dimension of extrapolation which is $310,000 \times 310,000 \times 31,000$ km.

Figure 2 shows the total magnetic energy for potential field and nonlinear force -free field for NOAA AR 5395 from 10 - 16 March 1989. The available energy is simply the difference between the nonlinear force-free energy and potential field energy. To calculate this total energy is integrated $\frac{B^2}{8\pi}$ over the volume of this active region as quoted above. Finally we show the flare location (a) and current distribution (b) in Figure 3. It appears that the flare occurred where the current system was at or near maximum value. However, we can only show the maximum current intensity is merely a necessary condition for flare occurrance.

4. CONCLUDING REMARKS

We have computed the magnetic structures, current system and total magnetic energy of the NOAA AR 5395 by using the nonlinear force-free (NLFF) model given by Wu *et al.* (1990). The study demonstrates that this newly developed NLFF model does provide new physical features which cannot be shown by the most currently used potential field model. We have only shown a portion of our results. A full report of this active region from 9 - 16 March 1989 will be presented elsewhere.

ACKNOWLEDGEMENT

S. T. Wu and F. S. Weng were supported by NASA Headquarters Grant NAGW-9. Operation of BBSO is supported by NAGA Grant NAGW-1972 and NSF Grant ATM-9122023.

REFERENCES

1. Haimin Wang, Frances Tang, Harold Zirin and Guoxing Ai, Motions, Fields, and Flares in the 1989 March Active Regions, *Astrophsy. J.*, **380**, 282, (1991).

2. S. T. Wu, M. T. Sun, H. M. Chang, M. J. Hagyard and G. A. Gary, On the Numerical Computation of Nonlinear Force-Free Magnetic Fields, *Astrophys. J.* **362**, 698, (1990).

3. H. U. Schmidt, Physics of Solar Flares (NASA SP-50), 107 (1964).

MAGNETIC DIFFUSION AND FLARE ENERGY BUILDUP

S. T. WU, C. L. YIN*, and W.-H. YANG

Center for Space Plasma and Aeronomic Research, University of Alabama in Huntsville, Huntsville, AL 35899, U.S.A.

(Received 23 March, 1992; in revised form 19 June, 1992)

Abstract. Photospheric motion shears or twists solar magnetic fields to increase magnetic energy in the corona, because this process may change a current-free state of a coronal field to force-free states which carry electric current. This paper analyzes both linear and nonlinear two-dimensional force-free magnetic field models and derives relations of magnetic energy buildup with photospheric velocity field. When realistic data of solar magnetic field ($B_0 \approx 10^3$ G) and photospheric velocity field ($v_{max} \approx 1$ km s^{-1}) are used, it is found that 3–4 hours are needed to create an amount of free magnetic energy which is of the order of the current-free field energy. Furthermore, the paper studies situations in which finite magnetic diffusivities in photospheric plasma are introduced. The shearing motion increases coronal magnetic energy, while the photospheric diffusion reduces the energy. The variation of magnetic energy in the coronal region, then, depends on which process dominates.

1. Introduction

It is recognized that the magnetic field plays a key role in solar activity. The motion of photospheric plasma may shear or twist the footpoints of the coronal magnetic field, therefore, generating free magnetic energy which has been considered to be the energy source for various kinds of solar active phenomena, particularly solar flares (Švestka, 1976; Sturrock, 1980). In such a dynamic process, the vertical component of the magnetic field at the photosphere remains unchanged. Photospheric motion increases the horizontal component of the magnetic field. The coronal magnetic field, therefore, may evolve from an initially current-free state to current-carrying force-free states of higher energy when the photospheric velocity is considerably slower than the Alfvén speed of the coronal plasma. Such a scenario is based on the assumption that the magnetic field lines are frozen in the solar atmospheric medium because of its high electric conductivity. However, the observed decay of photospheric magnetic fields indicates, at least in some situations, that at the photospheric level it may have non-zero magnetic diffusivity, which allows the magnetic field to diffuse through the plasma. It is suggested that a turbulent state of photospheric plasma may raise the magnetic diffusivity to a significantly high level. In fact, it is physically necessary to have turbulent plasma for the enhancement of diffusivity to lead the magnetic reconnection in which the conversion of magnetic energy becomes possible for the flare to occur. If this indeed happens in the photosphere, one would naturally ask what influence it brings on the magnetic structure at higher altitudes in the solar atmosphere. In this paper, we investigate how finite magnetic diffusivity affects the distribution of an emerging photospheric magnetic field and the energy buildup in the coronal region. Section 2 studies

* Permanent address: Purple Mountain Observatory, Nanjing, China.

Solar Physics **142:** 313–325, 1992.
© 1992 *Kluwer Academic Publishers. Printed in Belgium.*

PRECEDING PAGE BLANK NOT FILMED

the relation of magnetic energy in force-free coronal magnetic fields with a photospheric velocity field. Two-dimensional linear and nonlinear force-free field models are analyzed. Section 3 investigates how magnetic diffusion in photospheric plasma could affect the energy buildup in the coronal field. Some physical implication of this study will be discussed in the final section.

2. Magnetic Energy Buildup

In active regions, the coronal plasma is usually dominated by the magnetic force ($\beta \ll 1$). The magnetostatic state can then be described by the force-free equation, which is

$$\nabla \times \mathbf{B} = \alpha \mathbf{B}\,, \tag{1}$$

where α is a scalar function of position. Equation (1) denotes the magnetic configuration where the electrical current is parallel to the magnetic field. It is easy to see that

$$\mathbf{B} \cdot \nabla \alpha = 0\,, \tag{2}$$

which indicates that α is constant along individual magnetic field lines. Although Equation (1) has a simple form, to derive its general solution is difficult because of its nonlinearity. The simplest case occurs when α takes the same value on each field line. Equation (1) then defines a so-called linear or constant-α force-free field. The analytical solution for a two-dimensional magnetic arcade is well known:

$$B_x = -\frac{l}{\pi d} B_0 \cos \frac{\pi}{l} x\, e^{-z/d}\,, \tag{3}$$

$$B_y = -\left(1 - \frac{l^2}{\pi^2 d^2}\right)^{1/2} B_0 \cos \frac{\pi}{l} x\, e^{-z/d}\,, \tag{4}$$

$$B_z = B_0 \sin \frac{\pi}{l} x\, e^{-z/d}\,. \tag{5}$$

This force-free field is periodic in the x-direction (Priest, 1982), and l defines the width of each bipolar field (see Figure 1). It is required that $l \leq \pi d$. The situation that $l = \pi d$ defines a current-free field ($B_y = 0$). The inclination of the field lines to the x-direction is

$$\phi = \tan^{-1}\left(\frac{\pi^2 d^2}{l^2} - 1\right)^{1/2}, \tag{6}$$

from which we have

$$d = \frac{l}{\pi \cos \phi}\,. \tag{7}$$

We may rewrite Equations (3)–(5) in the form

$$B_x = -\cos\phi\, B_0 \cos\frac{\pi}{l}\, x\, e^{-z\pi\cos\phi/l}, \tag{8}$$

$$B_y = -\sin\phi\, B_0 \cos\frac{\pi}{l}\, x\, e^{-z\pi\cos\phi/l}, \tag{9}$$

$$B_z = B_0 \sin\frac{\pi}{l}\, x\, e^{-z\pi\cos\phi/l}. \tag{10}$$

This constant-α force-free field solution has

$$\alpha = \frac{\pi}{l}\sin\phi. \tag{11}$$

The magnetic energy density is

$$\frac{B^2}{8\pi} = \frac{B_0^2}{8\pi}\, e^{-2z\pi\cos\phi/l}, \tag{12}$$

which is a function of z only when the width l and the inclination angle ϕ are given. We can calculate the total magnetic energy per unit length in the y-direction for a single bipolar field by integrating Equation (12) in the domain $x = -l/2, l/2$; $z = 0, \infty$. We obtain

$$E = \frac{l^2}{\cos\phi}\,\frac{B_0^2}{16\pi^2}. \tag{13}$$

Since the case $\phi = 0$ represents the current-free state, Equation (13) can be rewritten as

$$E = \frac{E_0}{\cos\phi}, \tag{14}$$

where E_0 is the magnetic energy of the current-free state. Equation (14) shows how the shearing motion increases the coronal magnetic energy in the situation where the B_z-component at $z = 0$ remains unchanged. We find $E = 1.06,\ 1.31,\ 2,\ 5.8E_0$ for $\phi = 20°,\ 40°,\ 60°,\ 80°$, respectively. When $\phi \to 90°$, $E \to \infty$.

We consider that the magnetic field is initially in a current-free state and then evolves quasi-statically to force-free states due to slow photospheric motion. We assume that the maximum velocity at the boundary $x = l/2$ is v_{max} and the photospheric velocity field is linearly symmetric to the origin of the coordinates as shown in Figure 1. We have

$$Y = \frac{l}{2}\tan\phi, \tag{15}$$

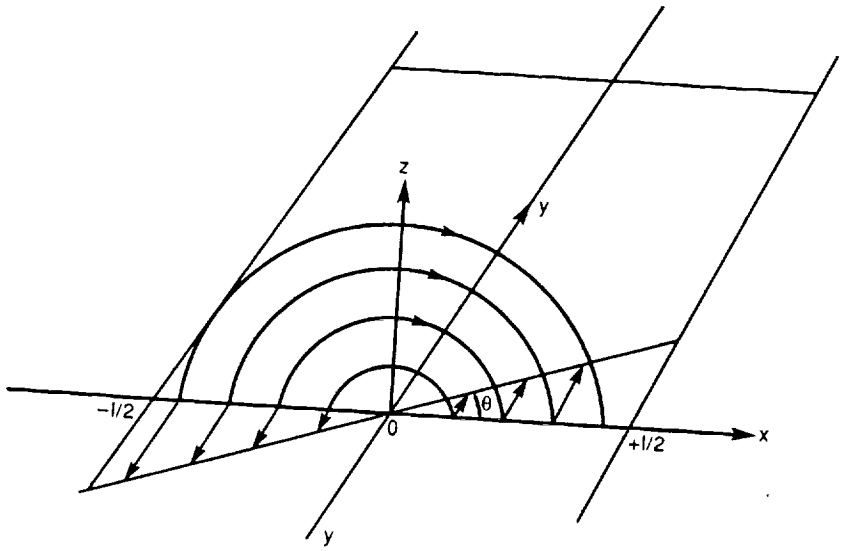

Fig. 1. Schematic representation of a bipolar magnetic field topology and shear configuration.

where Y is the maximum shearing displacement, and thus

$$v_{max} = \frac{dY}{dt} = \frac{l}{2\cos^2\phi}\frac{d\phi}{dt} . \tag{16}$$

From Equation (14), we obtain the magnetic energy change rate

$$\frac{dE}{dt} = \frac{2}{l} v_{max} \sin\phi E_0 . \tag{17}$$

If the length of the magnetic arcade in the y-direction is about $3l$, the total magnetic energy in the current-free state is approximately

$$W_0 = \frac{3l^3}{16\pi^2} B_0^2 . \tag{18}$$

In the case that $l = 1.6 \times 10^4$ km and $B_0 = 1000$ G, we get $W_0 = 4.3 \times 10^{31}$ erg. If $v_{max} = 1$ km s^{-1}, to build up an amount of free magnetic energy $\sim W_0$ ($\phi = 60°$) needs about 4 hours.

With the shearing of velocity and magnetic field configuration mentioned above, Wu *et al.* (1984) calculated the energy buildup for a flare-productive region by numerical modeling and obtained similar results. The linear force-free field model discussed above is restricted by its periodic boundary condition in the x-direction and the linear dependence of the photospheric velocity field in the x-coordinate. Several numerical techniques have been developed in recent years to compute more general cases of force-free magnetic fields and simulate the coronal magnetic fields (e.g., Yang, Sturrock, and Antiochos, 1986; Wu *et al.*, 1990). One important purpose of those efforts is to investigate magnetic energy buildup in the solar atmosphere through shearing or twisting

a potential field to a sequence of force-free fields. In the following, we adopt the two-dimensional magnetic field model previously used in deriving an empirical formula of estimating magnetic energy in a sheared field (Klimchuk, Sturrock, and Yang, 1988). The magnetic field model is two-dimensional, $\mathbf{B}(x, z)$. The B_z-distribution at $z = 0$ is assumed to have the form

$$B_z(x, 0) = B_0 \frac{2x}{x_0^2} e^{-x^2/x_0^2}, \tag{19}$$

so B_z changes sign at $x = 0$. The shearing displacement of footpoints in the y-direction is represented by

$$y(x, 0) = \begin{cases} y_0 + Y \sin\left(\frac{\pi x}{l}\right)\left|\sin\left(\frac{\pi x}{l}\right)\right|, & |x| \le l; \\ 0, & |x| > l. \end{cases} \tag{20}$$

The force-free field solution for the half-space domain ($z > 0$) can be obtained numerically by the so-called magneto-frictional method. However, the empirical formula derived would be convenient for the purpose of this study. The total magnetic energy on the base of both sheared and non-sheared fields can be estimated approximately by

$$E(S) = E_0[1 + a \ln(1 + bS^2)], \tag{21}$$

where E_0 is the energy of the current-free state ($Y = 0$), $S = Y/x_0$, a, b are parameters which depend on the field configuration. The energy buildup rate is

$$\frac{dE}{dt} = \frac{2abSE_0}{1 + bS^2} \frac{dS}{dt}. \tag{22}$$

To build up n-times magnetic energy in the field (i.e., $E = nE_0$), the maximum displacement of the footpoints is

$$Y = \frac{[e^{(n-1)/a} - 1]^{1/2}}{b^{1/2}} x_0; \tag{23}$$

and the time needed is

$$\Delta t = Y/v_{max}, \tag{24}$$

where $v_{max} = dY/dt$ is assumed to be constant. Using the results given by Klimchuk, Sturrock, and Yang (1988), we have $a = 0.8156$ and $b = 0.8318$. From Equations (21)–(24), we found that it takes ~ 3 hr to build up magnetic energy by a factor of two, $E = 2E_0$, with $v_{max} = 1$ km s^{-1} and $x_0 = l = 4 \times (1.6 \times 10^3)$ km.

3. The Effect of Magnetic Diffusion

It has been understood according to classic theory (Spitzer, 1962) that the solar atmosphere is highly conducting. The magnetic field, therefore, can be considered to be frozen in the plasma. The magnetic field lines are moving with the photospheric velocity field. However, it has been suggested that magnetic diffusivity may be enhanced in the presence of a plasma-turbulent state or fluid eddy.

Observation indicates that supergranulation plays an important role in the evolution of a solar active region. The generation of new magnetic regions and the decay of old magnetic fields relate to supergranule motion (Schröter, 1971). On the photospheric surface, the magnetic flux first appears in the upwelling at the center of a supergranulation cell, and then is swept to the cell's boundaries by the horizontal motion of the supergranulation. The eddy diffusion associated with random motion of the supergranulation causes magnetic flux decay. Observations of high resolution provide some evidence for diffusion on the decay of the active region's magnetic field. There is no lack of such examples in published observational data (e.g., Martin, Livi, and Wang, 1985).

The eddy magnetic diffusivity created by stochastic motion in granulation and supergranulation can be estimated by (Parker, 1979)

$$\eta = 0.2v^2\tau, \tag{25}$$

where v and τ are the velocity and lifetime of the fluid eddy, respectively. Observation indicates $v \approx 1$ km s^{-1}, $\tau \approx 10^3$ s for granulation; therefore, $\eta \approx 2 \times 10^8$ m^2 s^{-1}. For supergranulation $v \approx 0.2$ km s^{-1}, $\tau \approx 10^5$ s; hence, $\eta \approx 8 \times 10^8$ m^2 s^{-1}.

Leighton (1969) developed a kinematic model of the 22-yr cycle based on the random walk of fields diffusing from spotgroups and obtained a diffusivity of 7.7×10^8 m^2 s^{-1} to 1.54×10^9 m^2 s^{-1}. He found the poleward drift rate of fields could be matched by $\eta = 10^9$ m^2 s^{-1}. Mosher (1977) constructed a diffusion model of the solar magnetic field based on the cross-correlation equation fitting K line data and Hα data, and derived effective diffusion constants of 2×10^8 m^2 s^{-1} and 4×10^8 m^2 s^{-1}, respectively. Zirin (1985) got $\eta = 3 \times 10^8$ m^2 s^{-1} from the actual motion of network elements. However, Marsh (1978) suggested that the reconnection of ephemeral regions with the network would produce a diffusivity $\eta = 8 \times 10^8$ m^2 s^{-1}, but Wang and Sheeley (1991) disputed Marsh's suggestion. DeVore *et al.* (1985) proposed models of the evolution of magnetic regions by starting with an observed magnetogram and reproducing the field distribution observed a month later. They assumed a diffusivity $\eta = 3 \times 10^8$ m^2 s^{-1}. Wang (1988) analyzed the videomagnetogram data at Big Bear Solar Observatory, and suggested a value of 1.5×10^8 m^2 s^{-1}. More recently, Wang, Nash, and Sheeley (1989) suggested that a new value for diffusivity be 6×10^8 m^2 s^{-1}. It is then interesting to estimate how those diffusivities would affect the photospheric magnetic field distribution and the energy buildup process in the solar corona.

The induction equation is

$$\frac{\partial \mathbf{B}}{\partial t} = \nabla \times (\mathbf{v} \times \mathbf{B}) + \eta \nabla^2 \mathbf{B}, \tag{26}$$

where η is the magnetic diffusivity. We assume that the magnetic fields beneath the photospheric surface have z-component only, which has the same distributions of the force-free magnetic field models (at $z = 0$ plane) as adopted in Section 2. Since the photospheric shearing velocity v is set in the y-direction, in the present study Equation (26) could be reduced to a simple form of a one-dimensional diffusion equation

$$\frac{\partial B_z}{\partial t} = \eta \frac{\partial^2 B_z}{\partial x^2} . \tag{27}$$

In fact, the diffusion occurs in two directions on the Sun. The adoption of one dimension for the present study is merely for mathematical convenience and to understand the insight of the first-order physics during the process. For the periodic linear field model, the initial field is assumed to be

$$B_z = B_0 \sin \frac{\pi}{l} x . \tag{28}$$

We obtain the solution of Equation (27), which is

$$B_z = B_0 \sin \frac{\pi}{l} x \exp\left[- \eta \frac{\pi^2}{l^2} t \right]. \tag{29}$$

The magnetic field maintains the sinuous distribution, while its magnitude declines exponentially with time. We then assume that the coronal magnetic field evolves through consecutive force-free states corresponding to time-varying $B_z(x, 0, t)$. Its magnetic energy then varies in the manner

$$E = \frac{E_0}{\cos \phi} \exp\left(- \frac{2\pi^2}{l} \eta t \right) \tag{30}$$

and

$$\frac{dE}{dt} = \frac{E_0}{l \cos \phi} \left(v_{max} \sin 2\phi - \frac{2\pi^2}{l} \eta \right) \exp\left(- \frac{2\pi^2}{l^2} \eta t \right). \tag{31}$$

Equation (31) includes the influence of two factors: shearing by the photospheric plasma increases the energy in the coronal magnetic field; and photospheric diffusion reduces the field energy. To keep the magnetic energy, E, increasing with time requires

$$v_{max} > \frac{2\pi^2 \eta}{l \sin 2\phi} . \tag{32}$$

In the following, we compare four situations, in which η takes the values of 10^9 m^2 s^{-1}, 3×10^8 m^2 s^{-1}, 1.5×10^8 m^2 s^{-1}, and 0, respectively. Figure 2 illustrates the decrease of the magnitude of the $B_{z\max}/B_0$-distribution at $z = 0$. Then assuming v_{max} equal to 1 km s^{-1}, 0.5 km s^{-1}, 0.1 km s^{-1}, we calculate the variation of magnetic

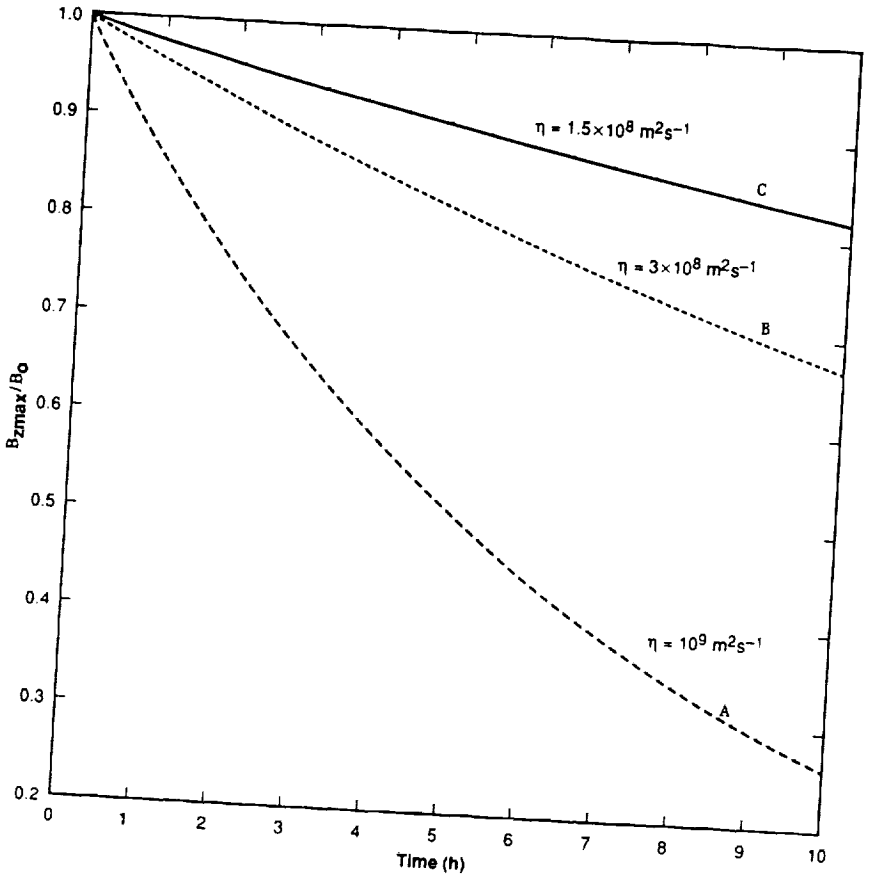

Fig. 2. Curves A, B, C show the decay of the photospheric magnetic field of model 1 when taking $\eta = 10^9$, 3×10^8, and $1.5 \times 10^8\ m^2\ s^{-1}$, respectively.

energy for the same magnetic diffusivities. These results are plotted in Figures 3(a), 3(b), and 3(c). In comparing these results, we notice that the total energy in the coronal field decreases for large magnetic diffusivity. For example, the case of $\eta = 3 \times 10^8\ m^2\ s^{-1}$ indicates that a fast photospheric velocity field ($1\ km\ s^{-1}$) is able to increase the magnetic energy in the corona; however, the energy decreases when the shearing motion becomes too slow (e.g., $0.1\ km\ s^{-1}$).

The second case of Section 2 is a problem of magnetic diffusion with an infinite boundary. The distribution of the B_z-field in the photosphere evolves as

$$B_z = \frac{B_0}{ht^{1/2}} \int_{-\infty}^{\infty} \xi \exp(-e\xi^2 + b\xi - e)\, d\xi, \tag{33}$$

where

$$c = \frac{x_0^2 + 4\eta t}{4\eta t x_0^2}, \qquad d = \frac{x}{2\eta t}, \qquad e = \frac{x^2}{4\eta t},$$

and

$$h = x_0^2(\eta\pi)^{1/2}.$$

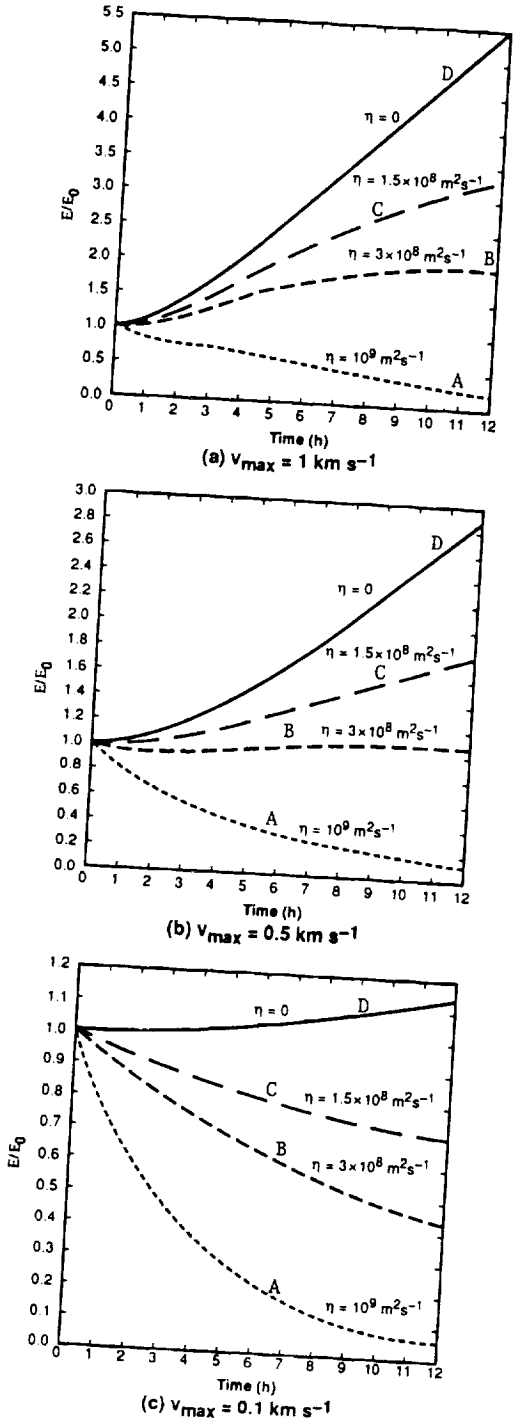

Fig. 3. Magnetic energy variation in the corona for different velocity fields in the photosphere: (a) v_{max} = 1 km s^{-1}; (b) v_{max} = 0.5 km s^{-1}; (c) v_{max} = 0.1 km s^{-1}. The labeled *A*, *B*, *C* denote the cases of the different magnetic diffusivities as shown in Figure 2. $\eta = 0$ case is labeled by *D*.

B_z in Equation (33) can be calculated directly by numerical integration. Figure 4 shows how the B_z-distribution varies with time at $z = 0$ for $\eta = 10^9$ m^2 s^{-1}. The time interval of each curve is 3 hours, and the curve *A* represents the initial distribution of B_z at $t = 0$. In comparison with Figure 1, the decay speed of this model is obviously slower.

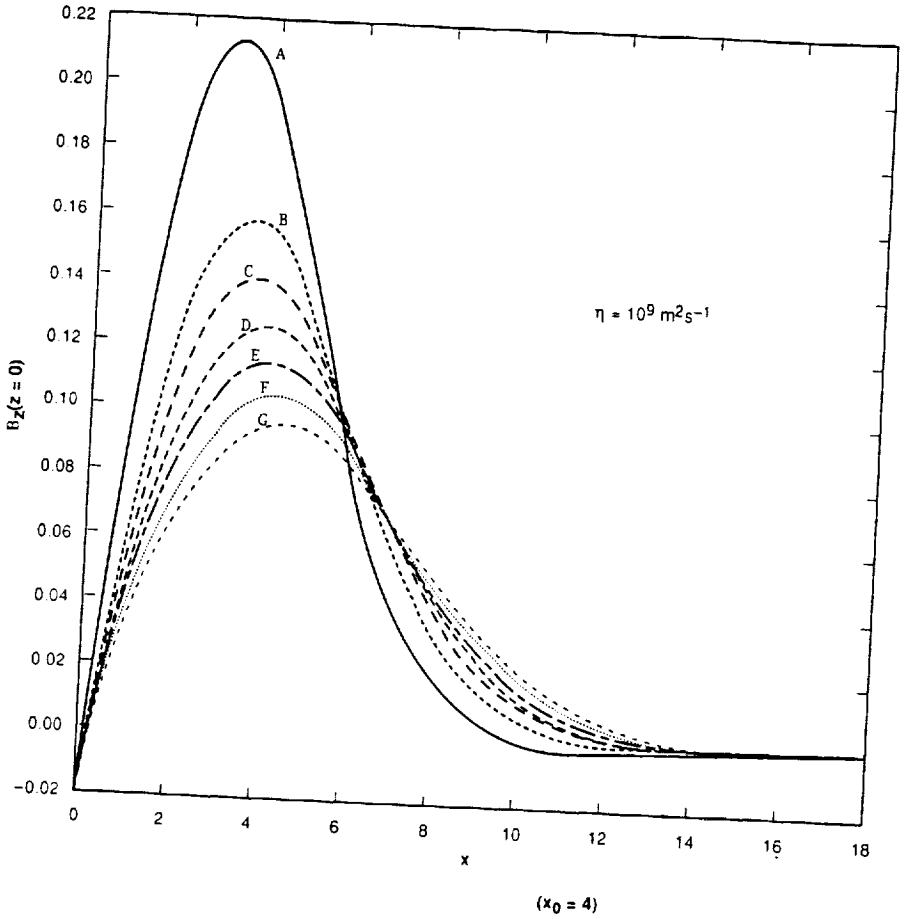

Fig. 4. B_z-distribution varies with time at $z = 0$ for $\eta = 10^9$. The time interval of each curve from A to G is 3 hours, and the curve A represents the initial distribution at $t = 0$.

Applying Equation (21), where the normalized shearing extent is modified as

$$S = \left[\frac{\int_0^{\infty} [y(x, 0)/x]^2 [B_z]^2 \, dx}{\int_0^{\infty} [B_z]^2 \, dx} \right]^{1.2}, \tag{34}$$

we can calculate the increase of free magnetic energy in a sheared field with diffusion (see Figure 5). Taking the same diffusivities ($\eta = 10^9\ m^2\ s^{-1}$, $3 \times 10^8\ m^2\ s^{-1}$, $1.5 \times 10^8\ m^2\ s^{-1}$, and 0) and shearing velocities ($v_{max} = 1$, 0.5, and 0.1 km s^{-1}) as in case 1, we find that the efficiency of energy buildup is higher than in the linear model. The increasing rate of magnetic energy decreases as diffusivity and time both increase so that the free magnetic energy cannot, in fact, become arbitrarily large.

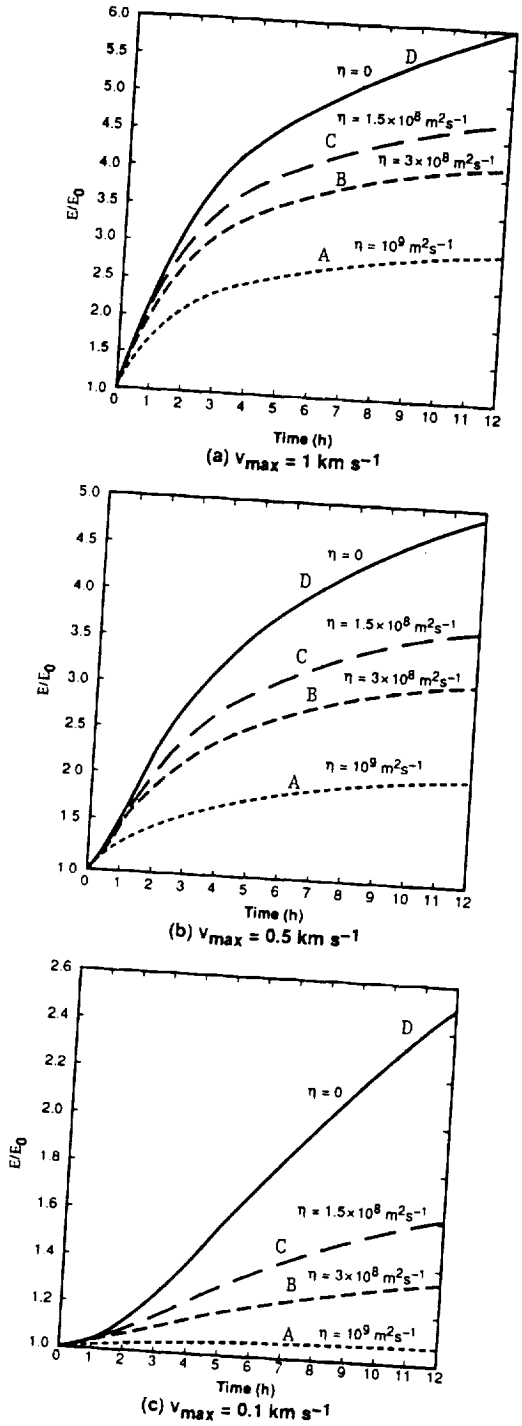

Fig. 5. The increase of free magnetic energy of the nonlinear model of Section 3 for different shearing velocities: (a) v_{max} = 1 km s^{-1}; (b) v_{max} = 0.5 km s^{-1}; (c) v_{max} = 0.1 km s^{-1}. The labeled *A*, *B*, *C*, *D* denote the cases of the different magnetic diffusivities.

4. Summary and Discussion

In this study we have presented a model to investigate the property of a nonlinear force-free magnetic field and the effects of magnetic diffusivity for flare energy buildup. The importance of our findings can be summarized as follows:

(i) Photospheric motion distorts magnetic field lines and enhances electric currents in the coronal region. The magnetic energy buildup depends on the photospheric magnetic field and velocity field. The linear, force-free magnetic field model simulates the situation of a bipolar magnetic field confined by a finite boundary, which involves interaction with the boundary during the shearing process. The magnetic field lines of the nonlinear field model of Section 2 are free to expand in a half-space domain with their footpoints rooted in the photosphere. When shearing becomes arbitrarily large, these two-dimensional models show an infinite magnetic energy (unit length in the y-direction), as indicated by Equation (14) and implied by Equation (21). The increasing energy rate, however, behaves differently because of the different boundary condition imposed. From Equations (17) and (22), the magnetic energy increase rate can be written in the form

$$\frac{dE}{dt} = \Gamma v_{max} E_0 , \tag{35}$$

where Γ is the function of the shearing extent. dE/dt is increasing with the shearing motion for the linear field model, but decreasing for the half-space field model. When we use some typical values of the solar magnetic field (1000 G) and velocity field (1 km s^{-1}), to create an amount of free magnetic energy $\sim E_0$ takes about 3–4 hours for both cases.

(ii) The suggestion of diffusion of photospheric magnetic fields is inferred from the observed decay of the magnetic field on the quiet Sun and the magnetic field in the active regions. The question is whether the magnetic diffusivity introduced affects magnetic energy storage in the solar corona, and if so, how? We investigate this problem by solving the diffusion equation using different values of magnetic diffusivity proposed by several authors. The calculations in Section 3 show the significant influence of magnetic diffusion, particularly for the linear field model, where fixed periodic magnetic neutral points are imposed. As a matter of fact, for high values of the magnetic diffusivity, the coronal field always decays when photospheric shearing motion is taken into account. We further note that in such a situation, shearing motion still stores free magnetic energy in the corona. The amount of free magnetic energy can be estimated by comparing with the possible current-free field energy at that time. The current-free field energy decreases with time because of magnetic diffusion of $B_z(x, 0)$. The physical nature of magnetic diffusion relating to turbulent photospheric plasmas is still not well understood. Further exploration of this subject would benefit the study of magnetic evolution and flare occurrence in the solar active region.

Finally, we may conclude on the basis of these results that

(i) to estimate the total energy storage in the magnetic field more accurately, the effect of diffusion of photospheric fields needs to be considered;

(ii) because of the inclusion of diffusion, the magnitude of the shear speed becomes a very important factor in the flare energy buildup process.

Acknowledgements

The authors wish to thank Drs Marcos Machado and E. Tandberg-Hanssen for reading the manuscript and giving critical suggestions. This work has been supported by a NASA Headquarters Grant (Space Physics Div./Solar Phys. NAGW-9).

References

DeVore, C. R., Sheeley, N. R., Jr., Young, T. R., Jr., and Harvey, K. L.: 1985, *Australian J. Phys.* **38**, 999.
Klimchuk, J. A., Sturrock, P. A., and Yang, W.-H.: 1988, *Astrophys. J.* **335**, 456.
Leighton, R. B.: 1964, *Astrophys. J.* **140**, 1547.
Marsh, K. A.: 1978, *Solar Phys.* **59**, 105.
Martin, F. S., Livi, S. H. B., and Wang, J.: 1985, *Australian J. Phys.* **38**(6), 929.
Mosher, J. M.: 1977, *Solar Phys.* **53**, 375.
Parker, E. N.: 1979, *Cosmical Magnetic Field*, Oxford University Press, New York, p. 509, p. 522.
Schröter, E. N.: 1971, in R. Howard (ed.), *Solar Magnetic Fields*, p. 167.
Spitzer, L.: 1962, *Physics of Fully Ionized Gases*, Interscience, New York.
Sturrock, P. A.: 1980, *Solar Flares*, Colorado Associated University Press, Boulder.
Švestka, Z.: 1976, *Solar Flares*, D. Reidel Publ. Co., Dordrecht, Holland.
Wang, H.: 1988, *Solar Phys.* **116**, 1.
Wang, Y.-M. and Sheeley, N. R., Jr.: 1991, *Astrophys. J.* **375**, 761.
Wang, Y.-M., Nash, A. G., and Sheeley, N. R., Jr.: 1989, *Science* **245**, 681.
Wu, S. T., Hu, K. R., Krall, K. R., Hagyard, M. J., and Smith, J. B., Jr.: 1984, *Solar Phys.* **90**, 117.
Wu, S. T., Sun, M. T., Chang, H. M., Hagyard, M. J., and Gary, G. A.: 1990, *Astrophys. J.* **362**, 698.
Yang, W.-H., Sturrock, P. A., and Antiochos, S. K.: 1986, *Astrophys. J.* **309**, 383.
Zirin, H.: 1985, *Astrophys. J.* **291**, 858.

Journal of Atmospheric and Terrestrial Physics, Vol. 55, No. 7, pp. 939–945, 1993.
Printed in Great Britain.

0021-9169/93 $6.00 + .00
© 1993 Pergamon Press Ltd

Numerical modeling of the energy storage and release in solar flares

S. T. Wu and F. S. Weng

Center for Space Plasma and Aeronomic Research and Department of Mechanical Engineering, The University of Alabama in Huntsville, Huntsville, AL 35899 U.S.A.

(*Received in final form* 22 *June* 1992; *accepted* 22 *June* 1992)

Abstract—This paper reports on investigation of the photospheric magnetic fieldline footpoint motion (usually referred to as shear motion) and magnetic flux emerging from below the surface in relation to energy storage in a solar flare. These causality relationships are demonstrated by using numerical magnetohydrodynamic simulations. From these results, one may conclude that the energy stored in solar flares is in the form of currents. The dynamic process through which these currents reach a critical value is discussed as well as how these currents lead to energy release, such as the explosive events of solar flares.

1. INTRODUCTION

It is understood that the Sun is the primary source of electromagnetic energy powering atmospheric and oceanic circulation and photosynthesis in the biosphere. Its continuous corpuscular emission, the solar wind, determines the shape and dynamics of the outer envelope, the magnetosphere, of Earth's environment. It is also recognized that the Sun is a variable star; its size oscillates in a variety of modes. Also, it is known that various solar processes affect the composition, structure and dynamics of Earth's atmosphere. Earth's atmosphere is directly influenced by the very complex behavior displayed by solar spectral irradiance from X-rays through the visible domain to the infra-red.

We limit ourselves, in this paper, to a discussion of a specific topic, the energy source propelling the solar flare. It is now generally understood that flare energy results from stressed solar magnetic fields. The physical processes that cause the solar magnetic field to be stressed could be due to photospheric shear motion and emerging flux from the convective zone. It has been shown both theoretically and observationally (Zirin and Tanaka, 1973; Tanaka and Nakagawa, 1973; Low, 1977; Wu *et al.*, 1984; Hagyard, 1990) that one of the physical processes involved in the storage of flare energy in the solar magnetic field is the shearing of magnetic fields due to photospheric motion. Zirin and Tanaka (1973) reported that they had observed proper motion of sunspots in relation to changes in a representative active region (McMath 11976) where flares occurred. Recently, Moore (1990) has summarized the observed properties for sunspots and solar active regions. This summary again shows that there is an intimate relationship between sunspots' motion and occurrence of flares. All these results are centered on photospheric motion whereby the solar magnetic field could be twisted due to the interaction between plasma motion and the magnetic field. Stresses build up in the magnetic field in such a way that the energy needed to propel the flare is thereby stored. On the other hand, some observations (Rust, 1972, 1974) showed that the emerging magnetic flux also will cause the field to be stressed, with a subsequent storage of additional energy which can be made available to propel the solar flare. Following this observational and theoretical evidence, we suggest the following scenario for flare energy storage and release: that is, the solar magnetic field will be stressed (twisted) due to both photospheric motion (i.e. shear motion) *and* emerging flux. When the magnetic field is twisted, electric currents are generated. As soon as the currents reach a critical value (Wu and Xu, 1992), the energy stored in these currents is released and will cause the occurrence of one or more flares.

In this paper, we employ a simulation model to illustrate these two physical processes. Section 2 of the paper presents the simulation model and initial boundary conditions appropriate for this study. Section 3 discusses the numerical results and Section 4 contains a discussion. Finally, Section 5 presents the concluding remarks.

2. SIMULATION MODEL

The simulation model used in this study is based on ideal (infinite electrical conductivity) magnetohydrodynamics (MHD) given by Wu *et al.* (1983). The basic set of MHD equations adequate to describe these physical processes consist of the conservation laws of mass, momentum and energy together with the induction equation of the magnetic field to account for the interaction between the plasma motion and the magnetic field. These two-dimensional, nonplanar, time-dependent MHD equations are identical to those given by Wu *et al.* (1983) and will not be reproduced

PRECEDING PAGE BLANK NOT FILMED

here. In seeking the numerical solution for this set of nonlinear partial differential equations, we are concerned with an initial boundary value problem. The initial condition is the steady-state solution of the set of MHD equations. Physically, this solution represents an isothermal hydrostatic equilibrium atmosphere with temperature (T_0) being 10^5 K and the number of density (n_0) at the lower boundary (i.e. $y = 0$) of 10^{14} cm^{-3}. The magnetic field configuration which satisfies this set of MHD equations can be either a potential or a force-free magnetic field configuration. For convenience, we have chosen a bipolar magnetic field topology as the initial magnetic field (see Fig. 1). Physically, this magnetic field configuration resembles a magnetic arcade that is usually observed on the solar surface beneath a helmet streamer. We chose the mathematical expressions representing this magnetic topology to be a potential dipole field given by the following equations:

$$B_x^0 = B_c \cos\left(\frac{\pi x}{2x_0}\right) e^{-\pi y/2x_0}$$

$$B_y^0 = -B_c \sin\left(\frac{\pi x}{2x_0}\right) e^{-\pi y/2x_0}$$

$$B_z^0 = 0 \qquad (1)$$

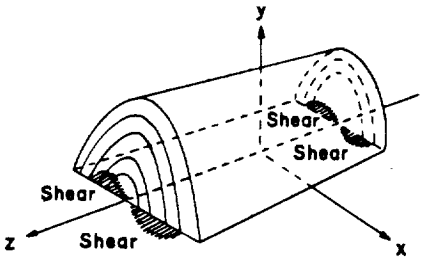

(a)

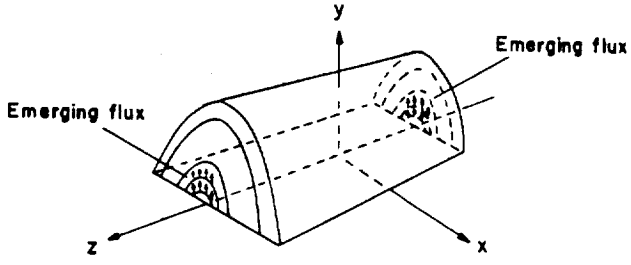

(b)

Fig. 1. Schematic description of an axisymmetric bipolar magnetic field subjected to (a) footpoint shearing motion at the photosphere; and (b) emerging magnetic flux from the sub-photosphere in the direction indicated by the arrows.

where B_c is the magnetic field strength at the solar surface, the commonly-observed neutral line (i.e. $x = 0, y = 0, z = 0$).

The boundary conditions used for this calculation are identical to those used by WU *et al.* (1984). They are as follows: the top boundary condition is the non-reflecting boundary condition (i.e. where all the gradients of the physical parameters are set equal to zero); the side boundaries are symmetric; finally, the lower boundary condition is prescribed on the solar surface. The initial atmosphere is needed for closure of the mathematical problem. To satisfy the magnetic topology which is chosen for this problem, the initial atmosphere is isothermal at hydrostatic equilibrium.

In order to simulate the physical conditions at the lower boundary, we describe the cases of photospheric shear and emerging magnetic flux as follows.

(i) *Photospheric shear case*

This case is similar to the one described by WU *et al.* (1984). Here, the photospheric motion of the footpoints of flux loops at the base (i.e. at $y = 0$, the x–z plane represents the photosphere) is simulated by the following expressions:

$$W = W_0(t) \sin\left(\frac{\pi x}{2x_0}\right)$$

where

$$W_0(t) = \begin{cases} (t/\tau) W_c, & 0 \leqslant t \leqslant \tau \\ W_c, & t \geqslant \tau \end{cases} \qquad (2)$$

where W_c is the velocity along the z-axis as shown in Fig. 1a. This velocity is a constant corresponding to the photospheric shear velocity. The magnitude of this velocity, chosen on the basis of observation, is a few hundred meters per second to an order of km s^{-1} at the peak of the shearing profile shown in Fig. 1a.

(ii) *Emerging flux case*

Observationally, it has been shown that emerging magnetic flux (RUST, 1972, 1974) could constitute another physical mechanism that can cause the magnetic field to be stressed with subsequent relaxation, thus propelling solar activity as discussed above. In order to simulate this case, the lower perturbed boundary conditions are mathematically expressed by the following equations:

$$B_x = B_c(1+\omega) \cos\left(\frac{\pi x}{2x_0}\right)$$

$$B_y = -B_c(1+\omega) \sin\left(\frac{\pi x}{2x_0}\right) \qquad (3)$$

where B_c is a constant which represents the magnetic field strength at the reference center. The parameter ω is chosen to scale the amount of the emerging flux's energy supply to the system. The energy supply is equivalent to the shear motion case and is given as follows:

$$\omega = -1+\sqrt{\varepsilon_1}, \qquad 0 \leqslant t \leqslant \tau$$
$$\omega = -1+\sqrt{\varepsilon_2}, \qquad t \geqslant \tau \tag{4}$$

with

$$\varepsilon_1 = \varepsilon\left(\frac{t}{\tau}\right)^4 + 1,$$
$$\varepsilon_2 = \varepsilon\left[2\left(\frac{t}{\tau}\right)-1\right]^2 + 1$$

where ε is an arbitrary constant, chosen as 7×10^{-5} for $\beta_0 = 1.0$ and 7×10^{-6} for $\beta_0 = 0.1$, respectively, in the present study. These values are determined by the strength of the emerging flux. A schematic representation of this physical situation is shown in Fig. 1b.

3. NUMERICAL RESULTS

In the present study, two separate numerical simulations were performed to investigate energy build-up via two different physical situations: (i) energy storage due to photospheric shear motion; and (ii) energy storage due to emerging magnetic flux from the subphotosphere. In these two cases, the simulation domain has the size of 1.6×10^4 km in the x direction and 2×10^4 km in the y direction; the z direction is a dummy variable. The results from these simulations are summarized as follows:

(i) *Energy storage due to photospheric shear motion*

In this simulation, two cases with different initial plasma beta (β_0) values are computed. For the case of $\beta_0 = 0.1$, the B_c is equal to ~1500 gauss, leading to characteristic Alfven speed and time as ~120 km s^{-1} and ~70 s, respectively. If we choose B_c to be somewhat smaller, ~500 gauss, the value β_0 is 1.0 and the Alfven speed and characteristic time are ~60 km

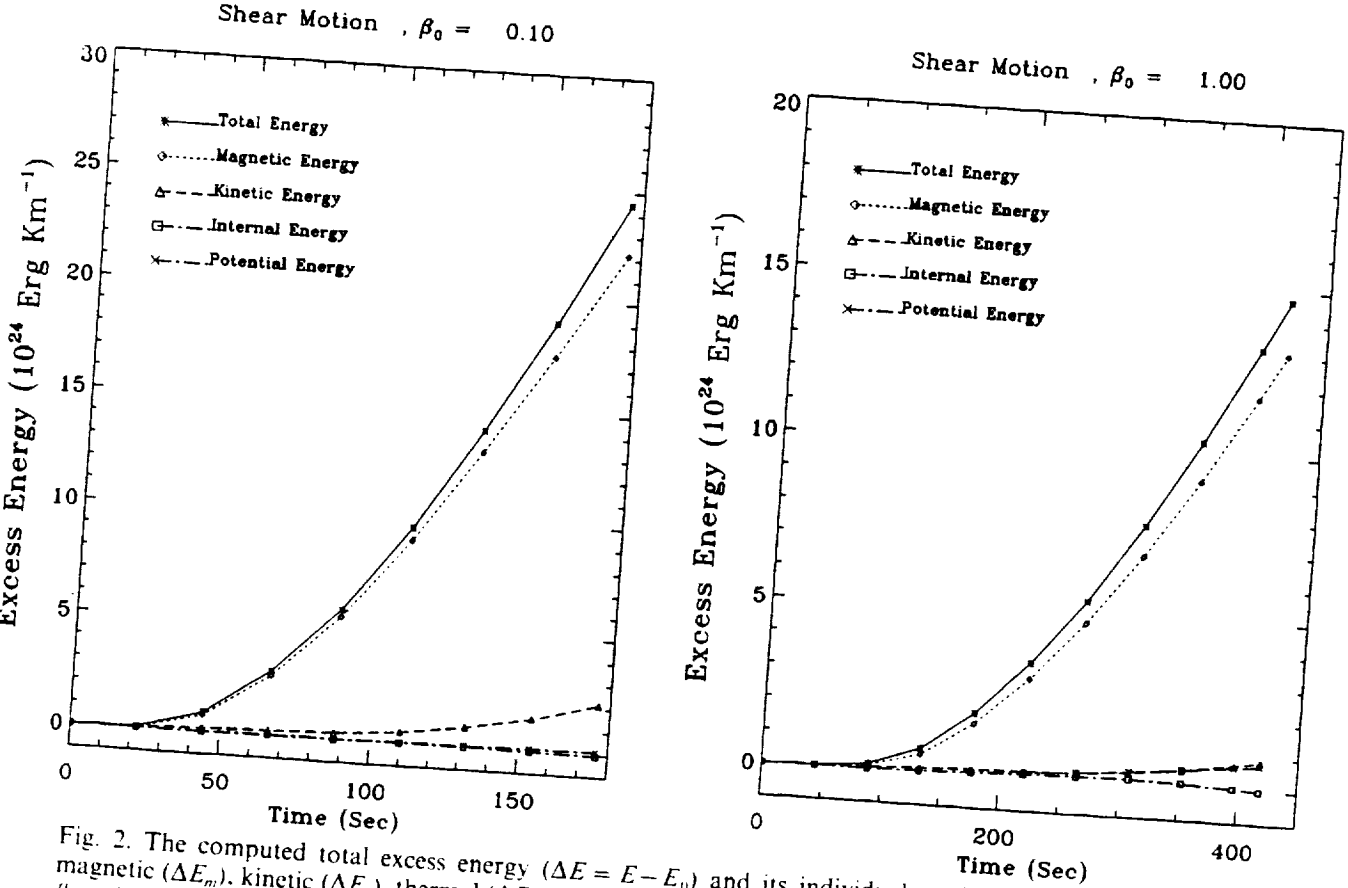

Fig. 2. The computed total excess energy ($\Delta E = E - E_0$) and its individual mode of excess energy of magnetic (ΔE_m), kinetic (ΔE_k), thermal (ΔE_T) and potential (ΔE_p) energies vs time for (a) $\beta_0 = 0.1$ and (b) $\beta_0 = 1.0$, respectively, due to photospheric shearing motion with a maximum shearing speed of 1.0 km s^{-1}.

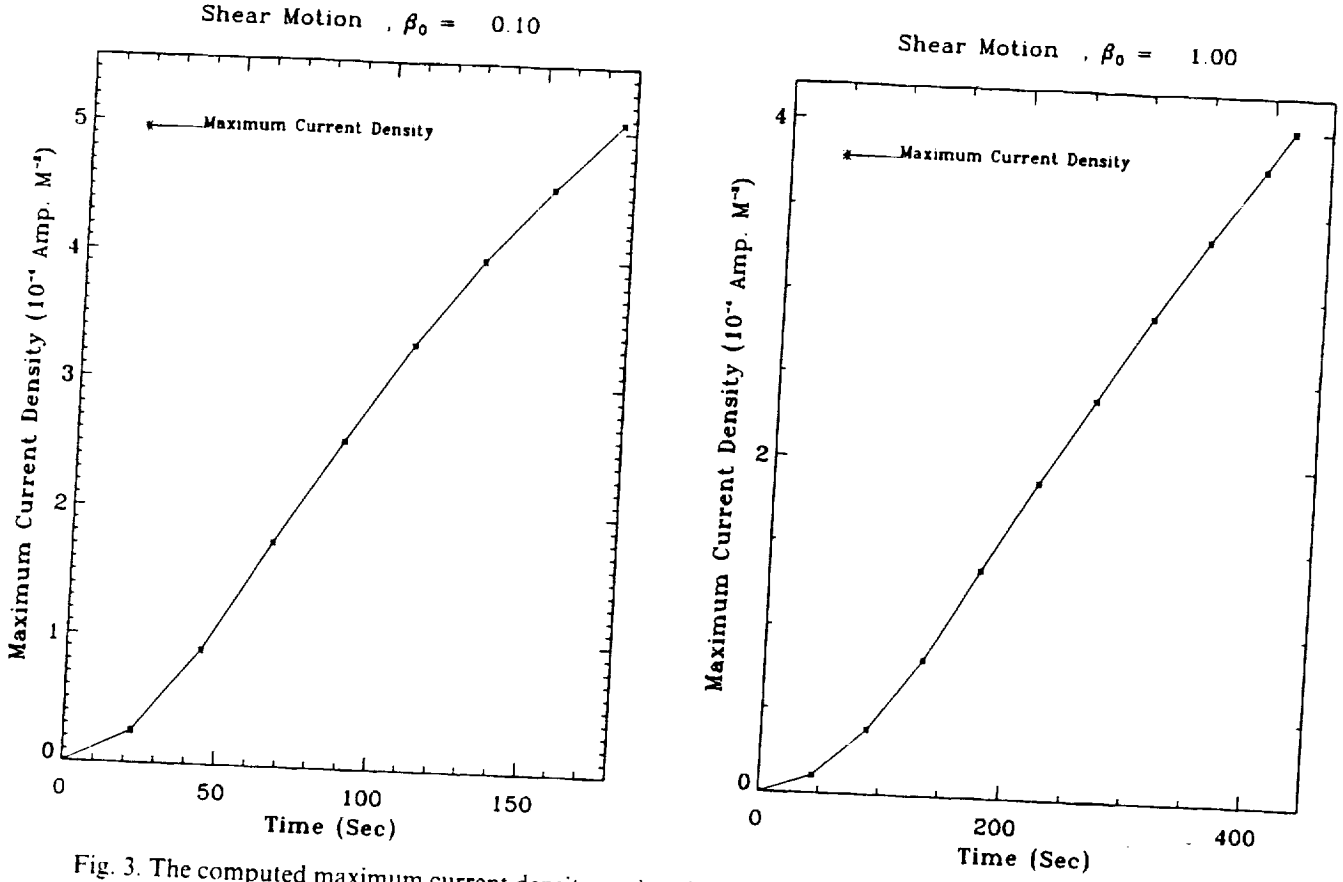

Fig. 3. The computed maximum current density vs time for (a) $\beta_0 = 0.1$ and (b) $\beta_0 = 1.0$, respectively, due to photospheric shearing motion with a maximum shearing speed of 1.0 km s^{-1}.

s^{-1} and 140 s, respectively. Figure 2 shows the excess energy ($E - E_0$) as a function of time due to a photospheric shear motion of 1 km s^{-1} for these two different values of initial plasma beta (β_0). It is immediately noticed that most of the energy build-up is stored in the magnetic mode. Also, it could be shown that the total energy build-up per unit depth in kilometers is ~ 20 times bigger for $\beta_0 = 0.1$ (i.e. 24×10^{24} ergs km^{-1}) in comparison with the case of $\beta_0 = 1.0$ (i.e. 1.20×10^{24} ergs km^{-1}) after a temporal duration of 150 s. The energy growth rate almost becomes a linear function of time after 150 s. Recently, Kahler *et al.* (1988) employed observations to show the correspondence of flare and filament (current) eruption occurrences. On the basis of the results given by Kahler *et al.* (1988), Wu and Xu (1992) have shown that there is an intimate relationship between the flare and filament current eruption, a relationship which depends upon the current density.

In order to further the understanding of the present results, Fig. 3 shows the maximum current density caused by photospheric shear motion as a function of time for (a) $\beta_0 = 0.1$ and (b) $\beta_0 = 1.0$, respectively. Again the figure shows that the current density is a factor of 4 larger for $\beta_0 = 0.1$ in comparison to the $\beta_0 = 1.0$ case. The growth rate for current density also has a linear behavior with time.

(ii) *Energy storage due to emerging magnetic flux from sub-photosphere*

In these simulations, all boundary and initial conditions are kept identical to those used in case (i) except for the perturbed lower boundary conditions which are given in equation (3). Figure 4 presents the total excess energy as a function of time for β_0 being 0.1 and 1.0, respectively. Figure 5 shows the maximum current density growth rate for β_0 as 0.1 and 1.0. It is again noted that the total excess energy is much bigger for $\beta_0 = 0.1$ in comparison to the $\beta_0 = 1.0$ case, a situation similar to case (i). However, the maximum current density and its growth rate are different in comparison to case (i). That is, a stronger field ($\beta_0 = 0.1$) case will resist the emerging flux; then it produces small maximum current density and its growth rate. On the other hand, when the field strength becomes weaker (i.e. larger beta, $\beta_0 = 1.0$), it is easier for the magnetic flux to emerge into the system. Thus, the increased flux produces stronger maximum current density and growth rate. In comparison to the photospheric shear motion case, the

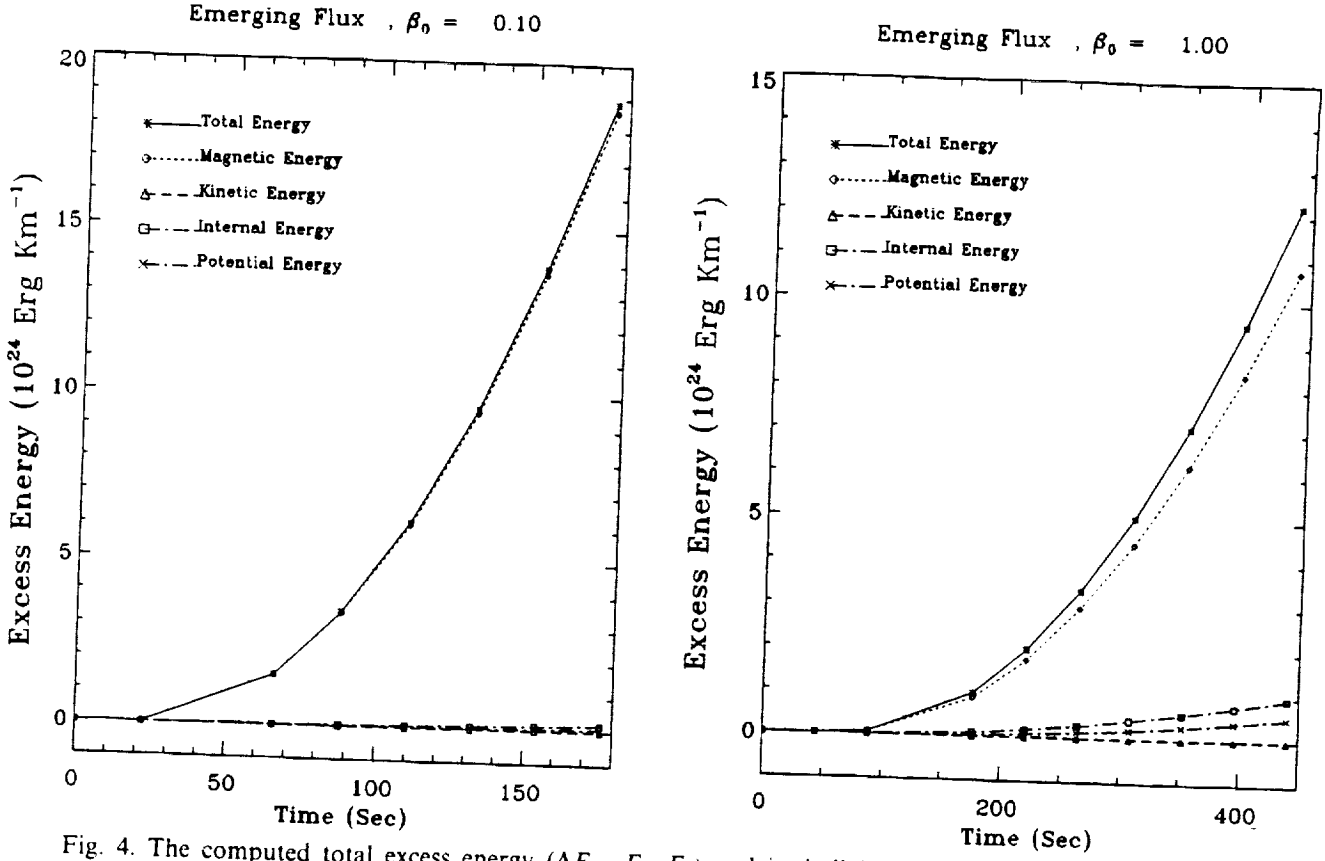

Fig. 4. The computed total excess energy ($\Delta E = E - E_0$) and its individual mode of excess energy of magnetic (ΔE_m), kinetic (ΔE_k), thermal (ΔE_T) and potential (ΔE_p) energies vs time for (a) $\beta_0 = 0.1$ and (b) $\beta_0 = 1.0$, respectively, due to emerging magnetic flux from the sub-photosphere.

stronger field (i.e. $\beta_0 = 0.1$) provides a much larger maximum current density and growth rate in the shear motion case because an additional magnetic field component perpendicular to the arcade is developed, thereby generating more current density. On the other hand, no additional field component is induced during the emerging flux case. In summary, it is again demonstrated that there is enough total energy to propel a typical flare of $\sim 10^{30}$ ergs.

4. DISCUSSION

On the basis of these MHD numerical simulations, it is possible to construct a physical scenario for solar flare energy storage and, thereby, to its release due to these two suggested physical processes (i.e. photospheric shear motion and emerging magnetic flux). The important physical characteristics related to the solar flare energy storage and release are (i) available energy and (ii) magnetohydrodynamic instability in relation to the triggering mechanism of a solar flare. We shall discuss these characteristics, based on the MHD numerical results, in some detail as follows:

(i) *Availability of magnetic energy*

The results given in Figs 2 and 4 demonstrate that the energy available to propel a solar flare is stored in the magnetic mode for both cases. The computed average energy growth rate is given as follows:

Average total energy growth rate (ergs s^{-1})

	(i) Shear motion		(ii) Emerging flux	
	$\beta_0 = 0.1$	$\beta_0 = 1.0$	$\beta_0 = 0.1$	$\beta_0 = 1.0$
dE_M/dt	2.16×10^{27}	6.6×10^{26}	2.13×10^{27}	7.2×10^{26}

In all of these simulations, we terminated our computation when the computed growth rate became almost a linear function of time: about 3–4 Alfven times (τ_A). Thus, by simply multiplying time with the magnetic energy growth rate, we are able to estimate the total energy available to propel the solar flare resulting from either a prescribed photospheric shearing motion or emerging magnetic flux from the sub-photosphere. For example, a typical energy buildup time for an active region is on the order of a few days. Hence, we obtain the following:

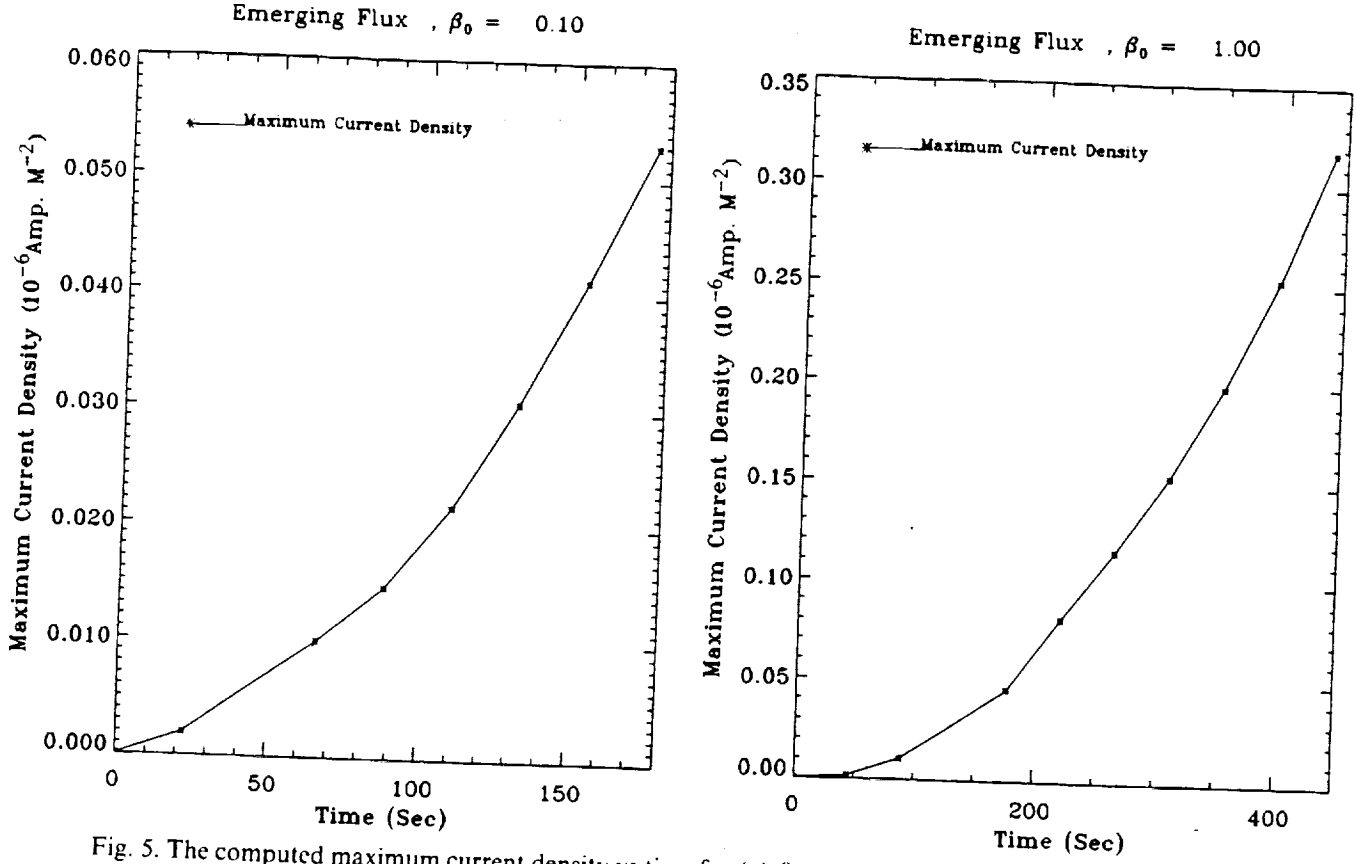

Fig. 5. The computed maximum current density vs time for (a) $\beta_0 = 0.1$ and (b) $\beta_0 = 1.0$, respectively, due to emerging magnetic flux from the sub-photosphere.

	Excess total energy ($\Delta E - E_0$) (ergs)			
	1 day (86,400 s)	3 days (259,200 s)	5 days (432,000 s)	7 days (604,800 s)
Shear motion				
$\beta_0 = 0.1$	1.87×10^{32}	5.61×10^{32}	9.35×10^{32}	1.31×10^{33}
$\beta_0 = 1.0$	5.7×10^{31}	1.71×10^{31}	2.85×10^{32}	4.00×10^{32}
Emerging flux				
$\beta_0 = 0.1$	1.84×10^{32}	5.52×10^{32}	9.2×10^{32}	1.29×10^{33}
$\beta_0 = 1.0$	6.22×10^{31}	1.87×10^{31}	3.11×10^{32}	4.35×10^{32}

In the estimations shown in the above table we have taken a typical length of filament of $\sim 10^4$ km and the total energy stored in an active region is on the order of 10^{31}–10^{32} ergs for one day and 10^{32}–10^{33} ergs for seven days. This indicates that there is enough energy to supply flaring. In order to examine the question as to how this stored energy could be released, we take the current practical view that it is due to an MHD instability that causes the explosive energy release. This is addressed in the next section.

(ii) *Triggering mechanism: MHD instability*

In this section, we shall examine the simulated physical system subjected to magnetohydrodynamic (MHD) instability. In order to perform a simple MHD instability analysis estimation, we shall use the principle of tearing mode MHD instability suggested by Tachi *et al.* (1983) and Van Hoven (1980) to test our simulated results. Tachi *et al.* (1983) concluded that if the magnetic Reynolds number, $Re_m = 10^{-2} aBT^{3/2}n^{-1/2}$, exceeds 3×10^5, both tearing mode and joule heating mode are possible for $\alpha = ka = 0.1$, with k being the wave number of the perturbation and 'a' being the characteristic length. In the present simulation, we have $B = 500$–1500 Gauss, $n = 10^{14}$ cm^{-3} and $T = 10^5$ K and the shear motion is prescribed in the form $\sin(\pi x/2x_0)$, where the x_0 is the horizontal length of the computation domain. We have chosen x_0 to be 8×10^8 cm; therefore, the wave number of the perturbation k is equal to $\pi/x_0 = 4 \times 10^{-9}$ cm^{-1}. With this information, we can compute the magnetic Reynolds number for the present simulation

$$Re_m = 10^{-2}\left(\frac{\alpha}{k}\right)B(T)^{3/2}(n)^{-1/2} \simeq 4 \times 10^8.$$

This value is much larger than the value (3×10^5) given by Tachi *et al.* (1983) for triggering both the tearing mode and joule heating mode of the MHD instability. However, it is impossible to discriminate between these two modes in the present simulation.

But it may be concluded that the simulation results for the present physical system will lead to MHD instabilities. Thus, energy release is possible to propel a solar flare. Using the observations analyzed by KAHLER *et al.* (1988), WU and XU (1992) have shown that the current intensity at the X-ray onset of the impulsive phase of a particular solar flare (26 April 1979 event) is $\sim 2 \times 10^4$ statamperes cm^{-2}. From the present simulation, as shown in Figs 3 and 5, the current density growth rate due to photospheric shear motion is converted to 0.75 statamperes cm^{-2} for $\beta_0 = 0.1$ and 0.3 statamperes cm^{-2} for $\beta_0 = 1.0$, respectively. However, the current density growth rate due to emerging flux is much smaller, namely 0.15×10^{-3} statamperes cm^{-2} for $\beta_0 = 0.1$ and 0.4×10^{-3} statamperes cm^{-2} for $\beta_0 = 1.0$, respectively. Hence, due to photospheric shear motion, the time needed to reach the flaring threshold is 2.67×10^4 s (7.4 h) for $\beta_0 = 0.1$ and 6.67×10^4 s (18.5 h) for $\beta_0 = 1.0$. In the case of emerging flux, the growth rates are too slow to generate the threshold current density required to trigger the instability for flaring. We do not mean to imply that the mechanism of emerging flux is not a viable mechanism. The present calculation is limited to a planar case for emerging flux; we did not examine the non-planar case, which would have potential for flaring.

5. CONCLUDING REMARKS

In this study, we utilized the MHD model given by WU *et al.* (1983) to investigate energy build-up and storage for a solar flare due either to photospheric shearing motion or to energy flux emergence from sub-photospheric levels. Furthermore, the simulation results were applied to a test of MHD instabilities (i.e. tearing-like mode and joule-heating mode) for a possible explanation of the physical mechanism of energy release. The interesting findings of this simulation study can be summarized as follows:

(i) The simulation results show that there is enough energy stored due to both shearing motion and emerging flux to supply the flare energy. All of this energy is stored in the magnetic mode.

(ii) Under the condition of MHD instabilities, these simulation results show that photospheric shear motion is more favorable for triggering a flare because it produces a large growth rate for current density in comparison with low growth rates for the emerging flux.

Acknowledgements—The work performed by STW and FSW was supported by a NASA HQ Space Physics Division Solar Physics Grant NAGW-9 and NOAA (50 RANR 7000/04).

REFERENCES

HAGYARD M. J. 1990 *Mem. S. A. It.* **60**, No. 2, 337.

KAHLER S. W., MOORE R. L., KANE S. R. and ZIRIN H. 1988 *Ap. J.* **328**, 824.

LOW B. C. 1977 *Astrophys. J.* **212**, 234.

LIVI S. H. B., MARTIN S. and WANG H. M. 1989 *Solar Phys.* **121**, 197.

MARTIN S. and LIVI S. H. B. 1992 *Eruptive Solar Flares*, Z. SVESTKA, B. V. JACKSON and M. E. MACHADO (eds), Proceedings of IAU Colloquium 133, Iguzau Fall, Argentina, August 1991. Springer, Heidelberg.

MOORE R. 1990 *Mem. S. A. It.* **61**, No. 2, 317.

RUST D. M. 1972 *Solar Phys.* **25**, 141.

RUST D. M. 1974 Flare-Related Magnetic Field Dynamics, HAO Conference, Boulder, Colorado, p. 243.

TACHI T., STEINOLFSON R. S. and VAN HOVEN G. 1983 *Phys. Fluids* **26**(10), 2976.

TANAKA K. and NAKAGAWA Y. 1973 *Solar Phys.* **33**, 187.

VAN HOVEN G. *et al.* 1980 *Solar Flares*, P. A. STUIRROCK (ed.). Colorado Associated University Press.

WU S. T., HU Y. Q., KRALL K., HAGYARD M. J. and SMITH J. B. JR 1984 *Solar Phys.* **90**, 117.

WU S. T., HU Y. Q., NAKAGAWA Y. and TANDBERG-HANSSEN E. 1983 *Astrophys. J.* **266**, 866.

WU S. T. and XU A. A. 1992 *Eruptive Solar Flares*, Z. SVESTKA, B. V. JACKSON and M. E. MACHADO (eds), Proceedings of IAU Colloquium 133, Iguzau Fall, Argentina, August 1991, pp. 55–58. Springer, Heidelberg.

ZIRIN H. and TANAKA K. 1973 *Solar Phys.* **32**, 173.

MAGNETOHYDRODYNAMIC SIMULATION OF THE EVOLUTION OF BIPOLAR MAGNETIC REGIONS

S. T. Wu and C. L. Yin

Center for Space Plasma and Aeronomic Research and Department of Mechanical Engineering
The University of Alabama in Huntsville, Huntsville, Alabama 35899 USA

P. McIntosh and E. Hildner

Space Environment Laboratory, National Oceanic and Atmospheric Administration
Boulder, Colorado 80303 USA

Reprinted from the
Astronomical Society of the Pacific Conference Series
Volume 46, pp. 98-107

THE MAGNETIC AND VELOCITY FIELDS OF SOLAR ACTIVE REGIONS

Edited by Harold Zirin, Guoxiang Ai, and Haimin Wang

PRECEDING PAGE BLANK NOT FILMED

The Magnetic and Velocity Fields of Solar Active Regions
ASP Conference Series, Vol. 46, 1993
Harold Zirin, Guoxiang Ai, and Haimin Wang (eds.)

MAGNETOHYDRODYNAMIC SIMULATION OF THE EVOLUTION OF BIPOLAR MAGNETIC REGIONS

S. T. WU AND C. L. YIN*
Center for Space Plasma and Aeronomic Research and Department of Mechanical Engineering The University of Alabama in Huntsville Huntsville, Alabama 35899 U.S.A.

P. MCINTOSH AND E. HILDNER
Space Environment Laboratory, National Oceanic and Atmospheric Administration, Boulder, Colorado 80303 U.S.A.

ABSTRACT It has been recognized that the magnetic flux observed on the solar surface appears first in low latitudes, and then this flux is gradually dispersed by super granular convective motions and meridional circulation. Theoretically, the magnetic flux transport could be explained by the interactions between magnetic fields and plasma flows on the solar surface through the theory of magnetohydrodynamics.

To understand this physical scenario, a quasi-three-dimensional, time-dependent, MHD model with differential rotation, meridional flow and effective diffusion as well as cyclonic turbulence effects is developed. Numerical experiments are presented for the study of Bipolar Magnetic Regions (BMRs). When the MHD effects are ignored, our model produced the classical results (Leighton, *Astrophys. J.*, **146**, 1547, 1964). The full model's numerical results demonstrate that the interaction between magnetic fields and plasma flow (i.e., MHD effects), observed together with differential rotation and meridional flow, gives rise to the observed complexity of the evolution of BMRs.

I. INTRODUCTION

Leighton's model of sunspots and solar cycle in relation to the expansion and migration of unipolar (UM) and bipolar (BM) magnetic regions was published in 1964. Since then, a number of investigators (DeVore *et al* 1984; McIntosh and Wilson, 1985; Sheeley, *et al* 1985; Sheeley, and Devore, 1986; Wilson, 1986; Wilson and McIntosh, 1991; Wang and Sheeley, 1991) have extensively studied the magnetic flux transport in relation to the solar cycle by means of a modified Leighton model with additional physics. Recent rapid development of numerical simulation gives us the capability to study highly complex, nonlinear mathematical systems. Wang and Sheeley (1991) have presented a numerical simulation including differential rotation, supergranular diffusion, and a poleward surface flow (i.e., meridional flow) of the redistribution of magnetic flux

erupting in the form of BMRs. They reproduced many of the observed properties of the Sun's large-scale field not encompassed by Babcock's (1961) or Leighton's (1964) model. Wilson and McIntosh (1991) compared observed evolutions of large-scale magnetic fields with simulated evolutions based on the kinematic model of Devore and Sheeley (1987). They concluded there must be significant contributions to the evolving patterns by non-random flux eruptions within the network structure, independent of active regions.

On the basis of magnetohydrodynamic theory, we understand that the nonlinear dynamical interactions between the plasma flow and magnetic field are essential to understand magnetic flux transport. However, none of the previous investigations have invoked MHD to study this problem. In this paper, we present a quasi-three-dimensional, time-dependent, MHD model with differential rotation, meridional flow and effective diffusion as well as cyclonic turbulence to study magnetic evolution of BMRs. The mathematical model, initial and boundary conditions are presented in Section II. Numerical results and concluding remarks are given in Sections III and IV respectively.

II. MATHEMATICAL MODEL, INITIAL AND BOUNDARY CONDITIONS

The mathematical model appropriate for the physical scenario we described in the previous section can be expressed by a set of incompressible simulated MHD equations including differential rotation, meridional flow and turbulent diffusion. These governing equations are:

$$\nabla \cdot \vec{u} = 0 \tag{1}$$

$$\rho\left[\frac{\partial \vec{u}}{\partial t} + (\vec{u}\cdot\nabla)(\vec{u}-\vec{u}\prime)\right] = -\nabla p + \frac{1}{4\pi}(\nabla\times\vec{B})\times\vec{B} + \vec{F}_g - 2\rho\vec{\omega}_0\times(\vec{u}-\vec{u}\prime) - \rho\vec{\omega}_0\times\left[\vec{\omega}_0\times(\vec{r}-\vec{r}\prime)\right] + \mu_t\nabla^2(\vec{u}-\vec{u}\prime) \tag{2}$$

$$\frac{\partial \vec{B}}{\partial t} = \nabla\times(\vec{u}\times\vec{B}) + \lambda(\nabla\times\vec{B}) + \kappa\nabla^2\vec{B} + \vec{S} \tag{3}$$

$$\frac{\partial p}{\partial t} + (\vec{u}\cdot\nabla)p = \Delta Q + (\gamma-1)\left[\frac{J^2}{\sigma_t} + \frac{\mu_t}{2}\left(\frac{\partial u_i}{\partial x_k} + \frac{\partial u_k}{\partial x_j}\right)^2\right] \tag{4}$$

where ρ is the plasma mass density, $\vec{u}$ the plasma flow velocity vector, p the plasma thermal pressure, and $\vec{B}$, the magnetic induction vector, respectively. The other quantities are defined as follows; $\vec{\omega}_o$ is the angular velocity of solar differential rotation referring to the center of the solar coordinate system, that is given by empirical value as

$$\vec{\omega}_o = \hat{i}_\phi \frac{(0.2337 - 0.04835\ \cos^2\theta_o)}{86400}\ \text{arc sec s}^{-1} \tag{5}$$

with θ_o being the latitude of the center of a sunspot (or active region) . The $\vec{u}\prime$ is the prescribed background plasma velocity field including differential rotation and meridional flow which is given by

$$\vec{u}\prime = u_{r}\prime\hat{i}_r + u_{\theta}\prime\hat{i}_\theta + u_{\phi}\prime\hat{i}_\phi \tag{6}$$

with $u_r\prime$ being the radial component velocity on the solar surface, u'_θ is the velocity of the meridional flow which is chosen to be $u_{\theta}\prime = 0.015/sin\ \theta$ for the present study and u'_ϕ is the velocity due to the differential rotation relative to the rotating coordinate system, that is

$$u\prime_\phi = \frac{0.04835(\cos^2\theta_o - \cos^2\theta)r\sin\theta}{86400} \qquad \text{arc sec s}^{-1} \tag{7}$$

$\vec{r}\prime$ is the dummy position vector referring to the location of the sunspot (or active region), $\vec{F}_g$ is the gravitational force of the sun, κ is the effective diffusivity and λ represents the coefficient of the cyclonic turbulence, $\vec{S}$ is the additional source terms such as emerging flux etc., the μ_t is the turbulent viscosity.

Finally the term ΔQ represents the heat source due to the initial dynamics of the quiet photospheric motion such that

$$\Delta Q = (\vec{u}\prime\cdot\nabla)p_o - (\gamma-1)\left[\frac{J_0^2}{\sigma_t} + \frac{\mu_t}{2}\left(\frac{\partial u\prime_i}{\partial x_k} + \frac{\partial u\prime_k}{\partial x_i}\right)^2\right] \tag{8}$$

This term is prescribed to assure the self-consistency of the MHD solution, namely, the initial dynamical equilibrium of the solar atmosphere is obtained.

This set of MHD equations differs from those of usual first principle MHD theory. These differences arise from additional physics we have included in this formulation. For example, the additional terms in Equation (2) represent the inertia centrifugal force (i.e. $2\rho\omega_0 \times (\vec{u} - \vec{u}\prime)$), the coriolis force (i.e. $2\rho\vec{\omega}_0 \times (\vec{\omega}_0 \times (\vec{r} - \vec{r}\prime))$) and effective diffusion due to random motion of the granules or the super-granules. The additional term in Equation (3) represents the cyclonic turbulence (i.e. $\lambda(\nabla \times \vec{B})$).

Ideally, we should solve this set of equations in full three dimensions. However, this is costly and unnecessary, as we are interested only in exploring the fundamental physical processes rather than in simulating the realistic situation on the sun. Consequently, we prescribe the behavior of the radial derivatives of velocity and magnetic field on the basis of the mathematical convenience. These functions are:

$$\vec{B} = B_r(r)B_r(\theta,\phi)\hat{i}_r + B_\theta(r)B_\theta(\theta,\phi)\hat{i}_\phi + B_\phi(r)B_\phi(\theta,\phi)\hat{i}_\phi \tag{9}$$

$$\vec{u} = u_r(r)u_r(\theta,\phi)\hat{i}_r + u_\theta(r)u_\theta(\theta,\phi)\hat{i}_\theta + u_\phi(r)u_\phi(\theta,\phi)\hat{i}_\phi \tag{10}$$

with

$$\begin{aligned}
\frac{\partial B_r}{\partial r} &= -(\frac{2}{r} + \frac{a}{H_o})B_r \\
\frac{\partial B_\theta}{\partial r} &= -(\frac{1}{r} + \frac{a}{H_o})B_\theta \\
\frac{\partial B_\phi}{\partial r} &= -(\frac{1}{r} + \frac{a}{H_o})B_\phi
\end{aligned} \tag{11}$$

$$\frac{\partial u_r}{\partial r} = -\frac{2}{r}u_r$$
$$\frac{\partial u_\theta}{\partial r} = \frac{1}{r}u_\theta \qquad (12)$$
$$\frac{\partial u_\theta}{\partial r} = \frac{1}{r}u_\phi$$

Substituting equation (12) and (13) into equation (2) by setting $u_r \equiv u'_r$, we have

$$\frac{\partial p}{\partial r} = \frac{p}{r}\Big[u_\theta(u\theta - u_{\theta'}) + u_\phi(u_\phi - u_{\phi'})\Big] + 2p\omega_o sin\theta(u_\phi - u_{\phi'}) - \rho g + \frac{1}{4\pi}\left[\frac{B_\theta}{r}\left(\frac{\partial B_\theta}{\partial\theta} - \frac{\partial(rB_\theta)}{\partial r}\right)\right] - \frac{B_\phi}{r}\left(\frac{\partial}{\partial r}(rB_\phi)\right) - \frac{1}{sin\theta}\frac{\partial B_r}{\partial\phi} \qquad (13)$$

where H_0 is the depth of the sunspot (i.e. $\sim 2 \times 10^4\ km$) and a is an arbitrary constant which is the measure of the decreasing rate of field strength against height.

Using these relationships, the computation reduces to a calculation on the solar surface. That is why we called our model a quasi-three-dimensional, time-dependent MHD model.

To assure self-consistency of the numerical simulation of the evolutionary MHD processes, proper initial and boundary conditions are needed. We obtain our initial conditions by assuming the solar atmosphere is in dynamical equilibrium. Thus, these initial conditions are:

$$\frac{1}{rsin\theta}\frac{\partial}{\partial\theta}(B_{\theta 0}sin\theta) + \frac{1}{rsin\theta}\frac{\partial}{\partial\phi}(B_{\phi o}) = \frac{a}{H_0}B_{r0}$$
$$\frac{B_{\theta 0}}{B_{\phi 0}} = -tan\alpha \qquad (14)$$

with

$$B_{ro} = \begin{cases} 0, & \phi^+ + \frac{d}{2} < \phi < \phi^{\cdot\cdot} - \frac{d}{2}; \\ B_{ro}, & \phi^+ - \frac{d}{2} < \phi < \phi^{\cdot\cdot} + \frac{d}{2}; \quad \theta^+ - \frac{d}{2} < \theta < \theta^+ + \frac{d}{2} \\ B_{ro}, & \phi^- - \frac{d}{2} < \phi < \phi^{\cdot\cdot} + \frac{d}{2}; \quad \theta^- - \frac{d}{2} < \theta < \theta^- + \frac{d}{2} \\ 0, & \phi^- + \frac{d}{2} < \phi < \phi^+ - \frac{d}{2}; \end{cases} \qquad (15)$$

where (ϕ^+, θ^+) and (ϕ^-, θ^-) represent the coordinates of sunspots with positive and negative polarity respectively and d represents the diameter of the sunspots.

(ii) Initial velocity field is given by

$$\begin{aligned} u_r = u_r{}' = 0 \quad or \quad 0.1 \quad & kms^{-1} \\ u_\theta = u_\theta{}' = \frac{0.015}{sin\theta}, \quad & kms^{-1} \\ u_\phi = u_\phi{}' = \omega_0(\theta) r sin\theta \quad & kms^{-1} \end{aligned} \tag{16}$$

(iii) Initial pressure field is

$$\frac{1}{r}\frac{\partial p_0}{\partial \theta} = \frac{1}{4\pi}\left[\frac{B_{\phi 0}}{1 sin\theta}\left(\frac{\partial B_{\theta 0}}{\partial \phi} - \frac{\partial}{\partial \theta}(B_\phi \sin\theta)\right)\right] - \frac{B_{r0}}{r}\left(\frac{ar}{H_0}B_{\theta 0} + \frac{\partial B_{r0}}{\partial \theta}\right) \tag{17}$$

$$\frac{1}{r\sin\theta}\frac{\partial p_0}{\partial \phi} = \frac{1}{4\pi}\left[\frac{B_{\theta 0}}{r\sin\theta}\left(\frac{\partial}{\partial \theta}(B_\phi \sin\theta) - \frac{\partial B_{\theta 0}}{\partial \phi}\right) - \frac{B_{r0}}{r}\left(\frac{ar}{H_0}B_{\phi 0} + \frac{1}{\sin\theta}\frac{\partial B_{r0}}{\partial \phi}\right)\right] \tag{18}$$

In addition, the $B_{r\phi}$, $B_{\theta 0}$ and $B_{\phi 0}$ are given to satisfy the solenoidal condition (i.e. $\nabla \cdot \vec{B} = 0$).

The boundary conditions employed here are computational boundary conditions which simply are the forward differencing linear extrapolation.

III. NUMERICAL SIMULATION RESULTS

The computational domain for the simulation is set as a rectangular region with 51 grids in the carrington longitude (ϕ) and 35 grids in the latitudinal direction (θ) in which we have chosen 0.5 degree for each grid in this study. It is assumed that the differential rotation and meridional flow velocity depend upon latitude only. Therefore, the prescribed flow pattern within the computational domain will depend on the domain's latitude but not on its longitude.

Before we carry out this simulation study, we need to know two important coefficients: effective diffusivity (κ) and cyclonic turbulence (λ). We know that the range of values of effective diffusivity is quite wide, for example, $\kappa = 160 - 300\ km^2\ s^{-1}$ given by Parker (1979); Leighton's value of κ is $800 - 1600\ km^2\ s^{-1}$ (Leighton, 1964); DeVore *et al* (1985) selected $\kappa = 30($ $km^2\ s^{-1}$ for their study. Wang (1988) derived a value of κ being $100 - 150$ $km^2\ s^{-1}$ on the basis of observations. The purpose of this study is to learn the fundamental physical processes due to the simulated MHD effects (i.e. photospheric dynamo) and is not to simulate a particular event. Therefore, we simply choose values within these ranges for this study. The value of cyclonic turbulence is chosen according to the scale law ($\lambda < \kappa/L$), where L is the characteristic length of sunspot, it is chosen to be 6000 km for the present study.

The first issue which we shall examine is how the simulated MHD process (i.e. photospheric dynamo) will effect the Leighton's results (1964). To achieve

this purpose, we simply reduce the present set of governing equations into a single diffusion type equation of Leighton's theory which is expressed by Eq. (3) with $\lambda = 0$. To perform such a simulation, we set up a bipolar magnetic region with strength $\pm$ 1800 G and two degrees apart, then, allow the mathematical system to evolve. The B_r contours for $\kappa = 120\ km^2\ s^{-1}$ at time 240 hrs after introduction of the bipolar magnetic region (BMR) are shown in Figure 1a which resembles the classical Leighton's results. As we have pointed out earlier, these results simply represent the magnetic field transport due to effective diffusion and differential rotation. Figure 1b shows the simulation results using the full set of governing equations with differential rotation and κ equal 120 $km^2\ s^{-1}$ at 240 hrs after introduction of the BMR. It shows the interaction between the plasma flow and magnetic fields. In such a case, the photospheric dynamo process sets in. Significant differences between Fig.1a and 1b are evident; (i) with MHD effects the simplicity of magnetic field strength contours disappeared, (ii) the magnetic field has migrated significantly in longitudinal direction, because we have ignored meridional flow in this calculation and (iii) the MHD effects lead to highly sheared neutral line.

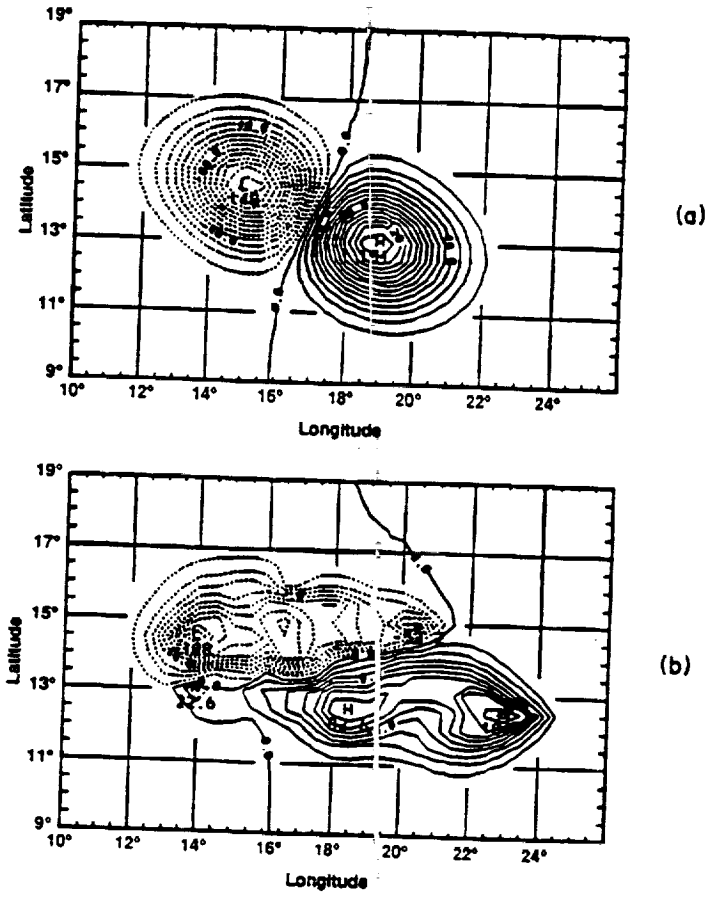

Fig. 1 The radial magnetic field strength (B_r) contours at 240 hrs after introduction of the BMR without (a) and with (b) simulated MHD effects.

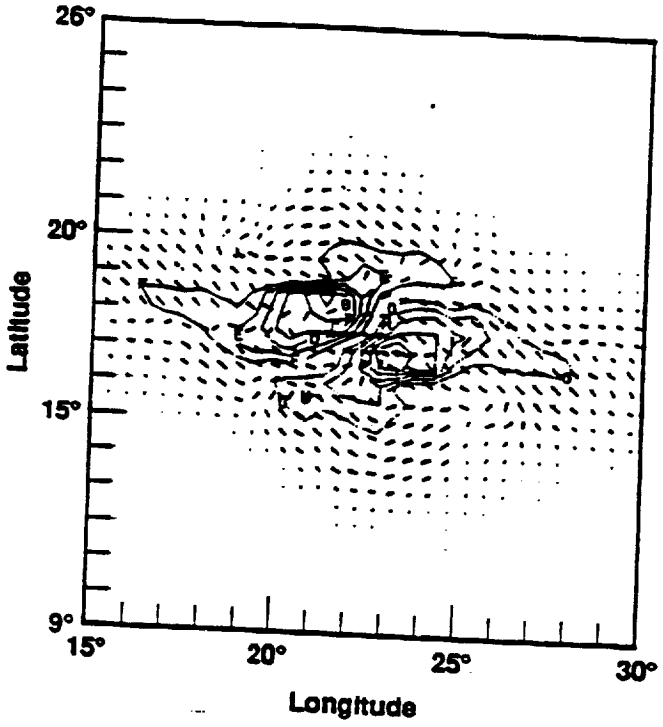

(a)

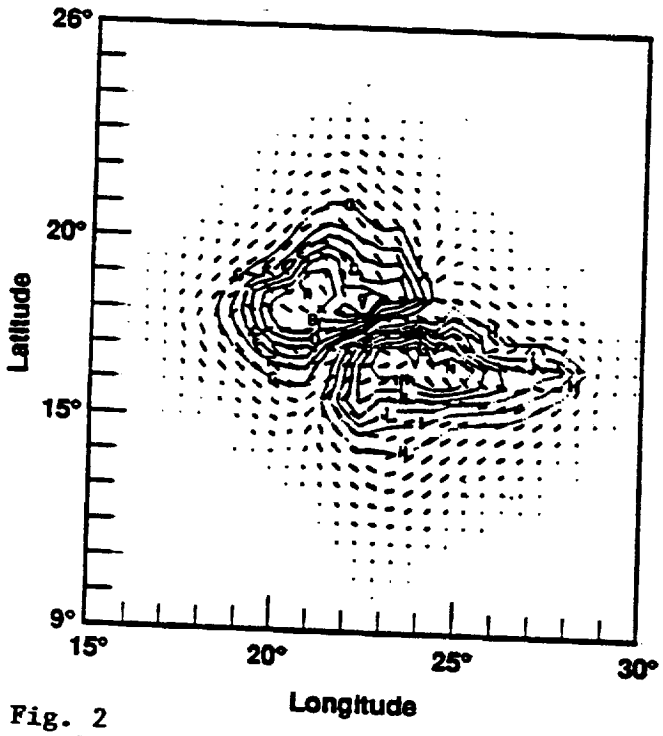

(b)

Fig. 2

The radial magnetic field strength (B_r) contours and transverse magnetic field at 120 hrs after introduction of the BMR without meridional flow (a) and with meridional flow (b) using the full set of simulated MHD equations.

Figure 2 shows the effects of the meridional flow on the magnetic field transport, Figure 2a exhibits the B_r strength contours and transverse field for $\kappa = 200\ km^2\ s^{-1}$ and $\lambda = 0.0125\ km\ s^{-1}$ without a meridional flow and Figure 2b shows the same case with meridional flow. It may note that the meridional flow produced a slightly poleward movement of the BMR.

Up to now, we have shown the computed evolution of the morphology of the BMR with and without MHD effects. It is interesting to understand the energy evolution during these processes. In Figure 3, we show the magnetic energy evolution for the cases with and without background velocity effects. Figure 3a shows the normalized magnetic energy (i.e., $E_m(t)/E_m(0)$) in the absence of prescribed differential rotation and meridional flow for the case when only diffusion and cyclonic turbulence are included. We notice that the normalized magnetic energy $E_m(t)/E_m(0)$ of the BMR through effective diffusion ($\kappa = 200\ km^2\ s^{-1}$) is decreasing almost linearly with time as represented by curve B. If both effective diffusion and cyclonic turbulence $\lambda = 0.25\ km\ s^{-1}$ are considered, $E_m(t)/E_m(0)$ decreased a little more slowly than curve A. Curve C represents the case for cyclonic turbulence only and $E_m(t)/E_m(0)$ shows a slight increase with time. This clearly informs us that the photosphere dynamo can be an energy production source. In Figure 3b we test the influence of effective diffusion (loss) and cyclonic turbulence (source) in the presence of differential rotation and meridional flow on the evolution of the normalized magnetic energy. Curve A represents the case for $\kappa = \lambda = 0$; it gives $E_m(t)/E_m(0)$ being constant, this informs us that this simulation model has maintained dynamical equilibrium throughout the process and it validates the accuracy of the simulation model. Curves B and C are for $\lambda = 0$ and $\kappa = 100\ km^2\ s^{-1}$ and $200\ km^2\ s^{-1}$, respectively. It is apparent that, when the effective diffusivity increases, the decay rate of normalized magnetic energy increases. Curves D and E in Figure 3b show the evolution of normalized magnetic energy for $\kappa = 0$ with $\lambda = 0.75\ km\ s^{-1}$ *and* $0.1\ km\ s^{-1}$, respectively. It is immediately noticed that the growth rate of normalized magnetic energy increased with increasing λ. From these studies, we realize that effective diffusion and cyclonic turbulence are competing physical mechanisms for the magnetic energy evolution in the magnetic flux transport process of a BMR. In Figure 4, we present the normalized magnetic energy *vs* time for a fixed value of cyclonic turbulence ($\lambda = 0.025\ km\ s^{-1}$) and effective diffusivity 0, 100 and $200\ km^2\ s^{-1}$ respectively. These results clearly show how these two competing mechanisms work; when $\kappa = 0$, the magnetic energy will increase with time but when effective diffusivity dominates cyclonic turbulence, then the magnetic energy of BMR decays.

IV. CONCLUDING REMARKS

The purpose of this study has been to show how a simulated magnetohydrodynamic (MHD) process which incorporates to the photospheric dynamo might affect the evolution of a bipolar magnetic region (BMR) and lead to the complex active region on the solar surface. To accomplish this purpose, a quasi-three-dimensional, time-dependent MHD model was developed. For the present exploratory simulation study, we realize that there are two major physical mechanisms which interplay during the evolutionary process of a BMR, and could

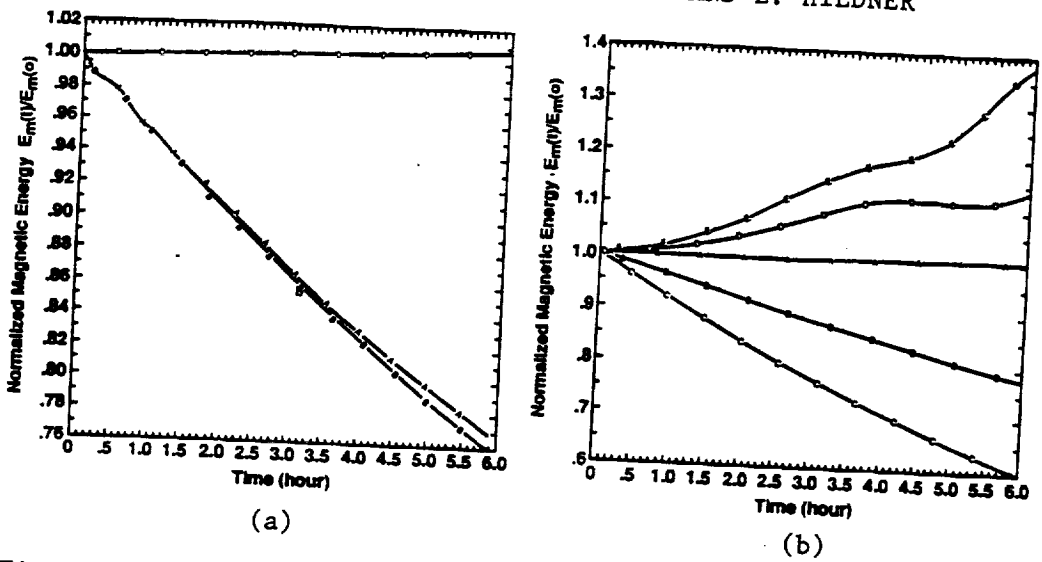

Fig. 3

(a) The evolution of the normalized magnetic energy without MHD effect: **A** ($\kappa = 200\ km^2\ s^{-1}, \lambda = 0.025\ km\ s^{-1}$), **B** ($\kappa = 200\ km^2\ s^{-1}, \lambda = 0\ km\ s^{-1}$), and **C** ($\kappa = 0, \lambda = 0.025\ km\ s^{-1}$). (b) The evolution of the normalized magnetic energy with MHD effect: **A** ($\kappa = 0, \lambda = 0$), **B** ($\kappa = 100\ km^2\ s^{-1}, \lambda = 0$), **C** ($\kappa = 200\ km^2\ s^{-1}, \lambda = 0$), **D** ($\kappa = 0, \lambda = 0.075\ km\ s^{-1}$), **E** ($\kappa = 0, \lambda = 0.1\ km\ s^{-1}$).

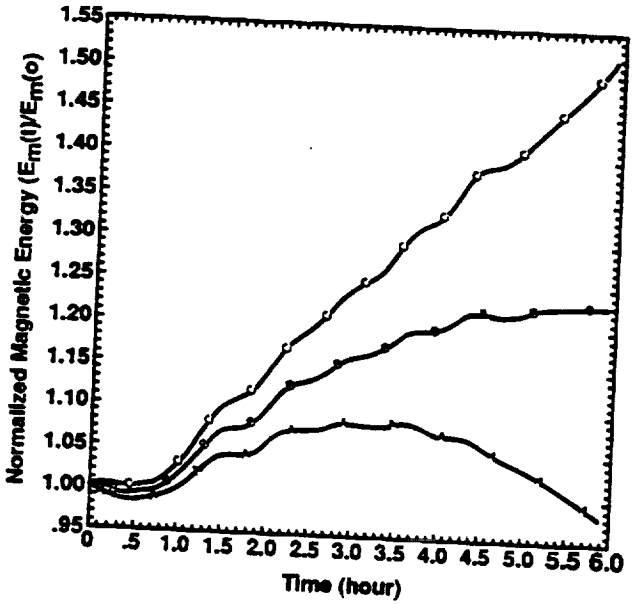

Fig. 4

The evolution of normalized magnetic energy with MHD effect and various magnitude of effective diffusion: **A** ($\kappa = 200\ km^2\ s^{-1}$), **B** ($\kappa = 100\ km^2\ s^{-1}$), and **C** ($\kappa = 0$), at fixed value of cyclonic turbulence ($\lambda = 0.025\ km\ s^{-1}$).

explain the magnetic flux transport on the solar surface. These two physical mechanisms are the effective diffusivity and cyclonic turbulence with simulated MHD process which triggers the photosphere dynamo. The most interesting results from the present simulation can be summarized as follows: (i) If the simulated MHD process is appropriate, the decay of a BMR will create more complex structures because the nonlinear interactions exist between the plasma flows and background magnetic fields and (ii) the magnetic energy of the BMR could be increased if the cyclonic turbulence process dominates. In summary, we may conclude that MHD interactions are important and needed in the study of magnetic field transport.

ACKNOWLEDGEMENT

The work by STW and CLY was supported by a NASA Headquarters grant NAGW-9 and NOAA (50RANR000104).
*Permanent Address: Purple Mountain Observatory, Nanjing, PRC

REFERENCES

1. DeVore, C. Richard, Sheeley, N. R., Jr., Boris, J. P., Young, R. T., Jr., and Harvey, K. L.: 1984, *Solar Phys.* **92**, 1.
2. DeVore, C. R., Sheeley, N. R., Jr., Boris, J. P., Young, R. T. Jr., and Harvey, K. L.: 1985 *Solar Phys.* **102**, 41.
3. DeVore, C. R., and Sheeley, N. R., Jr.: 1987 *Solar Phys.* **108**, 47.
4. Leighton, Robert B.: 1964, *Ap.J.* **140**, 1547.
5. McIntosh, P. S. and Wilson, P. R.: 1985, *Solar Phys.* **97**, 59.
6. Parker, E. N., *Cosmic Magnetic Fields*, Oxford University Press, England, p. 509, 1979.
7. Sheeley, N. R., Jr., DeVore, C. R., and Boris, J. P.: 1985 *Solar Phys.* **98**, 219.
8. Sheeley, N. R. Jr., and DeVore, C. R.: 1986, *Solar Phys.* **103**, 203.
9. Wang, H.: 1988, *Solar Phys.* **116**, 1.
10. Wang, Y.-M. and Sheeley, N. R., Jr.: 1991,*Ap. J.* **375**, 761.
11. Wilson, P. R.: 1986, *Solar Phys.* **106**, 1.
12. Wilson, P. R. and McIntosh, P. S.: 1991 *Solar Phys.* **136**, 221.

Physics of Fluids B: Plasma Physics, 1994 (submitted)

ON GENERATION AND PROPAGATION OF MHD BODY AND SURFACE WAVES: SINGLE MAGNETIC INTERFACE AND MAGNETIC SLAB

S. T. Wu, Y. C. Xiao,[1] Z. E. Musielak

Department of Mechanical and Aerospace Engineering and

Center for Space Plasma and Aeronomic Research

The University of Alabama in Huntsville

Huntsville, AL 35899 U.S.A.

and

S. T. Suess

Space Science Laboratory

NASA/Marshall Space Flight Center

Huntsville, AL 35812 U.S.A.

Abstract

Generation and propagation of magnetohydrodynamic (MHD) body and surface waves in a medium with a single and double (slab) magnetic interface are studied by using of a nonlinear, two-dimensional, time-dependent, ideal MHD numerical model constructed on the basis of a Lagrangian grid and semi-implicit scheme. The processes of wave confinement and wave energy leakage are discussed in detail. It is shown that the obtained results depend strongly on the type of perturbations imposed on the interface or slab and on the plasma parameter β.

[1] Intergraph Corporation, Huntsville, Alabama

I INTRODUCTION

It is commonly accepted that magnetohydrodynamic (MHD) waves may play a dominant role in the energy transfer and in the local heating in many laboratory devices containing structured and magnetized plasmas[1-3] as well as in some astrophysical settings[4-6]. Under typical laboratory or astrophysical conditions, plasma is usually highly inhomogeneous and, therefore, simple analytical methods[7] developed to study the propagation of linear MHD waves in homogeneous media cannot be applied. Conversely, a number of known analytical solutions are obtained for cases of only marginal practical interest[8-11]. In general, problems of propagation of MHD waves in a medium with smooth and/or sharp gradients in physical parameters are so complex that they must be investigated by means of numerical simulations.

In this paper, we present results of numerical studies of MHD wave generation and propagation in a magnetically structured medium. The adopted model is relatively simple because it takes into account only magnetic interfaces and the corresponding "jumps" in physical parameters across these interfaces. Despite simplicity of the present model, we are still able to study two important and previously unsolved physical problems, namely, the interaction of a single magnetic interface with the external medium and the interaction of a magnetic slab (two magnetic interfaces) with its surroundings. Some aspects of these problems have already been investigated[12-13], in particular, there is a class of known analytical solutions represented in the form of dispersion relation and obtained by making a Fourier transform in time and space[14-15]. However, to the best of our knowledge, time-dependent numerical calculations of the propagation of MHD body waves and MHD surface waves discussed in this paper have not been previously performed. In particular, it is presently not clear how effectively MHD surface waves can transfer energy along the single magnetic interface and along the magnetic slab, and how efficient are these waves in generating acoustic waves in the external medium. Our main aim is to gain a new physical insight into these two problems by calculating the efficiency of wave confinment

for a different form of the imposed perturbations and for a different range of the physical parameters.

We organize our paper as follows: the basic formulation and governing equations are given in Section II; the results of numerical simulations for the single magnetic interface and for the slab are presented in Sections III and IV, respectively; and finally Section V contains discussion and some concluding remarks.

II BASIC FORMULATION AND GOVERNING EQUATIONS

To describe the propagation of MHD waves in structured media, we consider two simple physical models. In the first model, we assume that the background medium is separated into magnetized and non-magnetized domains by a single magnetic interface (Figure 1a), and that there are no other gradients in these domains except at the interface. In the second model, we consider a thick, non-stratified, magnetic slab embedded in an otherwise non-magnetic and uniform medium (Figure 1b). In both models, we assume that there is a temperature equilibrium between magnetic and non-magnetic regions, and that the pressure balance across the interface is satisfied. Our approach is two-dimensional and based on the following set of ideal MHD equations written in cartesian coordinates

$$\frac{\partial \rho}{\partial t} = -\frac{\partial}{\partial x}(\rho v_x) - \frac{\partial}{\partial z}(\rho v_z) \tag{1}$$

$$\frac{\partial(\rho v_x)}{\partial t} = -\frac{\partial p}{\partial x} - \frac{\partial}{\partial x}(\rho v_x^2) - \frac{\partial}{\partial z}(\rho v_x v_z) + B_z\left(\frac{\partial B_x}{\partial z} - \frac{\partial B_z}{\partial x}\right) \tag{2}$$

$$\frac{\partial(\rho v_z)}{\partial t} = -\frac{\partial p}{\partial z} - \frac{\partial}{\partial x}(\rho v_x v_z) - \frac{\partial}{\partial z}(\rho v_z^2) - B_x\left(\frac{\partial B_x}{\partial z} - \frac{\partial B_z}{\partial x}\right) \tag{3}$$

$$\frac{\partial B_x}{\partial t} = \frac{\partial}{\partial z}\left(v_x B_z - v_z B_x\right) \tag{4}$$

$$\frac{\partial B_z}{\partial t} = \frac{\partial}{\partial x}\left(v_z B_x - v_x B_z\right) \tag{5}$$

$$\frac{\partial}{\partial t}\left(\frac{p}{\rho^\gamma}\right) = -v_x \frac{\partial}{\partial x}\left(\frac{p}{\rho^\gamma}\right) - v_z \frac{\partial}{\partial z}\left(\frac{p}{\rho^\gamma}\right) \tag{6}$$

$$\frac{\partial B_x}{\partial x} + \frac{\partial B_z}{\partial z} = 0 \tag{7}$$

and the equation of state,

$$p = \rho RT \tag{8}$$

where v_x and v_z are the horizontal (x-axis) and vertical (z-axis) components of the velocity, respectively. Similarly, B_x and B_z are the horizontal and vertical components of magnetic field. The other symbols have their usual meaning: ρ is the density; T is the temperature; p is the thermal pressure; γ is the specific ratio being taken as 5/3 and R is the universal gas constant. It must be noted that we have suppressed the factor 4π in the term of Lorentz's force through an adequate choice of the unit of magnetic field. This set of differential equations is solved numerically for the case of a single and double (magnetic slab) magnetic interface. Note that the presented equations are formally nonlinear and that these nonlinear equations have been solved numerically; however, in this paper we restrict our discussion the results due to a small finite amplitude perturbation to avoid shock formation in our computational domain. To relate the initial physical parameters in the magnetized and non-magnetized regions, we use the horizontal pressure balance given by

$$p_e = p_i + \frac{B_i^2}{8\pi}, \tag{9}$$

which can be also written as

$$p_i = \frac{\beta}{1+\beta} p_e, \tag{10}$$

where $\beta = 8\pi p_i / B_i^2$ and $T_i = T_e = const.$ All physical parameters in the magnetized (internal) and non-magnetized (external) regions are indicated by subscript "i" and "e", respectively (see Figure 1).

To carry out the studies of propagation of MHD body and surface waves in the considered models, we have developed a nonlinear, two-dimensional, time-dependent, ideal

MHD code constructed on the basis of a Lagrangian grid and semi-implicit scheme. The Lagrangian grid has been used because of its small numerical diffusion and because it easily allows tracing the interface. The semi-implicit scheme code means that we find solutions for fluid properties $(\vec{V}, p, \rho, T)$ by using an explicit scheme and then solve for the magnetic field using a non-iterative implicit scheme[16]. As shown in Figure 1, our computational domain always contains one magnetized region and either one or two non-magnetized regions. The perturbations are imposed on the system at $z = 0$ (which is also the lower boundary of the computational domain) and are restricted only to the magnetized region. The physical condition at the lower boundary is the so-called rigid free-slip wall condition, which means that transverse motion of the boundary is transmitted to the fluid only through the magnetic field. In our calculations concerning a single magnetic interface, the location of the interface is at the z-axis (see Figure 1) and nonreflecting boundary conditions are applied at all the computational domain boundaries parallel and perpendicular to the interface. For our computations concerning a single magnetic interface for longitudinal perturbations, the z-axis is the axis of symmetry, so the symmetry boundary conditions are used. At the remaining computational boundaries the nonreflecting boundary conditions are applied. In the case of magnetic slab, all the computational boundaries are non-reflecting boundaries.

Having prescribed the boundary conditions for our numerical calculations, we now briefly describe tests performed to confirm the validity and accuracy of our code. We have tested the code by performing simple acoustic and Alfven wave calculations and then comparing the obtained numerical results to known analytical solutions. We have compared numerical and analytical MHD surface wave speeds and found that the difference never exceeded 2%. To describe the results from one of the tests, we consider a small amplitude acoustic wave propagating in a homogeneous medium with a uniform magnetic field (for the purpose of this test, we have excluded the interface and consider the magnetic field to be present in the whole computational domain). It is assumed that the acoustic wave is excited at the height $z = 0$ (see Figure 1) by the motion $v_z(t) = v_o \; sin \; (2\pi t/\tau)$

with $v_o = 10^{-3}\ C_s$ (C_s is the speed of sound) and $\tau = 40\ sec.$ For this special case, we have found fully time dependent numerical solutions and then compared them to the well-known analytical solutions to the acoustic wave equation; note that the analytical solution is simply obtained by making a Fourier transform. The difference between the obtained numerical and analytical solution is less than one percent and the relative difference of wave energy in each wavelength is less than 2×10^{-5}. We have also performed similar tests for purely transverse MHD (Alfven) waves propagating in homogeneous and inhomogeneous (stratified and isothermal) media, and find that our numerical solutions are consistent with the known analytical solutions. All these details can be found in Ref. 16. After performing these tests, we feel confident in using the code to investigate the behavior of MHD body and surface waves on a single and double magnetic interface. In the following, we present the results of these studies.

III SINGLE MAGNETIC INTERFACE

The existence of a single magnetic interface in an otherwise homogeneous background medium (see Figure 1a) allows separating MHD waves into two classes, namely, body and surface waves. In our model, the body waves are confined only to the magnetized part of the computational domain and the surface waves exist on the magnetic interface. The waves are excited by imposing either transverse or longitudinal perturbations in the magnetized part of the computational domain. In the following, we shall consider both cases of perturbations and present the obtained numerical results. We begin with the transverse perturbations.

To introduce the transverse perturbations at the lower boundary of our computational domain, we impose the following velocity perturbations in the magnetized region: $v_x(t) = v_o\ sin\ (2\pi t/\tau)$, with v_o being $10^{-3}\ V_A$ (V_A is the Alfven velocity) and τ equals to $0.5L/V_A$ where L is the height of the computation domain. The reason we kept the amplitude of perturbation small is to avoid shocks in our computational domain. The

imposed perturbations generate purely transverse magnetic waves which propagate with the Alfven velocity inside the magnetized region; we shall call these waves the body waves (see Figure 2). The perturbations also excite the surface wave which propagates only along the magnetic interface with a velocity lower than the external sound speed. As seen in Figure 2, the wave velocity and magnetic field are predominantly in the direction of its propagation, therefore, we shall call this wave the slow MHD surface wave. In addition, the figure clearly shows that there are no disturbances (corresponding to acoustic waves) propagating into the external medium. This simply indicates that under the considered physical conditions the excitation of external acoustic waves by the internal (body) wave and/or by the slow MHD surface wave does not take place; note that the discussed results have been obtained for the plasma $\beta = 100$. It is interesting to explore whether there are any circumstances when the external acoustic waves can be generated by the purely transverse body waves. This may sound surprizing because the body waves considered here are purely transverse and, therefore, they do not have a longitudinal component (at least, in the first approximation). The results presented in Figure 3 correspond to $\beta = 1.2$ and 0.5, and clearly show that the external acoustic waves can indeed be excited by transverse MHD waves when the plasma β is of the order of unity or lower. Note that in the calculations discussed here, higher values of β are obtained by decreasing the strength of the magnetic field while keeping the other physical parameters unchanged.

The following physical picture emerges from the results presented above. The process of generation of the transverse body waves is simple to understand because it is a direct consequence of the imposed velocity perturbations at the lower (magnetized) part of the computational domain. Still, the overall picture of the interaction of the single magnetic interface with its non-magnetic surroundings is relatively simple only for a high β plasma; in this case, the wave preserves its transverse character during the propagation and the non-magnetic external medium is not disturb by the wave montion (see Figure 2). The problem is more complicated for lower β (see Figure 3) because the body wave changes its character

and the perturbed quantities become more aligned with the background magnetic field. The place where the process of changing the wave character is particularly prominent is marked "mode change" in Figure 3a. The physical reason for the observed mode change is the interaction of the body wave with the external medium and the energy leakage through the interface (see below for more detailed discussion). The same interaction determines the character of the MHD surface wave existing on the magnetic interface and leads to the excitation of external acoustic waves. It is interesting that the waves in the external medium are generated when the plasma β is close to unity (compare Figures 2 and 3). This can be explained by a well-known physical process considered for magnetic flux tubes[17]. Namely, the generation takes place only when the phase velocity of propagating waves in the magnetized medium (in the case under consideration, these are the body waves) is comparable or exceeds the characteristic propagation speed in the external medium (which here is the sound speed). The generation can occur only for β close to and lower than one and this is clearly demonstrated by the results presented in Figures 2 and 3. We calculated the energy leakage from the magnetized region to the external medium and found that for $\beta = 1.2$ almost 20% of the total energy leaks out to the surrounding medium[18]. This leakage through the magnetic interface is a source of energy for the generation of external acoustic waves. It must be also noted that the slow MHD surface wave confined to the interface does not contribute to this wave generation because its phase velocity is always smaller than the external speed of sound.

This physical picture of the interaction between the magnetic interface and the external medium will be helpful in the following studies of a magnetic slab.

IV MAGNETIC SLAB

We now introduce another magnetic interface into the background medium and form a magnetic slab. In this case, similar to the single interface, we assume that there are no other gradients in the surroundings. Here, we consider two different kinds of perturba-

tions, namely, purely transverse and purely longitudinal perturbations. We begin our presentation with the former.

A Purely Transverse Velocity Perturbations

The imposed velocity perturbations on the considered magnetic slab are similar to those discussed in the case of a single magnetic interface (see the previous section). Note that only the magnetized region of the computational domain is perturbed. The results of our simulations corresponding to three cases of $\beta = 100$, 1.2 and 0.1 are presented in Figures 4 and 5. The plotted wave energy density shows a significant increase at the interface due to the MHD surface waves; it is also seen that the energy leakage to the external medium increases when plasma β decreases. There are four general conlusions which can be drawn from the results presented in these figures. First, it is clear that the external medium becomes more perturbed when the plasma β decreases; this is consistent with the results described in the previous section. Second, the kink mode (body wave) being confined to the slab changes its character (from purely transverse to predominantly longitudinal) as a result of the interaction between the slab and the surroundings. Third, MHD surface waves propagate along both magnetic interfaces and they are predominantly longitudinal. Finally, the physical processes playing a dominant role in the behavior of the slab are essentially the same as those described above for the single magnetic interface.

At this point, it is interesting to compare the results obtained for the magnetic slab to those known for thin and vertical magnetic flux tubes.[17] Here, we are mainly interested in linear and transverse (kink) tube waves and want to compare the behavior of these waves to that shown by the slab kink waves. In a typical tube wave treatment[17], the waves propagate along magnetic flux tubes without exchanging energy with the external medium; this is one of the most fundamental assumptions of the approach. Our results clearly indicate that the oscillating magnetic slab strongly interacts with the external medium and that this interaction is particularly strong for low-β plasma. Therefore, calculations based on the approximation that the generated external acoustic energy can be neglected in the

process of transverse tube (slab) wave propagation must taken with caution.

B Purely Longitudinal Velocity Perturbations

Now, we impose the velocity perturbations along the magnetic field direction in the slab and investigate the interaction of the generated acoustic waves with the external medium. Note that similar to the cases previously considered the perturbations of the form $v_z(t) = v_o \; sin \; (2\pi t/\tau)$, with $v_o = 10^{-3} \; C_s$, and $\tau = 100\,\text{sec}$, are imposed only to the magnetized (slab) region. The considered problem shows symmetry with respect to the z-axis (see Figure 1b) which means that the calculations can be limited to only one half of the computational domain by assuming the symmetric boundary conditions at the z-axis and all the other three computational boundary conditions are nonreflecting. The results of our numerical calculations carried out for $\beta = 0.1$, 1.2 and 100 are presented in Figures 6 and 7, respectively. The comparison of these results to those presented in the previous subsection clearly shows the opposite dependence of the wave energy leakage on the plasma β. This can easily be explained by the fact that only strong magnetic fields (low-β plasma) can significantly confined acoustic waves to the magnetized region; the confinement is stronger for stronger fields (see Figure 7). In the case, however, of weak magnetic fields (high-β plasma) the waves generated at one corner of the computational domain propagate freely in all directions (Figure 7a) and almost all energy leaks out to the external medium. Note also that in all three cases the MHD surface wave existing on the interface is rather weak and cannot be well-resolved numerically.

V CONCLUDING REMARKS

In this investigation, we have presented a nonlinear two-dimensional, time-dependent, planar MHD body and surface model to study the behavior of MHD waves on a single and double (slab) magnetic interface separating magnetized and non-magnetized plasma regions with finite amplitude perturbations. The physical processes of generation and propagation of MHD body and surface waves on these magnetic interfaces have been investigated.

In addition, we have also studied the interaction of the magnetic interfaces with their surroundings and the problem of energy leakage from the magnetized medium to the non-magnetic surroundings. The obtained results clearly depend on the type of perturbations imposed on the magnetized region and on the plasma parameter β. We have shown that from a physical point of view there are several major differences between imposing purely transverse and purely longitudinal perturbations on the magnetized region. The former being perpendicular to the interface disturbs the external medium, however, the latter being parallel to the interface do not disturb the surroundings. The problem of wave confinment is more complicated because it shows a strong dependence on the plasma β. For a low-β plasma, the interfaces become more "rigid" boundaries in the medium than for a high-β plasma. This leads to the distinct behavior of the waves generated by the transverse and longitudinal perturbations. Namely, the "rigid" interfaces (a magnetic slab with rigid walls) will predominantly confine internal acoustic waves but will strongly influence the external medium when the transverse perturbations are imposed. In the case of a high-β plasma, the wave behavior will be exactly opposite: the internally generated acoustic waves will freely propagate in all directions but the energy carried by the kink slab waves will be predominantly confined to the magnetized region; the latter results from the fact that the interfaces are not so rigid as in the case of a low-β plasma and therefore they cannot much influence the external medium. In summary, the presented results show that the confinment of MHD surface waves to single magnetic interfaces and magnetic slabs significantly increases with increasing plasma β.

ACKNOWLEDGEMENTS

The work performed by S. T. Wu and Y. C. Xiao was supported by the National Aeroanutics and Space Administration (NASA) under grant NAGW-9. Z. E. Musielak acknowledges partial support of this research by the National Science Foundation (NSF) under grants AST-9115191 and ATM-9119580 and by NASA under grants NAGW-2933 and

NAG8-839. S. T. Suess was supported by the NASA Cosmic and Heliospheric Physics Branch.

REFERENCES

1. E. M. Barston, Ann. Phys. (NY) **29**, 282 (1964).

2. J. A. Tataronis and W. Grossmann, Z. Phys. **261**, 203 (1973).

3. L. Chen and A. Hasegawa, Phys. Fluids **17**, 1399 (1974).

4. F. C. Michel, Rev. Mod. Phys. **54**, 1 (1982).

5. L. M. B. C. Campos, Rev. Mod. Phys. **59**, 363 (1987).

6. Z. E. Musielak, Mem. Soc. Astr. Ital **63**, 635 (1992).

7. J. H. Thomas, Ann. Rev. Fluid Mech. **15**, 321 (1983).

8. V. C. A. Ferraro and C. Plumpton, Astrophys. J. **127**, 459 (1958).

9. D. C. Pridmore-Brown, Phys. Fluids **9**, 1290 (1966).

10. C. Uberoi, Phys. Fluids, **15**, 1673 (1972).

11. L. M. B. C. Campos, J. Phys. A: Math. Gen., **21**, 2911 (1988).

12. B. Roberts, In *The Physics of Sunspots*, Eds. L. E. Cram and J. H. Thomas (Sacramento Peak Observatory, Sunspot, N.M.) p. 369 (1981).

13. P. C. Cally, Austral. J. Phys., **38**, 825 (1985).

14. B. Roberts and A. R. Webb, Solar Phys., **56**, 5 (1978).

15. B. Roberts and A. R. Webb, Solar Phys., **64**, 77 (1979).

16. Y. C. Xiao, *Ph.D. Thesis*, University of Alabama in Huntsville (1988).

17. H. C. Spruit, In *The Sun as a Star*, Ed. S. D. Jordan (NASA SP-450) NASA (Scientific and Technical Information Branch), Washington, D. C. 20546, p. 385 (1981).

18. V. M. Cadez and V. K. Okretic, J. Plasma Phys., **41**, 23 (1989).

FIGURE CAPTIONS

- Fig. 1 Schematic description of (a) single magnetic interface model and (b) magnetic slab model.

- Fig. 2 The calculated (a) wave energy density, (b) disturbed magnetic field, and (c) wave-induced velocity field due to a transverse perturbation for $\beta = 100, C_s = 10km\ s^{-1}, V_A = 1.1km\ s^{-1}$ and $\tau = 900s$ in the case of single magnetic interface model.

- Fig. 3 The calculated (a) wave energy density and wave-induced velocity field for $\beta = 1.2, C_s = 10km\ s^{-1}, V_A = 10km\ s^{-1}$ and $\tau = 100s$ and (b) the same parameters for $\beta = 0.5, C_s = 10km\ s^{-1}, V_A = 16km\ s^{-1}$ and $\tau = 60s$ due to a transverse perturbation in the case of single magnetic interface model.

- Fig. 4 The calculated (a) wave energy density, (b) disturbed magnetic field, and (c) the wave-induced velocity field due to a transverse perturbation for $\beta = 100, C_s = 10km\ s^{-1}, V_A = 1.1km\ s^{-1}$ and $\tau = 900s$ in the case of magnetic slab model.

- Fig. 5 The calculated (a) wave energy density and wave-induced velocity field for $\beta = 1.2, C_s = 10km\ s^{-1}, V_A = 10km\ s^{-1}$ and $\tau = 100s$ and (b) same parameters for $\beta = 0.1, C_s = 10km\ s^{-1}, V_A = 35km\ s^{-1}$ and $\tau = 75s$ due to a transverse perturbation in the case of magnetic slab model.

- Fig. 6 The calculated (a) wave energy density, (b) disturbed magnetic field and (c) wave-induced velocity field due to a longitudinal perturbation for $\beta = 0.1, C_s = 10km\ s^{-1}, V_A = 35km\ s^{-1}$ and $\tau = 100s$ in the case of single magnetic interface model.

- Fig. 7 The calculated (a) wave energy density and wave-induced velocity field for $\beta = 100, C_s = 10km\ s^{-1}, V_A = 1.1km\ s^{-1}$ and $\tau = 100s$ and (b) same parameters $\beta = 1.2, C_s = 10km\ s^{-1}, V_A = 1.1km\ s^{-1}$ and $\tau = 100s$ due to a longitudinal perturbation in the case of the single magnetic interface model.

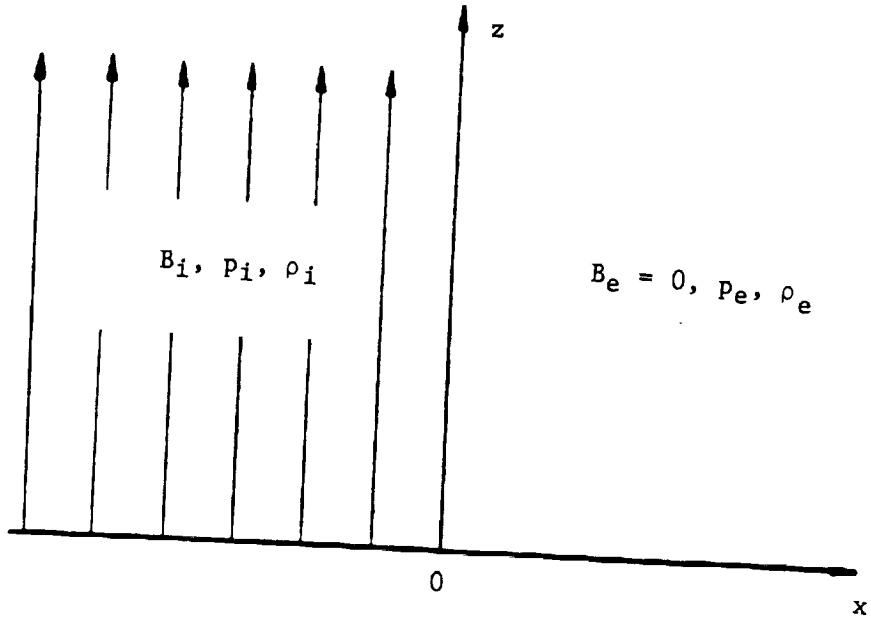
z
B_i, p_i, ρ_i
$B_e = 0$, p_e, ρ_e
0
x

(a)

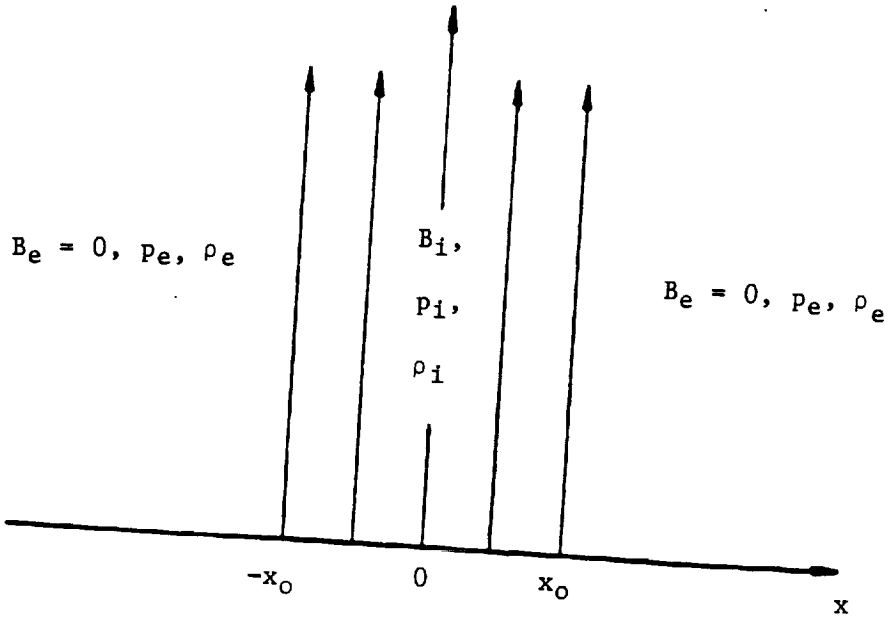
$B_e = 0$, p_e, ρ_e
B_i,
p_i,
ρ_i
$B_e = 0$, p_e, ρ_e
$-x_o$
0
x_o
x

(b)

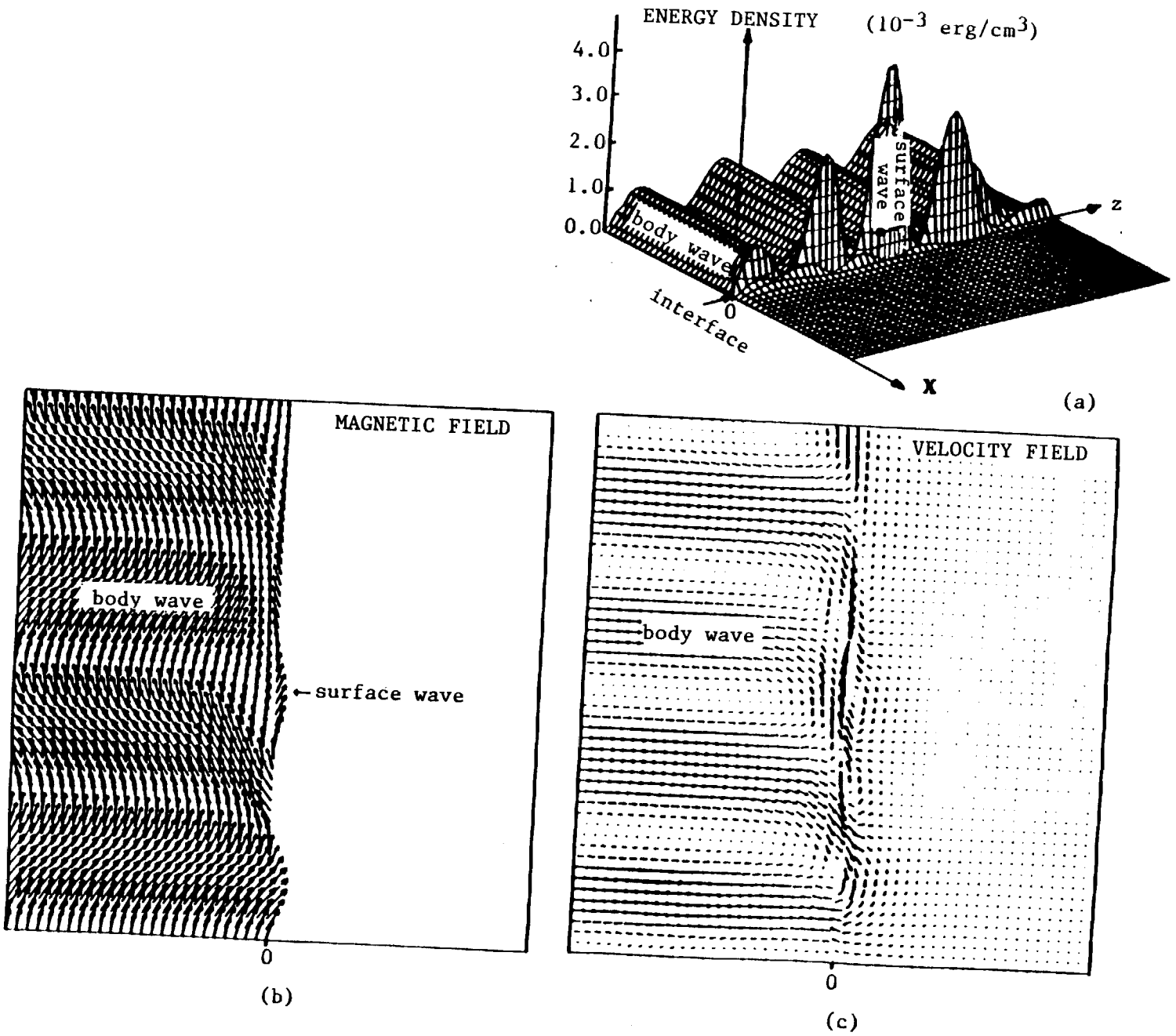
ENERGY DENSITY (10-3 erg/cm3)
4.0
3.0
2.0
1.0
0.0
surface wave
body wave
z
0
interface
X
(a)
MAGNETIC FIELD
body wave
surface wave
0
(b)
VELOCITY FIELD
body wave
0
(c)

Fig 2

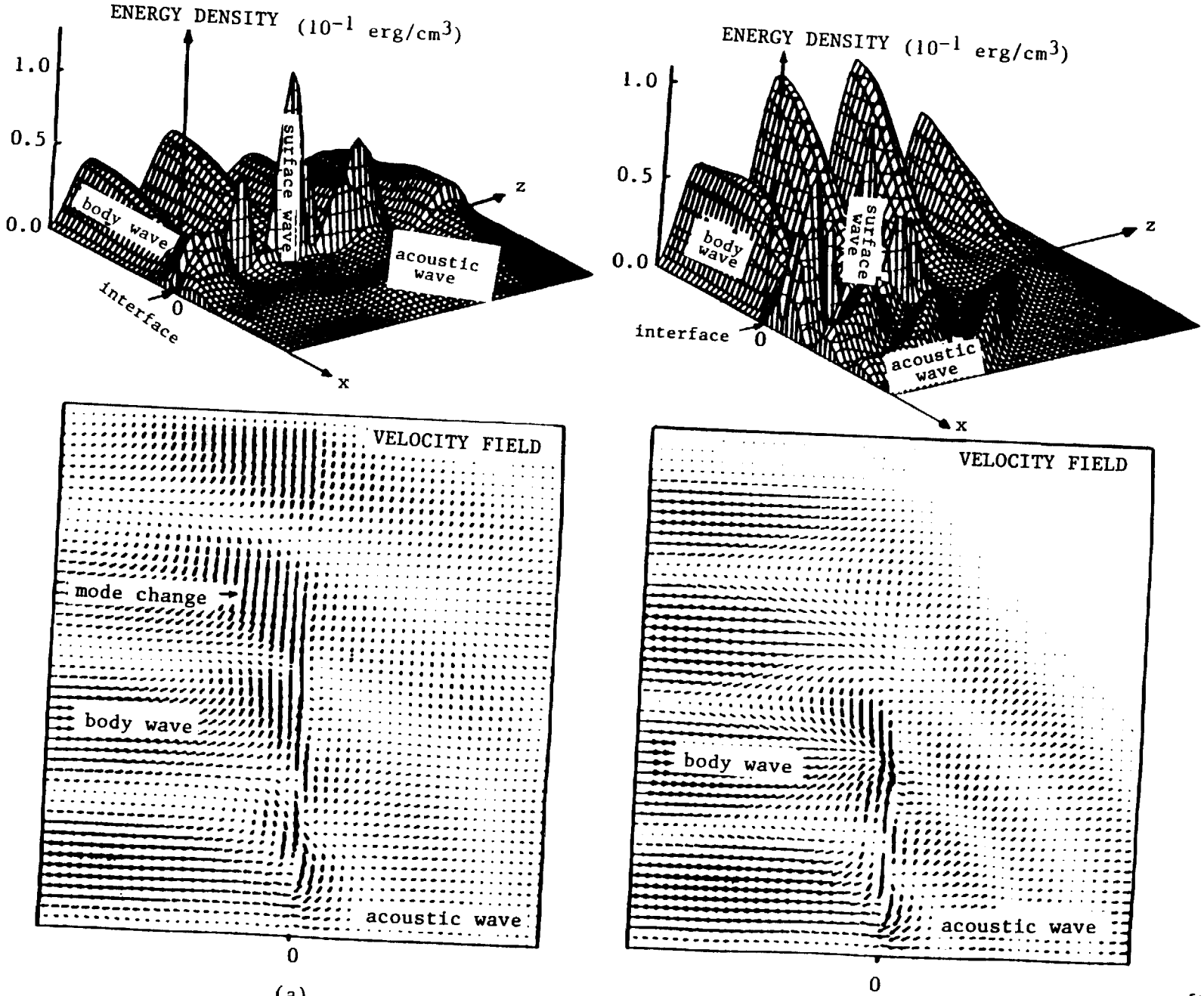
ENERGY DENSITY (10-1 erg/cm3)
1.0
0.5
0.0
body wave
surface wave
acoustic wave
interface
0
x
z
VELOCITY FIELD
mode change
body wave
acoustic wave
0
(a)
ENERGY DENSITY (10-1 erg/cm3)
1.0
0.5
0.0
body wave
surface wave
acoustic wave
interface
0
x
z
VELOCITY FIELD
body wave
acoustic wave
0
(b)

Fig 3

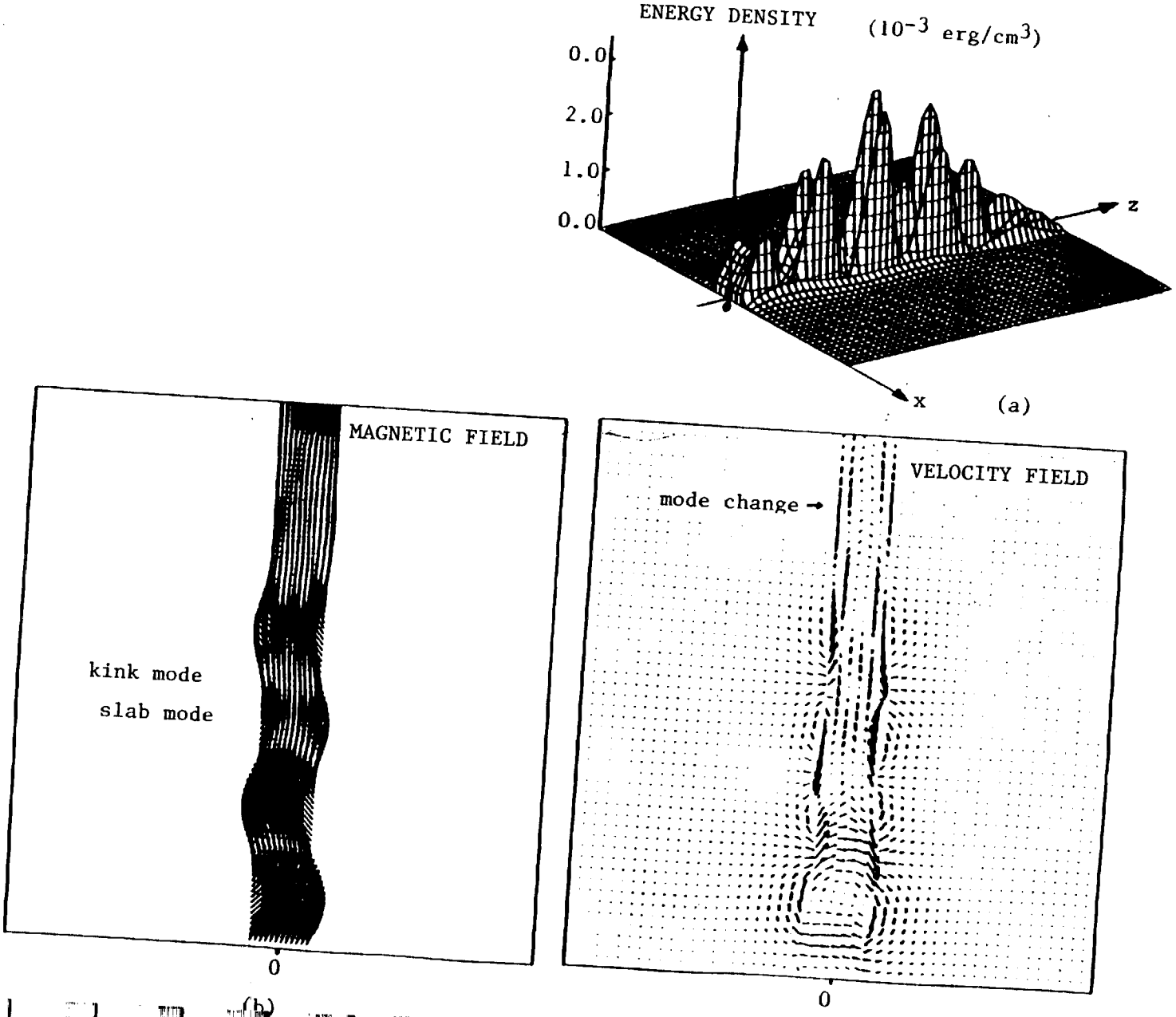
ENERGY DENSITY
(10-3 erg/cm3)
0.0
2.0
1.0
0.0
z
x
(a)
MAGNETIC FIELD
kink mode
slab mode
0
(b)
VELOCITY FIELD
mode change
0
(c)

Fig 4

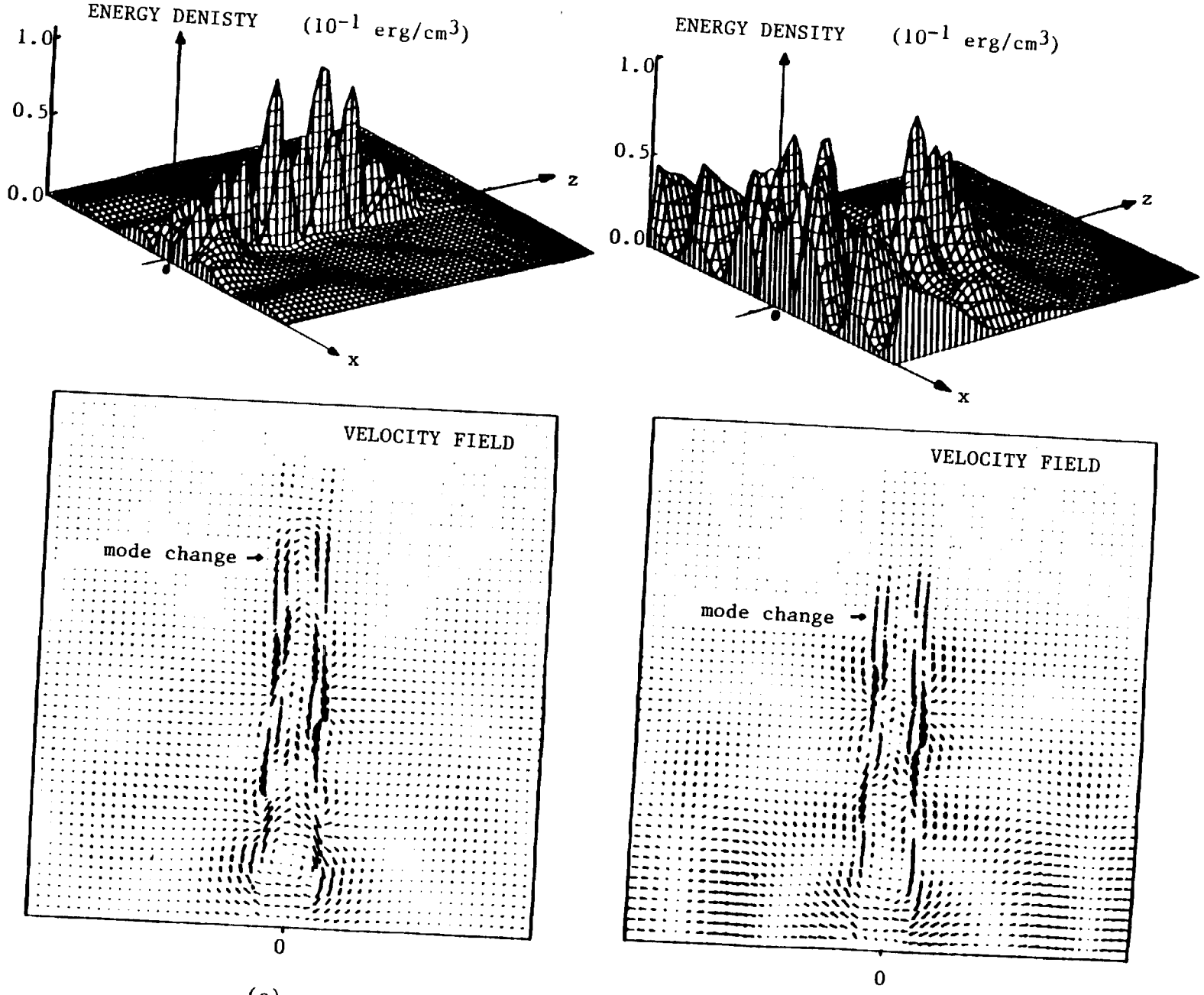
ENERGY DENISTY (10-1 erg/cm3)
1.0
0.5
0.0
z
x
ENERGY DENSITY (10-1 erg/cm3)
1.0
0.5
0.0
z
x
VELOCITY FIELD
mode change
0
(a)
VELOCITY FIELD
mode change
0
(b)

Fig 5

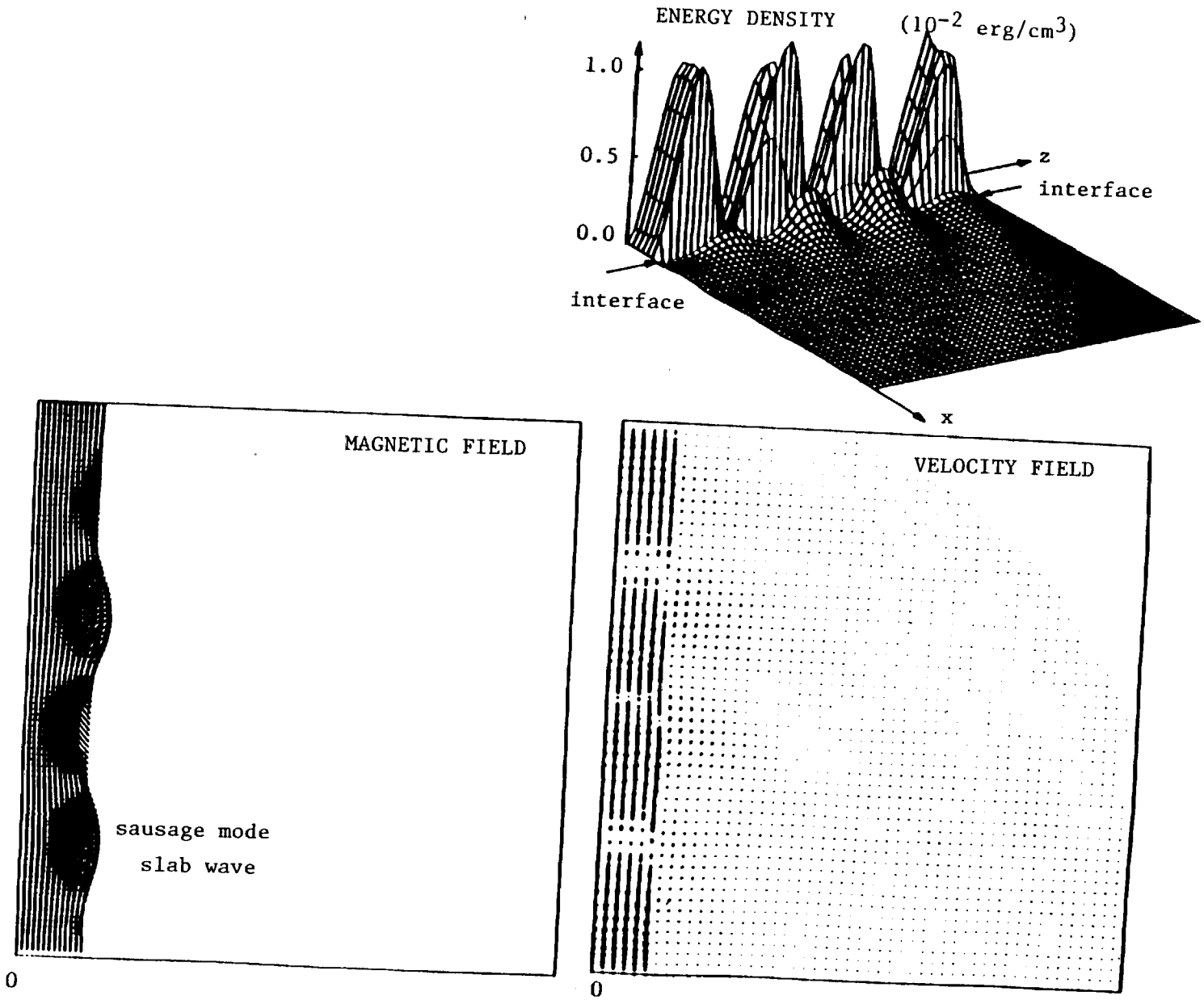
ENERGY DENSITY
(10-2 erg/cm3)
1.0
0.5
0.0
z
interface
interface
x
MAGNETIC FIELD
sausage mode
slab wave
0
VELOCITY FIELD
0

Fig 6

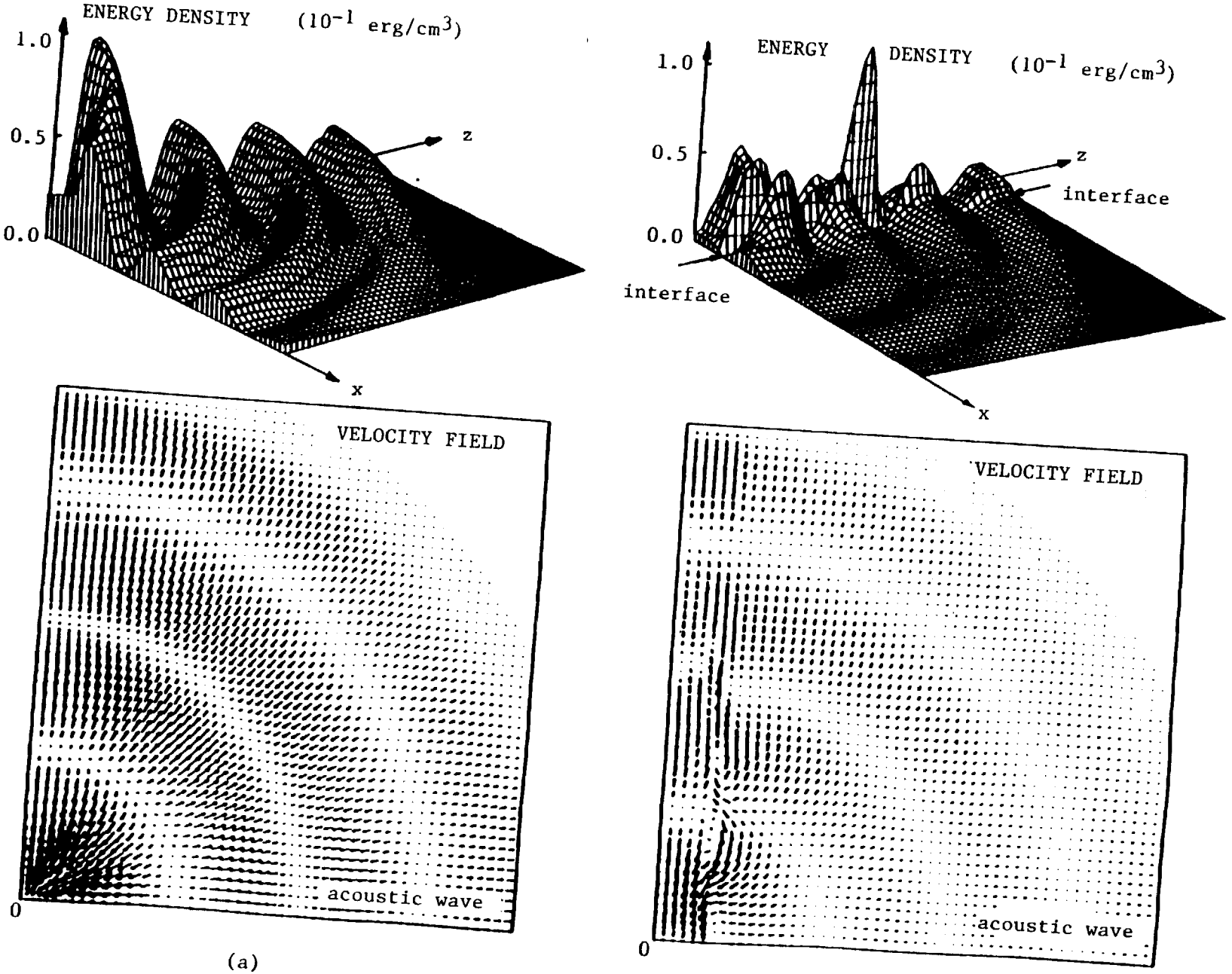
ENERGY DENSITY (10-1 erg/cm3)
1.0
0.5
0.0
z
x
VELOCITY FIELD
acoustic wave
0
(a)
ENERGY DENSITY (10-1 erg/cm3)
1.0
0.5
0.0
z
interface
interface
x
VELOCITY FIELD
acoustic wave
0
(b)

Fig 7

MODEL CALCULATIONS OF THE RISING MOTION OF A PROMINENCE LOOP

TYAN YEH

Space Environment Laboratory, NOAA Environmental Research Laboratories, Boulder, CO 80303, U.S.A.

and

S. T. WU

Center for Space Plasma and Aeronomic Research, The University of Alabama in Huntsville, Huntsville, AL 35899, U.S.A.

(Received 26 June, 1990; in revised form 23 October, 1990)

Abstract. Model calculations are presented for the rising motion of the top section of a prominence loop, which is represented by a straight flux rope immersed in a coronal medium permeated with a bipolar magnetic field. Initially the prominence is at rest, in equilibrium with the surrounding coronal medium. When the magnetic monopoles that account for the source current for the bipolar field strengthen, the upward hydromagnetic buoyancy force overcomes the downward gravitational force so that the prominence is initiated into rising motion. The illustrative examples show that prominences can move away from the solar surface by the action of the hydromagnetic buoyancy force, which is preponderant with the diamagnetic force due to the current carried by the prominence interacting with the coronal magnetic field produced by the photospheric currents, if the changes in the photospheric magnetic field are sufficiently large.

1. Introduction

A new dynamical model of prominence loops was recently constructed on the basis of the theory of hydromagnetic buoyancy force for flux ropes (Yeh, 1989). A prominence loop immersed in the solar atmosphere is regarded as an extraneous body in the sense that it is magnetically separated from its surrounding medium. Thus its magnetic field, mass density, temperature, and motion are quite different from those of the surrounding medium. The important feature is the polarization current induced on the periphery of the prominence that makes the ambient magnetic field tangential. The exertion of the ambient hydromagnetic pressure gives rise to the hydromagnetic buoyancy force. Its predominant constituent is the diamagnetic force which amounts to the force exerted on the currents in the prominence by the external currents that sustain the coronal magnetic field. For a prominence to be in stationary equilibrium with its surrounding medium, the hydromagnetic buoyancy force counterbalances the gravitational force exerted by the massive Sun. When the coronal magnetic field evolves, the changed diamagnetic force no longer matches the gravitational force. Once the forces become unbalanced, the prominence is initiated into motion. The evolving motion may be either upward or downward, depending on whether the hydromagnetic buoyancy force is greater or less than the gravitational force. That the evolving motion of prominence filaments is driven by the evolution of the global magnetic field has been inferred from observations (Kahler *et al.*, 1988).

Solar Physics **132:** 335–351, 1991.
© 1991 *Kluwer Academic Publishers. Printed in Belgium.*

In this paper we apply the dynamical theory to study the motion of the top section of a prominence loop arched above the solar surface. The calculation presented is mathematically one-dimensional in space (viz., the heliocentric distance) although it involves two-dimensional geometry and the magnetic field is three-dimensional (see Figure 1). The governing equations for the dynamical evolution are MHD equations of motion supplemented with equations of mass conservation, flux conservation, and energy conservation. Since we are mainly interested in the dynamics of prominences, energetics is dealt with only to the extent necessary to provide a closed system of equations for the dynamics. Accordingly, in our present calculations we neglect all entropy-generating processes that are pertinent to the thermodynamics of prominences.

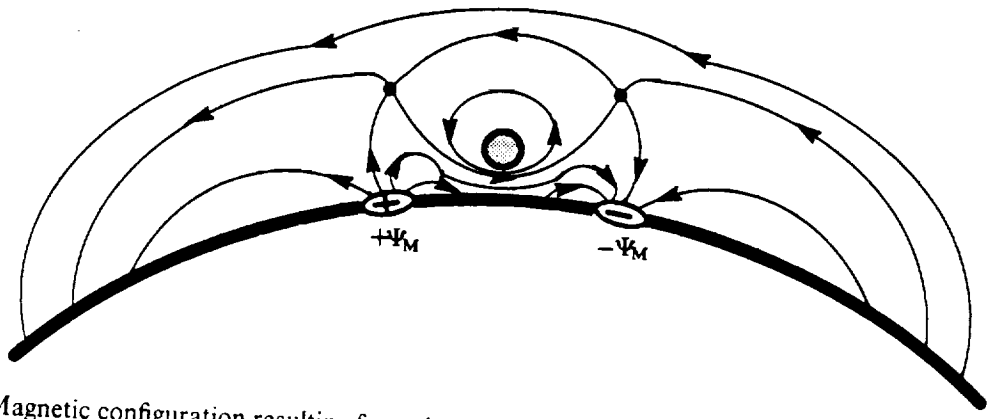

Fig. 1. Magnetic configuration resulting from the interaction between a couple of magnetic monopoles on the solar surface and a large current carried by the prominence, with a polarization current induced on the interface.

Several illustrative examples of dynamical evolution of a prominence loop are shown. First, we construct an equilibrium configuration for a prominence loop immersed in a coronal medium that has a bipolar magnetic field permeated into a magnetohydrostatic atmosphere. For a prominence loop to be stationary, it must have neither translational motion as a whole nor expansional motion relative to its axis. The former requires that the downward pull of the gravitational force exerted by the Sun is balanced by the upward lift of the hydromagnetic buoyancy force exerted by the surrounding coronal medium. The latter requires that the outward push of the force by the gas pressure and the azimuthal current of the prominence is balanced by the inward pinch of the force by the hydromagnetic pressure of the ambient medium and the axial current of the prominence. Next, we calculate the motion of the prominence loop when the equilibrium is lost because of a temporal change of the bipolar field. The change can be caused by strengthening and/or displacement of the magnetic monopoles for the bipolar field. These examples demonstrate that the prominence can move away from the solar surface when the change is sufficiently large.

The model calculations illustrate the mechanism involving hydromagnetic buoyancy force that is likely to be important in the eruption of prominences. Such calculations in conjunction with analytical study also serve to narrow down the range of the

parameters as an aid to MHD numerical simulations of the eruptive motion of prominences. Very often the difficulties with numerical simulations lie in the large number and extensive range of the pertinent parameters that characterize the phenomenon under study (Wu *et al.*, 1990).

2. Assumptions

The geometry of the prominence loop may be described by its axis and its cross-section. We assume that the varying cross-section is well accounted for by a circular cross-section whose radius changes in time. In this treatment of the top section of a prominence loop, a prominence is represented by a flux rope with a straight axis, whose heliocentric distance may change. The corona is represented by a magnetized medium that has a transverse magnetic field, perpendicular to the axis of the prominence, which is bipolar and a longitudinal magnetic field, parallel to the axis, which varies with the heliocentric distance only. The current that produces the bipolar field is below the solar surface; it is to be accounted for by a couple of magnetic monopoles on the photosphere. These monopoles are chosen to be line monopoles to make the problem two-dimensional. The current that produces the longitudinal magnetic field is in the corona. The coronal current is in magnetohydrostatic equilibrium with a stratified gas pressure of the coronal gas which is acted upon by solar gravity.

The prominence loop carries helical field lines. The helical magnetic field in the straight prominence is represented by

$$\mathbf{B}_E = \mathbf{1}_z B_0 \left(1 - \frac{q^2}{Q^2}\right)^{1/2} + \mathbf{1}_\phi \tfrac{1}{2}\mu J_0 q \tag{1}$$

in cylindrical coordinates (z, q, ϕ), with the azimuthal angle ϕ measured from the radial line pointing downward (μ being the magnetic permeability in mks units). The axial component decreases from the axial value B_0 at the axis $q = 0$ to zero at the boundary $q = Q$. The azimuthal component increases from zero at the axis to the boundary value $B_B \equiv \frac{1}{2}\mu J_0 Q$ at the boundary. The total axial flux is $\Psi_E \equiv \frac{2}{3}\pi Q^2 B_0$ and the total azimuthal flux is $\frac{1}{4}Q^2 \mu J_0$ per unit axial length. This helical magnetic field is produced by the current density

$$\mathbf{J}_E = \mathbf{1}_z J_0 + \mathbf{1}_\phi \mu^{-1} \frac{B_0}{Q} \frac{q/Q}{(1 - q^2/Q^2)^{1/2}}, \tag{2}$$

which has an axial component that is uniform and an azimuthal component that increases from zero at the axis to infinity at the boundary. The total axial current is $I_E \equiv \pi Q^2 J_0$ and the total azimuthal current is $\mu^{-1} B_0$ per unit axial length. The Lorentz-force density

$$J_E \times \mathbf{B}_E = \mathbf{1}_q \left(\mu^{-1} \frac{B_0^2}{Q} - \tfrac{1}{2}\mu J_0^2 Q\right) \frac{q}{Q} \tag{3}$$

acting at various mass elements of the prominence is in the radial direction, perpendicular to the axis of the prominence loop. It increases from zero at the axis to $\mu^{-1}B_0^2/Q - \frac{1}{2}\mu J_0^2 Q$ at the boundary, in proportion to the radial distance. The axial current produces a pinching force toward the axis whereas the azimuthal current produces an anti-pinching force away from the axis.

The immersion of the prominence loop in the coronal medium causes a polarization current that keeps the internal field lines of the prominence separated from the external field lines of the corona. The induced current, which is concentrated in a thin peripheral layer by virtue of the high electrical conductivity of the solar plasma, produces a magnetic field that makes the ambient field tangential by cancelling the radial component of the coronal field on the interface and essentially doubling the azimuthal component there (Yeh, 1983). With the coronal mass density ρ_∞, the coronal gas pressure p_∞, and the coronal magnetic field $\mathbf{B}_\infty \equiv \mathbf{1}_z B_{\infty\parallel} + \mathbf{B}_{\infty\perp}$ pre-existing at the site of the prominence, the ambient magnetic field on the outer surface of the current layer is

$$\mathbf{B}_A(\phi) = \mathbf{1}_z B_{\infty\parallel}|_{q=Q} + \mathbf{1}_\phi 2(\mathbf{1}_\phi \cdot \mathbf{B}_{\infty\perp})|_{q=Q} + \mathbf{1}_\phi \frac{\mu I_E}{2\pi Q}. \tag{4}$$

The boundary magnetic field on the inner surface is

$$\mathbf{B}_B(\phi) = \mathbf{1}_\phi \frac{\mu I_E}{2\pi Q}. \tag{5}$$

The polarization current, given by $\mathbf{i}_P \equiv \mathbf{1}_q \mu^{-1}(\mathbf{B}_A - \mathbf{B}_B)$ per unit circumferential length, shields off the coronal field from permeating into the prominence. Across the massless layer of peripheral current the sum of gas pressure and magnetic pressure is invariant. The ambient gas pressure

$$p_A(\phi) = p_\infty|_{q=Q} \tag{6}$$

on the outer surface is essentially equal to the pre-existing coronal gas pressure at the periphery since the gas pressure in the exterior region is hardly perturbed by the intrusion of the prominence. The boundary gas pressure

$$p_B(\phi) = p_\infty|_{q=Q} + \tfrac{1}{2}\mu^{-1}B_{\infty\parallel}^2|_{q=Q} + 2\mu^{-1}B_{\infty\perp}^2|_{q=Q}\cos^2\phi + \\ + \frac{I_E}{\pi Q}B_{\infty\perp}|_{q=Q}\cos\phi \tag{7}$$

on the inner surface has a circumferential inhomogeneity which is spatially transformed from that of the ambient hydromagnetic pressure. The gas pressure inside the prominence is well represented by

$$p_E(q,\phi) = [p_0 - (p_\infty + \tfrac{1}{2}\mu^{-1}B_{\infty\parallel}^2)|_{q=0}]\left(1 - \frac{q^2}{Q^2}\right) + p_\infty(q,\phi) + \\ + \tfrac{1}{2}\mu^{-1}B_{\infty\parallel}^2(q,\phi) + \mu^{-1}B_{\infty\perp}^2(q,\phi) +$$

$$+ \mu^{-1} B^2_{\infty\perp}|_{q=0} \left(2 \frac{q^2}{Q^2} \cos^2 \phi - 1 \right) +$$

$$+ \mu^{-1} (B^2_{\infty\perp}|_{q=Q} - B^2_{\infty\perp}|_{q=0}) \frac{q^2}{Q^2} \cos 2\phi + \frac{I_E}{\pi Q^2} B_{\infty\perp}|_{q=Q} \cos \phi .$$

It varies from the axial value p_0 at the axis to the boundary value p_B. The gradient of this gas pressure yields the force density

$$-\nabla p_E = -\nabla(p_\infty + \tfrac{1}{2}\mu^{-1}\mathbf{B}^2_\infty + \tfrac{1}{2}\mu^{-1}B^2_{\infty\perp}) + \mathbf{1}_r \frac{I_E B_{\infty\perp}|_{r=r_0}}{\pi Q^2} +$$

$$+ \mathbf{1}_q \frac{2p_0 - (2p_\infty + \mu^{-1}B^2_{\infty\parallel})|_{r=r_0}}{Q} \frac{q}{Q} , \qquad (9)$$

ignoring insignificant terms. The term proportional to q/Q represents a radial force density that results from the difference between the internal gas pressure and the circumferential average of the external hydromagnetic pressure. The other terms, resulting from the circumferential inhomogeneity of the ambient hydromagnetic pressure, represent the spatial spreading of the hydromagnetic buoyancy force. The latter amounts to $\mathbf{1}_r \rho_\infty G M_\odot / r_0^2 + \mathbf{I}_E \times \mathbf{B}_\infty / \pi Q^2 + \mathbf{1}_r \Gamma \mu^{-1} B^2_{\infty\perp} / R_c$ by virtue of the magnetohydrostatic state of the coronal medium (see Equations (24) and (25) for the definitions of R_c and Γ). The coefficient Γ has the value of 2 in the above elucidation.

The prominence moves with the velocity

$$\mathbf{u}_E = \mathbf{1}_r u_0 + \mathbf{1}_q V \frac{q}{Q} , \qquad (10)$$

which consists of a translational velocity common to all mass elements of the prominence loop and an expansional velocity proportional to the distance from the axis. The translational motion is driven by the part of the force density that is uniform and the expansional motion is driven by the part of the force density that is in various radial directions. The former part includes the gravitational force exerted by the Sun and the hydromagnetic buoyancy force exerted by the surrounding medium. The latter part includes the Lorentz force that results from the interaction among the internal currents inside the prominence and the gradient force that results from the pressure difference between the internal and external gases.

The dynamical evolution of the prominence depends on its inertia. We assume that the mass density is uniform over the cross section, ignoring the higher-order effect of the spatial variation of the mass distribution. The value of mass density ρ_E changes in time.

3. Governing Equations

A prominence which is located initially equidistant from the two magnetic line monopoles will remain so when its heliocentric distance changes temporally (Figure 1).

The prominence loop is characterized by eight parameters: r_0, Q, u_0, V, ρ_E, B_0, J_0, and p_0.

The characterizing parameters evolve in accordance with the differential equations

$$\frac{\mathrm{d}}{\mathrm{d}t} r_0 = u_0 , \tag{11}$$

$$\frac{\mathrm{d}}{\mathrm{d}t} Q = V , \tag{12}$$

$$\rho_E \frac{\mathrm{d}}{\mathrm{d}t} u_0 = -\rho_E \frac{GM_\odot}{r_0^2} + \rho_\infty \frac{GM_\odot}{r_0^2} + J_0 B_{\infty\perp} + \Gamma \frac{\mu^{-1} B_{\infty\perp}^2}{R_c} , \tag{13}$$

$$\rho_E \frac{\mathrm{d}}{\mathrm{d}t} V = \frac{2p_0 + \mu^{-1} B_0^2}{Q} - \frac{2p_\infty + \mu^{-1} B_{\infty\parallel}^2 + \frac{1}{2}\mu J_0^2 Q^2}{Q} , \tag{14}$$

supplemented by the temporal invariances of total mass, axial magnetic flux, azimuthal magnetic flux, and total thermal energy:

$$\pi Q^2 \rho_E = M_E , \tag{15}$$

$$\tfrac{2}{3}\pi Q^2 B_0 = \Psi_E , \tag{16}$$

$$\tfrac{1}{4} Q^2 J_0 = \frac{1}{4\pi} I_E , \tag{17}$$

$$\tfrac{3}{2}\pi Q^{2+4/3} [\tfrac{1}{2} p_0 + \tfrac{1}{2}(p_\infty + \tfrac{1}{2}\mu^{-1} B_{\parallel\infty}^2)] = E_E . \tag{18}$$

For a prominence to be initially in stationary equilibrium with the surrounding coronal medium the requisite current density is

$$J_0 = \frac{\rho_E - \rho_\infty}{B_{\infty\perp}} \frac{GM_\odot}{r_0^2} - \Gamma \frac{\mu^{-1} B_{\infty\perp}}{R_c} \tag{19}$$

in terms of the mass density (or the requisite ρ_E in terms of the current density) and other quantities. The requisite magnetic field, in either direction, is

$$B_0 = \pm (2\mu p_\infty + B_{\infty\parallel}^2 + \tfrac{1}{2}\mu^2 J_0^2 Q^2 - 2\mu p_0)^{1/2} \tag{20}$$

in terms of the gas pressure (or the requisite p_0 in terms of the magnetic field) and other quantities. The first constraint makes the upward hydromagnetic buoyancy force exactly balance the downward gravitational force. The second constraint makes the outward forces due to the gas pressure and the azimuthal current of the prominence exactly balance the inward forces due to the hydromagnetic pressure of the ambient medium and the axial current of the prominence. These two constraints are depicted in Figures 2 and 3, which show the required values of $\frac{1}{2}\mu Q J_0$ and B_0 for various values of r_0, Q, ρ_E, p_0, ρ_∞, T_∞, $B_{\infty\parallel}$, and $B_{\infty\perp}$, in the neighborhood of the equilibrium values used in the examples (see Section 6).

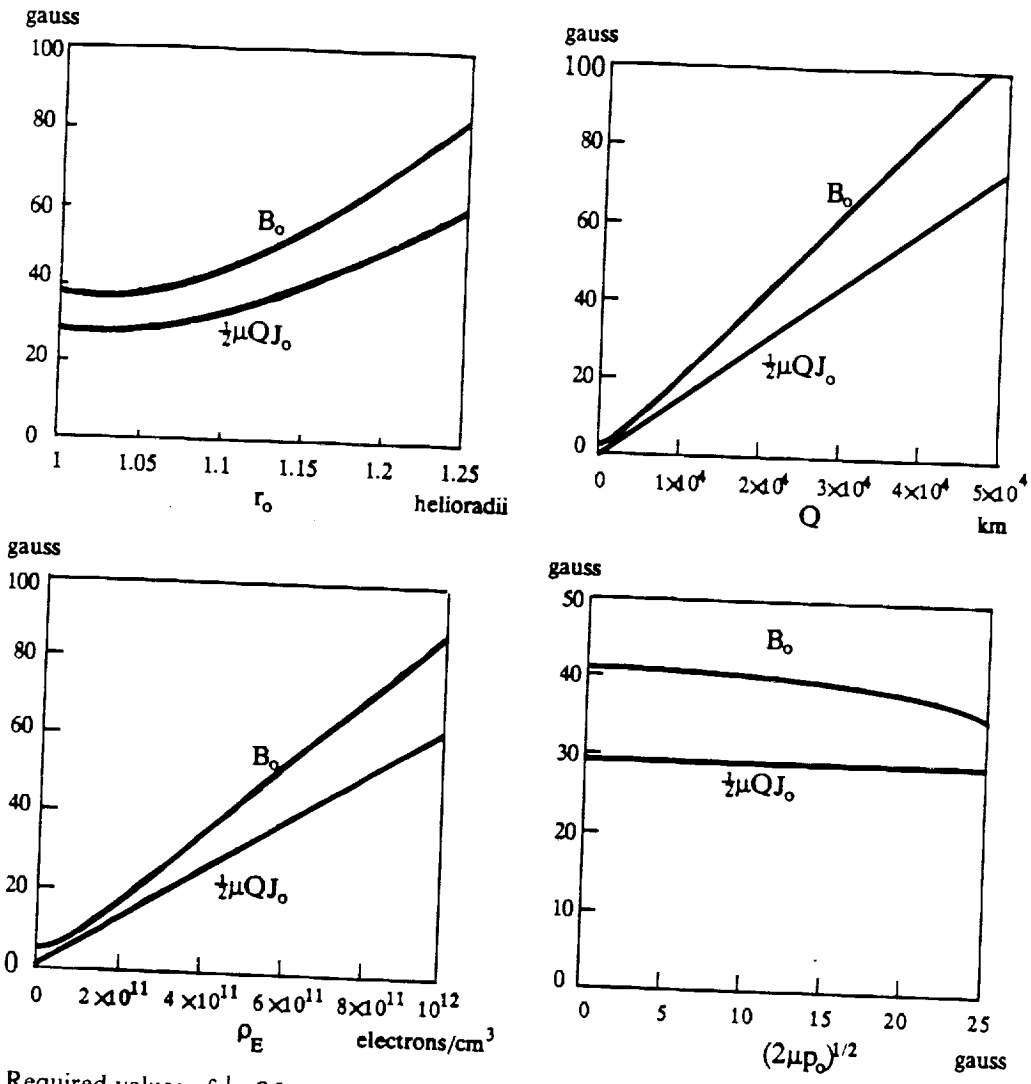

Fig. 2. Required values of $\frac{1}{2}\mu QJ_0$ and B_0 for an equilibrium prominence with various values of r_0, Q, ρ_E, or p_0.

4. Coronal Medium

We choose the line monopoles for the bipolar magnetic field to have strengths of $\pm \Psi_M$ and angular separation of $2\theta_M$. The two monopoles produce the bipolar magnetic field

$$\mathbf{B}_{\times\perp} = \mathbf{1}_n B_{\times\perp} \tag{21}$$

in the midplane between them. Its direction, from the positive monopole to the negative monopole, is perpendicular to the midplane. Its magnitude is

$$B_{\times\perp} = \frac{\Psi_M}{\pi} \frac{R_\odot \sin\theta_M}{r^2 - 2rR_\odot \cos\theta_M + R_\odot^2} \tag{22}$$

at a heliocentric distance of r. There the associated magnetic pressure has the gradient

$$-\nabla \tfrac{1}{2}\mu^{-1} B_{\times\perp}^2 = \mathbf{1}_r \frac{\mu^{-1} B_{\times\perp}^2}{R_c} \tag{23}$$

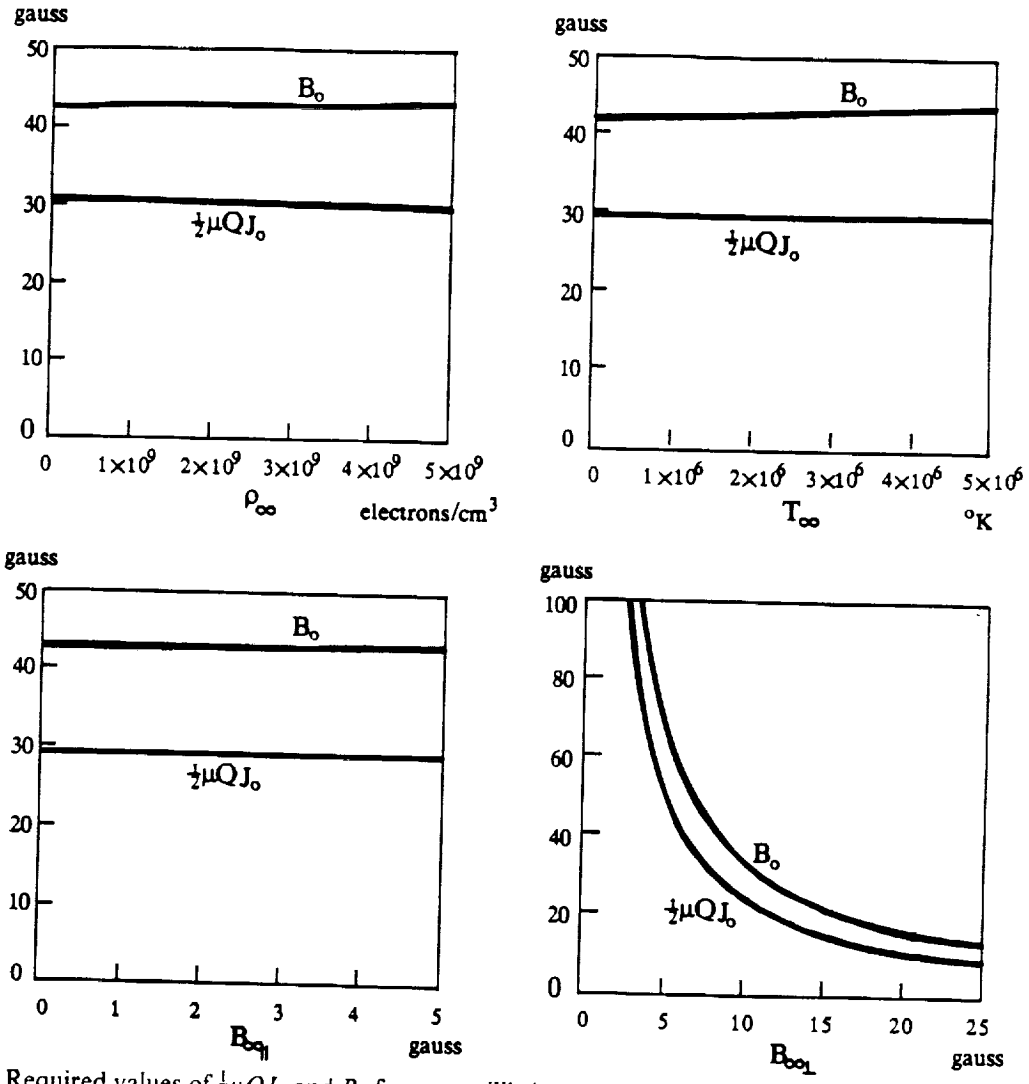

Fig. 3. Required values of $\frac{1}{2}\mu QJ_0$ and B_0 for an equilibrium prominence in a coronal medium with various values of ρ_∞, T_∞, $B_{\infty\parallel}$, or $B_{\infty\perp}$.

in the vertical direction, with the radius-of-curvature

$$R_c = \tfrac{1}{2}\frac{r^2 - 2rR_\odot \cos\theta_M + R_\odot^2}{r - R_\odot \cos\theta_M} \tag{24}$$

for the circular field line. (By virtue of the current-freeness of the bipolar field, the gradient force of its magnetic pressure is exactly opposite to its tensile force density.) This magnetic pressure gradient is enhanced by a factor

$$\Gamma = \frac{2}{(1 - Q^2/q_M^2)[(1 - Q^2/q_M^2)^2 + 4(Q^2/q_M^2)\sin^2\phi_M]} \tag{25}$$

by the polarization current

$$\mathbf{i}_P = \mathbf{1}_z \mu^{-1} B_{\infty\perp} \frac{2q_M^2(Q^2 + q_M^2)\cos\phi - 4Qq_M^3\cos\phi_M}{[Q^2 - 2Qq_M\cos(\phi - \phi_M) + q_M^2][Q^2 - 2Qq_M\cos(\phi + \phi_M) + q_M^2]}. \tag{26}$$

Here $q_M \equiv (r_0^2 - 2r_0 R_\odot \cos\theta_M + R_\odot^2)^{1/2}$ is the distance from the prominence to either monopole and $\phi_M \equiv \arcsin(R_\odot \sin\theta_M / q_M)$ is the azimuthal angle for the monopole. The field strength $B_{\perp\infty}$ increases with Ψ_M and becomes maximized when $\cos\theta_M$ is equal to $2rR_\odot/(r^2 + R_\odot^2)$. In terms of the field strength on the solar surface midway between the two monopoles, the monopole strength has the value

$$\Psi_M = 2\pi \frac{1 - \cos\theta_M}{\sin\theta_M} R_\odot B_{\infty\perp}|_{r=R_\odot} . \tag{27}$$

The monopole strength Ψ_M and the separation angle $2\theta_M$ may undergo temporal changes.

We choose the longitudinal magnetic field

$$\mathbf{B}_{\infty\parallel} = \mathbf{1}_z B_{\infty\parallel} \tag{28}$$

produced by the coronal current to be horizontal. The associated current density is $\mathbf{1}_n \mu^{-1} \mathrm{d}B_{\infty\parallel}/\mathrm{d}r$. It provides a magnetic force in the force balance

$$-\frac{\mathrm{d}}{\mathrm{d}r}(p_\infty + \tfrac{1}{2}\mu^{-1} B_{\infty\parallel}^2) = \rho_\infty \frac{GM_\odot}{r^2} \tag{29}$$

between the gravitational force and the gradient of hydromagnetic pressure. In addition to the equation of force balance, two more constraints are needed in order to determine the vertical variation of the coronal mass density, gas pressure, and longitudinal magnetic field. We shall assume that the gas pressure varies in proportion to the mass density and the magnetic pressure varies in proportion to the gas pressure, viz.,

$$p_\infty = \frac{p_\infty|_{r=R_\odot}}{\rho_\infty|_{r=R_\odot}} \rho_\infty , \tag{30}$$

$$B_{\infty\parallel}^2 = \frac{B_{\infty\parallel}^2|_{r=R_\odot}}{p_\infty|_{r=R_\odot}} p_\infty . \tag{31}$$

These assumptions ensure that the pressure and mass density decrease with the heliocentric distance. They allow us to calculate the mass density by numerical integration of the differential equation

$$\frac{\mathrm{d}}{\mathrm{d}r}\rho_\infty = -\frac{1}{1 + \tfrac{1}{2}\mu^{-1} B_{\infty\parallel}^2|_{r=R_\odot}/p_\infty|_{r=R_\odot}} \frac{GM_\odot}{KT_\infty} \frac{\rho_\infty}{r^2} \tag{32}$$

from the solar surface. The ratio p_∞/ρ_∞ divided by the gas constant of the solar plasma is the constant temperature T_∞ of the coronal medium.

5. Conditions for Upward and Outward Accelerations

In order for the translational motion to have an upward acceleration away from the Sun, the hydromagnetic buoyancy force must overcome the gravitational force. The former

ORIGINAL PAGE IS
OF POOR QUALITY

will exceed the latter if the bipolar field is sufficiently large so that

$$B_{\infty\perp} > \frac{1}{\frac{1}{2} + [\frac{1}{4} + \Gamma\mu^{-1} GM_\odot(\rho_E - \rho_\infty)/r_0^2 J_0^2 R_c]^{1/2}} \frac{GM_\odot}{r_0^2} \frac{\rho_E - \rho_\infty}{J_0}. \quad (33)$$

On the other hand, in order for the expansional motion to have an outward acceleration away from the axis, the outward force must overcome the inward force. The former will exceed the latter if the surrounding medium has a hydromagnetic pressure sufficiently small so that

$$p_\infty + \tfrac{1}{2}\mu^{-1} B_{\infty\parallel}^2 < p_0 + \tfrac{1}{2}\mu^{-1} B_0^2 - \tfrac{1}{4}\mu J_0^2 Q^2. \quad (34)$$

Upon the use of the equilibrium values at $t = 0$ and the conservation invariants, the condition for upward acceleration can be written as

$$B_{\infty\perp} > B_{\infty\perp}|_{t=0} \left(\frac{r_0|_{t=0}}{r_0}\right)^2 \frac{1 - (\rho_\infty/\rho_E|_{t=0})(Q/Q|_{t=0})^2}{1 - \rho_\infty|_{t=0}/\rho_E|_{t=0}} \quad (35)$$

if we ignore the higher-order part of the diamagnetic force associated with the pre-existing gradient of the coronal magnetic pressure. The condition for outward acceleration can be written as

$$p_\infty + \tfrac{1}{2}\mu^{-1} B_{\infty\parallel}^2 < \left\{ p_\infty|_{t=0} + \tfrac{1}{2}\mu^{-1} B_{\infty\parallel}^2|_{t=0} + \tfrac{1}{4}\mu^{-1} B_0^2|_{t=0} \left[\left(\frac{Q|_{t=0}}{Q} \right)^{2/3} - 1 \right] + \right.$$

$$\left. + \tfrac{1}{8}\mu J_0^2|_{t=0} Q^2|_{t=0} \left[1 - \left(\frac{Q}{Q|_{t=0}} \right)^{4/3} \right] \right\} \left(\frac{Q|_{t=0}}{Q} \right)^{2+4/3}. \quad (36)$$

It follows from the inequality (35) that in the region where ρ_∞ is small, the translational motion will have an upward acceleration when the bipolar magnetic field encountered, $B_{\infty\perp}(t)$, is not less than its initial value by a factor of $(r_0|_{t=0}/r_0)^2$. On the other hand, it follows from the inequality (36) that the expansional motion will have an outward acceleration in the region where $p_\infty + \frac{1}{2}\mu^{-1} B_{\infty\parallel}^2$ is less than its initial value when $Q(t)$ is less than $Q|_{t=0}$ and in the region where $p_\infty + \frac{1}{2}\mu^{-1} B_{\infty\parallel}^2$ is sufficiently less than its initial value when $Q(t)$ is greater than $Q|_{t=0}$.

6. Examples

In mks units, the magnetic permeability has the value $\mu = 4\pi \times 10^{-7}\,\mathrm{T^2\,m^3\,J^{-1}}$, the gravitational constant times solar mass has the value

$$GM_\odot = (6.67 \times 10^{-11}\,\mathrm{N\,m^2\,kg^{-2}}) \times (1.99 \times 10^{30}\,\mathrm{kg}),$$

and the gas constant for the proton-electron plasma has the value

$$K = (1.38 \times 10^{-23}\,\mathrm{J\,deg^{-1}})/\tfrac{1}{2}(1.67 \times 10^{-27}\,\mathrm{kg} + 9.11 \times 10^{-31}\,\mathrm{kg}).$$

ORIGINAL PAGE IS
OF POOR QUALITY

To facilitate the numerics, we choose to measure time, length, and magnetic field in the units of 1 hour, one helioradius, and 1 G, respectively, viz., $t_{ref} = 3.6 \times 10^3$ s, $r_{ref} = 6.96 \times 10^8$ m, and $B_{ref} = 10^{-4}$ T. We further choose to measure speed, mass density, pressure, current density, and temperature in the units of r_{ref}/t_{ref}, $(\mu^{-1}B_{ref}^2)\,(r_{ref}/t_{ref})^2$, $\mu^{-1}B_{ref}^2$, $\mu^{-1}B_{ref}/r_{ref}$, and $(r_{ref}/t_{ref})^2/K$. Namely, $u_{ref} = 193.3$ km s^{-1}, $\rho_{ref} = 2.129 \times 10^{-13}$ kg m^{-3} (corresponding to 1.274×10^8 electrons cm^{-3}), $p_{ref} = 7.958 \times 10^{-3}$ J m^{-3}, $J_{ref} = 1.143 \times 10^{-7}$ A m^{-2}, and $T_{ref} = 2.263 \times 10^6$ deg. In these normalized units, henceforth, both the magnetic permeability, given by

$$(4\pi \times 10^{-7}\,\mathrm{T^2\,m^3\,J^{-1}})/(B_{ref}/J_{ref}r_{ref}),$$

and the gas constant, given by

$$(1.65 \times 10^4\,\mathrm{J\,kg^{-1}\,deg^{-1}})/(u_{ref}^2/T_{ref}),$$

have the value of unity whereas the gravitational constant times solar mass has the value of 5.102 helioradius^3 h^{-2}, given by $(1.333 \times 10^{20}\,\mathrm{m^3\,s^{-2}})/(r_{ref}u_{ref}^2)$.

For the magnetohydrostatic coronal atmosphere, we choose a mass density of 3×10^9 electrons cm^{-3}, a temperature of 2×10^6 K (hence, $T_\infty = 0.8838$) and a longitudinal magnetic field of 2 G at the solar surface. For the magnetic monopoles, to have a transverse magnetic field of 10 G at the solar surface midway between the two

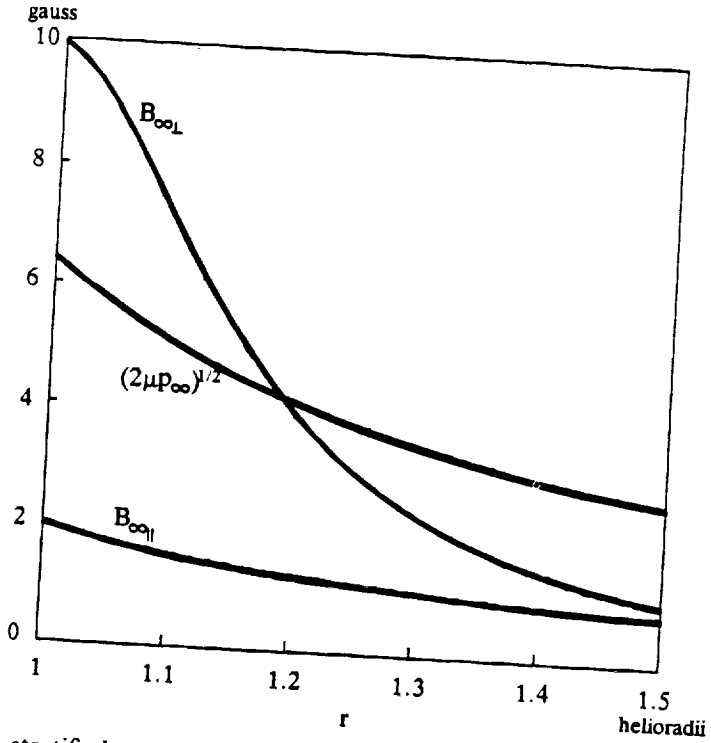

Fig. 4. Profile of a stratified magnetohydrostatic corona at 2×10^6 K, with a mass density of 3×10^9 electrons cm^{-3}, a longitudinal magnetic field of 2 G, and a transverse magnetic field of 10 G at the solar surface.

monopoles, we choose

$$\Psi_M = 5.497 \text{ G helioradius}, \quad \theta_M = 10°.$$

The calculated profiles are shown in Figure 4.

For a stationary prominence loop, we choose a height of 5×10^4 km, a radius of 2×10^4 km, a mass density of 5×10^{11} electrons cm^{-3}, and a temperature of 5×10^4 K so that:

$$r_0 = 1.0718, \quad Q = 0.02874, \quad \rho_E = 3924.2, \quad p_0 = 86.704.$$

At the site where the prominence resides we have

$$\rho_\infty = 16.535, \quad p_\infty = 14.614, \quad B_{\infty\parallel} = 1.676, \quad B_{\infty\perp} = 8.054.$$

The conditions of force balance require

$$J_0 = 2080.9, \quad B_0 = 40.574.$$

In other words, for the prominence loop to be in stationary equilibrium with the surrounding medium, it must carry a total axial current I_E of 3.0×10^{11} A and carry an azimuthal current that sustains a total axial magnetic flux Ψ_E of 3.4×10^{12} webers. These values are within the range of typical values for quiescent prominences

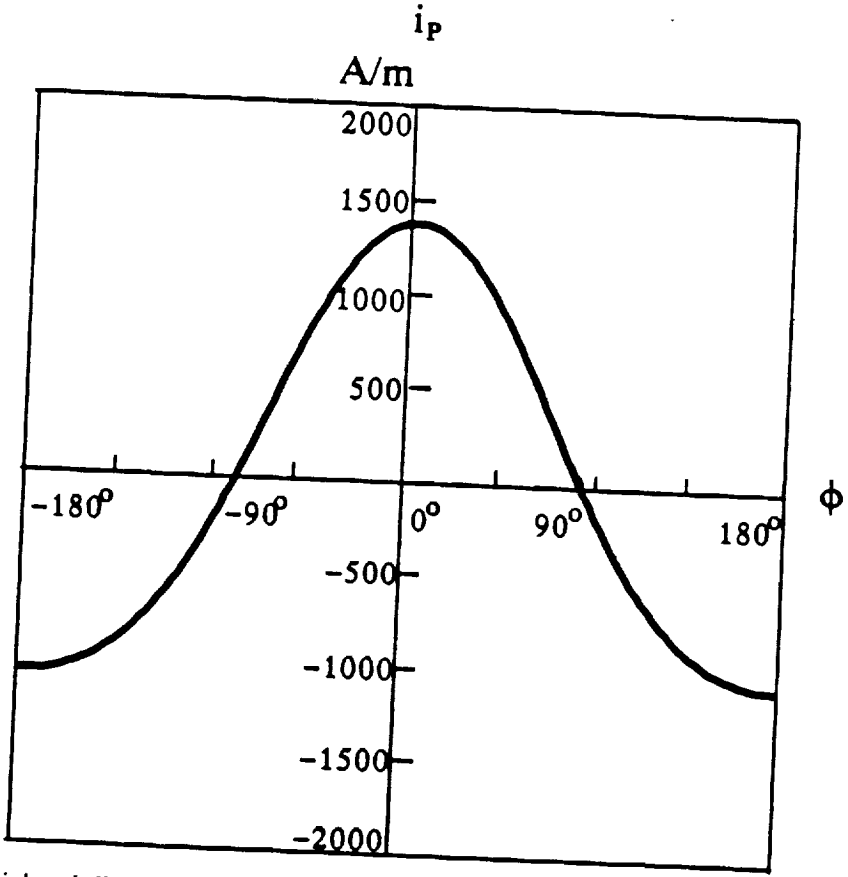

Fig. 5. Peripheral distribution of the polarization current in the equilibrium configuration.

(Tandberg–Hanssen, 1974). It is seen from

$$\rho_E \frac{GM_\odot}{r_0^2} = 17428.7, \qquad \rho_\infty \frac{GM_\odot}{r_0^2} = 73.61, \qquad \frac{I_E B_{\infty\perp}}{\pi Q^2} = 16759.7,$$

$$\Gamma \frac{\mu^{-1} B_{\infty\perp}^2}{R_c} = 595.4$$

that the gravitational force is largely balanced by the diamagnetic force (the part due to the inhomogeneity of the coronal magnetic field is only 3.55% of the part due to the prominence current). The hydrostatic buoyancy force is very small, accounting for only 0.42%. On the other hand, it is seen from

$$p_0 = 86.704, \qquad \tfrac{1}{2}\mu^{-1} B_0^2 = 823.14, \qquad \tfrac{1}{4}\mu J_0^2 Q^2 = 893.82,$$

$$p_\infty = 14.615, \qquad \tfrac{1}{2}\mu^{-1} B_{\infty\parallel}^2 = 1.405$$

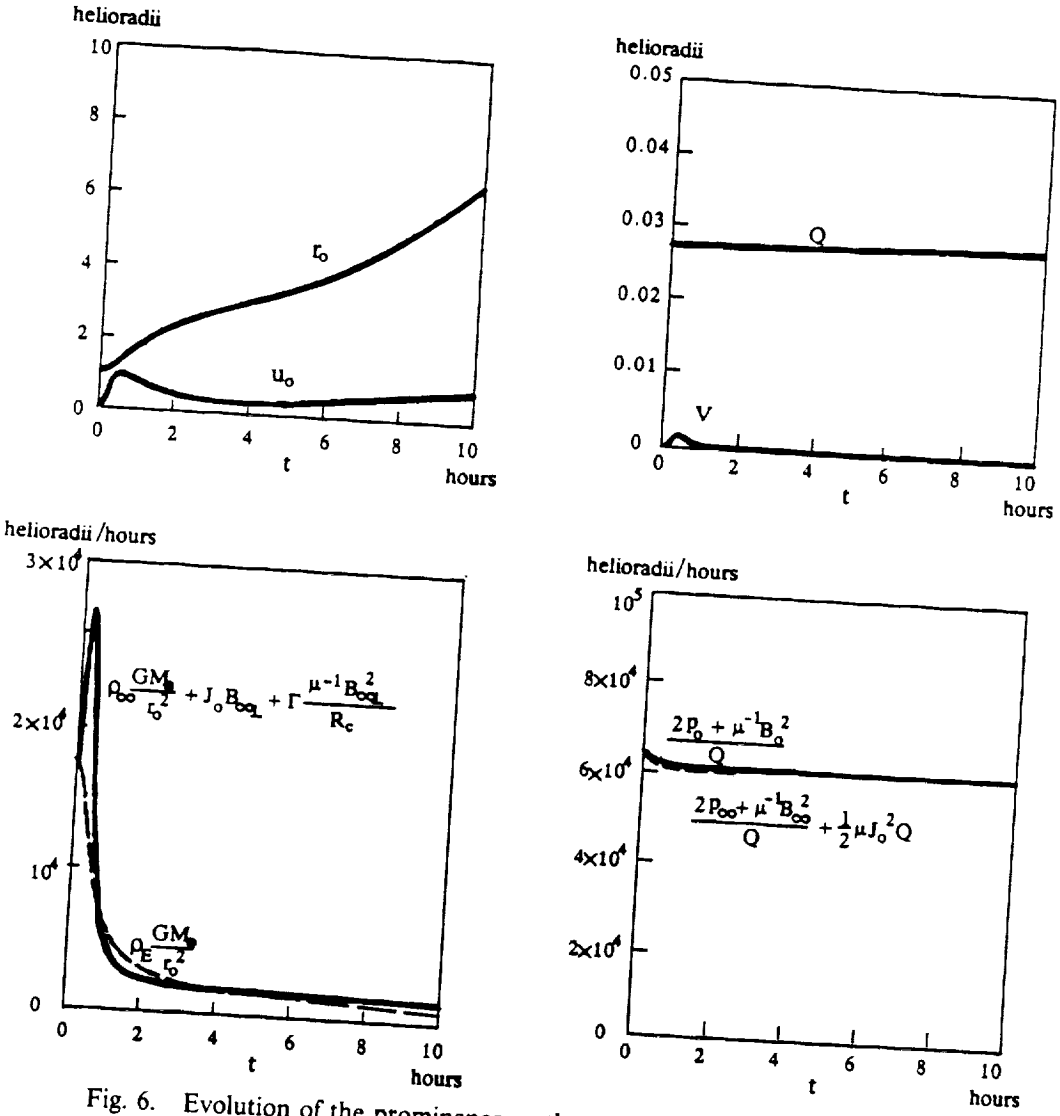

Fig. 6. Evolution of the prominence as the monopole strength increases, with $d\Psi_M/dt = 20$ G helioradius h^{-1}.

that the pinching force of the axial current is largely balanced by the anti-pinching force of the azimuthal current and to a lesser extent by the internal gas pressure. The ambient hydromagnetic pressure provides only a very small pinching. To facilitate comparison, these values may be translated to $(2\mu p_\infty)^{1/2} = 5.4063$ G, $\frac{1}{2}\mu J_0 Q = 29.903$ G, and $(2\mu p_0)^{1/2} = 13.168$ G. The plasma beta at the axis is 0.1053. The transverse projection of the field lines in the equilibrium configuration is as shown in Figure 1. With the ratio $\mu I_E/\Psi_M = 0.9684$, the bipolar field has two neutral points located at $q = 0.187$, $\phi = \pm 118.7°$. Figure 5 shows the peripheral distribution of the polarization current with $q_M = 0.194$ and $\phi_M = 63.4°$. The polarization current flows in the direction of the prominence current in the lower periphery $|\phi| < 82.6°$ and flows in the opposite direction in the upper periphery. It is zero at the two points where the two neutral points would be located in the case I_E happens to be zero. Of course, the total polarization current sums up to zero.

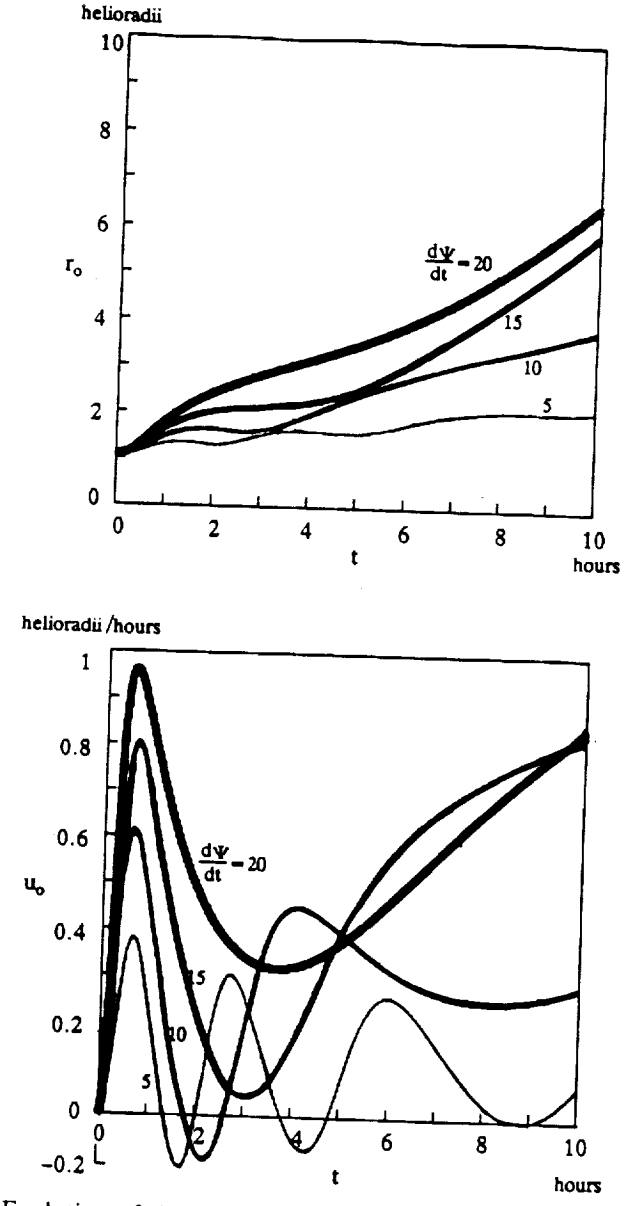

Fig. 7. Evolution of the prominence with various values of $d\Psi_M/dt$.

ORIGINAL PAGE IS
OF POOR QUALITY

Now, we consider the motion of the prominence loop when the equilibrium is lost. The initiated motion is caused by a temporal change of the bipolar magnetic field due to the strengthening of the monopoles. Figure 6 shows the evolution with

$$\frac{\mathrm{d}}{\mathrm{d}t}\Psi_M = 20.0 \text{ G helioradius h}^{-1} \quad \text{for} \quad 0 < t < 10 \text{ h},$$

revealed by the numerical solution of the dynamical equations. The initial increase in the bipolar field makes the hydromagnetic buoyancy force exceed the gravitational force, so that the prominence rises from its equilibrium position. The prominence keeps moving upward, even during the short while $0.6 < t < 3.5$ when the prominence is decelerated because the hydromagnetic buoyancy force is not large enough to exceed the gravitational force. Likewise, the radius of the prominence keeps increasing. Its rate of increase is small in this case because the encountered coronal hydromagnetic pressure decreases very slowly. To see the dependence on the speed of the evolution of the photospheric magnetic field, we show in Figure 7 the evolution caused by smaller values of $\mathrm{d}\Psi_M/\mathrm{d}t$. It is seen that the prominence may move up and down in oscillational motion if the evolution is slow. With a sufficiently rapid evolution, the prominence will move away from the Sun. In passing, we mention that the prominence would move downward in response to negative values of $\mathrm{d}\Psi_M/\mathrm{d}t$.

7. Discussion

The calculations show the importance of the hydromagnetic buoyancy force, which includes the diamagnetic force, in the dynamics of prominence loops. In the illustrative examples, not only in equilibrium but also during the motion, the hydromagnetic buoyancy force is preponderant with the diamagnetic force due to the current carried by the prominence interacting with the coronal magnetic field produced by the photospheric currents. The part of the diamagnetic force due to the inhomogeneity of the coronal magnetic field only amounts to a few percent and the hydrostatic buoyancy force is even much smaller. Their percentages diminish in heliocentric distance. Therefore, we conclude that without the action of the diamagnetic force due to the prominence current, prominences are not likely to move away from the solar surface.

In fact, when the prominence is close to the photospheric surface, the diamagnetic force is enhanced by the mirror-current effect (Kuperus and Raadu, 1974). The polarization current induced on the photosphere will exert an additional upward force on the prominence current in the amount of $\mu I_E^2 R_\odot^2 / 2\pi r_0 (r_0^2 - R_\odot^2)$ (cf. Van Tend and Kuperus, 1978). Inclusion of this force will modify Equation (13) to

$$\rho_E \frac{\mathrm{d}}{\mathrm{d}t} u_0 = -\rho_E \frac{GM_\odot}{r_0^2} + \rho_\infty \frac{GM_\odot}{r_0^2} + J_0 B_{\infty\perp} + \Gamma \frac{\mu^{-1} B_{\infty\perp}^2}{R_c} + \mu J_0^2 \frac{Q^2 R_\odot^2}{2 r_0 (r_0^2 - R_\odot^2)}. \tag{37}$$

ORIGINAL PAGE IS OF POOR QUALITY

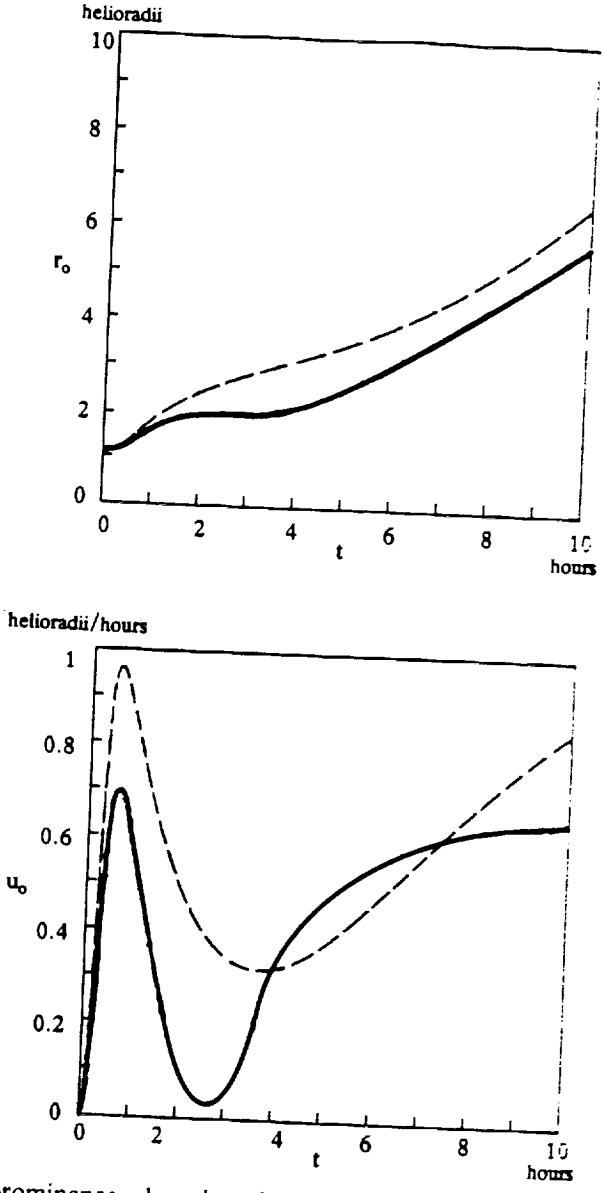

Fig. 8. Evolution of the prominence when the mirror-current effect is included in the hydromagnetic diamagnetic force, with $d\Psi_M/dt = 20$ G helioradius h^{-1}. Dashed lines indicate the corresponding evolution without the mirror currents.

Accordingly, for the prominence in the illustrative examples, the requisite current density reduces to $J_0 = 1426.5$ and the requisite magnetic field reduces to $B_0 = 26.44$. With the monopoles strengthening at the rate of $d\Psi_M/dt = 20$, the prominence rises slightly slower. See Figures 8. This is due to a smaller prominence current. The reduced $I_E B_{\infty\perp}$ is not sufficiently compensated by the added $\mu I_E^2 R_\odot^2/2\pi r_0(r_0^2 - R_\odot^2)$. This calculation serves as an *a posteriori* justification for the simplified model by Van Tend and Kuperus (1978).

The dynamical model illustrated by the calculations presented in this paper applies to prominence eruptions driven by gradual evolution of the photospheric magnetic field in weak field regions. It also applies to filament eruptions in active regions, with other parameter values.

Acknowledgements

The authors thank Dr Ernest Hildner and Dr Petrus Martens for some useful suggestions. This work was supported by U.S. Air Force Office of Scientific Research under contract AFOSR–88–0013.

References

Kahler, S. W., Moore, R. L., Kane, S. R., and Zirin, H.: 1988, *Astrophys. J.* **328**, 824.
Kuperus, M. and Raadu, M. A.: 1974, *Astron. Astrophys.* **31**, 189.
Tandberg-Hanssen, E.: 1974, *Solar Prominences*, D. Reidel Publ. Co., Dordrecht, Holland.
Van Tend, W. and Kuperus, M.: 1978, *Solar Phys.* **59**, 115.
Wu, S. T., Bao, J. J., Ahn, S. H., and Tandberg–Hanssen, E.: 1990, *Solar Phys.* **125**, 277.
Yeh, T.: 1983, *Astrophys. J.* **264**, 630.
Yeh, T.: 1989, *Solar Phys.* **124**, 251.

SHEAR-INDUCED INSTABILITY AND ARCH FILAMENT ERUPTION: A MAGNETOHYDRODYNAMIC (MHD) NUMERICAL SIMULATION

S. T. WU and M. T. SONG*

Department of Mechanical Engineering and Center for Space Plasma and Aeronomic Research, The University of Alabama in Huntsville, Huntsville, AL 35899, U.S.A.

P. C. H. MARTENS

Harvard–Smithsonian Center for Astrophysics, Cambridge, MA 02138, U.S.A.

and

Lockheed Palo Alto Research Laboratories, Palo Alto, CA 94304, U.S.A.

and

M. DRYER

Space Environment Laboratory, National Oceanic and Atmospheric Administration, Boulder, CO 80303, U.S.A.

(Received 22 October, 1990; in revised form 8 March, 1991)

Abstract. We investigate, via a two-dimensional (nonplanar) MHD simulation, a situation wherein a bipolar magnetic field embedded in a stratified solar atmosphere (i.e., arch-filament-like structure) undergoes symmetrical shear motion at the footpoints. It was found that the vertical plasma flow velocities grow exponentially leading to a new type of global MHD-instability that could be characterized as a 'Dynamic Shearing Instability', with a growth rate of about $\sqrt{8}\,\overline{V}_A a$, where $\overline{V}_A$ is the average Alfvén speed and a^{-1} is the characteristic length scale. The growth rate grows almost linearly until it reaches the same order of magnitude as the Alfvén speed. Then a nonlinear MHD instability occurs beyond this point. This simulation indicates the following physical consequences: the central loops are pinched by opposing Lorentz forces, and the outer closed loops stretch upward with the vertically-rising mass flow. This instability may apply to arch filament eruptions (AFE) and coronal mass ejections (CMEs).

To illustrate the nonlinear dynamical shearing instability, a numerical example is given for three different values of the plasma beta that span several orders of magnitude. The numerical results were analyzed using a linearized asymptotic approach in which an analytical approximate solution for velocity growth is presented. Finally, this theoretical model is applied to describe the arch filament eruption as well as CMEs.

1. Introduction

More than a quarter century ago, Gold and Hoyle (1960) suggested that horizontal photospheric motion can move the footpoints of magnetic field lines and twist the flux tubes because of the highly electric conducting plasma at the photospheric levels. A number of investigators (Tanaka and Nakagawa, 1973; Low and Nakagawa, 1975; Low, 1977; Klimchuk, Sturrock, and Yang, 1988; Klimchuk and Sturrock, 1989) studied the evolution of force-free fields and its role in energy storage (build-up) for solar flares.

* Permanent address: Purple Mountain Observatory, Nanjing, China.

Solar Physics **134**: 353–377, 1991.
© 1991 *Kluwer Academic Publishers. Printed in Belgium.*

PRECEDING PAGE BLANK NOT FILMED

All of these studies were limited to the case of magnetostatics; self-consistent dynamical effects were ignored. Recently, Wu, Hu, and Nakagawa (1983), Wu, Hu, and Krall (1984), and Wu *et al.* (1986) presented a self-consistent MHD model for the purpose of examining flare energy build-up and wave-mass interactions due to shear and converging-diverging motions at the photospheric level. More recently, Mikic, Barnes, and Schnack (1988) and Biskamp and Welter (1989) have presented numerical results on the dynamical evolution of a magnetic arcade type due to shear motion. However, their models are restricted to symmetric boundary conditions, while in this study self-consistent boundary conditions were used (see, for example, Wu and Wang, 1987; Nakagawa, Hu, and Wu, 1987).

In this paper, we use the time-dependent MHD simulation model devised by Wu, Hu, and Nakagawa (1983) to reveal a nonlinear solution for the evolution of the magnetic field configuration driven by shear motion. In this solution, we find that the plasma velocity in the vertical plane perpendicular to the shear, grows exponentially in a process which can be analytically described by a linear MHD instability. This upward velocity steadily increases until it reaches the average Alfvén speed. At later times, a nonlinear instability sets in. A field line pinch occurs in the lower shear region in the numerical results. At the same time, mass and field line expulsion appears in higher parts of the region and the closed field tends to open locally. We suggest that these new effects (i.e., mushroom cloud-like flow, pinch, and expulsion) can explain the formation of current sheets, the opening of a closed bipolar field, and the ability of particle streams to escape from the solar surface. Specifically, we suggest that this model applies to the eruption of arch filament systems (AFEs) and their relation to non-flare-associated coronal mass ejections (CMEs). The mathematical description of the model and numerical results are given in Section 2. A general physical interpretation of these results is presented in Section 3. An application of this model to specific coronal phenomena is given in Section 4, and the concluding remarks are presented in Section 5.

2. Numerical Simulation

In order to illustate how shear-induced non-equilibrium occurs, we use a theoretical model in which a two-dimensional bipolar field undergoes a steady shear velocity at the footpoints of its magnetic loops. The shearing motion is sketched in Figure 1(a), and the initial bipolar field is shown explicitly in Figure 1(b).

First, we perform a simulation of the dynamic response of the bipolar field to the shear. Then we use an analytical method to interpret the simulation results. The simulation model is based on a two-dimensional, time-dependent, MHD model (Wu, Hu, and Nakagawa, 1983; Hu and Wu, 1984) with an improved FICE (Full-Implicit-Continuous-Eulerian) numerical scheme (Wu and Wang, 1987). Symmetrical side boundary conditions have been replaced with non-reflecting boundary conditions. This implies that the physical phenomena are determined by the solution at a specific time and are not determined by the specified boundary conditions as in the case studied by Mikic, Barnes, and Schnack (1988). The physical conditions on these

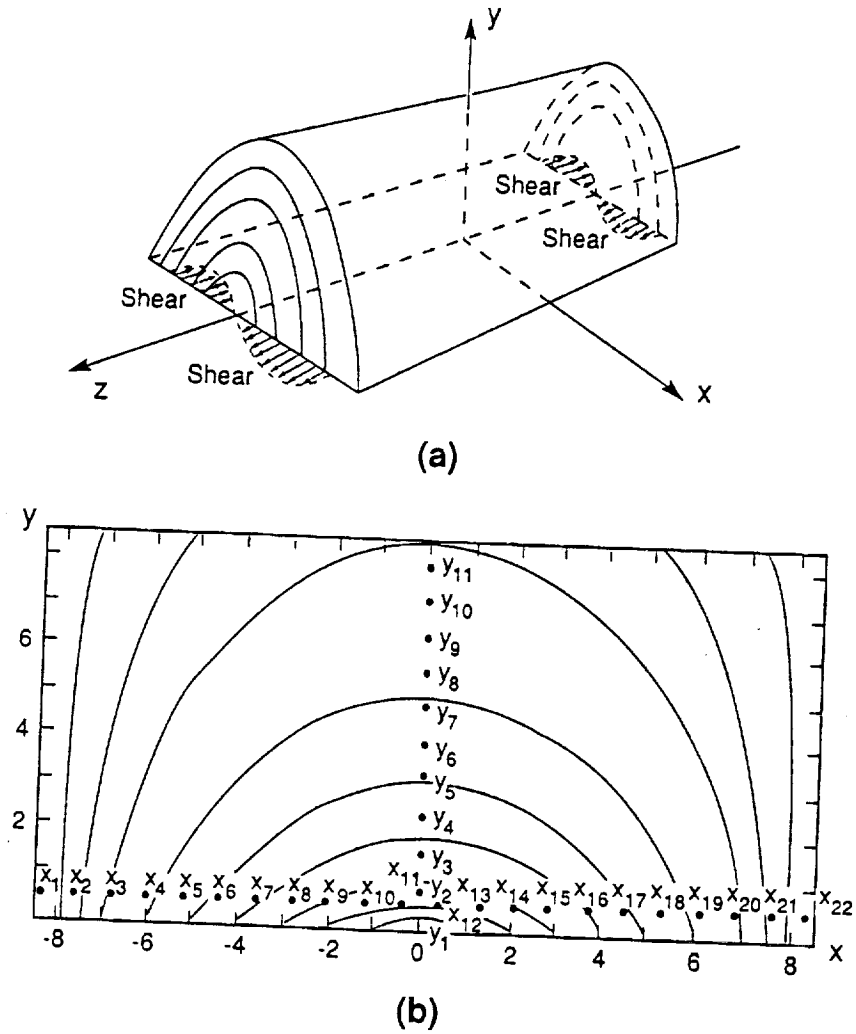

Fig. 1. (a) Sketch of a two-dimensional bipolar magnetic field that is subjected to a footpoint shearing motion as indicated by the arrows. (b) Explicit bipolar magnetic topology prior to the shearing motion (see Equation (1)). The photospheric boundary extends to $|x| = 8.4 \times 10^3$ km in both directions from the origin. The vertical extent into the corona is to $y = 8 \times 10^3$ km. The positions $y = y_1, y_2, \ldots, y_{10}$ indicate the vertical levels at which horizontal surveys will be shown of various physical quantities during the shearing motion at the footpoints.

two side boundaries are determined mathematically through compatibility relations that are given in detail by Wu and Wang (1987). Thus, the computation domain (i.e., $|x| \leq 8.4 \times 10^3$ km, $0 \leq y \leq 8 \times 10^3$ km) consists of three free non-reflecting boundaries (i.e., top and sides), while the bottom boundary ($y = 0$) is treated with the method of projected characteristics (Nakagawa, Hu, and Wu, 1987; Hu and Wu, 1984). The basic equations for this model are the time-dependent MHD equations with infinite conductivity, no viscosity and symmetry in one direction (Wu, Hu, and Nakagawa, 1983). Solar gravity, plasma pressure gradients, and compressibility are explicitly considered. None of these characteristics were considered in the work of Mikic, Barnes, and Schnack (1988), and Biskamp and Welter (1989) have only considered compressibility in a special way.

The initial conditions are (see Figure 1(b)):

$$\rho_0 = \rho_c \exp\left(-\frac{gy}{RT_c}\right), \quad T_0 = T_c, \quad v_x, v_y, v_z = 0,$$

$$B_{x0} = B_0 [\cos(ax)]\, e^{-ay}, \quad B_{y0} = -B_0 [\sin(ax)]\, e^{-ay}, \quad B_{z0} = 0, \qquad (1)$$

$$a = \pi/2x_0, \quad x_0 = 8.4 \times 10^3 \text{ km}, \quad g = 2.71 \times 10^4 \text{ cm s}^{-2}.$$

The plasma parameters are taken to be $\rho_c = 1.67 \times 10^{-12}$ g cm^{-3} and $T_c = 10^5$ K. The scale height ($b^{-1} = RT_c/g \sim 6.1 \times 10^3$ km) and $a^{-1} \sim 6.3 \times 10^3$ km are the same order of magnitude. These parameters are representative for solar conditions at the higher chromosphere and lower corona. The computation grid points are:

$$x_i = -8.4 \times 10^3 + (i-1)\Delta x, \quad i = 1, 2, \ldots, 22,$$

$$y_i = (j-1)\Delta y, \quad j = 1, 2, \ldots, 11,$$

$$\Delta x = \Delta y = 8 \times 10^2 \text{ km} \sim 1 \text{ arc sec}.$$

The non-reflecting boundary conditions, as noted above, are used for the top ($y = y_{11}$), left-hand side ($x = x_1$), and right-hand side ($x = x_{22}$). The conditions at the bottom boundary ($y = y_1$) are taken as follows:

$$\rho = \rho_c, \quad T = T_c, \quad B_y = B_{y0}, \quad v_x = 0, \quad \text{but} \quad v_y, v_z \neq 0,$$

$$v_z = \begin{cases} w_c \sin(ax) & \text{if } |x| \leq 5.2 \times 10^3 \text{ km}, \\ \dfrac{(6.8 \times 10^3 - |x|)}{1.6 \times 10^3}\, w_c (\operatorname{sgn} x) \sin(5.2 \times 10^3 a) & \\ \qquad \text{if } 5.2 \times 10^3 < |x| \leq 6.8 \times 10^3 \text{ km}, & \\ 0 \qquad \text{if } 6.8 \times 10^3 < |x| < 8 \times 10^3 \text{ km}. & \end{cases} \qquad (2)$$

The other physical quantities (p, T, v_y, B_x, B_z) are computed by means of the compatibility equations for the non-reflecting boundary condition which assures the consistency of the numerical computation.

In order to understand the general physical behaviour of the nonlinear solution from the mathematical model, we have performed three numerical experiments. These three cases use combinations of magnetic field intensity and magnitudes of the shear velocity. The results for these three cases are described as follows.

2.1. Large plasma beta ($\beta_0 \simeq 154$)

In this numerical experiment, we choose the initial plasma beta (β_0) to be 154 where β_0 is defined as $\beta_0 = p_0/(B_0^2/8\pi)$ with p_0 and B_0 being the plasma pressure and magnetic field strength at the lower boundary (i.e., $y = y_1$). This is not a physically realistic case for a solar active region; but it does provide a basis for comparison with the other cases. This case corresponds to a local, exceedingly low, magnetic field strength of

2.12 G at the origin, $x = y = 0$, as shown in Figure 1(b). The shear velocity, w_c, was taken to be 5 km s^{-1}. Figure 2 shows the evolution of the magnetic field lines due to the shear motion at 200 s $\leq t \leq$ 3200 s. It is useful to examine the evolutionary behaviour at various Alfvén times (defined as $\tau_A = [\Delta y \text{ (or } \Delta x)]/V_A \simeq 1700$ s where

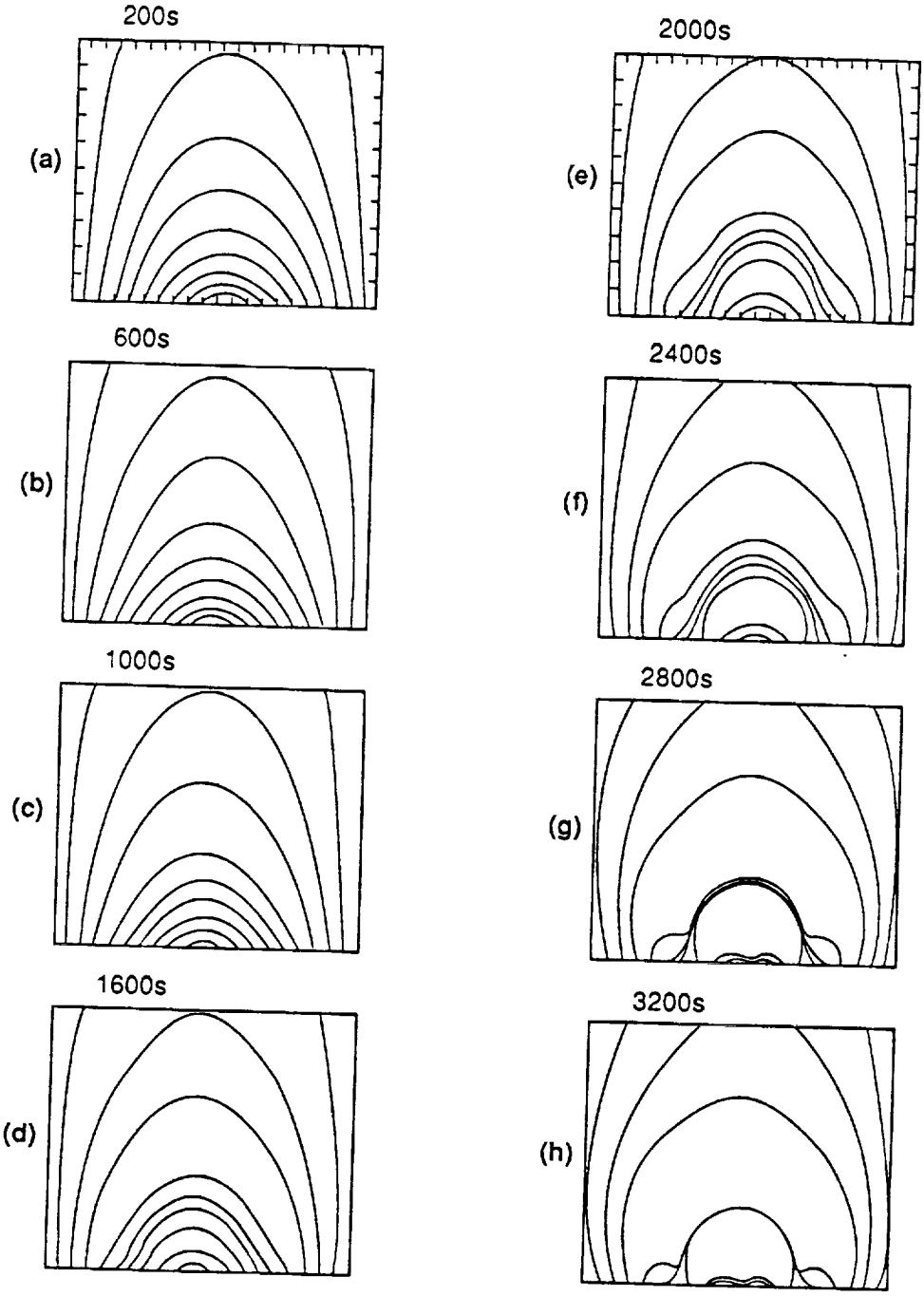

$\beta_0 \sim 15.4$, $\tau_a \sim 1700$s

Fig. 2. Magnetic field line evolution as a function of time during induced footpoint shearing motion for case (i): $\beta_0 = 154$ and the Alfvén time, $\tau_A = 1700$ s. The horizontal axis represents the distance from $x_1 \ldots x_{22}$ as shown in Figure 1(b).

ORIGINAL PAGE IS
OF POOR QUALITY

$V_A = B_0/\sqrt{4\pi\rho_0} = 4.6$ km s^{-1}). During the early stages of evolution (that is, within the first Alfvén time), the magnetic field lines rise together in an orderly fashion in response to the shearing motion. This behaviour is also presented in the analytical solution of Low (1981) and the force-free numerical solutions of Klimchuk and Sturrock (1989) although they do not consider dynamics and gravitational effects. After the first Alfvén time period, the evolutionary behaviour of the field lines becomes more complicated. Nonlinear interactions take place between the shear-induced mass motion, magnetic field and gravity with the result that in some regions the field lines are bunched together to form a current sheet (see Figures 2(g) and 2(h)). Further understanding of these phenomena is provided by the representation of the shear induced mass motion as shown by the vectorial velocity field in Figure 3. Notice that the inclusion of magnetohydrodynamic effects, in contrast to the kinematic study of Low (1981), causes upward mass motion in addition to the up-lifting of the magnetic field lines because the plasma has to move with the field lines under the conditions of infinite conductivity as manifested by the upward component of Lorentz force. Note, however, that some of the uplifted plasma (in the region displaced from the origin) slows down under the action of gravity, reverses direction, and falls back to the surface. Most of the motion, however, is upward. These upward mass motions are also found by Mikic, Barnes, and Schnack (1988) and Biskamp and Welter (1989). However, these workers did not include compressibility, pressure gradient, and gravitation as noted above. The present study, which does so explicitly, demonstrates a different evolution in the later stages.

This induced upward motion can be explained via our governing equations. When we introduce the shear motion (v_z), an axial field component, B_z, will be induced through the induction equation. The additional magnetic field will cause an additional magnetic pressure gradient in the momentum equation. This additional pressure gradient induces both the horizontal (v_x) and upward (v_y) motions as shown in Figure 3. Subsequently, the mass motion interacts with both the magnetic field and gravity. Closer to the surface, the combined effect is dominated by gravity, and the result is the cluster of magnetic field lines in which a current sheet is formed as shown in Figures 2(g) and 2(h) at nearly twice the Alfvén time.

Figure 4 shows the plasma properties (i.e., density temperature, and pressure enhancement in terms of percentage change from the initial values at each level) at the end of this simulation ($t = 3600$ s; more than $2\tau_A$). These properties are shown at various heights (y_1, y_2, y_4, y_6, and y_{10}, as shown in Figure 1(b)) as a function of horizontal distance. These results also help to explain the magnetic field line distribution. That is, the high density magnetic field region shown in Figures 2(g) and 2(h) within the mid-horizontal range (at the altitudes: y_2, y_4) corresponds to the increase of plasma density by 20% (i.e., $\Delta\rho/\bar{\rho} \sim 0.2$), temperature decrease of 20% (i.e., $\Delta T/\bar{T} \sim -0.2$), and magnetic field strength ($\Delta B/B_0$) increase by a factor of 3. These properties are similar to those for a current sheet. With these properties in mind, let us now turn our attention to the plasma flow patterns as shown in Figure 3. The plasma flow rises initially above the zone of maximum shear velocity. At later times (say, from 1000 to 2000 s), the plasma flow moves toward the central region in a pattern reminiscent of a mushroom

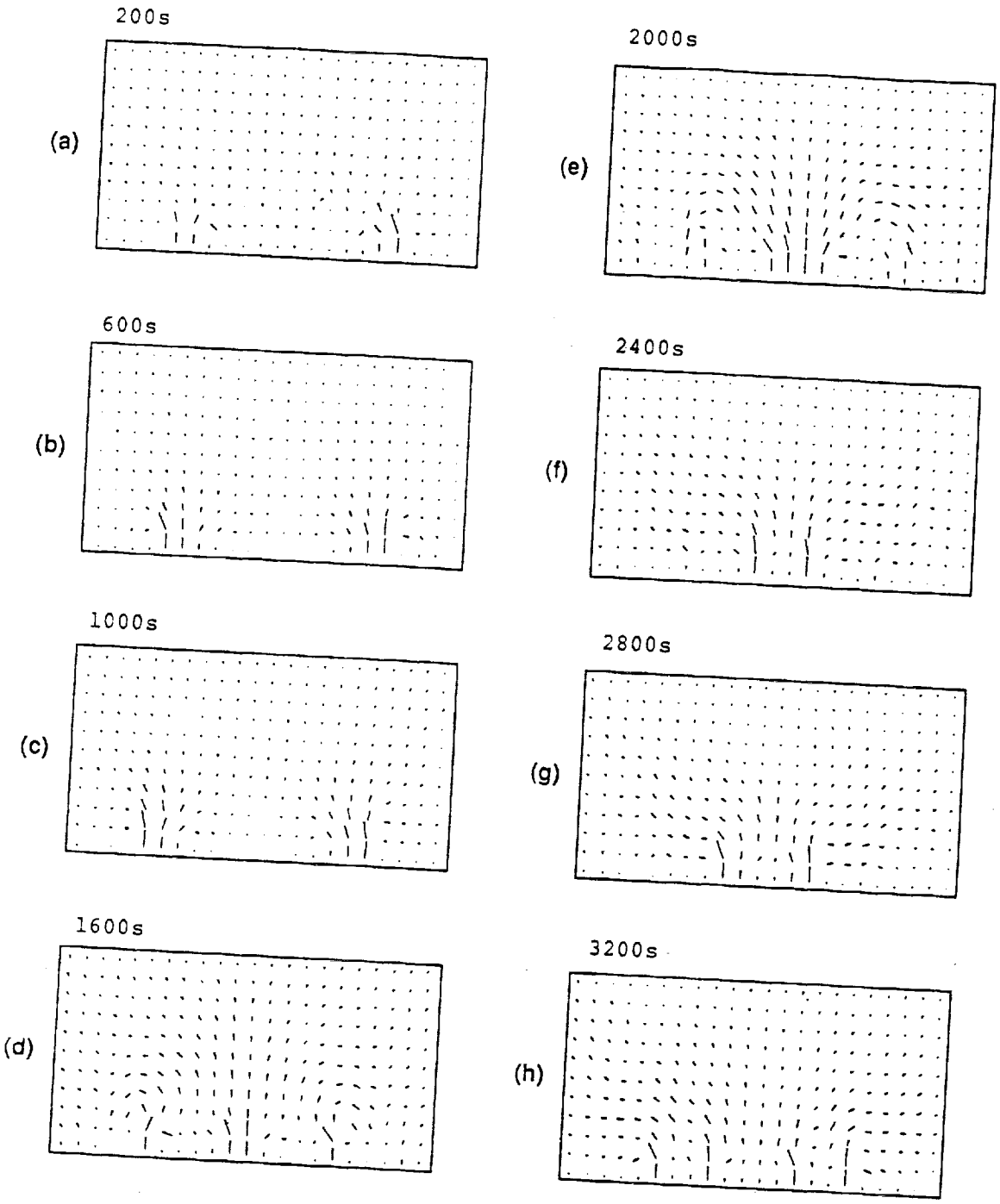

Fig. 3. Vectorial velocity field as a function of time during induced footpoint shearing motion for case (i): $\beta_0 = 154$; $\tau_A = 1700$ s.

cloud. In the later stages as shown in Figures 3(g) and 3(h), the significant plasma motion is again concentrated in the neighbourhood of the sheared region. This is also the region where the magnetic field lines have been clustered as seen in Figures 2(g) and 2(h).

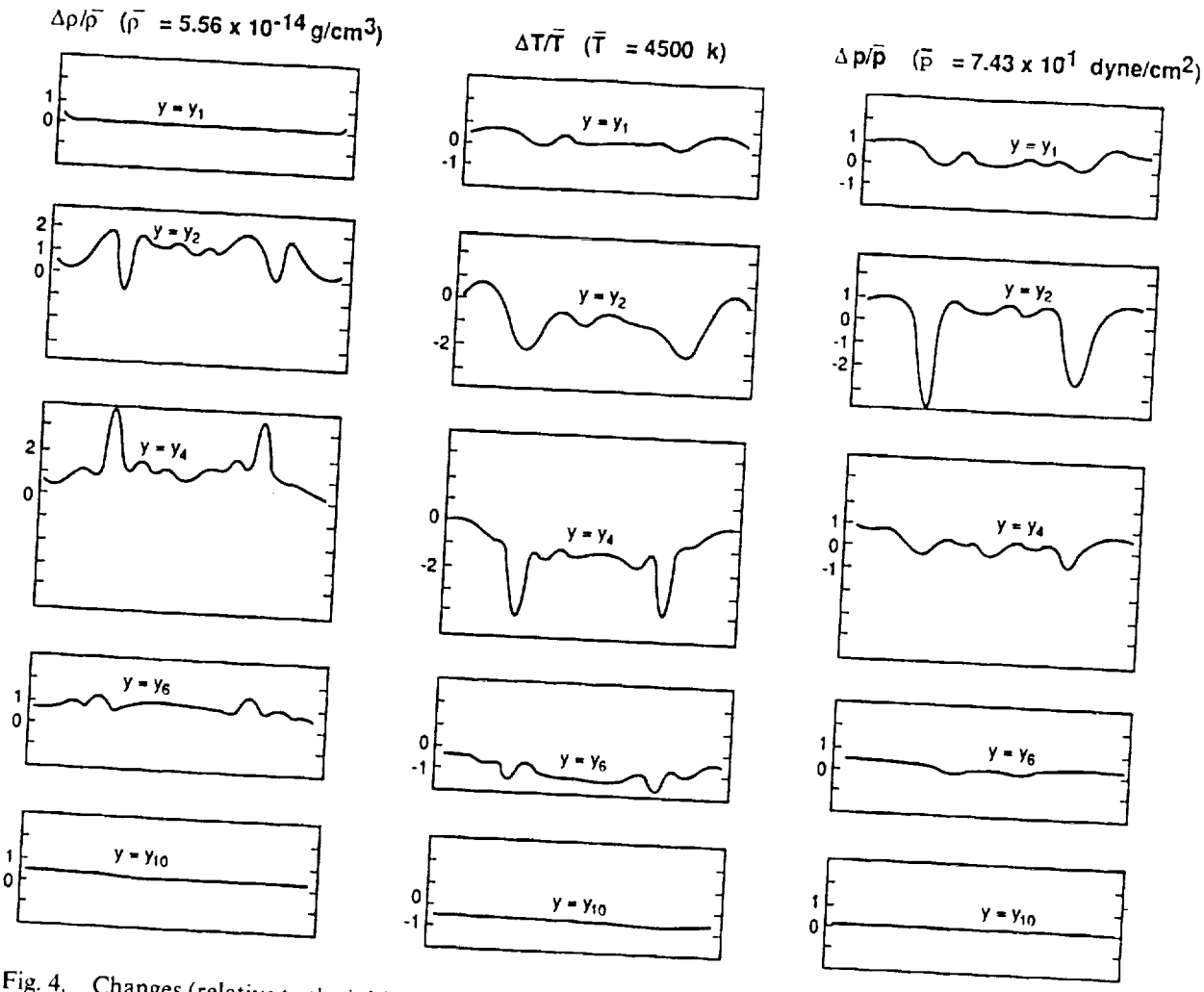

Fig. 4. Changes (relative to the initial local values) of density ($\Delta\rho = \rho - \rho_0(y)$), temperature ($\Delta T = T - T_c$), and pressure ($\Delta p = p - p_0(y)$) normalized by a proper value as shown at the end of the simulation (case (i): $\beta_0 = 154$), $t = 3600$ s which is more than two Alfvén time periods. The distributions are plotted along the entire horizontal scale of the domain and at various levels; y_1, y_2, y_4, y_6, and y_{10} as shown in Figure 1(b). All the values are normalized by a reference quantity as indicated.

2.2. Intermediate plasma beta (i.e., $\beta_0 = 1.54$)

In this case, our simulation is performed with an initially modest magnetic field strength ($B_0 = 21.3$ G) and with a shear velocity (w_c) of 15 km s^{-1} and $V_A \sim 46.5$ km s^{-1}. The qualitative behaviour of the evolution of the vectorial fields (i.e., magnetic and velocity fields) and plasma parameters (i.e., density, temperature, and pressure) are similar to case (i). Therefore, we shall not repeat a full presentation. Nevertheless, there are some interesting features that appear in the evolutionary results of the magnetic and velocity fields as shown in Figure 5.

The most pronounced result is the induced velocity distribution shown on the right side panels of Figure 5. The high velocity of the ascending movement in the central region is especially notable. As a result, the closed bipolar field tends to be opened up. We attribute this to the force created by the ascending movement of mass motion initiated by the shear prescribed at the lower boundary. The highest velocity attained by the mushroom cloud-like ascending mass motion is about 25 km s^{-1} at $t = 700$ s

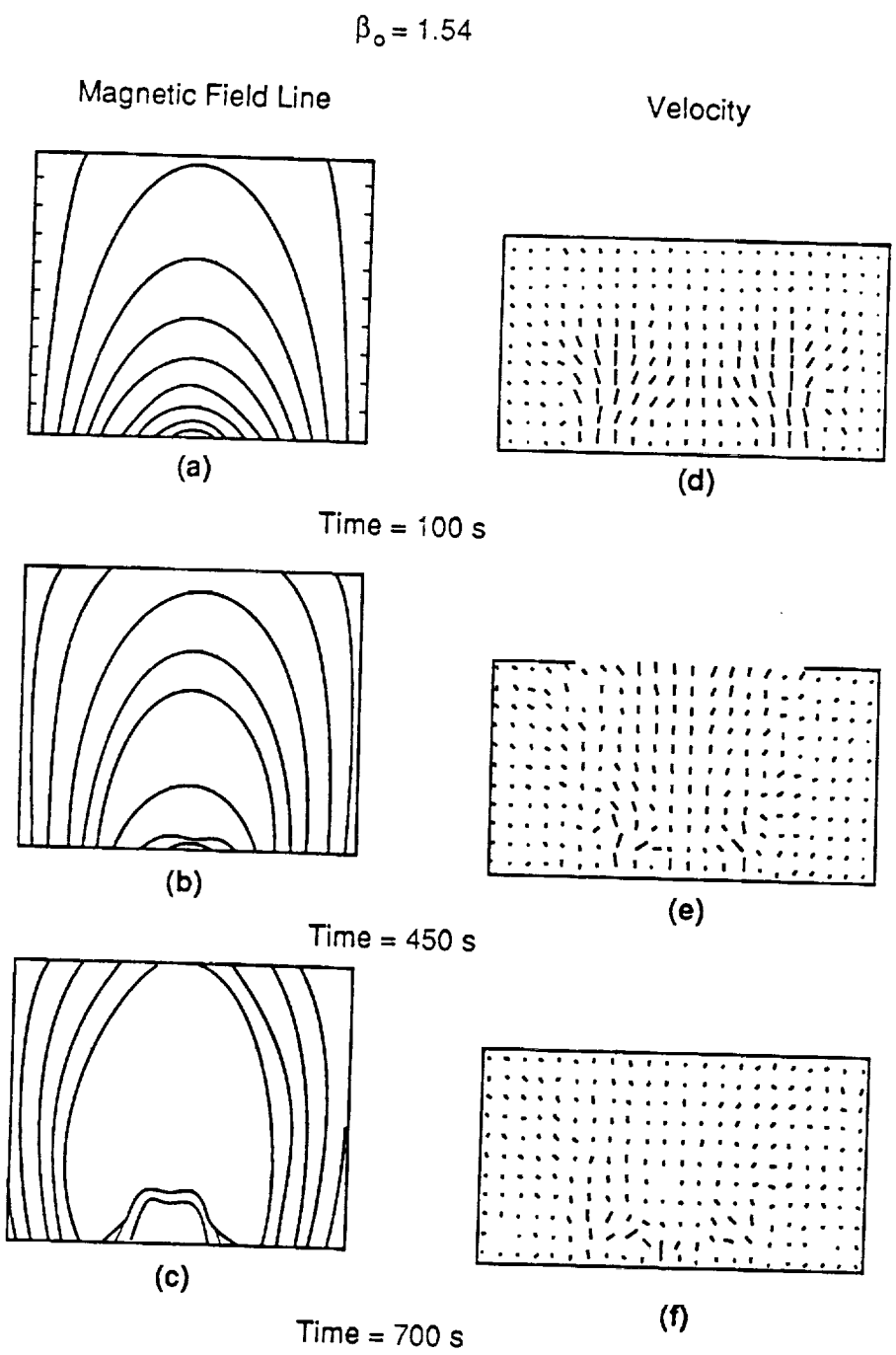

Fig. 5. Evolution of magnetic field lines and vectorial velocity fields at various times for case (ii): $\beta_0 = 1.54$. The characteristic Alfvén time for this case is $\tau_A = 174$ s.

(i.e., ~ 4 Alfvén times) after introduction of the shear motion. The corresponding plasma parameters can be summarized as follows: the density decreases by about 50% at the legs of the intermediate loops marked by the footpoints x_4, x_5, and x_6 as labeled in Figure 1(b). Again, the pinch effects discussed for case (i) occur and a current sheet is formed where the density increases by 25%; the temperature decreases by 30%; and the field strength increases by a factor of 2.

2.3. Low plasma beta (i.e., $\beta_0 = 0.06$)

In this case the initial magnetic field strength is increased to a more realistic value of 106.3 G $w_c = 15$ km s^{-1} and $V_A = 232$ km s^{-1} without changing the other plasma parameters. The initial plasma beta is equal to 0.06 which is 250 times smaller than case (ii) and 2500 times smaller than case (i). Again, the evolution of the magnetic field and velocity field exhibits patterns similar to those of cases (i) and (ii). Figure 6 shows the evolution of the magnetic field and the velocity vector field for this case. The maximum upward velocity is a factor of 4 higher than for case (ii) and a factor of 40

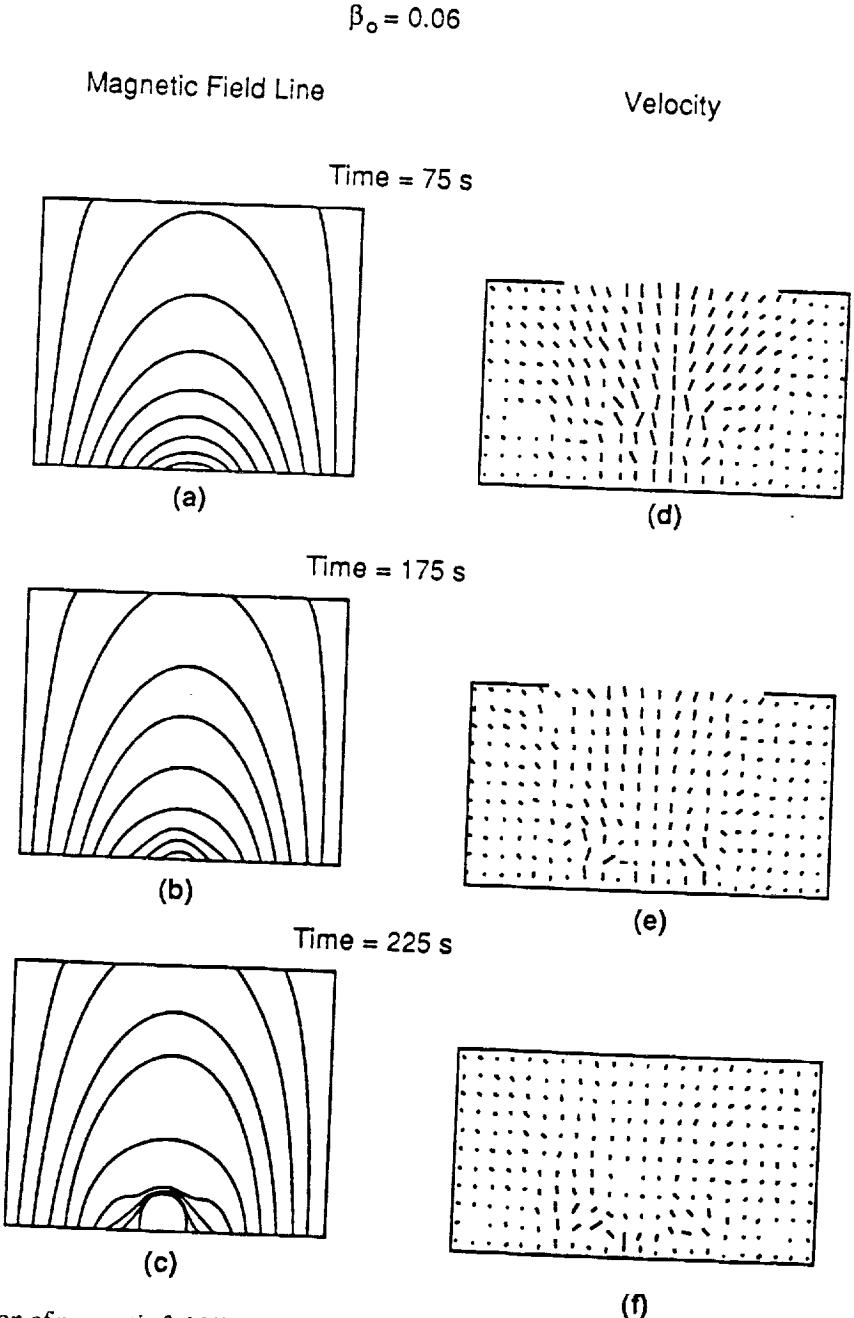

Fig. 6. Evolution of magnetic field lines and vectorial velocity fields at various times for case (iii): $\beta_0 = 0.06$. The characteristic Alfvén time for this case is $\tau_A = 35$ s.

higher than for case (i). We note that the time required to reach the maximum velocity is much shorter than in the other two cases.

In order to examine this phenomenon further, we plotted in Figure 7 the planar maximum absolute velocity (i.e., $(v_x^2 + v_y^2)^{1/2}_{\max}$) in the neighbourhood of the apex of the arcade as a function of time for the three different cases. We choose to plot this parameter instead of the upward velocity, v_y, because the representative parameter $[v_x^2 + v_y^2]^{1/2}$ is related to our analytical analysis that is discussed later (and in the Appendix). Actually, the numerical results show that the horizontal velocity, v_x, is only 25% of the vertical velocity, v_y. First, we point out the change of scales that was required for the three cases (i), (ii), and (iii). Second, we direct attention to the common features: an approximately linear initial phase followed by a smooth transition to an explosive upward mass motion. The latter phenomenon is representative of the upward regions as discussed earlier.

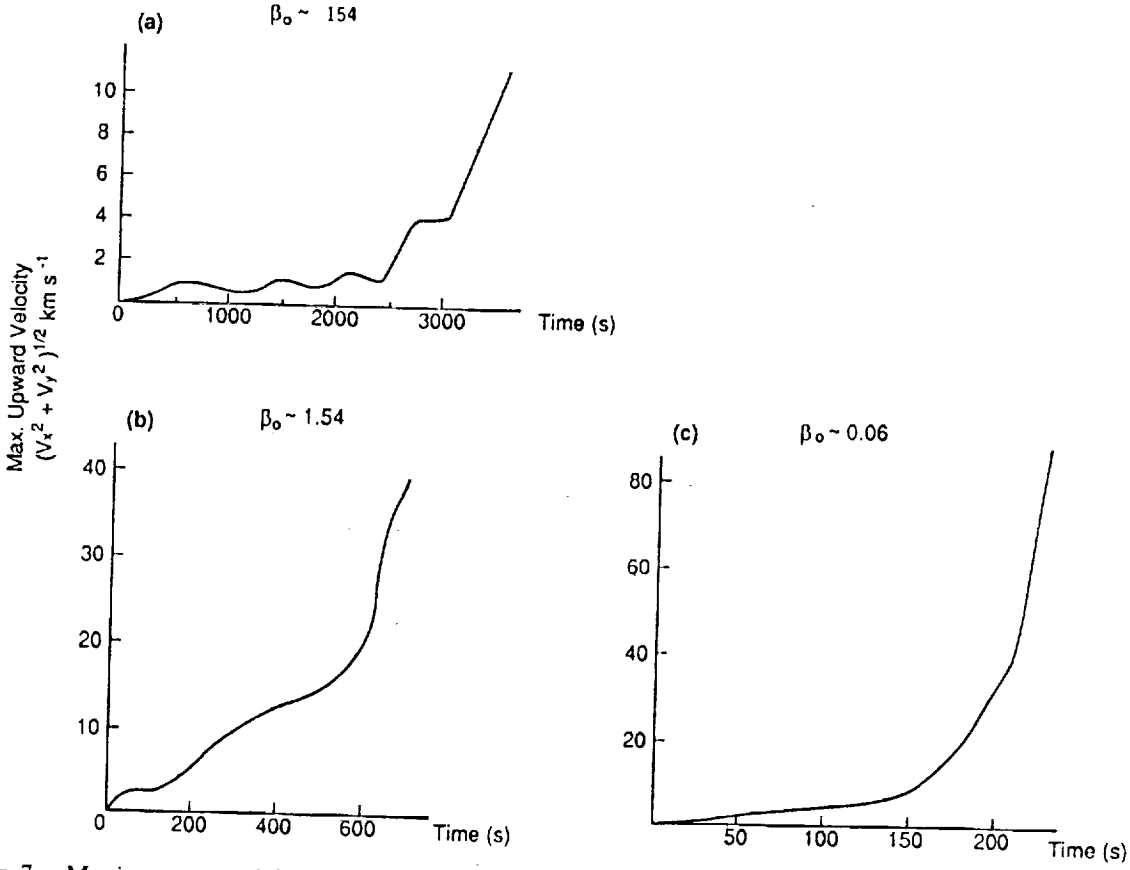

Fig. 7. Maximum vectorial velocity that is representative of the upward vertical mass motion for cases (i), (ii), and (iii). Note the change of scales. The representative Alfvén times for the three cases (β_0 = 154, 1.54, and 0.06, respectively) are τ_A = 1700 s, 174 s, and 35 s.

It is interesting to relate these results to the magnetic field evolution. For example, we direct attention to Figures 2, 5, and 6 where, in the early stages of the evolution, the change of field lines is regular with a slowly ascending movement. This upward motion is also present in the force-free analyses of Low (1981) and Klimchuk and Sturrock (1989), and the numerical incompressible simulations of Mikic, Barnes, and Schnack

(1988), and Biskamp and Welter (1989). However, the change of field lines in the present case becomes quite irregular in the later stages of the evolution. From Figures 2, 5, and 6, we notice that the lower field lines are pinched together and the upper field lines tend to open up when the maximum planar velocity exceeds the Alfvén speed. The Alfvén speed for these three cases is 4.67 km s^{-1}, 46.7 km s^{-1}, and 232 km s^{-1}, respectively. The maximum footpoint shear motion, v_z, is slow compared to the Alfvén velocity in the latter two cases but fast compared with resistive diffusion in all three cases. Thus a sequence of essentially quasi-static, force-free states with frozen-in magnetic fields is found in the early stages, which ends when the magnitude of planar maximum velocity exceeds the Alfvén speed, and the system becomes unstable. We claim that this is a shear-induced instability that could not be found in the earlier numerical simulations that omitted compressibility, pressure gradient, gravity, and the different treatment of boundary conditions. We shall return to this point later for further discussion utilizing analytical results.

3. Further Interpretation of the Simulation Results

From these simulation results, we have found that the buoyancy force leads to a mushroom cloud-like ascending movement that pushes the closed magnetic field upward. In order to understand this result further, we supplement our numerical simulation with an approximate analytical solution:

3.1. Creation of Mushroom Cloud-Like Ascending Motion

From the numerical simulation of all three cases, we observe that the shear-induced mushroom cloud-like ascending movement can be ascribed to the out-of-plane component of the magnetic field, B_z. This component gives an upward magnetic pressure gradient (i.e., $\nabla(B_z^2/8\pi)$) which causes the ascending movement of magnetic field and corresponding plasma flows. On the other hand, we notice that no B_z component is generated near the origin ($x = 0$, $y = 0$) due to shear. This leads to a downward force, such that we observe the field lines being squeezed together to form a current sheet as shown in Figures 2, 5, and 6. This point can be illustrated further by using a linear approximation. The justification for the use of linear theory is seen from the numerical results that show that the initial stage of the shear-induced motion behaves regularly as shown in Figures 2, 3, 5, and 6.

A closed form linearized solution for the induced field component B_z is the following (for the derivation, see the Appendix):

$$\frac{B_z}{\sqrt{4\pi\rho_0}} = c_1 e^{-ay} \cos(ax) \cos[Lax (e^{-ay}\cos(ax))^{-1}] \sin[(t + t_0)L\omega_0]\,. \qquad (3)$$

This result expresses that the induced magnetic field B_z rises from the lower boundary (i.e., $y = 0$) and spreads upward with a characteristic time scale $L\omega_0$, where L is defined by Equation (A.8). It could be noticed from Equation (3) that B_z decreases exponentially

with respect to the increase of y (height), because the term, $\cos[Lax\,(e^{-ay}\cos(ax))^{-1}]$ in the central region, varies slowly with height.

Finally, the coefficient c_1 corresponds to the shear velocity (w_c). The part of the total upward Lorentz force ($-J_xB_z = -\partial/\partial y(B_z^2/2)$), that causes upward acceleration is independent of the sign of the coefficient c_1 (or w_c).

3.2. Shear-induced instability

From the simulation results shown in Figure 7, we found earlier that instability sets in when the absolute maximum planar velocity exceeds the Alfvén speed. In order to substantiate this claim, we performed a linearized analysis in which an approximate linearized solution for the planar velocities (u, v) was constructed as shown in the Appendix (Equation (A.13)). These velocities are as follows:

$$u_1 = \delta'\, e^{-2ay}\sin(2ax)\,,$$
$$v_1 = \delta'\, e^{-2ay}[1 + \cos 2(ax)]\,. \tag{4}$$

The electric current along the z-axis can be estimated, to the first order, as

$$\frac{4\pi}{c}\,J_z = \frac{\partial B_y}{\partial x} - \frac{\partial B_x}{\partial y} = 16a^2B_0\,e^{-3ay}\cos ax\int_0^t \delta'\,\mathrm{d}t\,, \tag{5}$$

which means that the Lorentz force $c^{-1}(J_zB_x - J_xB_z)$ leads to ascending flow, because it has been shown in the Appendix that δ' is always positive and has an exponential growth rate as shown in Equation (A.16). We have identified this phenomenon as the shear-induced instability since the numerical simulation results shown in Figure 7 are consistent with the analytical analysis. It is further noted from numerical results that the term $-c^{-1}J_xB_z$ is always upward.

The results for the evolution of the magnetic field configuration shown in Figures 2, 5, and 6 show clearly the two-stage evolution that we discussed earlier. The first stage of the evolution can be described by the linearized solution given in Equation (4). The second stage of the evolution involves the pinching together of field lines in the region where the shear motion was applied. If the three factors noted earlier (compressibility, pressure gradients, and gravity) had been absent, we believe that our results would have been similar to those of Mikic, Barnes, and Schnack (1988). Our current sheet, however, developed horizontally, whereas their current sheet was vertical. We explain this phenomenon by examining the distribution of upward component of the Lorentz force (i.e., $c^{-1}(J_zB_x - J_xB_z)$). To illustrate this viewpoint, we use the results for $\beta_0 = 0.06$ because this case best resembles the real physical conditions in active regions. The results are plotted in Figure 8. The left-most panels show the horizontal distribution of the vertical component of the Lorentz force at different heights from y_1 to y_{10} (as shown in Figure 1(b)) at 25 s after the introduction of the shear motion at the lower boundary. A noted earlier, the Alfvén time for this case is ~ 35 s. This result clearly indicates the first stage of the evolution due to the introduction of shear. All the forces are in the

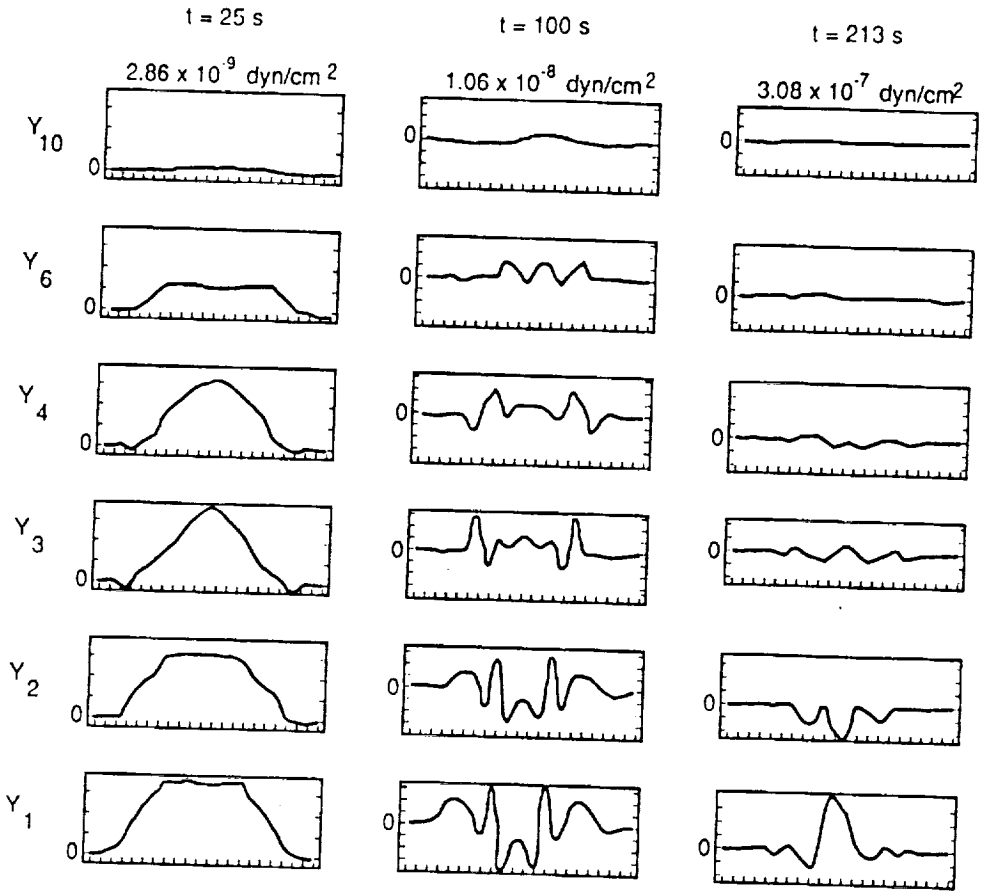

Fig. 8. The total y-component of the Lorentz force per unit area at t = 25 s, 100 s, and 213 s and at various levels in the solar atmosphere ($y = y_1, y_2, \ldots$, etc.). The representative Alfvén time for case (iii) is 35 s and $\beta_0 = 0.06$. At t = 100 s (about $3\tau_A$) during the nonlinear stage of evolution, the Lorentz forces at the intermediate heights have a combination of upward and downward directions that causes magnetic field line pinching (see text). This pinch effect is more pronounced at t = 213 s (about $7\tau_A$) at lower altitudes. The horizontal axis represents the distance $x_1 \ldots x_{22}$ as shown in Figure 1(b) also shown for Figures 2–6.

upward direction which means that all field lines are lifted up in an orderly fashion. The magnitude of these forces is of the order of 3×10^{-9} dyne cm^{-2}. The middle panels show the resultant upward component of the Lorentz force at t = 100 s which is about three Alfvén periods. These results are reflected in the nonlinear nature of the evolution in which the Lorentz forces have both upward and downward direction at the intermediate altitudes.

This bi-directional nature of the Lorentz forces causes the field lines to be pinched together in the lower regions as shown, for example, in Figure 6 for $\beta_0 = 0.06$. This particular feature is most pronounced in the results shown in the right-most panels which show the vertical component of Lorentz force at t = 213 s; this is about seven Alfvén periods after the introduction of the shear. We note that the vertical component of this Lorentz force decreases at high levels, but, in lower levels (i.e., y_1 and y_2), two very strong oppositely-directed vertical components of Lorentz force ($\sim 3 \times 10^{-7}$ dyne cm^{-2}) appear. The force at y_1 is upward and the force at y_2 is downward.

These two forces cause the field lines to be pinched together as shown in Figure 6(c). Further discussion of this point will be included in the next section as part of a general scenario for shearing motions of magnetic arches or bipolar regions.

4. Scenario

From these simulation results, supported by the linearized analytical solution, a physical scenario is proposed for the formation of an 'Arch Filament System (AFS)' and its eruption as part of a more general scenario for 'Coronal Mass Ejections (CMEs)'. A schematic representation of this scenario is presented in Figure 9. After introduction of shear motion at a bi-polar region, all of the field lines will first be lifted up in an orderly fashion due to the shear-induced upward Lorentz force before the absolute maximum upward velocity reaches the local Alfvén speed; this is the linear stage of the evolution. When this upward velocity is in the neighbourhood of the local Alfvén speed, the lower parts of the magnetic field lines are pinched together, and an arch filament system is formed. At the same time, the upper part of the magnetic field lines is pushed upward, and a certain amount of mass is carried upward. This upward mass motion is shown in Figure 10 in terms of contours of $\Delta\rho$ and Δp that move upward at all but the lowest gravitationally-bound heights.

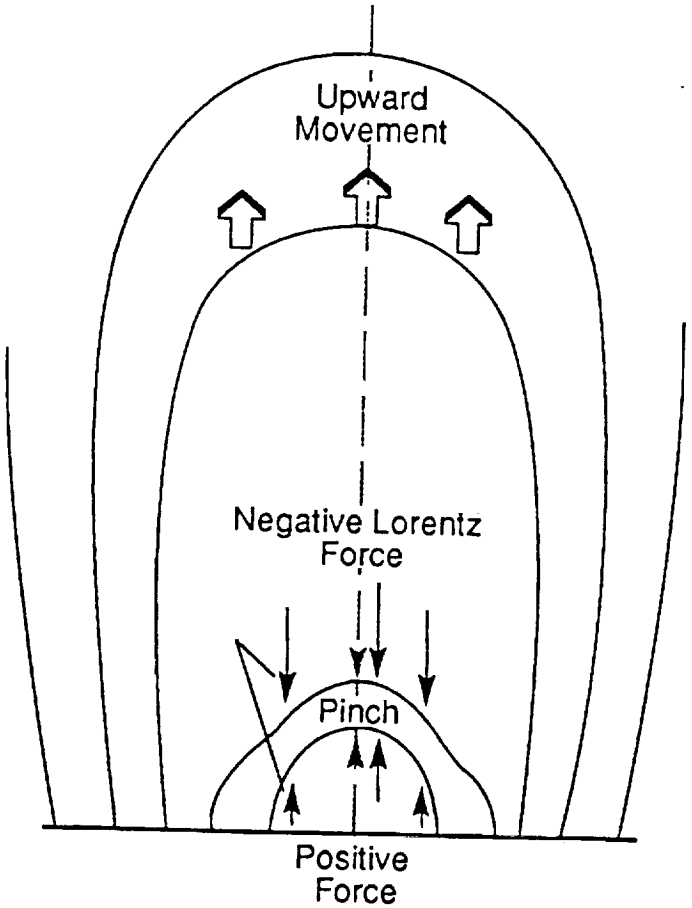

Fig. 9. Scenario for the formation of an arch-filament system (AFS) and upper level movement outward in the initial stage of a coronal mass ejection (CME) as a result of shear-induced instability.

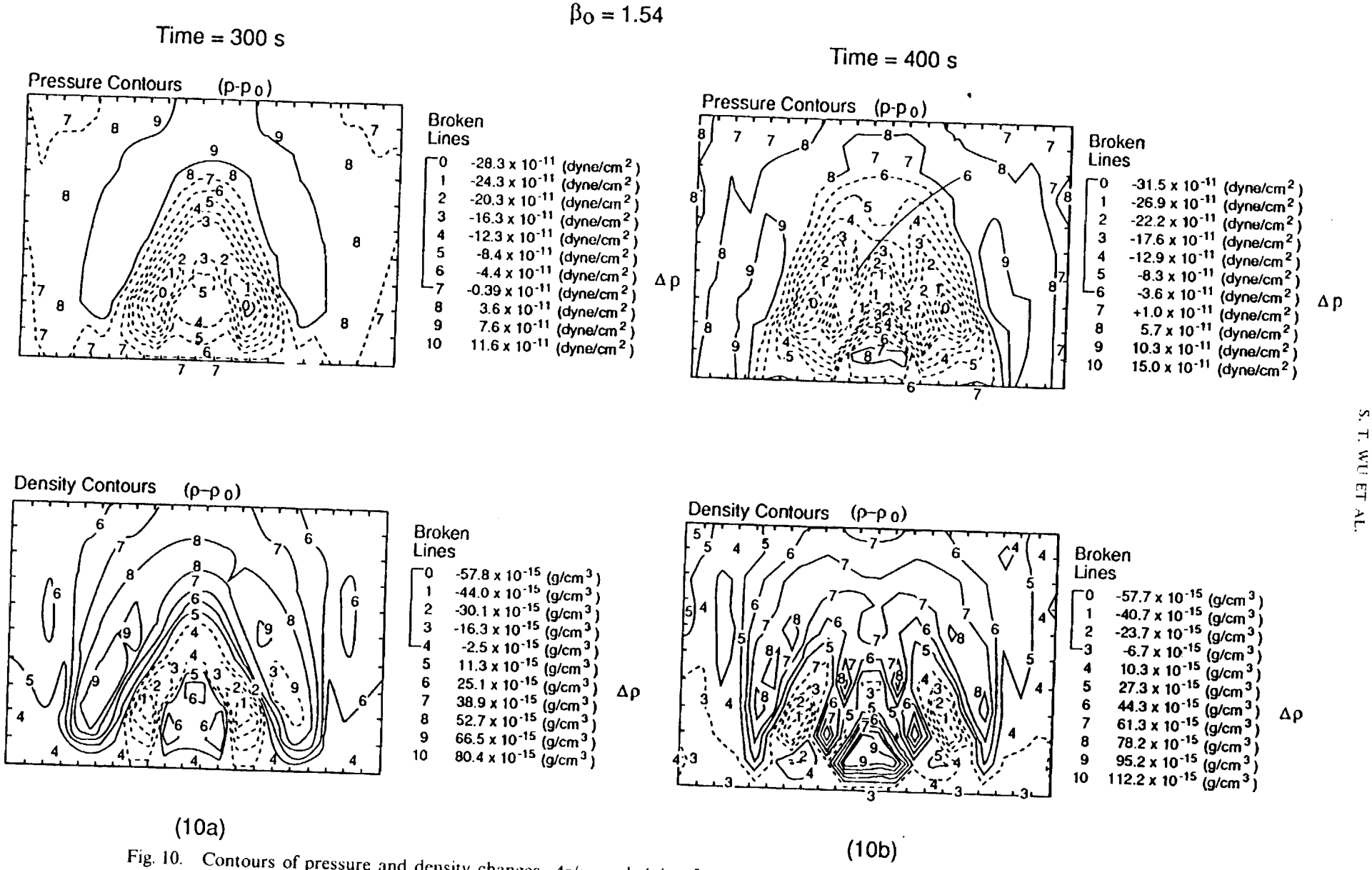

Fig. 10. Contours of pressure and density changes, $\Delta p/p_0$ and $\Delta\rho/\rho_0$, for case (ii) [$\beta_0 = 1.54$] at several times.

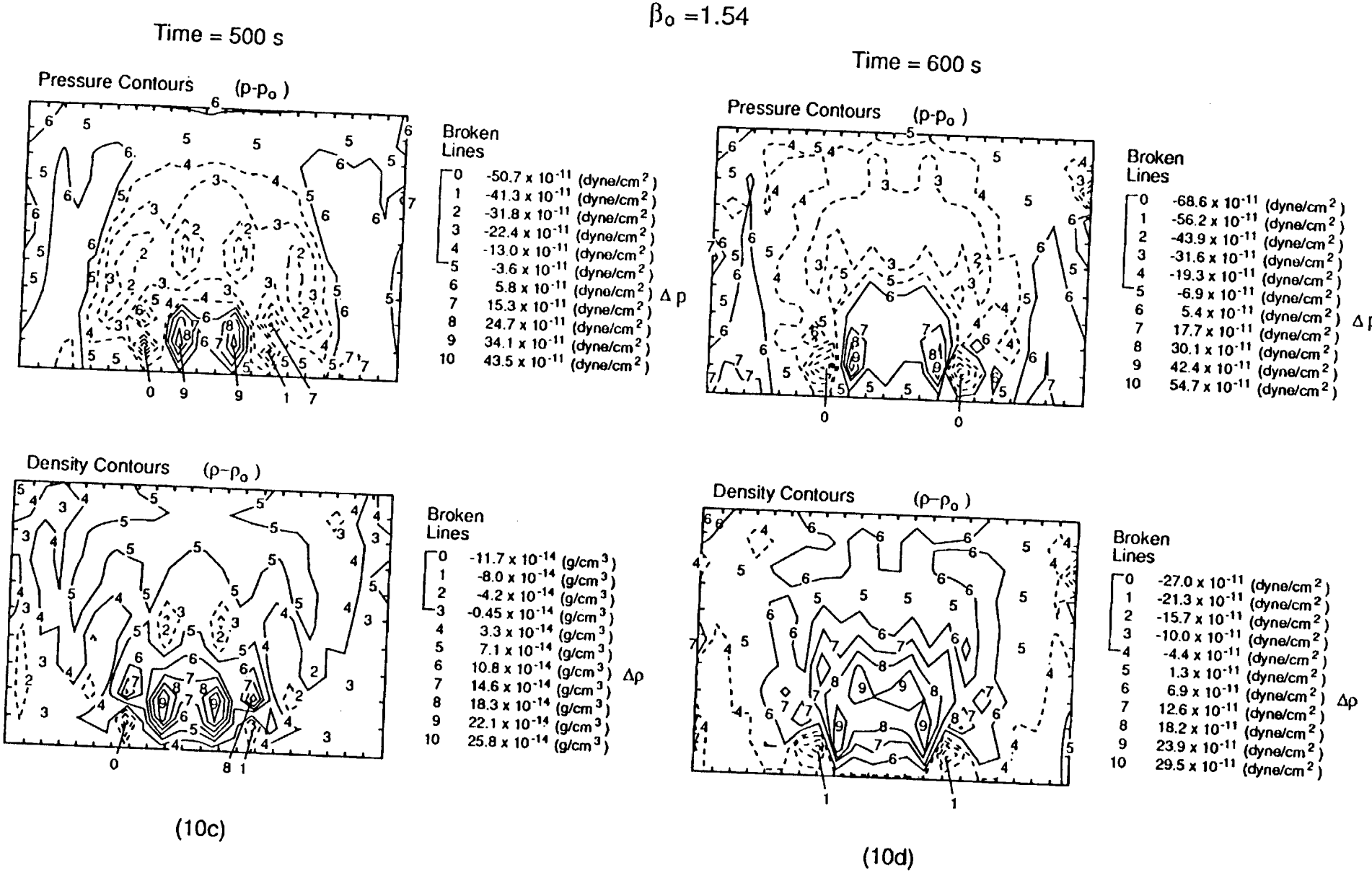

Fig. 10 (continued).

Finally, when this absolute upward velocity exceeds the Alfvén speed, the shear-induced instability sets in as shown by the numerical results of Figure 7 and the analytical solution in the Appendix (Equation (A.16)). In the following we compare this scenario with the available observations.

Arch filament systems and coronal mass ejections have been investigated by many authors (Bruzek, 1967, 1968, 1969; Bumba and Howard, 1965; Martres *et al.*, 1966; Harrison, 1986). These authors have noted that arch filament systems (AFS) always connect areas of opposite polarities and cross the neutral line in the longitudinal magnetic field. Bruzek (1969) has pointed out that the occurrence of AFS is associated with evolution of young bipolar spot groups. As for the motion of AFS, its characteristic feature is its expansion in height with an ascending velocity of 16–25 km s^{-1} with footpoints rooted in the two opposite spot regions. This behaviour is quite similar to the early stage of the simulated magnetic field line evolution and mass motion shown in Figures 2, 3, 5, and 6 where the apex of the magnetic loops is rising but their legs have little lateral movement. It was further noted that the AFS has both descending and ascending motions in loops. Bruzek (1968) attributed this phenomenon to the mass injection at one leg and its return to the chromosphere via another leg that has opposite polarity. On the other hand, shearing motion, if it has a line-of-sight component, would always lead to a blue shift in one leg and red shift in the other. Therefore, observations of flows in filaments are not evidence of shearing. However, such evidence is not needed since the relative motion of bipolar spots is both necessary and sufficient evidence of shearing. Nevertheless, this concept of descending and ascending motion is based on Doppler shift measurements which can easily, at least partially, be recognized as complementary evidence of horizontal shear motion that occurs on both sides of the neutral line. This statement considers the fact that the spot group area is often not strictly perpendicular to the line of sight of the observer; thus the Doppler shift velocity must have an appreciable horizontal component (Harvey and Harvey, 1976).

On the basis of our numerical simulations, the analytial solution and observed characteristics, a physical model for the formation of AFS and subsequent CME can be constructed as follows. First, a young bipolar sunspot group emerges from the sub-photosphere. As it rises, its area increases and the neutral line dividing the opposite polarities gets longer and longer. Then a portion of the field can be reasonably regarded as a two-dimensional bipolar field (as is used in our mathematical model). In the meantime, the opposite polarity areas rotate with respect to each other. Associated with this rotation are horizontal shear motions that appear on both sides of the neutral line (thereby justifying our construction of the shearing velocity used herein). The Lorentz force generated by this process (see, for example, Figure 8) pushes the magnetic loops upward during an initial stage. At the later times, the magnetic field becomes distorted, nonlinear MHD effects force field lines to pile-up and, then, the pinch phenomenon ensues. Such pinched magnetic flux tubes could be identified as arch filaments which are visible as a set of dark loops. The simulation has shown that in this region the plasma has high density and low temperature. From the analytical solution, we notice that the growth time $(V_A a)^{-1}$ of the shearing instability is about 30 min which is a typical

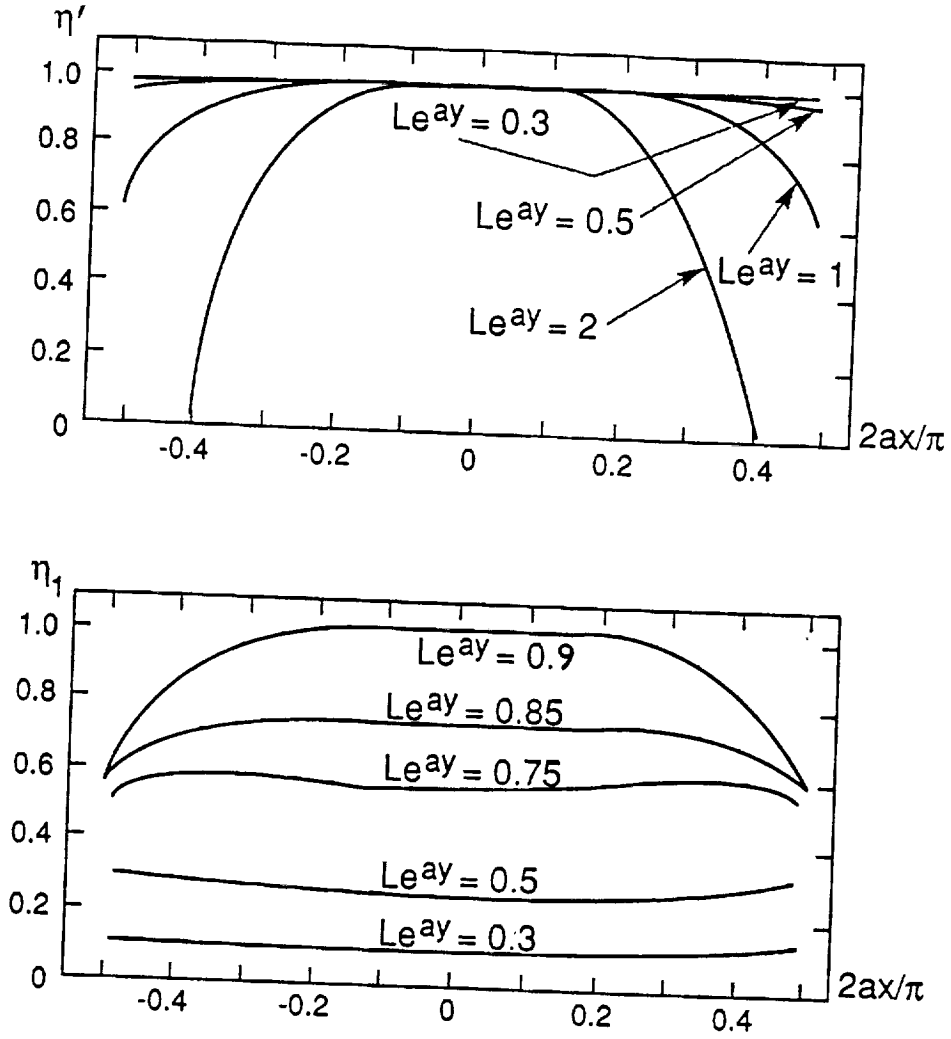

Fig. 11. Behaviour of η' and η_1. See Appendix (Equation (A.12)).

average life time of AFS. Thus, this simulation model may be appropriate to describe the formation of AFS and the eruption which leads to some CMEs.

5. Concluding Remarks

We have used a time-dependent, nonplanar MHD model for a bipolar magnetic region that was subjected to shearing motion at its foot points. The characteristic plasma beta was varied over a wide range – from 154 to a more realistic value of 0.06. Common features were identified for all cases with the differences primarily occurring in the timing of the events vis-à-vis the characteristic Alfvén times. An essentially linear, early phase of upward mass motion was followed until the Alfvén speed was reached, and a shear-induced instability is initiated. This nonlinear instability may be the basic mechanism for arch filament formation and subsequent coronal mass ejections.

In our opinion, the early evolution in our simulation is in accord with *quasi-static* evolution of magnetic arcades demonstrated by Klimchuk and Sturrock (1989). In their work, a very low beta plasma was assumed, and therefore the magnetic field is unaffected

by pressure and gravitational forces. Our simulations are also in accord with the dynamic evolution of magnetic arcades demonstrated by the numerical simulations of Mikic, Barnes, and Schnack (1988) and Biskamp and Welter (1989) in both the *early* and *intermediate* stages of this evolution despite their neglect of compressibility, pressure gradient, and gravity. We did not find the reconnection and formation of an ejected plasmoid, as Mikic, Barnes, and Schnack (1988) did, since we assumed electrical resistivity and viscosity to be zero. During the *late* stages of the evolutionary development, when the plasma velocities surpassed the Alfvén speed, our numerical simulations demonstrate nonlinear instability and catastrophic upward motion at high altitudes.

As a final remark, it can be shown that these numerical results are valid over a wide range of parameters according to the scaling rule for dynamic similitude. For example, the present numerical results, computed on the basis of $T_0 = 10^5$ K and $\rho_0 = 1.67 \times 10^{-12}$ g cm^{-3}, can be scaled to initial conditions of $T_1 = 10^6$ K and $\rho_1 = 1.67 \times 10^{-13}$ g cm^{-3} by introducing a set of scaling parameters; $t_1 = \sqrt{\lambda}\, t_0$, $L_1 = \lambda L_0$, $v_1 = \sqrt{\lambda}\, v_0$, $T_1 = \lambda T_0$, $\rho_1 = \lambda^{-1}\rho_0$, $p_1 = p_0$, and $B_1 = B_0$ which leave the governing equations invariant for a given plasma beta. In a recent study of similitude theory, Wu *et al.* (1988) have shown that the present results also apply to the physical condition represented by these different initial conditions.

As another example of the use of dynamic similitude, we may pose the following question: if the footpoints are moved slowly enough that the evolution is quasi-static, would the magnetic field closely approximate the static equilibrium states? Although, we suggested above (as did Mikic, Barnes, and Schnack, 1988, and Biskamp and Welter, 1989) that the answer is 'yes', the reader is reminded of the values of the shearing velocity v_z used in the present studies (e.g., 15 km s^{-1}, maximum, for $\beta_0 = 0.06$) and in the above-mentioned work (30 km s^{-1}, assumed by Mikic, Barnes, and Schnack, 1988, for $\beta \sim 0.03$). Although these maximum footpoint shearing velocities are much less than the Alfvén speed, they are a factor of about 10 larger than observed photospheric velocities.

In summary, we consider the results given here to be representative of a realistic dynamical evolution of the posed physical problem of sheared magnetic arches and their evolution into arch filament eruption and coronal mass ejections.

Finally, we remark on the relevance of our results to the observations of some CMEs as reported by Harrison (1986). The major point of his work is that a small X-ray burst is often found at the very onset of a CME, often followed by a large X-ray flare later on during the CME. In the present work, the formation of the current sheet coincides with the rapid increase in the velocity of the upper portion of the field lines. One could interpret the latter, as already discussed, as the onset of CME, while the current sheet formation could lead to a burst of energy dissipation (not shown here) which would be visible as a small X-ray burst. The simultaneity of these two events is consistent with the observations of Harrison (1986). This could be another indication that these numerical results indeed represent a basic mechanism for the initiation of CMEs.

ORIGINAL PAGE IS
OF POOR QUALITY

Acknowledgement

The work performed by STW was supported by Air Force Office of Scientific Research grant AFSOR-88–0013, National Aeronautics and Space Administration/Headquarters grant NAGW-9, and National Oceanic and Atmospheric Administration contract (50RANR-7000104). The work of PM was supported at CFA by NASA Grant NAGW-112. The work of MD was supported in part by NASA Interagency Order 17015..

Appendix

To obtain an asymptotic solution for the relationship between the footpoint shearing velocity, w, and B_z in the first stage (linear stage) of evolution during which ρ, p, T, B_x, B_y vary slightly, we write

$$\begin{aligned} &\rho = \rho_0 + \rho_1\,, \quad p = p_0 + p_1\,, \quad T = T_0 + T_1\,, \quad B_x = B_{x0} + B_{x1}\,, \\ &B_y = B_{y0} + B_{y1}\,, \quad B_z = B_{z1}\,, \quad v_x = v_{x1}\,, \quad v_y = v_{y1}\,, \quad v_z = v_{z1}\,, \end{aligned} \tag{A.1}$$

where subscript 0 and 1 indicate the zero-order and first-order quantities. And, $|v_{x1}|$, $|v_{y1}|$, $|v_{z1}| \ll B_0/\sqrt{4\pi\rho_0}$ = Alfvén speed, $|B_{z1}| \ll B_0$. Inserting (A.1) into Equations (2.4) and (2.7) formerly given by Wu, Hu, and Nakagawa (1983) and leaving out the higher-order quantities, we obtain the linearized equations

$$\begin{aligned} \frac{\partial v_{z1}}{\partial t} &= \frac{B_{x0}}{\sqrt{4\pi\rho_0}}\,\frac{\partial(B_{z1}/\sqrt{4\pi\rho_0})}{\partial x} + \frac{B_{y0}}{\sqrt{4\pi\rho_0}}\,\frac{\partial(B_{z1}/\sqrt{4\pi\rho_0})}{\partial y} - \frac{b}{2}\,\frac{B_{y0}}{\sqrt{4\pi\rho_0}}\,\frac{B_{z1}}{\sqrt{4\pi\rho_0}}\,, \\ \frac{\partial(B_{z1}/\sqrt{4\pi\rho_0})}{\partial t} &= \frac{B_{x0}}{\sqrt{4\pi\rho_0}}\,\frac{\partial v_{z1}}{\partial x} + \frac{B_{y0}}{\sqrt{4\pi\rho_0}}\,\frac{\partial v_{z1}}{\partial y}\,, \end{aligned} \tag{A.2}$$

where $\rho_0 = \rho_c\, e^{-by}$, $b = g/RT_c$. To solve Equation (A.2), we construct the auxiliary equations

$$\begin{aligned} \frac{\partial v_z^*}{\partial t} &= B_{x0}(4\pi\rho_0)^{-1/2}\,\frac{\partial(B_z^*/\sqrt{4\pi\rho_0})}{\partial x} + B_{y0}(4\pi\rho_0)^{-1/2}\,\frac{\partial(B_z^*/\sqrt{4\pi\rho_0})}{\partial y}\,, \\ \frac{\partial(B_z^*/\sqrt{4\pi\rho_0})}{\partial t} &= B_{x0}(4\pi\rho_0)^{-1/2}\,\frac{\partial v_z^*}{\partial x} + B_{y0}(4\pi\rho_0)^{-1/2}\,\frac{\partial v_z^*}{\partial y}\,. \end{aligned} \tag{A.3}$$

Substituting

$$F^+ = \frac{\left(v_z^* + \dfrac{B_z^*}{\sqrt{4\pi\rho_0}}\right)}{2}\,, \qquad F^- = \frac{\left(v_z^* - \dfrac{B_z^*}{\sqrt{4\pi\rho_0}}\right)}{2}\,,$$

ORIGINAL PAGE IS OF POOR QUALITY

Equations (A.3) reduce to

$$\frac{\partial F^+}{\partial t} = B_0(4\pi\rho_c)^{-1/2}\, e^{-(a-b/2)y}\left(\cos ax\,\frac{\partial F^+}{\partial x} - \sin ax\,\frac{\partial F^+}{\partial y}\right),$$
$$\frac{\partial F^-}{\partial t} = B_0(4\pi\rho_c)^{-1/2}\, e^{-(a-b/2)y}\left(-\cos ax\,\frac{\partial F^-}{\partial x} + \sin ax\,\frac{\partial F^-}{\partial y}\right). \tag{A.4}$$

Since solving Equations (A.4) is equivalent to solving their corresponding ordinary differential equations (Courant and Hilbert, 1962), it is easy to write down the solutions as follows:

$$F^+ = \phi(e^{-ay}\cos ax,\, t\omega_0 + f(ax)\,(e^{-ay}\cos ax)^{-1+b(2a)^{-1}}),$$
$$F^- = \psi(e^{-ay}\cos ax,\, t\omega_0 - f(ax)\,(e^{-ay}\cos ax)^{-1+b(2a)^{-1}}), \tag{A.5}$$

where

$$\omega_0 = aB_0(4\pi\rho_c)^{-1/2}, \qquad f(x) \equiv \int_0^x (\cos x')^{-b/2a}\,dx'.$$

Considering the boundary value of v_z (the nature of shearing) and using Equation (A.5) we can find the following solutions:

$$v_z^* = c_1 e^{-ay}\cos ax\cos(L\zeta)\sin(L\eta),$$
$$\left(\frac{B_z^*}{\sqrt{4\pi\rho_0}}\right) = c_1\, e^{-ay}\cos ax\sin(L\zeta)\cos(L\eta), \tag{A.6}$$

where

$$\zeta \equiv (t + t_0)\omega_0, \qquad \eta \equiv f(ax)\,(e^{-ay}\cos ax)^{-1+b(2a)^{-1}}.$$

t_0, L, and c_1 are integration constants. Back to solving Equations (A.2) suppose v_{z1}, $(B_z/\sqrt{4\pi\rho_0})$ satisfy the equalities (A.6) except that L, c_1 are now not constants but functions of x, y. Thus

$$v_{z1} = c_1(x, y)\, e^{-ay}\cos(ax)\cos(L(x, y)\zeta)\sin(L(x, y)\eta),$$
$$\left(\frac{B_{z1}}{\sqrt{4\pi\rho_0}}\right) = c_1(x, y)\, e^{-ay}\cos(ax)\sin(L(x, y)\zeta)\cos(L(x, y)\eta). \tag{A.7}$$

Inserting (A.7) into (A.2), c_1 and L can be determined uniquely by solving two ordinary differential equations. First, L satisfies the equation

$$\cos ax\,\frac{\partial L}{\partial x} - \sin ax\,\frac{\partial L}{\partial y} = Q(x, y, L),$$
$$Q(x, y, L) \equiv -(b/4)\sin(ax)\sin(2L\bar{\zeta})\sin(2L\eta)\times$$
$$\times\,[\bar{\zeta}\sin(2L\eta) - \eta\sin(2L\bar{\zeta})]^{-1}, \tag{A.8}$$

with boundary condition $L|_{y=0} = L(x)$. After L has been found, $(\ln c_1)$ can be obtained in the same manner using the following equation:

$$\cos(ax)\,\frac{\partial(\ln c_1)}{\partial x} - \sin(ax)\,\frac{\partial(\ln c_1)}{\partial y} = [\bar{\zeta}\,\mathrm{tg}(L\bar{\zeta}) - \eta\,\mathrm{ctg}(L\eta)]\,Q(x, y, L)\,. \tag{A.9}$$

In fact, we only apply (A.7) to explain the physical nature in the lower shearing region where $\bar{\rho}_0 \simeq 0.8\rho_c$, therefore L and c_1 can roughly be regarded as constants.

It is difficult to find an asymptotic solution for v_x and v_y. Let us consider case (iii) of strong magnetic field, in which the inertial force and $-\nabla p$ and ρg can safely be ignored. Inserting (A.1) into (2.2) and (2.3) of Wu, Hu, and Nakagawa (1983), the linearized equations are given as follows:

$$\begin{aligned}
\bar{\rho}_0\,\frac{\partial v_{x1}}{\partial t} &= \frac{1}{4\pi}\,B_{y0}\left(\frac{\partial B_{x1}}{\partial y} - \frac{\partial B_{y1}}{\partial x}\right) - \frac{1}{4\pi}\,B_{z1}\,\frac{\partial B_{z1}}{\partial x}\,,\\
\bar{\rho}_0\,\frac{\partial v_{y1}}{\partial t} &= -\frac{1}{4\pi}\,B_{x0}\left(\frac{\partial B_{x1}}{\partial y} - \frac{\partial B_{y1}}{\partial x}\right) - \frac{1}{4\pi}\,B_{z1}\,\frac{\partial B_{z1}}{\partial y}\,,
\end{aligned} \tag{A.10}$$

where the terms

$$-\frac{1}{4\pi}\,B_{z1}\,\frac{\partial B_{z1}}{\partial x}\,, \qquad -\frac{1}{4\pi}\,B_{z1}\,\frac{\partial B_{z1}}{\partial y}\,,$$

which are second-order quantities, must be kept in view of actual mathematical manipulation. From (A.7) the partial Lorentz force can be written as

$$\begin{aligned}
-(4\pi\bar{\rho}_0)^{-1}B_{z1}\,\frac{\partial B_{z1}}{\partial x} &= (c_1^2 a/2)\,(\eta' + \eta_1)\,e^{-2ay}\sin(2ax)\sin^2(L\zeta)\,,\\
-(4\pi\bar{\rho}_0)^{-1}B_{z1}\,\frac{\partial B_{z1}}{\partial y} &= (c_1^2 a/2)\,\eta'\,e^{-2ay}[1 + \cos(2ax)]\sin^2(L\zeta)\,,
\end{aligned} \tag{A.11}$$

where η' and η_1 are slow-varying functions of x, y. The representations for η', η_1 are very complicated in the case with gravity, but we only deal with the lower central part of the domain where $\rho \simeq$ const. Thus, the gravitational effects could be ignored in Equation (A.2), then leading to the solution, $\eta \simeq ax\,e^{ay}(\cos ax)^{-1}$, $B_{z1} \simeq B_z^*$. Therefore, η' and η_1 asymptotically approach the case with no gravity. In such case η' and η_1 take simple forms as

$$\begin{aligned}
\eta' &= (\cos\Pi)^2 + \Pi\cos\Pi\sin\Pi\,,\\
\eta_1 &= L\,e^{ay}\cos\Pi\sin\Pi\,(\sin ax)^{-1}\,,\\
\Pi &= L\,e^{ay}ax\,(\cos ax)^{-1}\,.
\end{aligned} \tag{A.12}$$

Figure 11 shows the behaviour of η' and η_1. Note that if $L\,e^{ay}$ is less than 0.5, then $0 < \eta_1 \ll \eta' \simeq 1$. Therefore we will pay no attention to the difference between η and $\eta' + \eta_1$ within the range $|ax| < \pi/4$. (A.11) reminds us of analogy between shearing velocity and force, so we suppose velocity having a mushroom-like form as

$$v_{x1} = \delta'\, e^{-2ay} \sin ax\,, \qquad v_{y1} = \delta'\, e^{-2ay}[1 + \cos(2ax)]\,, \tag{A.13}$$

where δ' is a function of t, x, y (but weakly depends on x, y) being determined later. Inserting (A.13) into the linearized equations of (2.5) and (2.6), of Wu *et al.* (1983) the time variation of current J_{z1}/c can be found as

$$\frac{\partial}{\partial t}\left(\frac{\partial B_{y1}}{\partial x} - \frac{\partial B_{x1}}{\partial y}\right) = 16a^2 B_0 \delta'\, e^{-3ay} \cos(ax)\,. \tag{A.14}$$

In deriving Equation (A.14) the weak dependence of δ' on x, y has been used. Differentiating (A.10) with respect to t and inserting (A.14) and (A.11) into it and then letting it go to limitation when y goes to zero, we obtain one equation

$$\frac{\partial^2}{\partial t^2}\,\delta'|_{y=0} = 8v_A^2 a^2 \delta'|_{y=0} + (c_1^2 a/2)\eta'|_{y=0} L\omega_0 \sin[2L\omega_0(t+t_0)] \tag{A.15}$$

to determine δ' uniquely (here $v_A^2 = B_0^2/4\pi\bar{\rho}_0$). Noticing δ', η' only weakly depend on x, y, Equation (A.15) can be regarded as an ordinary differential equation and, therefore, can be easily integrated with respect to t. Giving the initial condition: $\delta'|_{y=0} = 0$, $\mathrm{d}\delta'/\mathrm{d}t|_{y=0} = 0$ when $t = 0$, we obtain an asymptotic solution as

$$\delta'|_{y=0} = [(\alpha+\beta)/2]\exp(\sqrt{8}\,v_A a t) + [(\alpha-\beta)/2]\exp(-\sqrt{8}\,v_A a t) - \\ - \alpha\,\frac{\sin[2L\omega_0(t+t_0)]}{\sin[2L\omega_0 t_0]}\,, \tag{A.16}$$

with

$$\alpha = \frac{L\omega_0 a c_1^2 \eta'|_{y=0}}{8(L^2\omega_0^2 + 2v_A^2 a^2)}\,\sin(2L\omega_0 t_0) \sim \frac{L\eta' c_1^2/v_A}{8\sqrt{2}\,(L^2+2)} > 0\,,$$

$$\beta = \frac{L^2\omega_0^2 c_1^2 \eta'|_{y=0}}{8\sqrt{2}\,v_A(L^2\omega_0^2 + 2v_A^2 a^2)}\,\cos(2L\omega_0 t_0) \sim \frac{L^2\eta' c_1^2/v_A}{16(L^2+2)} > 0\,.$$

Generally, we can find an approximate solution for the average $\bar{\delta}'$, the representation of which is the same as (A.16) except for the substitutions $\delta'|_{y=0}$, $\eta'|_{y=0}$, $v_A^2 b_y \bar{\delta}'$, $\bar{\eta}'$, $\bar{v}_A^2$, where

$$\bar{\delta}' = \int_0^{y_2} \delta'\,\mathrm{d}y/y_2\,, \qquad \bar{\eta}' = \int_0^{y_2} \eta'\,\mathrm{d}y/y_2\,, \qquad \bar{v}_A^2 = V_A^2 \int_0^{y_2} e^{-2ay}\,\mathrm{d}y/y_2\,.$$

From (A.16) it can be seen that δ' will grow exponentially, and that the shearing velocity c_1 acts like a 'seed'. If there is no 'seed', the mushroom flow velocities (v_x, v_y) will never arise. The growth rate is independent of c_1 but depends on the Alfvén speed $v_A = B_0/\sqrt{4\pi\rho_0}$. Therefore, shear motion can induce linear MHD-instability. However, this instability soon attains saturation, and the flow becomes quasi-steady and increases gradually until the velocities (v_x, v_y) exceed v_A.

References

Biskamp, D. and Welter, H.: 1989, *Solar Phys.* **120**, 49.
Bruzek, A.: 1967, *Solar Phys.* **2**, 451.
Bruzek, A.: 1968, in K. O. Kiepenheuer (ed.), 'Structure and Development of Solar Active Region', *IAU Symp.* **35**, 293.
Bruzek, A.: 1969, *Solar Phys.* **8**, 29.
Bumba, V. and Howard, R.: 1965, *Astrophys. J.* **141**, 1492.
Courant, R. and Hilbert, D.: 1962, *Methods of Mathematical Physics*, Interscience Publ., New York.
Gold, T. and Hoyle, F.: 1960, *Monthly Notices Roy. Astron. Soc.* **120**, 89.
Hagyard, M. J.: 1991, *Mem. Soc. Astron. Ital.* (in press).
Harrison, R.: 1986, *Astron. Astrophys.* **162**, 283.
Harvey, J. W. and Harvey, K. L.: 1976, *Solar Phys.* **47**, 233.
Hu, Y. Q. and Wu, S. T.: 1984, *J. Comp. Phys.* **55**, 33.
Klimchuk, J. A. and Sturrock, P. A.: 1989, *Astrophys. J.* **345**, 1034.
Klimchuk, J. A., Sturrock, P. A., and Yang, W.-H.: 1988, *Astrophys. J.* **335**, 456.
Krall, K. R. *et al.*: 1982, *Solar Phys.* **79**, 59.
Low, B. C.: 1977, *Astrophys. J.* **212**, 234.
Low, B. C.: 1981, *Astrophys. J.* **251**, 352.
Low, B. C. and Nakagawa, Y.: 1975, *Astrophys. J.* **199**, 237.
Martres, M. J. *et al.*: 1966, *Ann. Rev. Astron. Astrophys.* **29**, 245.
Mikic, D. Z., Barnes, D. C., and Schnack, D. D.: 1988, *Astrophys. J.* **328**, 830.
Nakagawa, Y., Hu, Y. Q., and Wu, S. T.: 1987, *Astron. Astrophys.* **179**, 354.
Švestka, Z.: 1976, *Solar Flares*, D. Reidel Publ. Co., Dordrecht, Holland.
Tanaka, K. and Nakagawa, Y.: 1973, *Solar Phys.* **33**, 187.
Wu, S. T. and Wang, J. F.: 1987, *Comp. Methods Applied Mech. Eng.* **64**, 267.
Wu, S. T., Hu, Y. Q., and Nakagawa, Y.: 1983, *Astrophys. J.* **266**, 866.
Wu, S. T., Hu, Y. Q., and Krall, K. R.: 1984, *Solar Phys.* **90**, 117.
Wu, S. T., Hu, Y. Q., Nakagawa, Y., and Tandberg-Hanssen, E.: 1986, *Astrophys. J.* **306**, 751.
Wu, S. T., Wang, S., Wang, A. H., and Dryer, M.: 1988, *Adv. Space Sci.* **8**(11), 221.

PREV. ACC.
91A29530

NUMERICAL SIMULATION OF EXTENDED CORONA

S. T. Wu and Ai-Hwa Wang

Center for Space Plasma and Aeronomic Research and Department of Mechanical Engineering, The University of Alabama in Huntsville, Huntsville, AL 35899, U.S.A.

ABSTRACT

A three-dimensional, time-dependent magnetohydrodynamic (MHD) model is presented for the study of coronal dynamics. The model, written in spherical coordinates, extends from the solar surface ($1R_s$, where $1R_s = 6.95 \times 10^5$ km) to 15 R_s. This model was developed with two major issues in mind, namely for interpretation of various steady state and evolutionary dynamical structures in the corona. In order to achieve these objectives we have employed two different numerical techniques to seek solutions for these two different, but related, problems; steady state structures and evolutionary structures. These two numerical techniques are: (i) relaxation technique for steady state structures; and (ii) FICE (Full-Implicit-Continuous-Eulerian) technique for evolutionary structures.

To illustrate this model, we present numerical results for examples of both the steady state and evolutionary structure of the corona. These results show the additional physical features which cannot be shown by a two-dimensional model. Finally, on the basis of the exploratory calculation, we outline some interesting physical features which can be considered for the observing programs of future space missions such as SOHO, OSL, CORONAS, etc.

I. INTRODUCTION

Since the Skylab-ATM experiments in the seventies, we have recognized that the corona is in a transient state in contrast to the previous understanding whereby the corona is always in a quiet orderly state (Billings, 1966). It is also further realized that the relationship between the flare and the coronal mass ejection is not as consistently intimate as originally thought (Hildner et al. 1976). In order to understand the physics of this fascinating phenomena of so-called "coronal transients", a number of theoretical models has been presented in the literature (Hundhausen et al. 1984). All of these theoretical models are based on magnetohydrodynamic theory. The methodology used to treat these theoretical models could be classified into two categories: (i) analytical methods and (ii) numerical methods. Those models treated by analytical methods have to conform to certain strict conditions in which a full description of nonlinear dynamical behavior is difficult to achieve; nevertheless, the solutions are exact. On the other hand, the models treated by numerical methods could obtain global descriptions of nonlinear dynamics, but these descriptions are not unambiguous and may mislead the physical interpretations. A further limitation to these two categories is the fact that all of these models are confined to a two-dimensional geometry. Thus, it is inevitable that some arguments in the interpretation of observations have taken place.

In this paper. we present a newly developed *three-dimensional*, time-dependent, magnetohydrodynamic model for an extended corona. We will suggest that this model could be used to understand the physical processes from the comparison of this model's results with observational data. The theoretical description of the model presents the basis for the addition of dissipative mathematical terms that could be used to understand additional physical processes from specific observational data. The theoretical description of the model are included in Section II. The numerical results are presented in Section III. Finally, the concluding remarks are included in Section IV.

II. ANALYSES

Mathematical Model

In this study, we have assumed that the solar atmosphere behaves as a single fluid with negligible dissipative effects. With these assumptions, the time-dependent magnetohydrodynamic (MHD) equations that describe

PRECEDING PAGE BLANK NOT FILMED

atmospheric flows in three-dimensions for a spherical coordinate system can be written as follows:

$$\frac{\partial \rho}{\partial t} = -\frac{1}{r^2}\frac{\partial(r^2 \rho v_r)}{\partial r} - \frac{1}{r\sin\theta}\frac{\partial(\rho v_\theta \sin\theta)}{\partial \theta} - \frac{1}{r\sin\theta}\frac{\partial(\rho v_\phi)}{\partial \phi} \tag{1}$$

$$\frac{\partial v_r}{\partial t} = -v_r\frac{\partial v_r}{\partial r} - \frac{v_\theta}{r}\frac{\partial v_r}{\partial \theta} - \frac{v_\phi}{r\sin\theta}\frac{\partial v_r}{\partial \phi} - \frac{1}{\rho}[\frac{\partial(\rho RT)}{\partial r} + B_\theta(\frac{\partial B_\theta}{\partial r} - \frac{1}{r}\frac{\partial B_r}{\partial \theta}) - B_\phi(\frac{1}{r\sin\theta}\frac{\partial B_r}{\partial \phi} - \frac{\partial B_\phi}{\partial r})] + \frac{{v_\phi}^2 + {v_\theta}^2}{r} - \frac{{B_\phi}^2 + {B_\theta}^2}{\rho r} - \frac{GM}{r^2} \tag{2}$$

$$\frac{\partial v_\theta}{\partial t} = -v_r\frac{\partial v_\theta}{\partial r} - \frac{v_\theta}{r}\frac{\partial v_\theta}{\partial \theta} - \frac{v_\phi}{r\sin\theta}\frac{\partial v_\theta}{\partial \phi} - \frac{1}{\rho}[\frac{\partial(\rho RT)}{r\partial \theta} - B_r(\frac{\partial B_\theta}{\partial r} - \frac{1}{r}\frac{\partial B_r}{\partial \theta}) - B_\phi(\frac{1}{r\sin\theta}\frac{\partial B_\theta}{\partial \phi} - \frac{\partial B_\phi}{r\partial \theta})] - \frac{v_r v_\theta - {v_\phi}^2\cot\theta}{r} - \frac{B_r B_\theta - {B_\phi}^2\cot\theta}{\rho r} \tag{3}$$

$$\frac{\partial v_\phi}{\partial t} = -v_r\frac{\partial v_\phi}{\partial r} - \frac{v_\theta}{r}\frac{\partial v_\phi}{\partial \theta} - \frac{v_\phi}{r\sin\theta}\frac{\partial v_\phi}{\partial \phi} + \frac{B_r}{\rho}\frac{\partial B_\phi}{\partial r} - \frac{B_\theta}{r}\frac{\partial B_\phi}{\partial \theta} - \frac{1}{r\rho\sin\theta}(\frac{\partial(\rho RT)}{\partial \phi} + B_r\frac{\partial B_r}{\partial \phi} + B_\theta\frac{\partial B_\theta}{\partial \phi}) + \frac{B_\phi}{\rho r}(B_r + B_\theta\cot\theta) - \frac{v_\phi}{r}(v_r + v_\theta\cot\theta) \tag{4}$$

$$\frac{\partial B_r}{\partial t} = \frac{1}{r\sin\theta}[\frac{\partial}{\partial \theta}(\sin\theta(v_r B_\theta - v_\theta B_r) - \frac{\partial}{\partial \phi}(v_\phi B_r - v_r B\phi)] \tag{5}$$

$$\frac{\partial B_\theta}{\partial t} = \frac{1}{r\sin\theta}\frac{\partial}{\partial \phi}(v_\theta B_\phi - v_\phi B_\theta) - \frac{1}{r}\frac{\partial}{\partial r}[r(v_r B_\theta - v_\theta B_r)] \tag{6}$$

$$\frac{\partial B_\phi}{\partial t} = \frac{1}{r}\frac{\partial}{\partial r}[r(v_\phi B_r - v_r B_\phi)] - \frac{1}{r}\frac{\partial}{\partial \theta}(v_\theta B_\phi - v_\phi B_\theta) \tag{7}$$

$$\frac{\partial T}{\partial t} = -(\gamma - 1)T[\frac{1}{r^2}\frac{\partial(r^2 v_r)}{\partial r} + \frac{1}{r\sin\theta}\frac{\partial(v_\theta\sin\theta)}{\partial \theta} + \frac{1}{r\sin\theta}\frac{\partial v_\phi}{\partial \phi}] - v_r\frac{\partial T}{\partial r} - \frac{v_\theta}{r}\frac{\partial T}{\partial \theta} - \frac{v_\phi}{r\sin\theta}\frac{\partial T}{\partial \phi} \tag{8}$$

where the dependent variables are the density ρ, temperature T, velocity (v_r, v_θ, v_ϕ), and magnetic field (B_r, B_θ, B_ϕ). The independent variables are the radius r, the meridional angle θ and azimuthal angle ϕ as well at time "t". The constants are the polytropic index γ, solar total mass M and gravitational constant G. In addition, the standard equation of state ($p = \rho RT$) was used to obtain the above set of governing equations.

The region, within which we will present the numerical solution to the above set of governing equations, is shown in Figure 1. This region is bounded by the solar surface and 15 solar radii (R_s) in radial distance, by the equator and the pole in meridional distance (θ-coordinate), and by azimuthal extent (ϕ-coordinate) of 45°.

Method of Solution

The equations are solved numerically using a modified FICE (Full-Implicit-Continuous-Eulerian) scheme which is based on the original FICE scheme developed by Hu and Wu (1984); and Wu and Wang (1987). The grid spacings used are $\delta r_i = R_s(1 + \delta\theta)^{i-1}$, and $\delta\theta = \delta\phi = 4.5°$. It should be noted that the radial spacing is not uniform and is chosen so as to; (1) assure the initial state as being in isothermal and hydrostatic equilibrium (Wang et al. 1982); (2) initialization of the computation procedure; and (3) to ensure numerical accuracy. The time step can be arbitrarily chosen because of the flexibility of the FICE scheme.

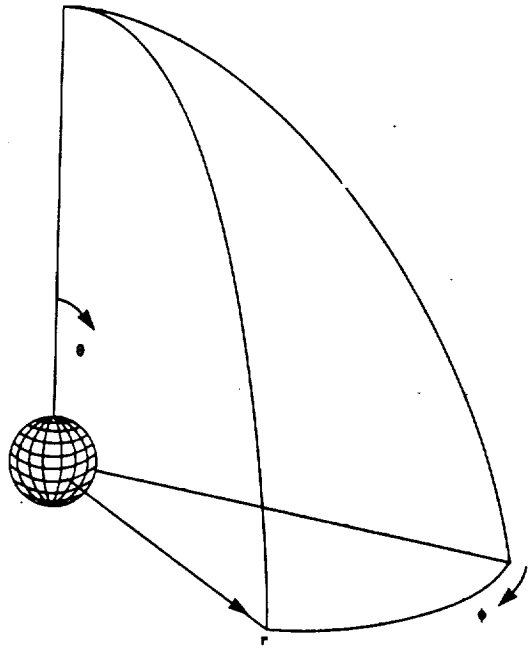

Fig. 1. A schematic description of the portion of a three- dimensional configuration in which the solution is calculated. Note that the computational domain extends from the pole to the equator within a 45° extent of heliolongitude. In the present paper, symmetry is assumed below the solar equatorial plane.

Initial State and Boundary Conditions

In order to seek a solution of this problem, we need to specify the initial conditions. These initial conditions include the magnetic field configuration, velocity field and corresponding thermodynamic properties of the plasma.

The boundary conditions are rather complicated, hence a detailed account of the derivation of the boundary conditions will be presented later (Wang and Wu, 1990). We shall only briefly describe these boundary conditions here. There are a total of six sides in which the boundary conditions need to be specified; they are:

(1) $r = R_s$, eight compatibility conditions are obtained from the set of governing equations (Wu and Wang, 1987);
(2) $r = 15R_s$, non-reflecting boundary conditions are used (Hu and Wu, 1984);
(3) $\theta = 0$ (pole) and $\theta = 90°$ (equator), symmetric conditions are chosen because of the chosen field configuration;
(4) $\phi = 0$ and $\phi = 45°$, the boundary conditions are obtained by extrapolation techniques.

III. NUMERICAL RESULTS

In order to carry out this simulation, we first introduced an initial state at isothermal and hydrostatic equilibrium with $\gamma = 1.67$ together with a potential field in one case and, in a separate case, a linear force-free magnetic field topology. These two separate cases were introduced into the set of governing equations in order to ensure that the isothermal and hydrostatic equilibrium does exist. We then introduced a steady-state, Parker-type, velocity field. The numerical solution of this mathematical system led to a magnetohydrodynamic equilibrium state via the relaxation technique. This MHD equilibrium state is then taken as the simulated undisturbed coronal (i.e., quiet corona) with an outflowing solar wind around multiple helmet magnetic topologies.

The initial plasma and fields (magnetic and velocity) parameters incorporated in this simulation are the following representative conditions of a non-rotating sun with an initial plasma $\beta_\circ (= 16\pi n_\circ k_\circ T_\circ / B_\circ^2)$ being unity, at r = R_s, $\theta = 90°$ and $\phi = 22.5°$.

- Isothermal and hydrostatic equilibrium atmosphere.
  $T_0 = 10^6$ K
  $\rho_0 = \rho_0^0 \exp((\frac{1}{R_{(1)}} - 1)\frac{R_s g_0}{RT_0})$

where ρ_0^0 is the density (the value of 1.67×10^{-16} gm cm^{-3} is used in this study and g_0 is the gravity on the solar surface.

- Magnetic field configuration
  (i) A hexapole potential field (Jackson, 1962); and, in a separate calculation,
  (ii) A hexapole linear force-free field (Nakagawa et al ., 1978)

- Velocity Field
  $v_r(1, \theta, \phi) = 15$ km s^{-1},
  $v_r(15, \theta, \phi) = 200$ km s^{-1},
  $v_\theta(r, \theta, \phi) = v_\phi(r, \theta, \phi) = 0.$

Figure 2 shows the simulated morphology of the quiet corona which consists of a three-dimensional representation of the brightness (integrated density along the path of the line-of-sight), steady state solar wind velocity vectors and magnetic field for two cases: (a) initially potential field topology; and (b) initially linear force-free field topology, respectively. It is easy to recognize that the shape of the quiet corona depends on the initial magnetic field topology. The bright corona is related to the closed magnetic field configuration, and the dark region corresponds to the open field configuration which corresponds to the out- flowing solar wind from the coronal hole. Also it shows that the solar wind velocity is almost radial.

In order to examine the physical structure of the quiet, steady-state, corona, we plot the radial distribution of the density and temperature at the pole and equator for the initially potential and linear force- free magnetic field topologies, respectively, as shown in Figure 3. The radial distribution of the three velocity components (i.e., v_r, v_θ, v_ϕ) at the pole and equator is shown in Figure 4 for both types of magnetic field topology. Finally, we plot the radial distribution of Alfven and sonic speed at the pole and equator in Figure 5.

Comparison of each of these parameters demonstrates the well-known inference and important fact that the magnetic field is the dominant factor that determines both the morphology and physical structure of the corona. The spatial diversity of these important, fundamental steady-state parameters is obvious.

For the completeness of this presentation, we shall show some results for a disturbed corona in Figure 6. This numerical result is obtained by introducing a pressure pulse ($p/p_o = 10$) distributed over three grid points centered at $\theta = 35°$, $\phi = 22.5°$ and $r = R_s$ for the case of the initially linear force-free magnetic field topology of the quiet corona as shown in Figure 2b. In Figure 6, at $t = 600$ s, we show simulated brightness (i.e. line-of-sight integrated density enhancement), disturbed magnetic field and solar wind velocity vectors in the $\phi = 22°$ plane. According to the results shown, we may interpret that the brightness was caused by the flow interaction with the magnetic field. This density enhancement consists of both the mass carried by plasma flow motion and local wave compression.

IV. CONCLUDING REMARKS

In this study, we have presented a newly-developed, three-dimensional, time-dependent magnetohydrodynamic model for the study of corona structures in both quiet and disturbed states. This model extends from the solar surface to 15 R_s and, thereby, includes the region of outflowing solar wind from the subsonic, sub-Alfvenic to super-sonic and super-Alfvenic regions. Therefore, we assert that it is, indeed, a model which could be used to study coronal/interplanetary coupling problems.

In these preliminary results, we clearly recognize that the magnetic field topology and strength controls both the structures and physical parameters' morphology of the corona. Also, this model has the capability to convert the fundamental physical parameters (i.e. ρ, T, v) to observables such as brightness (see Fig. 2) and doppler shifts (not shown). Therefore, we may claim that this model has the potential whereby it could be used as a diagnostic tool that can be applied to the interpretation and guidance of the observations. For example, we may use the physical properties obtained from this model to compute line profiles. As a final

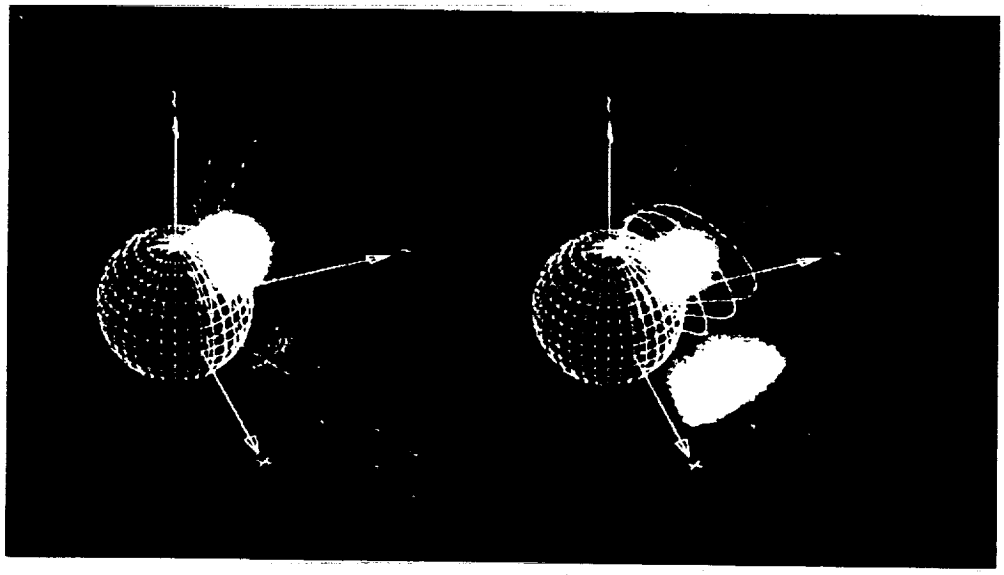

Fig. 2. The three-dimensional simulated brightness, steady state solar wind velocity vectors and magnetic field of the confined plasma corona for; (a) initially potential field configuration (upper left panel) and (b) initially linear force-free field configuration (upper right panel).

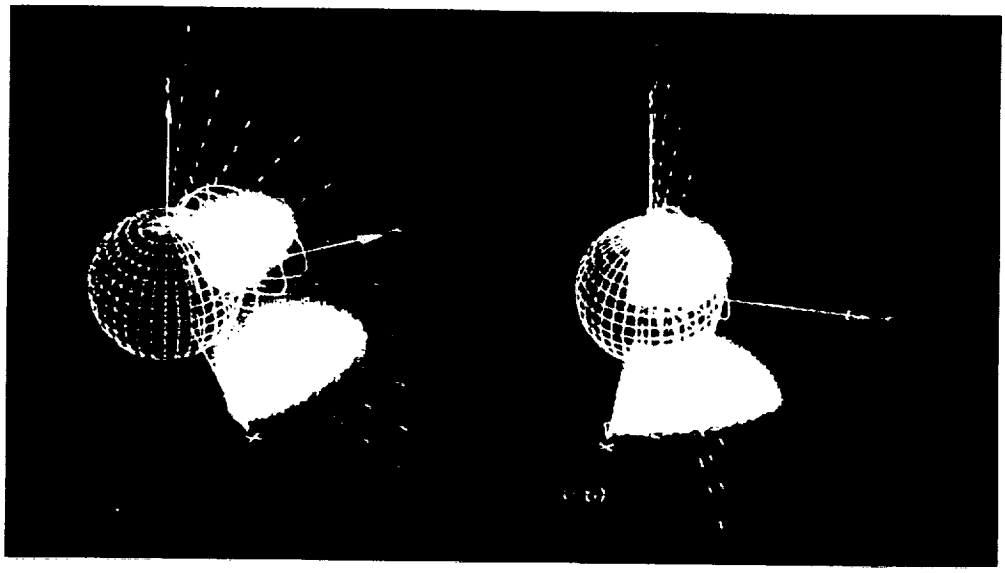

Fig. 6. The three-dimensional simulated brightness, magnetic field and solar wind velocity of a disturbed corona at 600 s after introduction of a pressure pulse (simulated flare) at solar surface of the quiet corona given in Figure 2b, (a) Viewed from $\theta = 50°, \phi = -20°$, and (b). viewed from $\theta = 50°, \phi = 10°$.

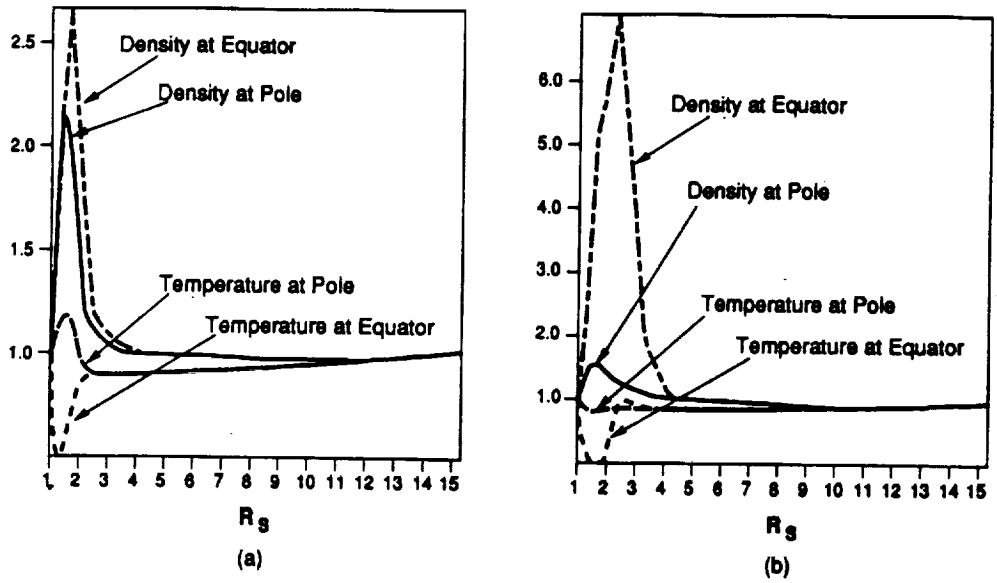

Fig. 3. Radial distribution of the density $(\rho/\rho_o)$and temperature (T/T_o) at the pole and the equator, respectively for; (a) initially potential field configuration and (b) initially linear force-free field configuration with ρ_o and T_o given in page 6 of the text.

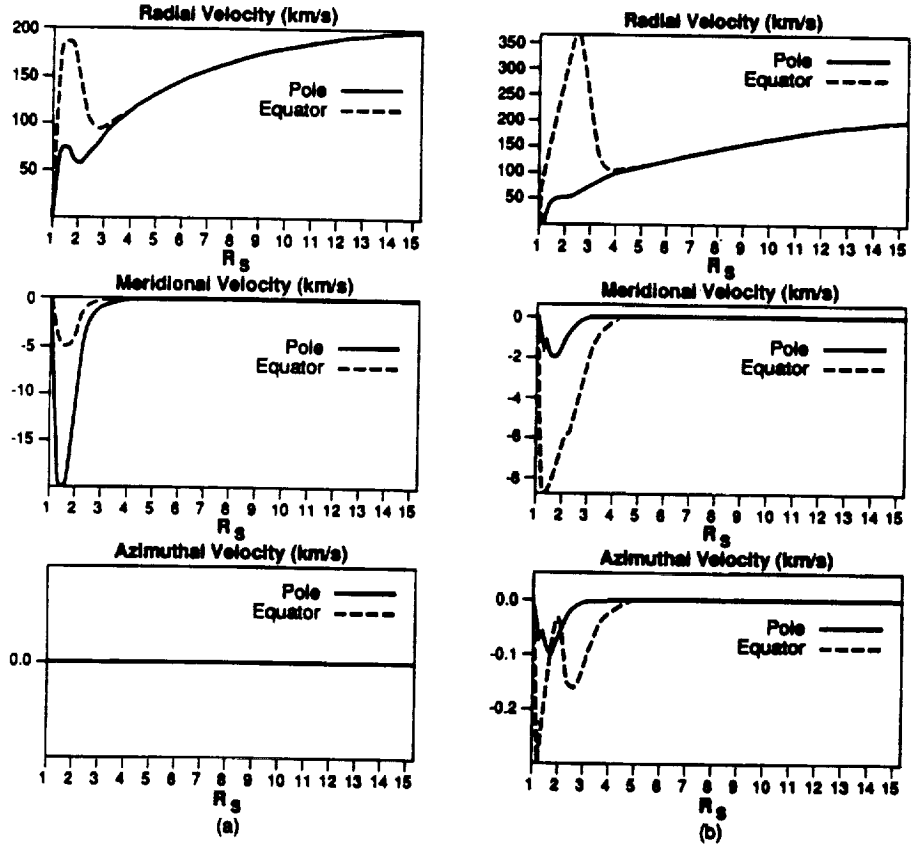

Fig. 4. Radial distribution of the three velocity components (v_r, v_θ, v_ϕ) at the pole and equator for; (a) initially potential field configuration and (b) initially linear force-free field configuration.

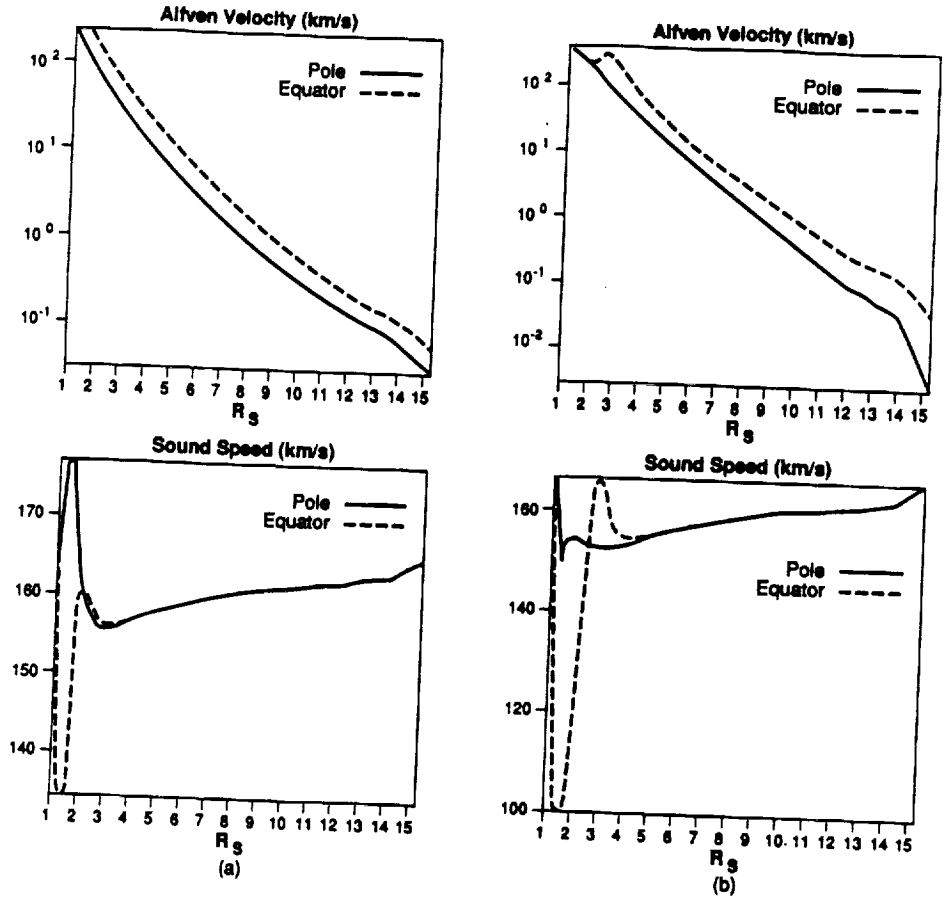

Fig. 5. Alfvenic speed and sonic speed as function of radial distance at pole and equator for (a) initially potential field configuration and (b) intially linear force-free field configuration.

remark, we recognize that the development of this model is far from complete.. The improvements can be tackled in two major catagories as follows:

- Mathematical Improvement

  We should establish the accuracy of the numerical results. In order to achieve this purpose, we should conduct a grid size test for this model.

- Physical Improvement

  Presently, the model includes dissipative mechanisms that were not invoked for the present demonstration of its three-dimensional, temporal capability. Namely, the present model results are based on "ideal" MHD theory. We realize that dissipative MHD is important to many solar physics problems in which finite electrical conductivity, thermal conductivity, radiation and turbulence are undoubtedly present. We plan to incorporate these effects in our model via a conservative and rational step-by-step approach. However, the current ideal MHD model, because of its inherent and natural three-dimensional resemblance to the real world, is essential for the construction of solutions which resemble observed realistic topologies. We have obtained in the present demonstration, for example, induced meridional and aximuthal flows which existing two-dimensional models cannot provide.

ACKNOWLEDGEMENT

We are indebted to Dr. Murray Dryer for reading this manuscript and making invaluable suggestions and M. T. Sun for preparing the three-dimensional color graphics. This work is supported by AFOSR-88-0013, NAGW-9 and NOAA (50RANR000104).

REFERENCES

Billings, D. E., 1966, *A Guide to the Solar Corona*, Academic Press, New York

Jackson, John David, 1962, *Classical Electrodynamics*, John Wiley and Sons, Inc., New York,-London-Sydney

Hildner, E., Gosling, J. T., MacQueen, R. M., Munro, R. H., Poland, A. I. and Ross, C. L., 1976, *Solar Physics*, **48**, 127.

Hu, Y. Q. and Wu. S. T., 1984, *J. Comp. Phys*, **55**, 33.

Hundhausen, A. J., Burlaga, L. F., Feldman, W. C., Gosling, J. T., Hildner, E., House, L. L., Howard, R. A., Krieger, A. S., Kundu, M. R., Low, B. C., Sheeley, N. R., Jr., Steinolfson, R. S., Stewart, R. T., Stone, R. G. and Wu, S. T., 1984, *Solar Terrestrial Physics: Present and Future*, (Butler, D. M. and Papadopoulos, K., eds) **NASA Reference Publication 1120**, Chapter 6.

Nakagawa, Y., Wu, S. T., and Tandberg-Hanssen, E., 1978, *Astron. Astrophys.* **69**, 43.

Wang, A. H., and Wu, S. T., 1990, *J. Comp. Phys.* (to be submitted).

Wang, S., Hu, Y. Q. and Wu, S. T., 1982, *Scientia Sinica (Series A)* , **XXV**, 1305.

Wu, S. T., and Wang, J. F., 1987, *Comp. Meth. in Applied Mechanics and Engineering*, **64**, 267.

SOLAR WIND SEVEN

Proceedings of the 3rd COSPAR Colloquium held in Goslar, Germany, 16–20 September 1991

Edited by

E. MARSCH

and

R. SCHWENN

Max-Planck-Institut für Aeronomie, Postfach 20, D-W3411 Katlenburg-Lindau, Germany

PERGAMON PRESS

OXFORD · NEW YORK · SEOUL · TOKYO

PREV. ANN
93A33618

A TWO-DIMENSIONAL MHD GLOBAL CORONAL MODEL: STEADY-STATE STREAMERS

A. -H. Wang,* S. T. Wu,* S. T.Suess** and G. Poletto***

* *Center for Space Plasma and Aeronomic Research and Department of Mechanical Engineering,The University of Alabama in Huntsville, Huntsville, AL 35899, U.S.A.*
** *NASA Marshall Space Flight Center, Space Science Lab/ES52, Huntsville, AL 35812, U.S.A.*
*** *Osservatorio di Arcetri, Firenze, Italy*

ABSTRACT

A two-dimensional, time-dependent, numerical, MHD model for the simulation of coronal streamers from the solar surface ($r = 1R_\odot$) to $15R_\odot$ is presented. Three examples are given; for dipole, quadrupole and hexapole (Legendre polynomials P_1, P_2, and P_3) initial field topologies. The computed properties are density, temperature, velocity, and magnetic field. The calculation is set up as an initial-boundary value problem wherein a relaxation in time produces the steady state solution. In addition to the properties of the solutions, their accuracy is discussed. Besides solutions for dipole, quadrupole, and hexapole geometries, the model permits use of realistic values for the density and Alfvén speed while still meeting the requirement that the flow speed be super-Alfvénic at the outer boundary by extending the outer boundary to $15R_\odot$.

1. INTRODUCTION

We present results from a recently-developed numerical model of coronal structure. The reasons for a new model are to extend the outer boundary farther from the Sun and to gain the experience necessary for development of a three-dimensional model. In addition, an immediate application will be to the simulation of streamers in support of the Ultraviolet Coronagraph and Spectroheliograph (UVCS) and the Large Angle Spectrometric Coronagraph (LASCO) on the Solar Heliospheric Observatory (SoHO). These instruments will be able to measure the temperature, density, and flow vector in the corona so, with model calculations, it will be possible to estimate the magnetic field vector.

2. THE PHYSICAL AND NUMERICAL MODEL

We assume axisymmetric, single fluid, polytropic, time-dependent ideal magnetohydrodynamic flow and calculate the flow in a meridional plane defined by the axis of the magnetic field. The coordinates are (r, θ, ϕ) with ϕ being the ignorable coordinate. For the magnetic field boundary condition, we take the variation of the radial component at the lower boundary to be given by Legendre polynomials, so that the flow has reflective symmetry across the equator and the calculation need be done in only one quadrant. For P_1, the radial field thus has a dipole variation. The equations describing such flow can be found in many places (e.g. /3/).

The equations are solved in a computational domain extending from the Sun ($1R_\odot$) to $15R_\odot$, from the pole to the equator. It is assumed that meridional flow is zero at the pole and equator. The grid is divided so that there are 37 gridpoints in the radial direction and 22 gridpoints in the meridional direction, with the radial grid size slowly increasing with radius. The algorithm adopted here is the Full-Implicit Continuous Eulerian (FICE) scheme described by Hu and Wu /1/; for time stepping a second-order accurate forward differencing scheme is used and the step size is of the same order as given by the Courant condition. Smoothing is inserted when gradients become too large - i.e. at shocks (which do not occur here). At the inner boundary, the flow is subsonic and sub-Alfvénic so that some variables are calculated using compatibility relations /1/. We choose to specify the radial magnetic field, pressure (or temperature), and density. The meridional field, radial and meridional flow speed, and pressure are computed from the compatibility relations. At the outer boundary, the flow is restricted to being both supersonic and super-Alfvénic. In this case, all variables at the boundary can be calculated by simple linear extrapolation from the first (or first two) grid points inside the boundary.

We start with an essentially arbitrary initial state and allow the flow to relax in time while holding the

PRECEDING PAGE BLANK NOT FILMED

boundary values constant. In the present case the initial flow field is a polytropic, hydrodynamic solution to the steady state radial flow equation of motion (e.g. /2/) superimposed on a potential magnetic field. That this is neither a self-consistent nor stable solution to the steady state MHD equations is irrelevant since the flow is allowed to evolve in time under the control of the equations of motion. The main concerns are that the numerical solution be stable and of sufficient accuracy to define the physically interesting aspects of the solution, and that the relaxation proceed long enough that an acceptably close approximation to the steady state has been reached. We address these issues briefly in section 4.

3. THE CALCULATIONS

As stated, we present results from three simulations; for a dipole ($B_r(R_\odot) \propto P_1(\cos\theta)$), a quadrupole ($B_r(R_\odot) \propto P_2(\cos\theta)$), and a hexapole ($B_r(R_\odot) \propto P_3(\cos\theta)$). At the lower boundary, the conditions are that $n = 2.25 \times 10^8 cm^{-3}$ and $T = 1.80 \times 10^6 K$. The polytropic index is chosen to be $\gamma = 1.05$. The magnetic field strength at the equator ($B_r(\theta = 90°)$) is 1.67 gauss so that $\beta = 0.5$ in all three cases (where β is the ratio of the internal pressure to the magnetic pressure at the lower boundary, at the equator). The final steady state magnetic field geometry for the three cases is shown in Fig. 1.

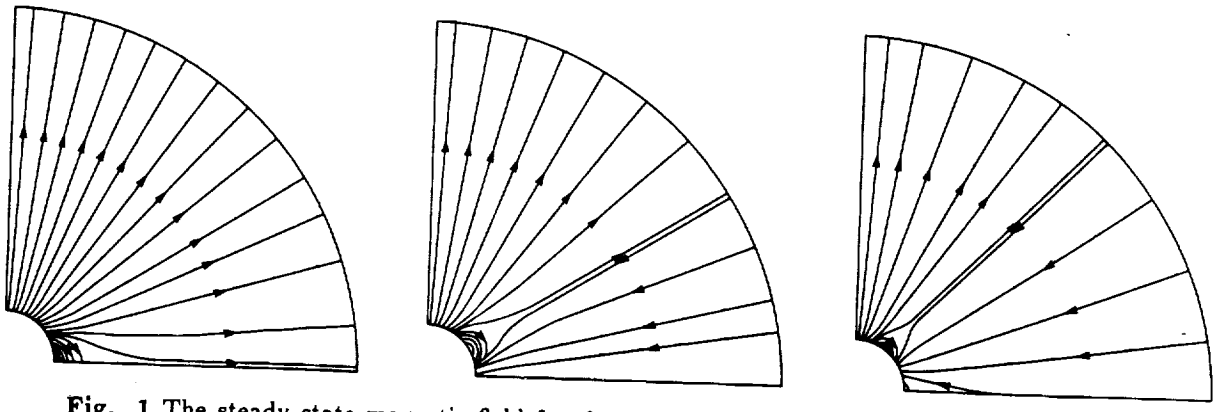

Fig. 1 The steady state magnetic field for the three cases. The left panel is for an initial dipole ($P_1(\cos\theta)$), the middle panel for an initial quadrupole ($P_2(\cos\theta)$), and the right panel for an initial hexapole ($P_3(\cos\theta)$). In all cases, $\beta = 0.5$ at the base, at the equator, in the initial state. At the same location, the total magnetic field strength is 1.67 Gauss in all three examples. The times allowed for the relaxation are: dipole - 22.22 hours, quadrupole - 16.67 hours, hexapole - 18.06 hours.

This figure shows the well-known property that the flow is essentially radial beyond $3-4R_\odot$. Having begun with large closed field volumes, only small magnetically closed volumes remain, underlying the coronal streamers. Flow is field aligned everywhere. Fieldlines which cross the outer boundary reach to ∞. The fieldlines are seen to diverge most rapidly on the edges of the close field regions and apparently most slowly near the center of open regions.

The radial velocity is shown in Fig. 2, at the pole and equator for the dipole; at the pole and centered over the mid-latitude streamer for the quadrupole; and at pole, over the mid-latitude streamer, and over the equatorial streamer for the hexapole. As is generally the case in this type of model, the flow speed in the center of the open regions is similar to the undisturbed initial flow speed - because the flow direction is approximately radial above a few solar radii. In the streamer, the flow speed is essentially zero on closed magnetic field lines and is greatly reduced on the open lines - the field has undergone rapid overexpansion on the flanks of the streamer. The density and temperature for the three examples are shown in Fig. 1, in the directions specified in Fig. 2. Most obviously, the density is enhanced in the closed field regions. There is, of course, also some depletion along rapidly diverging fieldlines.

Several physical aspects of such models as these need to be emphasized. First, the temperature that has been calculated is an "effective temperature." This is because a polytropic energy equation is assumed - with a polytropic index of 1.05, which is equivalent to a large amount of energy being added to the flow. Nowhere is the form of this energy specified, nor what the conversion and dissipation mechanisms are. However, it has been shown that a polytropic index on the order 1.05 is required to reproduce observations of coronal densities /5/.

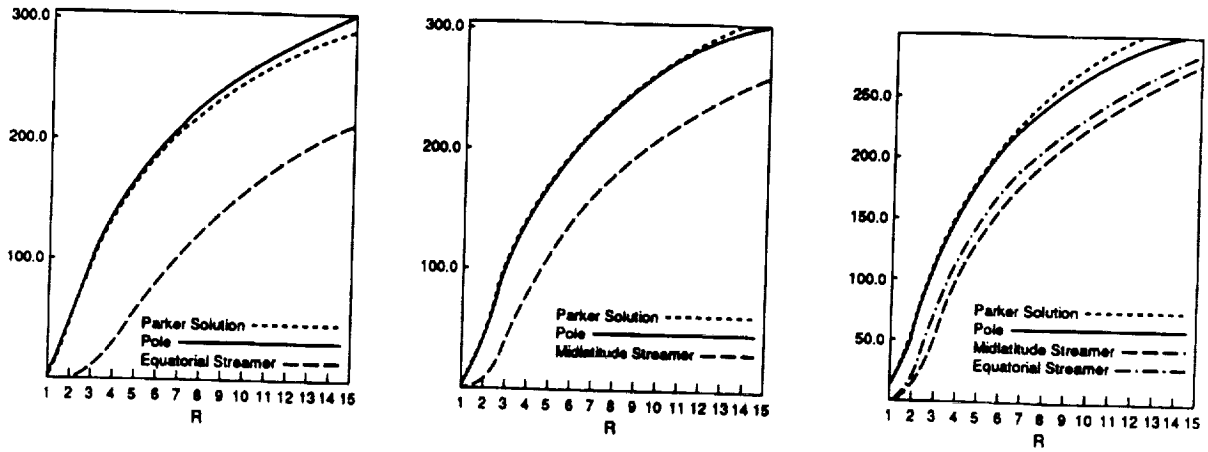

Fig. 2 The radial velocity for the three cases shown in Fig. 1. Left: Dipole field, showing the radial flow speed along a polar radius and an equatorial radius. Middle: Quadrupole field, showing the speed along a radius over the pole and over the mid-latitude streamer. Right: Hexapole field, showing the speed along a radius over the pole, over the mid-latitude streamer, and at the equator.

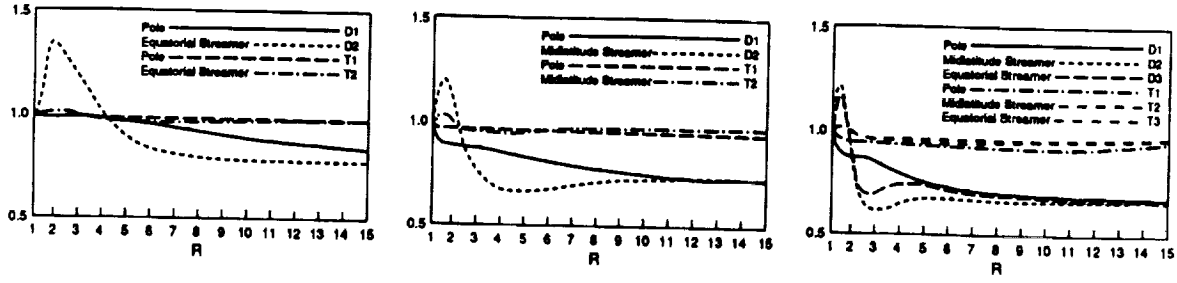

Fig. 3 The density and temperature for the three examples shown in Fig. 1. Left: Dipole field, showing the density and temperature, scaled to their starting values, along a polar radius and an equatorial radius. Middle: Quadrupole field, showing the temperature and density along a radius over the pole and over the mid-latitude streamer. Right: Hexapole field, showing the temperature and density along a radius over the pole, the mid-latitude streamer, and at the equator.

Second, the magnetically open regions, although equivalent to coronal hole flows, do not simulate coronal holes because the flow speeds are far too small. To obtain reasonable flow speeds in this model it would be necessary to have the temperature vary across the base of the open region - which is well within the capability of the model. Such a variation has been shown to reproduce all the known properties of coronal hole flow and lead to accurate simulations of the geometry, with the effective temperature being larger in the center of the hole than at the edge /5/.

In contrast to the open regions, the densities in the closed regions are similar to observed streamer densities and we feel this model is therefore a good approximation to streamer geometry. The temperature must still be qualified as an effective temperature, but can be used for diagnostic purposes in combination with planned observations on SoHO/UVCS.

4. ACCURACY AND STABILITY OF CALCULATIONS

This model has been found to be weakly subject to the Courant condition on size of time step. Therefore, the size of the time step decreases as the largest values of the temperature and magnetic field increase - along with the maximum sound and Alfvén speeds anywhere in the grid. Counteracting this, the higher characteristic speeds lead to a somewhat faster relaxation time. However, generally more time steps are required for smaller β calculations. The flow speed also plays an important role in determining the relaxation time to a steady state - the initial state is a disequilibrium configuration. This imbalance must have time to be advected from the base through the outer boundary. The physical time this takes can be estimated by taking a typical (but small) value for the flow speed and calculating how long it would take the plasma to flow at this speed from the base to the outer boundary. For example, at 150 km/s, to $15R_\odot$, this takes 18 hours (relaxation times we have used are given in Fig. 1).

A second consideration is gridpoint resolution. The grid used in these examples is about 4.5^o in latitude and $0.24R_\odot$ in radius near the base - increasing slowly with radius. This is sufficient to adequately resolve the geometry and flow on the scale shown in Fig. 1. However, if finer scale information is required in, for example, the core of the streamers, a denser grid would be required.

Always a serious consideration in these time-dependent, non-cartesian MHD calculations is the conservation of magnetic flux - that $\nabla \cdot \vec{B} = 0$ is maintained at all times. The condition is maintained here through accurate differencing rather than a self-correcting scheme, but we are able to conserve magnetic flux divergence to within one part in 10^5. The numerical scheme is pressure-based so it is limited by stability to large and moderate β values (e.g. $\beta \geq 0.1$) - which turns out to be the same restriction for maintaining $\nabla \cdot \vec{B} = 0$ to the required degree.

Finally, the energy equation:

$$\left(\frac{\partial}{\partial t} + \vec{v} \cdot \nabla\right)\left(\frac{p}{\rho^\gamma}\right) = 0$$

reduces to $\vec{v} \cdot \nabla(p/\rho^\gamma) = 0$ when a steady state is reached, which means that (p/ρ^γ) is then a streamline constant. This becomes an analytic test of the achievement of a steady state solution in our case. The boundary values of p and ρ are the same at all latitudes. Therefore, (p/ρ^γ) has the same value everywhere in the computation regime as it has on the boundary if a steady state has been reached. We have checked this for the three cases shown in Fig. 1 and find that for the dipole and quadrupole it is constant to within a maximum of 1% and for the hexapole it is constant to within a maximum of 4% (average values over the whole grid are less than 1% in all cases).

5. NEW RESULTS

The utility of this model is that the outer boundary has been extended to $15R_\odot$. Although this is not a big advance conceptually, this and the stability and ruggedness of the code make it useful for simulating realistic coronal conditions. We present results for quadrupole and hexapole fields, with their accompanying midlatitude streamers and open magnetic field regions. The Alfvén speed ranges between 800 km/s and a few tens of km/s. This is lower than is believed appropriate for the corona /2/, but we expect our model will now enable simulations with higher Alfvén speeds.

Acknowledgement: AHW and STW are supported by NASA Grant NAGW-9. STS has been supported by a grant from the Cosmic and Heliospheric Physics Branch of NASA. GP acknowledges support from ASI (Italian Space Agency) and the University of Alabama in Huntsville.

REFERENCES

1. Hu, Y. Q., and Wu, S. T., *J. Comput. Phys.*, **55(1)**, 33 (1984).
2. Parker, E. N., *Interplanetary Dynamical Processes*, Interscience, New York (1963).
3. Steinolfson, R. S., Suess, S. T., and Wu, S. T., *Astrophys. J.*, **255**, 730-742 (1982).
4. Suess, S. T., *Solar and Stellar Coronal Structure and Dynamics*, R. C. Altrock, ed., Proc. of the 9th Sacramento Pk. Summer Symp., Sunspot, New Mexico, 130-139 (1988).
5. Suess, S. T., Richter, A. K., Winge, C. R., Jr., and Nerney, S., *Astrophys. J.*, **217**, 296-305 (1977).

93N31360

PREDICTING LY-α INTENSITIES IN CORONAL STREAMERS

G. Noci[1], G. Poletto[2], S.T. Suess[3], A.-H. Wang[4], S.T. Wu[4]

[1]Dipartimento di Astronomia e Scienza dello Spazio, Università di Firenze, Italy
[2]Osservatorio Astrofisico di Arcetri, Largo E. Fermi 5, 50125 Firenze, Italy
[3]NASA Marshall Space Flight Center, SSL/ES52 Huntsville, AL 35812, U.S.A.
[4]Center for Space Plasma and Aeronomic Research, UAH, Huntsville, AL 35899, U.S.A.

ABSTRACT

In the near future, SOHO UVCS will make long-term observations of coronal streamers in UV lines, providing a new tool for the analysis of structures which have been known for decades but are still far from being adequately described. The purpose of this work is to evaluate the Ly-α brightness of coronal streamers, adopting the streamer models obtained, via a time-dependent numerical relaxation technique, by Wang et al. (Ref. 1). This will allow us both to understand the role of geometric vs. physical factors in determining the streamer Ly-α intensity and to provide guidelines for UVCS observational operations. Future prospects along this line of research are also briefly summarized.

1. INTRODUCTION

It is well known that streamers have been observed, and their structure reproduced in detailed drawings, since far back in time. This is not surprising, as these prominent features can be easily seen during eclipses. Nevertheless, although observed for so long, their physical properties are largely speculative and comparatively little literature has been dedicated to streamers. This situation is due to the limited means by which these features can be analyzed: only recently coronagraphs, radio telescopes and space experiments offered an alternative to the traditional white light technique.

Still, so far, only streamers' densities have been extensively analyzed. Neither temperatures, nor magnetic field values have been derived - other than in a few occasional studies. Quite obviously, these parameters are crucial to the understanding of the physical structure of the middle corona and have a bearing on our understanding of the solar wind, whose slow streams supposedly originate from streamer areas. However, flow velocities in the streamers' cusp regions have never been measured.

SOHO UVCS will expand dramatically our knowledge of these structures. By observing streamers, in Ly-α and possibly other UV lines, from close to the solar limb ($\cong 1.2\ R_\odot$) up to several solar radii, we will be able to determine the height profile of density, electron and proton temperature and flow velocity throughout their whole extent. Magnetic field values may be inferred, by analyzing the tangential discontinuities which are almost systematically parts of large streamers (provided that the temperature keeps constant across the discontinuity).

With SOHO a thorough description of these features is within reach.

In view of the large effort which will be dedicated to these studies as soon as SOHO data will be acquired, we deemed it worthwhile to provide simulated UV observations of streamers under a variety of situations. To this end, we adopted the model developed by Wang et al. (Ref. 1), to describe the physical state of streamers. Our simulations might be used as guidelines in devising the observational strategies and operational sequences which will allow the best usage of data. In this paper we describe briefly the initial stage of this project, where the Ly-α brightness is evaluated for streamers of different geometries and different plasma β, seen from different aspect angles. Future developments of our work are also shortly outlined. We refer the reader to Noci et al. (Ref. 2) for a more thorough description of what is illustrated here.

2. THE MODEL

The physical streamer models that we use for calculating Ly-α intensities are the result of a numerical simulation of global coronal structure. The simulation is a solution of the magnetohydrodynamic equations for two-dimensional, axisymmetric, single fluid, polytropic, time-dependent flow. The steady state is found by starting with an essentially arbitrary initial state having the desired boundary conditions and allowing a relaxation in time until the solution is no longer changing. The resulting model is therefore assured both of being a self-consistent solution for the specified physical boundary conditions and of being stable. The model, since axisymmetric, describes a single continuous streamer that extends all the way around the Sun at a specific latitude. The simulation is further described by Wang et al. (Ref. 1).

The boundary conditions at $1\ R_\odot$ are that the temperature and density are constant in latitude and that the vector magnetic field is potential. Three magnetic field geometries are used: a dipole, a quadrupole, and a hexapole; the scalar potentials are proportional to $P_2(\cos\theta)$, $P_3(\cos\theta)$, and $P_4(\cos\theta)$, respectively (here P_i is the Legendre polynomial of degree i and θ is the colatitude). There are two dimensionless numbers: the

Proceedings of the First SOHO Workshop, Annapolis, Maryland, USA, 25–28 August 1992 (ESA SP-348, November 1992)

polytropic index, γ, and the ratio of internal to magnetic energy densities, β. We use $\gamma = 1.05$ in all cases, $\beta = 0.5$ for all three field geometries, and, in addition, do a dipole calculation for $\beta = 0.2$. These values of β correspond to a heliocentric distance of 1.0 $R_\odot$, at the equator, where the field strength is 1.67 gauss for both $\beta = 0.5$ and $\beta = 0.2$. For the high β case, the base temperature and density are 1.8×10^6 K and 2.25×10^8 cm^{-3}. For the low β case, they are 1.44×10^6 K and 5.61×10^7 cm^{-3}. The three magnetic field geometries naturally lead to a single equatorial streamer, a mid-latitude streamer, and both an equatorial and a mid-latitude streamer for the dipole, quadrupole and hexapole, respectively.

As we mentioned in the Introduction, we know so little about streamers, that it is difficult to check model predictions against observations. The only comparison we can make is between predicted and observed densities. By comparing model densities with densities derived from white light and radio observations it turns out that the most realistic densities - irrespective of the streamer configuration - are those evaluated for the $\beta = 0.5$ case. A plasma $\beta = 0.2$ results in too low densities, at least with the boundary conditions we assumed. As a consequence, we will, at the moment, dismiss this case, and evaluate the Ly-α brightness only for high β streamers.

Before describing the results we obtained for our simulation, we note that model densities in open field regions are not realistic, being too high, both in the high and low β case. In order to reproduce the high velocities and low densities that characterize the coronal hole regions, within the limits of a polytropic model, one should use an *ad hoc* temperature vs. latitude profile. This is beyond the scope of the present work, as, due to the higher streamer density, we don't expect surrounding open field areas to affect appreciably the streamer Ly-α brightness. We conclude that the behavior of the model in open field areas, at this stage, is inconsequential to us. Hence, we proceed to evaluate the Ly-α from streamers, in a variety of test cases.

3. LY-α BRIGHTNESS IN STREAMERS

The formation of the Ly-α line in the corona is due to the presence, at coronal heights, of a tiny percentage of neutral hydrogen atoms that resonantly scatter the chromospheric Ly-α photons (see, for instance, Gabriel, Ref. 3). The total (i.e. integrated over the line profile) Ly-α intensitity, as observed along the direction $\mathbf{n}$ is given by

$$I = \frac{h B_{12} \lambda_0}{4\pi} N_L \int_\Omega p(\varphi)\, d\omega' \int_0^\infty I_{chrom}(\lambda, \mathbf{n}')\, \psi(\lambda - \lambda_0)\, d\lambda$$

where $N_L = \int_{-\infty} N_1\, dx$ and N_1 is the number density of hydrogen atoms in the ground level; h is the Planck constant; B_{12} the Einstein coefficient for the line; λ_0 is the rest value for the central wavelength λ of the Ly-α transition; the unit vector $\mathbf{n}$ is along the line of sight x and the unit vector $\mathbf{n}'$ is along the direction of the incident radiation; φ is the angle between $\mathbf{n}$ and $\mathbf{n}'$; $p(\varphi)$ $d\omega'$ - where ω' is the solid angle around $\mathbf{n}'$ - is the probability that a photon travelling along the direction $\mathbf{n}$ was travelling, before scattering, along the direction $\mathbf{n}'$; Ω is the solid angle subtended by the chromosphere at the point of scattering; I_{chrom} is the exciting chromospheric radiation and ψ is the coronal absorption profile. In the following we assume that the intensity of the chromospheric Ly-α radiation is constant across the solar disk and that the velocity distribution of the scattering hydrogen atoms is Maxwellian.

In order to use the previous equation to calculate the Ly-α intensity in coronal streamers, one needs to evaluate N_L, i.e. the total number of hydrogen atoms along the line of sight. Unless the 3-D streamer is known, N_L cannot be evaluated. Because our model is 2-D, we do not have this information and we have to make an *a priori* assumption about the 3-D streamer geometry. As a first hypothesis, we may assume that streamers extend all the way around the equator, in a continuous belt. By comparing the resulting Ly-α intensities with those obtained in a rocket flight by Kohl et al. (Ref. 4), we conclude, however, that this assumption is not realistic, as the model predicted values are about one order of magnitude larger than the observed ones. Recalling that model densities seem to be realistic, the discrepancy should be ascribed to geometrical, rather than physical, factors.

Figure 1 shows the Ly-α Intensity vs. distance profile along the axis of a streamer which lies in the plane of the sky (identified with the plane of the model). Three different assumptions have been made as to the streamer's

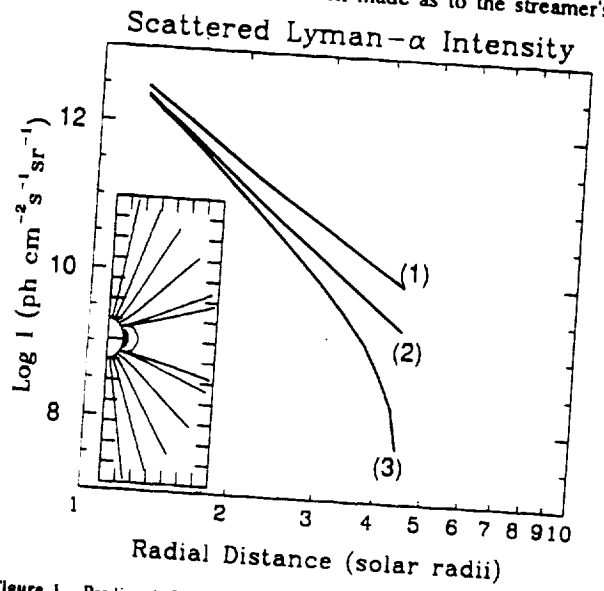

Figure 1. Predicted Ly-α intensity vs. radial distance along the axis of an equatorial streamer in a dipolar geometry, for a plasma $\beta = 0.5$. The streamer thickness in a direction normal to the plane of the sky is assumed either to have a constant angular width (curve (1)) equal to its angular base width ($\approx 76°$) or to be constant with height (curve (2)) and equal to its base width ($\approx 1\ R_\odot$) or to decrease linearly with height (curve (3)) up to the cusp height ($R_{cusp} = 4.5\ R_\odot$).

configuration along the line of sight: curve (1) refers to a streamer whose angular width is constant with height; curve (2) refers to a streamer whose linear width is constant with height; curve (3) refers to a streamer whose width decreases linearly with height up to a vertex, identified with the streamer's cusp. Densities along the line of sight have been assumed equal to those given by the model at the same latitude and radial distance. We warn the reader that, in the evaluation of N_L, the integration length is dictated by our assumptions

PRECEDING PAGE BLANK NOT FILMED

about the streamer 3-D shape and the effect of the outer atmosphere is completely neglected by truncating the integration at the edge of the streamer, in accordance with our conclusion that the contribution from the open field areas is inconsequential. The global magnetic configuration for which these simulations have been made is also illustrated in the Figure. Clearly SOHO data will allow us to discriminate between the different geometries, by analyzing the behavior of the intensity profile at large heliocentric distances: in the case of a cone-shaped structure (curve (3)) the steep intensity decline at large distances is due to the decrease with height of the integration length, a factor which singles out this case from the others.

UVCS field-of-view (FOV) - 141' x 40' - is large enough to allow the imaging of an entire streamer, from 1.2 $R_\odot$ to its cusp. In the hypothesis of the equatorial streamer of Figure 1, for instance, the streamer's axis is in the equatorial plane, the streamer's base has a width of $\approx 70°$ and its cusp reaches a height of ≈ 3.5 - $4.5\ R_\odot$. This sort of configuration is observed at solar minimum, when streamers are concentrated along the solar equator, and is representative of the situation that SOHO will meet in its early operational phase. UVCS with an appropriate slit width, will take measurements on the streamer at increasing heliocentric distances, along the axis of the structure as well as in a direction normal to the latter. These observations will enable us to check the capability of the model in predicting realistic profiles of the physical parameters of the streamer both along and *across* its axis. Consistency between model predictions and observations, proving the reliability of the model, will provide indirectly the distribution of the magnetic field vector throughout the streamer, a factor which can be hardly underestimated.

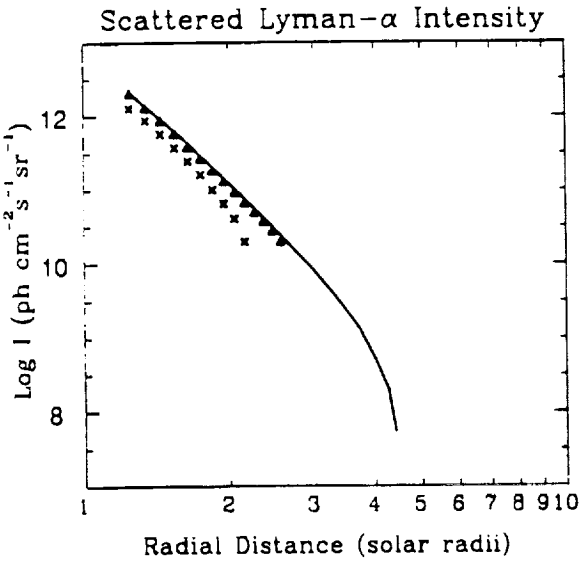

Figure 2. Predicted Ly-α intensity vs. distance (measured along the axis of an equatorial streamer) for different off-equator offset in a cone-shaped equatorial streamer: solid-line, intensity along the axis of the streamer, zero offset; Δ, intensity for an offset of 0.2 $R_\odot$; ×, intensity for an offset of 0.4 $R_\odot$. As in Figure 1, the configuration is dipolar, the base width is = 38° and the cusp height is 4.5 $R_\odot$.

Figure 2 shows the results of our simulations of Ly-α off-axis intensities for the cone shaped streamer, whose on-axis behavior has been shown in curve (3) of Figure 1 and is given here (solid line) as a reference. Crosses (triangles) refer to Ly-α observed at an offset of 0.4 (0.2) R_O along a direction parallel to the streamer's axis. The progressive decrease in the integration length as we move to larger offsets is responsible for the intensity drop which occurs at increasingly lower heliocentric distances. It is this geometric effect, rather than the transverse density gradient, that determines the intensity vs. distance profile for off-axis observations. Obviously, this result has to be considered as preliminary, as it depends heavily on our hypotheses about the behavior of the physical parameters of the streamer in the third dimension. On the theoretical side, it points to the need of a 3-D model; on the observational side, it shows that we badly need a technique to derive densities, independently of the streamer's geometry.

Before addressing this problem, we notice that all our examples refer to a global dipolar magnetic configuration. However, our results can be extended to the quadrupolar and hexapolar model geometry by taking into account the differences in the streamer's thickness. Densities predicted by our model are about the same for low and high latitude streamers. Therefore, the Ly-α brightness from these features turns out to scale, with respect to that originating in a dipolar equatorial configuration, in the same proportion as the streamers' thickness. The Ly-α brightness from an equatorial hexapolar streamer, for instance, will be a factor 2-3 smaller than that from an equatorial dipolar streamer and about equal to the brightness from the high latitude hexapolar streamer.

4. TOMOGRAPHY FOR DENSITY DIAGNOSTIC

Tomographic techniques are currently used to reconstruct the 3-D configuration of a structure which can be observed from different orientations. In order to adopt this methodology to derive densities at different positions within a streamer, we have to take advantage of solar rotation and observe the feature at different aspect angles. This constraint has a severe drawback: the streamer has to be stable throughout the observational period, if we want to attach any meaning to the inferred values. Whether this is a reasonable assumption is debatable and has possibly to be checked in individual cases.

In the hypothesis that streamers meet this requirement, it is easy to understand why the technique can be successfully applied to a field so distant from its more common usage. We remind the reader that the emergent Ly-α radiation is obtained by summing over the contribution from all regions along the line of sight. Depending on the streamer aspect angle and on the transverse vs. axial density gradient, it may happen, when the line of sight cuts obliquely through the structure, that the highest contribution to the emergent intensity originates from an element at some distance from the streamer's axis: hence the possibility of deriving the density of this element and, as a consequence, the density structure of the streamer, across its axis, independently of its geometry.

The capabilities of the tomographic technique in the diagnostic of streamer's density can be extensively tested only when a 3-D model is available. At present, we used this technique on the 2-D model, assuming, contrary to what done so far, that the plane of the model is the equatorial plane. In this case the streamer footpoints lie on the equator and the model provides the gradient of density in the direction normal to the streamer's axis (i.e.

along the line of sight), so far assumed *a priori*. The results we obtained are preliminary, since large densities in the open field areas result in a too high contribution from the ambient regions.

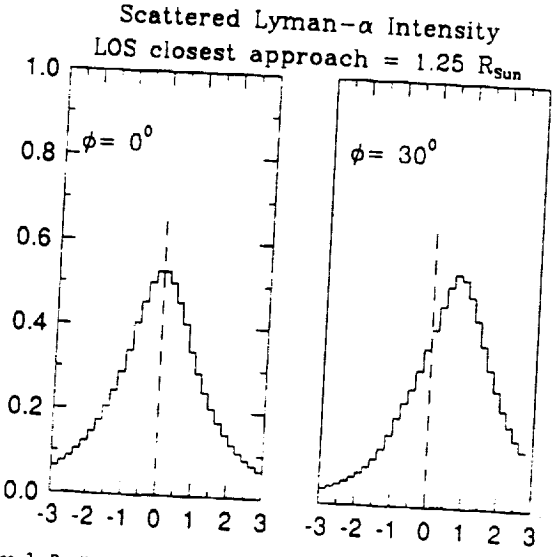

Figure 3. Predicted contribution of individual elements along the line of sight to the total Ly-α intensity from the usual dipolar, β = 0.5 streamer, supposed to lie in the equatorial plane, as a function of their distance along the line of sight. Negative (positive) distances are away from (towards) the observer, as measured with respect to the axis of the streamer. The line of sight intersects the plane of the sky at a distance of 1.25 $R_\odot$ and cuts obliquely through the streamer, unless the streamer's axis is in the plane of the sky (streamer longitude: 90°). The contribution of individual elements to the total intensity is shown (left) for a streamer whose axis is in the plane of the sky (streamer longitude: 90°, and (right) for a streamer at a longitude of 120° (aspect angle ϕ = 30°). The position of the streamer axis is shown as a dashed line in the figure.

Figure 3 shows how individual elements along the line of sight contribute to the Ly-α intensity measured in the equatorial plane at a distance of 1.25 $R_\odot$ in two cases: when the streamer's axis is in the plane of the sky (streamer longitude 90°, aspect angle ϕ = 0°) and when the streamer is behind the plane of the sky at a longitude of 120° (aspect angle ϕ = 30°). In the latter case, the highest contribution to the emergent intensity comes from the element at a distance of ≈ 0.72 $R_\odot$ along the line of sight. Thus, by taking an extended set of data, at different locations along the axis of the streamer and at different aspect ratios, we may eventually get a complete map of the density of the structure. A more thorough analysis of the capabilities of the tomographic technique has to be deferred to the time a 3-D model is available, both in open field regions and in streamer structures.

5. DISCUSSION AND CONCLUSIONS

As we stated in the Introduction, we meant, in this work, to provide a number of Ly-α brightness simulations to be used as a first guess of SOHO UVCS forthcoming measurements. To this end, we have presented a set of predicted profiles of Ly-α intensity vs. distance, representative of a variety of situations. This set provides a first-hand tool for observational planning and its consistency with the scanty available observations proves the capability of our approach.

A critical examination of the model used in the present simulations leads us to define the theoretical objectives we have to attain in order to improve our predictions. As we noticed, appropriate boundary conditions have to be chosen in open field regions to allow a better description of the ambient medium: this can be done also in a 2-D framework, before getting to our main purpose, i.e., the development of a 3-D global coronal model. Besides this main objective, an extension of our modeling efforts to different plasma β seems to be mandatory: streamer cusps reach up to a variety of heights, possibly representative of the range of plasma β over which these structures develop.

Following these theoretical developments, much work has to be done in preparation of the SOHO mission. Here it suffices to mention, for instance, that more realistic simulations imply the usage of different Ly-α profiles for different solar regions: it is well known that the chromospheric Ly-α profile is not constant across the solar disk, thus implying a not constant chromospheric exciting Ly-α radiation. Still, we have not yet addressed the field which looks more promising: if we will be able to prove, on the basis of our model and ensuing simulations, that the Doppler dimming technique can be used in the streamer cusp regions, we will open a new research area from which unsolved problems - like that of the origin of the slow solar wind streams - may benefit to the point that they are no longer a riddle. We will proceed on this work with these exciting perspectives.

ACKNOWLEDGEMENTS

The work of G. Noci and G. Poletto has been partially supported by ASI (Italian Space Agency). S.T. Suess acknowledges support from GNA (Gruppo Nazionale di Astronomia) and MURST (Ministero dell'Università e della Ricerca Scientifica) during his visit to Florence, where this work was initiated. Partial support by a grant from the Cosmic and Heliospheric Physics branch of NASA is also acknowledged. A.-H. Wang and S.T. Wu are supported by NASA Grant NAGW-9.

REFERENCES

1. Wang, A.-H. & al. 1992, A two dimensional MHD global coronal model: steady-state streamers, Solar Phys., submitted.

2. Noci, G. & al. 1992, Ly-α intensities in coronal streams, Solar Phys., submitted.

3. Gabriel, A.H. 1971, Measurements on the Lyman Alpha corona, Solar Phys., 21, 392.

4. Kohl, J.L. 1980, Measurements of coronal kinetic temperatures from 1.5 to 3 Solar Radii. Astrophys. J. 241, L117.

SEE ALS
93A33618

A TWO-DIMENSIONAL MHD GLOBAL CORONAL MODEL: STEADY-STATE STREAMERS

A.-H. WANG, S. T. WU
Center for Space Plasma and Aeronomic Research and Department of Mechanical Engineering, The University of Alabama in Huntsville, Huntsville, AL 35899, U.S.A.
S. T. SUESS
Space Science Lab, ES52, NASA Marshall Space Flight Center, Huntsville, AL 35812, U.S.A.
and
G. POLETTO
Osservatorio Astrofisico di Arcetri, 50125 Firenze, Italy

(Received 4 August, 1992; in revised form 22 February, 1993)

Abstract. We describe a two-dimensional time-dependent, numerical, magnetohydrodynamic model for the determination of the physical properties of coronal streamers from the top of the transition zone ($R_\odot = 1$) to 15 $R_\odot$. Four examples are given: for dipole, quadrupole, and hexapole initial field topologies. The computed parameters are density, temperature, velocity, and magnetic field. In addition to the properties of the solutions, their accuracy is discussed. We use the model as the basis for a general discussion of the way boundary conditions are specified in this and similar simulations.

1. Introduction

We present results from a recently-developed numerical model of coronal structure. The immediate reasons for a new model were to extend the outer boundary farther from the Sun and to gain the experience necessary for development of a three-dimensional model. A result of this process has been a close examination of the physical details of the solution and how they depend on the way the boundary conditions are specified. An immediate application will be the simulation of streamers in support of the Ultraviolet Coronagraph and Spectroheliograph (UVCS) and the Large Angle Spectrometric Coronagraph (LASCO) on the Solar Heliospheric Observatory (SOHO). These instruments will be able to measure the temperature, density, and flow vector in the corona. With model calculations, it will be possible, for example, to estimate the magnetic field vector.

Numerical models of coronal structure have been published sporadically, at long intervals, over the past twenty years. The first (Pneuman and Kopp, 1971) demonstrated the feasibility of such models, treating isothermal flow and arriving at the solution by iterating on the electrical currents. However, a more efficient and flexible method is to consider an initial-boundary value problem in which the steady state is found holding the boundary conditions constant and allowing the solution to relax in time from an essentially arbitrary initial state. Steinolfson, Suess, and Wu (1982) applied this later technique to the analysis of a polytropic dipole configuration for a range of plasma β (ratio of internal pressure to mag-

Solar Physics **147**: 55–71, 1993.
© 1993 *Kluwer Academic Publishers. Printed in Belgium.*

PRECEDING PAGE BLANK NOT FILMED

netic pressure). Steinolfson (1989, 1991) and Guo *et al.* (1992) have used this steady-state solution as the basis for studying coronal mass ejections and streamer evolution with shear, which can be simulated using a nearly identical numerical model. Details of the numerical schemes and results can be found in the referenced publications.

We revisited this problem for the reasons mentioned above. However, we also consider that such complex numerical models are rarely without problems or uncertainties. When the models are used for analysis of data and for predictions, the only reliable validation is to develop an independent model and compare the results. Even when both (or all) models are fundamentally correct, this process generally leads to new or deeper understanding of the problem. In the present case, this is precisely what has happened. We have gained a better insight into the physical basis of the criteria which should be adopted in specifying boundary conditions. The results from this constitute an important part of the present study.

The physical and numerical simulation is described in Section 2. Section 3 details numerical models of dipole, quadrupole, and hexapole magnetic fields. Section 4 is a discussion of numerical precision of the solution and the boundary conditions, putting the discussion into context with earlier models so far as is possible. Section 5 contains our summary and conclusions.

2. The Physical and Numerical Simulation

We assume axisymmetric, single fluid, polytropic, time-dependent ideal magnetohydrodynamic flow and perform the calculation in a meridional plane defined by the rotational symmetry axis of the magnetic field. The coordinates are (r, θ, ϕ) with ϕ being the ignorable coordinate. For the magnetic field boundary condition, we take the radial field component at the lower boundary to be that given by a vacuum dipole, quadrupole, or hexapole potential magnetic field. The flow therefore has reflective symmetry across the equator and the calculation need be done in only one quadrant. The equations of motion that describe this flow are:

$$\frac{\partial \rho}{\partial t} + \frac{\partial}{\partial r}(\rho v_r) + \frac{\partial}{\partial \theta}\left(\rho \frac{v_\theta}{r}\right) = -\frac{2\rho v_r}{r} - \frac{\rho v_\theta}{r}\cot\theta\,, \tag{1a}$$

$$\frac{\partial v_r}{\partial t} + v_r\frac{\partial v_r}{\partial r} + \frac{B_\theta}{\mu\rho}\frac{\partial B_\theta}{\partial r} + \frac{1}{\rho}\frac{\partial p}{\partial r} - \frac{v_\theta}{r}\frac{\partial v_r}{\partial \theta} - \frac{B_\theta}{\mu\rho r}\frac{\partial B_r}{\partial \theta} = $$

$$= -\frac{GM_\odot}{r^2} + \frac{v_\theta^2}{r} - \frac{B_\theta^2}{\mu\rho r}\,. \tag{1b}$$

$$\frac{\partial v_\theta}{\partial t} + v_r\frac{\partial v_\theta}{\partial r} - \frac{B_r}{\mu\rho}\frac{\partial B_\theta}{\partial r} + \frac{v_\theta}{r}\frac{\partial v_\theta}{\partial \theta} + \frac{B_r}{\mu\rho r}\frac{\partial B_r}{\partial \theta} + \frac{1}{\rho r}\frac{\partial p}{\partial \theta} =$$

$$= \frac{B_r B_\theta}{\mu\rho r} - \frac{v_r v_\theta}{r}\,. \tag{1c}$$

ORIGINAL PAGE IS
OF POOR QUALITY

$$\frac{\partial B_r}{\partial t} - \frac{\partial}{\partial \theta}\left(\frac{v_r B_\theta - v_\theta B_r}{r}\right) = \frac{1}{r}(v_r B_\theta - v_\theta B_r)\cot\theta\,. \tag{1d}$$

$$\frac{\partial B_\theta}{\partial t} + \frac{\partial}{\partial r}(v_r B_\theta - v_\theta B_r) = -\frac{1}{r}(v_r B_\theta - v_\theta B_r)\,. \tag{1e}$$

$$\frac{\partial p}{\partial t} + \gamma p\frac{\partial v_r}{\partial r} + v_r\frac{\partial p}{\partial r} + \frac{\gamma p}{r}\frac{\partial v_\theta}{\partial \theta} + \frac{v_\theta}{r}\frac{\partial p}{\partial \theta} = -\frac{\gamma p}{r}(2v_r + v_\theta\cot\theta)\,. \tag{1f}$$

The dependent variables are the density, ρ, the pressure, p, the radial and meridional velocities, v_r and v_θ, and the radial and meridional magnetic fields, B_r and B_θ. The constants $M_\odot$, G, γ, and μ are the solar mass, gravitational constant, the polytropic index and the magnetic permeability.

These equations are solved in a computational domain extending from the Sun (1 $R_\odot$) to 15 $R_\odot$, from the pole to the equator. It is assumed that meridional flow is zero at the pole and equator. The grid is divided so that there are 37 gridpoints in the radial direction and 22 gridpoints in the meridional direction, with the radial grid size slowly increasing with radius. The meridional grid is divided so that points lie equidistant on either side of $\theta = 0$ and $\theta = 90°$, at $\theta = -2.25°$, 2.25°, 6.75°, ..., 87.75°, 92.25°. The algorithm adopted here is the Full-Implicit Continuous Eulerian (FICE) scheme described by Hu and Wu (1984). For time stepping a second-order accurate forward differencing scheme is used, with the step size being of the same order as given by the Courant condition because the magnetic field is calculated explicitly. Smoothing is used when gradients become too large, i.e., at shocks (which do not occur here). At the inner boundary, the flow is subsonic and sub-Alfvénic so that two of the six independent variables are calculated using compatibility relations (Hu and Wu, 1984). A brief summary of the compatibility conditions for the present model is given in the Appendix, along with details on how the boundary values and conditions are applied. We choose to specify the radial and meridional magnetic fields, temperature, and density. The radial and meridional flow speeds are computed from compatibility relations (i.e., Equations (A.1) and (A.2)). At the outer boundary, the flow is restricted to being both supersonic and super-Alfvénic. In this case, all variables at that boundary can be calculated by simple linear extrapolation from the first (or first two) grid points inside the boundary. In this study, we did not perform the comparison between the present boundary conditions and conventional boundary conditions. However, in a recent study by Sun (1991), it was shown that the statement of the boundary conditions in the Appendix eliminates the spurious waves generated by boundary disturbances and which can cause numerical instability.

We start with an essentially arbitrary initial state and allow the flow to relax in time while holding the boundary values constant. In the present case the initial flow field is a polytropic, hydrodynamic solution to the steady-state radial flow equation of motion (e.g., Parker, 1963) superimposed on a potential magnetic field. That this is neither a self-consistent nor stable solution to the steady-state MHD equations is irrelevant since the flow is allowed to evolve in time under the control

ORIGINAL PAGE IS
OF POOR QUALITY

of the equations of motion. The main concerns are that the numerical solution be stable and of sufficient accuracy to define the physically interesting aspects of the solution, and that the relaxation proceed long enough that an acceptably close approximation to the steady state has been reached. We address these issues briefly in Section 4.

3. Detailed Results from Four Specific Models

We report here on four specific models. The results are grouped first according to the way in which the physical variables are plotted (i.e., either versus radius or versus polar angle) and second according to which of the four examples the plot is for. In these four examples, three magnetic field geometries are used: a dipole, a quadrupole, and a hexapole; the scalar potentials are therefore proportional to $P_2(\cos\theta)$, $P_3(\cos\theta)$, and $P_4(\cos\theta)$, respectively, where $P_n(\cos\theta)$ is the Legendre polynomial of degree n. There are two dimensionless free parameters: the polytropic index, γ, and the plasma β. We use $\gamma = 1.05$ in all cases, $\beta = 1.0$ for all three field geometries, and, in addition, do a dipole calculation for $\beta = 0.2$. In these case, β is evaluated at 1.0 $R_\odot$ at the equator, where the field strength is 1.67 G both for $\beta = 1.0$ and $\beta = 0.2$. For the high β cases, the base temperature and density are 1.8×10^6 K and 2.25×10^8 cm^{-3}. For the low β case, they are 1.44×10^6 K and 5.61×10^7 cm^{-3}. The three magnetic field geometries naturally lead to a single equatorial streamer, a mid-latitude streamer, and both an equatorial and a mid-latitude streamer for the dipole, quadrupole and hexapole, respectively.

Results from the four examples will be referred to as follows:

(a) Dipole, $\beta = 1.0$.
(b) Quadrupole, $\beta = 1.0$.
(c) Hexapole, $\beta = 1.0$.
(d) Dipole, $\beta = 0.2$.

The initial state temperature, density, and velocity profiles are shown in Figure 1. The temperature curves appear irregular due to the small change in temperature over the relatively large radial range – a consequence of the polytropic index being near unity. Only three significant figures were retained after the calculation so what is seen here is roundoff error in the plotted results rather than in the computed results.

The final, steady-state magnetic field geometries for the four cases are shown in Figure 2. Here is seen the well-known property that the flow is nearly radial beyond 3–4 $R_\odot$. The flow is field-aligned everywhere and field lines which cross the outer boundary reach to ∞. The streamers are those volumes which are magnetically closed (i.e., the field lines return to the surface of the Sun) and it is evident that relatively small volumes in the streamers remain magnetically closed in comparison to the initial state where all field lines were closed. These closed volumes are surrounded by a low density shell but, as will be shown below, the densities in the large coronal hole-like open regions are otherwise only slightly lower than in the

ORIGINAL PAGE IS
OF POOR QUALITY

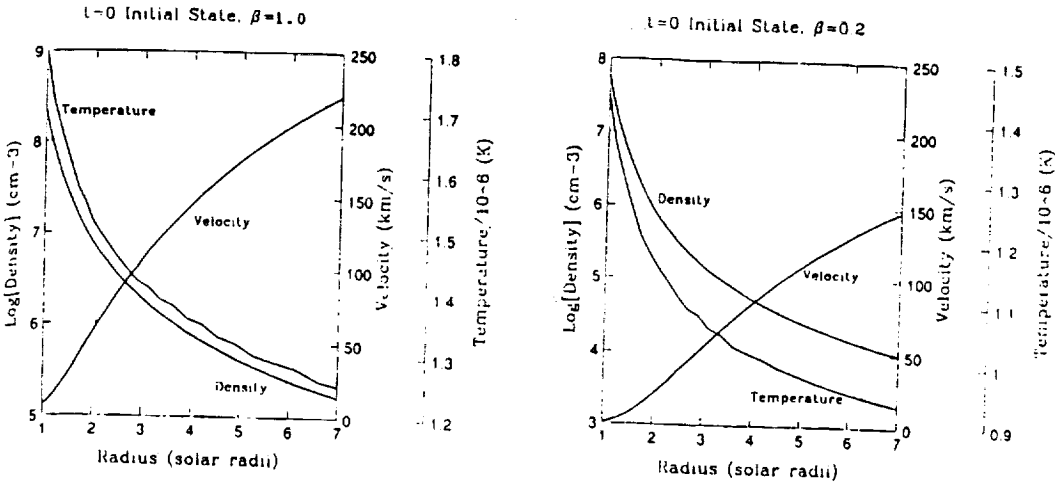

Fig. 1. Density, temperature, and velocity profiles in radius that were used for the initial ($t = 0$) state in the relaxation. On the left are the profiles for the $\beta = 1.0$ cases and on the right are the profiles for the $\beta = 0.2$ case. Note that, except for the velocity scales, the scales differ between the two panels. Because the polytropic index is near unity, temperature changes slowly with radius and the irregularities in the temperature profiles should be interpreted as noise.

streamers. In each panel of Figure 2, four dashed lines are shown and labelled A, B, C, or D. These lines indicate the radial directions used below to plot variables versus radius.

The physical times allowed for the relaxation in these four examples were: (a) 22.22 hours for the $\beta = 1.0$ dipole; (b) 16.67 hours for the $\beta = 1.0$ quadrupole; (c) 18.06 hours for the $\beta = 1.0$ hexapole; (d) 19.44 hours for the $\beta = 0.2$ dipole. These times are determined by how long it takes for any fluctuation to be advected out through the outer boundary of the solution domain. This in turn depends on how large the flow speed is and whether the fluctuations represent inward propagating waves. In general, the times listed above are the minimum required for a stationary fluctuation (i.e., non-propagating in the solar wind frame) to be advected from 1 $R_\odot$ to 15 $R_\odot$ at a typical flow speed in the open regions. This sometimes leads to small residuals in the relaxation near the outer boundary at 15 $R_\odot$, but the solutions inside 7 $R_\odot$ that are shown here are quite steady. This is another point that will be reviewed in Section 4.

Figures 3 and 4 are plots of density and radial velocity versus radius. The plots are made in the directions indicated in Figure 2 so that, for example, in each panel of Figure 3 the density is plotted in the four directions A, B, C, and D indicated in the corresponding panel of Figure 2. In both of Figures 3 and 4, the four panels corresponding to the four panels in Figure 2 are clearly labeled. The density profiles have been divided by their corresponding initial state ($t = 0$) profiles from Figure 1 because the density changes by several orders of magnitude between the Sun and 15 $R_\odot$. The plots here extend only to 7 $R_\odot$ because there is no new information

ORIGINAL PAGE IS
OF POOR QUALITY

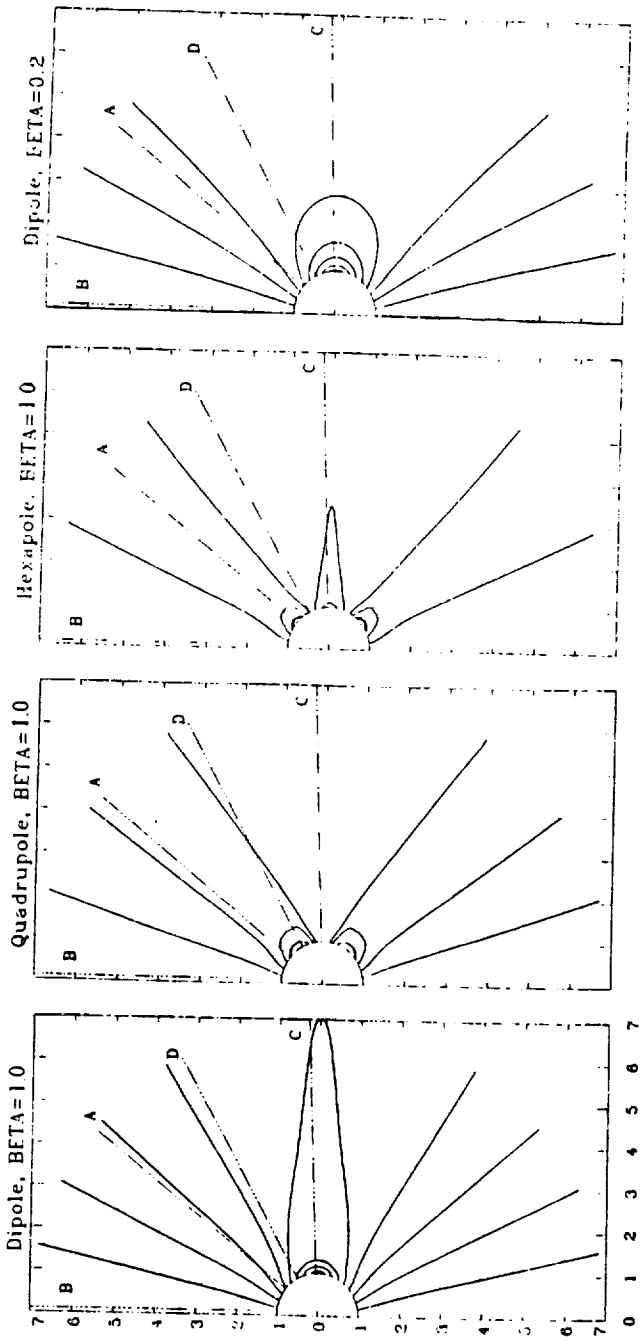

Fig. 2. Steady-state magnetic field-line plots for the four cases: (a) dipole, $\beta = 1.0$, (b) quadrupole, $\beta = 1.0$, (c) hexapole, $\beta = 1.0$, and (d) dipole, $\beta = 0.2$. The relaxation times allowed to reach these equilibria are: (a) 22.22 hours, (b) 16.67 hours, (c) 18.06 hours, (d) 19.44 hours, respectively. In each plot, four dashed lines are labelled 'A, B, C, or D'. These show the radial directions used for plotting the variables versus radius in each case. Thus, the $\beta = 1.0$ quadrupole plots will have variables plotted versus radius at the pole (B), at the edge of the polar open region (A), through the mid-latitude streamer (D), and in the equatorial open region (C). The dashed lines are along the directions of the grid. Since there is no grid point either exactly on the equator or exactly at the pole, these lines are slightly offset from those positions.

ORIGINAL PAGE IS
OF POOR QUALITY

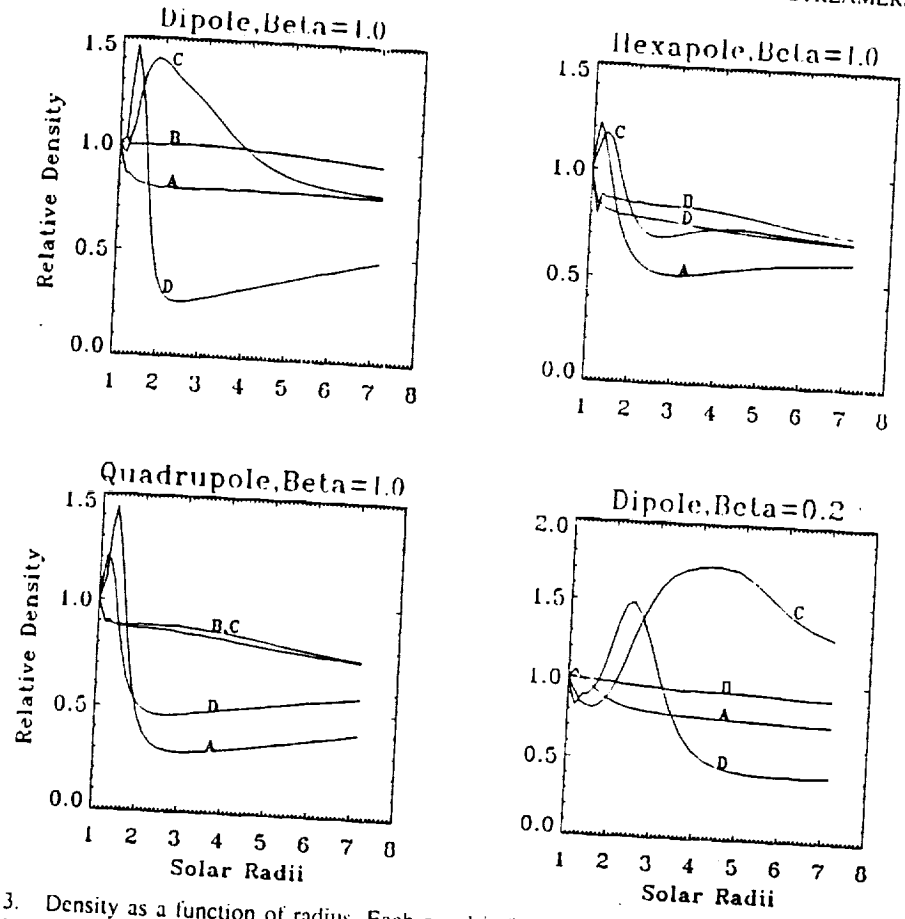

Fig. 3. Density as a function of radius. Each panel is for the corresponding case in Figure 2, as labelled. The curves are plotted along the directions shown in Figure 2. For example, the four curves for the $\beta = 1.0$ hexapole labelled A, B, C, D, are along the four directions shown in the third panel of Figure 2 and labelled in the same manner. Each curve has been divided by the initial profile (see Figure 1). A density enhancement is indicated by values greater than unity, and *vice versa*. The density concentrations in the streamers are clearly visible, generally being on the order of 25% to 50% above the initial state.

contained outside this radius – the flow is already supersonic and essentially radial.

Turning briefly to each figure individually, we begin by noting that a density enhancement is indicated by values greater than unity, and *vice versa*. The density concentrations in the streamers here are clearly visible, generally being on the order of 25% to 50% above the initial state. The base density for the $\beta = 1.0$ cases is close to that reported by Allen (1955) for the base of the quiet corona and the density profile shown here has generally the right behavior for streamers – as shown by curves C for cases (a), (c), and (d), and curve D in case (b). Curve D for case (a), the $\beta = 1.0$ dipole, is an example of the density deficit on the flank of a streamer that is typical of the results for all the examples. In contrast, the density in the

ORIGINAL PAGE IS
OF POOR QUALITY

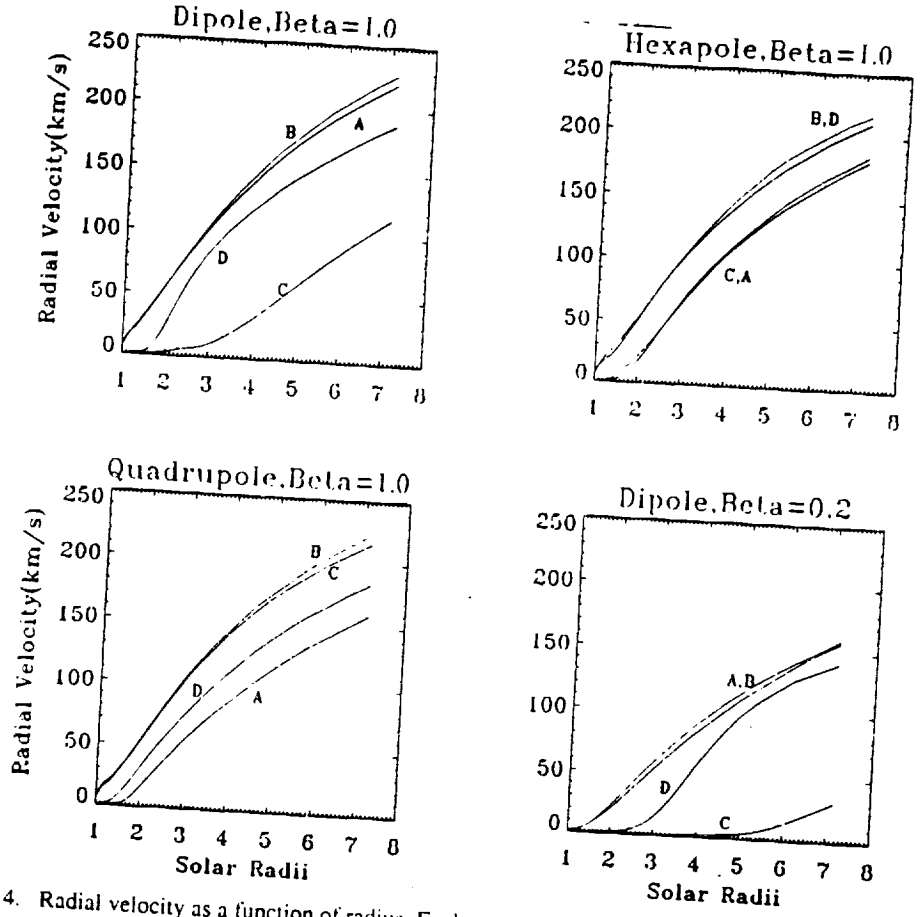

Fig. 4. Radial velocity as a function of radius. Each panel is for the corresponding case in Figure 2. The curves are plotted along the directions shown in Figure 2, as in Figure 3. The velocity inside the streamers is seen to be essentially zero.

centers of the open regions (curve B in all cases, curve C in case (b), and curve D in case (c)) is little different from the initial state, being only slightly smaller. This is only surprising when comparison is made to coronal hole observations (Munro and Jackson, 1977) wherein the density was reported to be more than an order of magnitude less than in streamers. This difference is a natural consequence of the properties of a polytropic model and the choice we have made for the boundary conditions on temperature and density – that they be independent of polar angle. The choice leads to both the high density shown here and the low flow speeds shown below on open field lines, irrespective of the open streamline geometry. To model true coronal hole flow with a polytropic gas would require at least an elevated temperature in the open regions and probably also a lower density at the base (Suess *et al.*, 1977; Suess, 1979).

The radial velocity is shown in Figure 4, at the positions indicated in Figure 2.

As described above, and as is generally the case in polytropic models, the flow speed in the open regions is similar to the undisturbed initial flow speed shown in Figure 1. In the streamer, the flow speed is essentially zero and it is reduced on the adjacent open field lines due, apparently, to the strongly inclined flow direction more than to geometry. The nonzero outflow above streamers (e.g., at $R = 7.14\ R_\odot$, at the equator of the $\beta = 1.0$ dipole) refers to the open field region above the streamer's cusp. The $\beta = 0.2$ dipole is the most extreme example of this – and the flow speed is nearly identical to the initial speed everywhere except on closed field lines, directly above the center of the streamer, and on the highly inclined field lines immediately adjacent to the streamer – where the difference is still rather small.

We do not plot the temperature since, due to the polytropic index being 1.05, it varies by only a few percent throughout the computation domain. However, this is an 'effective temperature' because a polytropic energy equation with a polytropic index of 1.05 is equivalent to a large amount of energy being added to the flow. Nowhere is the form of this energy specified, nor what the conversion and dissipation mechanisms are. However, it has been shown that a polytropic index on the order 1.05 is required to reproduce observations of coronal densities (Suess *et al.*, 1977).

Finally, the magnetically open regions, although euqivalent to coronal hole flows, do not simulate coronal holes because the flow speeds are far too small. To obtain reasonable flow speeds in this model it would be necessary to have the temperature vary across the base of the open region – which is well within the capability of the model. Such a variation has been shown to reproduce all the known properties of coronal hole flow and lead to accurate simulations of the geometry, with the effective temperature being larger in the center of the hole than at the edge (Suess *et al.*, 1977). In contrast to the open regions, the densities in the closed regions are similar to observed streamer densities and we feel this model is therefore a good approximation to streamer geometry. The temperature must still be qualified as an effective temperature, but can be used for diagnostic purposes in combination with planned observations on SOHO/UVCS.

Some of the results can be better viewed and more easily understood when plotted versus polar angle at different heliocentric distances, than versus radius at constant polar angles. Such plots are shown for the density, radial velocity, and total field strength in Figures 5, 6, and 7, respectively.

Figure 5 shows the density drop adjacent to the streamer. In the panel for the $\beta = 1.0$ dipole, this drop is quite large, well resolved, and leads into the density enhancement inside the equatorial streamer. The only place this does not occur is at the base – where the density is held constant. The width of the density enhancement in the streamer decreases with height, just as the width of the streamer itself decreases with height (e.g., Figure 2). Essentially the same thing is seen for the $\beta = 0.2$ dipole wiht the following quantitative differences: (i) The streamer is much higher and wider. (ii) The density depletion on the flanks has a smaller amplitude.

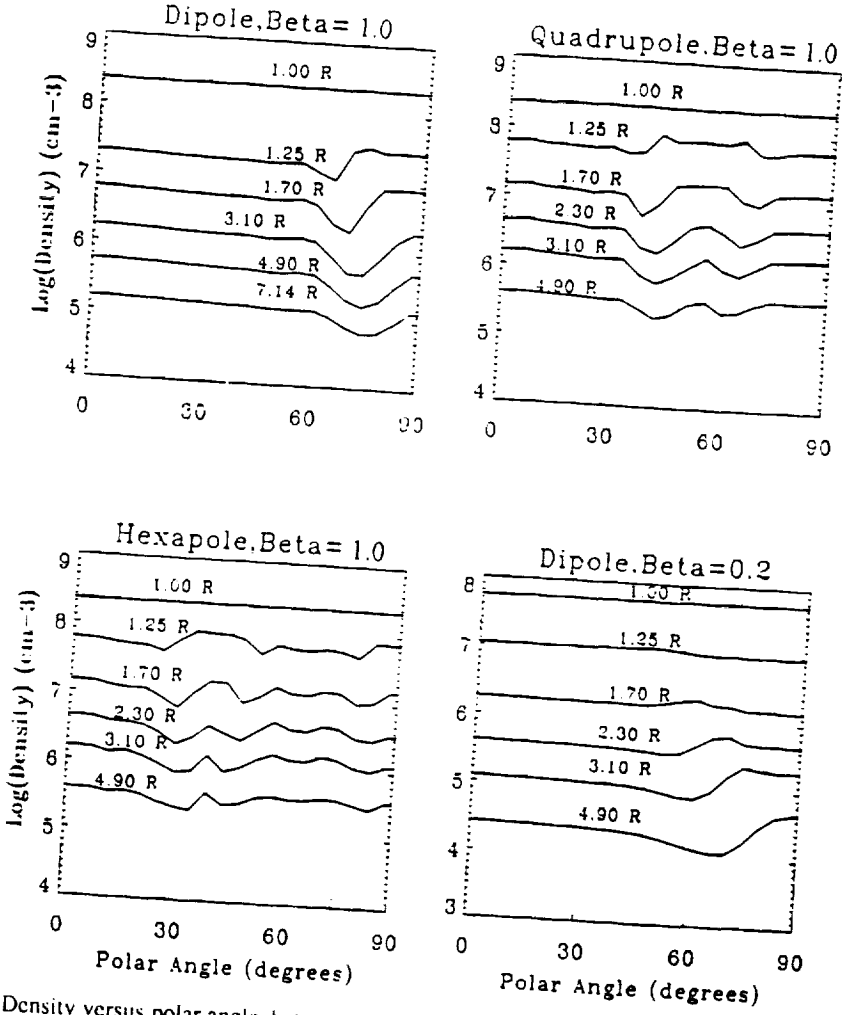

Fig. 5. Density versus polar angle, between the pole (0°) and the equator (90°). Each of the curves is labelled according to the heliocentric distance it refers to. Thus, the curves labelled 1.70 R indicate the density at 1.70 $R_\odot$ heliocentric radius. The density at the base is constant and so the curves there are flat. Above the base, there is a small density enhancement in the streamer (ca. 5% to 50%) and a trough in density at the edge of the streamer. In the middle of the open region, the density is very close to what it was in the initial state (see also Figure 3). The reason it is not small is that we have used constant temperature and density at the base. To produce a true coronal hole-like profile would have required at least an increase in the temperature at the base of the open region (Suess *et al.*, 1977).

These differences are the primary reason we conclude that solar streamers are better described by a $\beta = 1.0$ plasma than by a $\beta = 0.2$ plasma. Qualitatively, a similar result is found for the quadrupole and hexapole. However, it is obvious that the hexapole is only marginally resolved with the present grid density – there is really only one meridional grid point inside the mid-latitude streamer at any given height.

The radial velocity in Figure 6 drops precipitously from the magnetically open region to the inside of the streamer. That the velocity is not identically zero inside the streamer is a result of numerical diffusion and is a measure of this numerical artifact in the FICE scheme. For example, at 1.70 $R_\odot$ in the $\beta = 1.0$ dipole, the velocity drops from ca. 60 km s^{-1} at the edge of the streamer to about 3 km s^{-1} inside the streamer. 3 km s^{-1} is hardly above the noise level in the plots and the associated kinetic energy is too small to affect the dynamics of the solution. Such 'slippage' will, nevertheless, occur in all numerical solutions. At larger heights (e.g., 4.90 and 7.14 $R_\odot$) there is small, but finite flow near and in the neutral sheet dividing regions of opposite magnetic polarity. This is qualitatively like what is observed in the solar wind in the interplanetary medium. The $\beta = 0.2$ dipole again exhibits properties unlike the Sun in the sense that the very low flow speeds inside the streamer seem to still exist even at 7.14 $R_\odot$ – far outside the observed extent of closed streamers.

Figure 7 shows the variation of the total magnetic field strength, $(B_r^2 + B_\theta^2)^{1/2}$, across the streamers. The most interesting thing to note in these plots is the enhancement in total field strength on the flanks of the streamers. This is what 'confines' the streamers. The field strength for the $\beta = 0.2$ dipole is seen to vary smoothly, with little distinct evidence of the streamer. This is just another indication that the presence of the plasma has had little effect on the field geometry in this low-β case.

4. Accuracy and Stability of Calculations

This numerical model has been found to be weakly subject to the Courant condition on size of time step. Therefore, the size of the time step decreases as the largest values of the temperature and magnetic field increase – along with the maximum sound and Alfvén speeds anywhere in the grid. Counteracting this, the higher characteristic speeds lead to a somewhat faster relaxation time. However, generally shorter time steps are required for smaller β calculations. The flow speed also plays an important role in determining the relaxation time to a steady state – the initial state is a disequilibrium configuration. This imbalance must have time to be advected from the base through the outer boundary. The physical time this takes can be estimated by taking a typical (but small) value for the flow speed and caculating how long it would take the plasma to flow at this speed from the base to the outer boundary. For example, at 150 km s^{-1}, to 15 $R_\odot$, this takes 18 hours (relaxation times we have used here are given in Figure 1).

A second consideration is gridpoint resolution. The grid used in these examples is 4.5° in latitude and about 0.24 $R_\odot$ in radius near the base – increasing slowly with radius. This is sufficient to adequately resolve the geometry and flow on the scale shown in Figure 2. However, if finer scale information is required in, for example, the core of the streamers, a denser grid would be required.

Always a serious consideration in these time-dependent, non-Cartesian MHD calculations is the conservation of magnetic flux – that $\nabla \cdot \mathbf{B} = 0$ is maintained

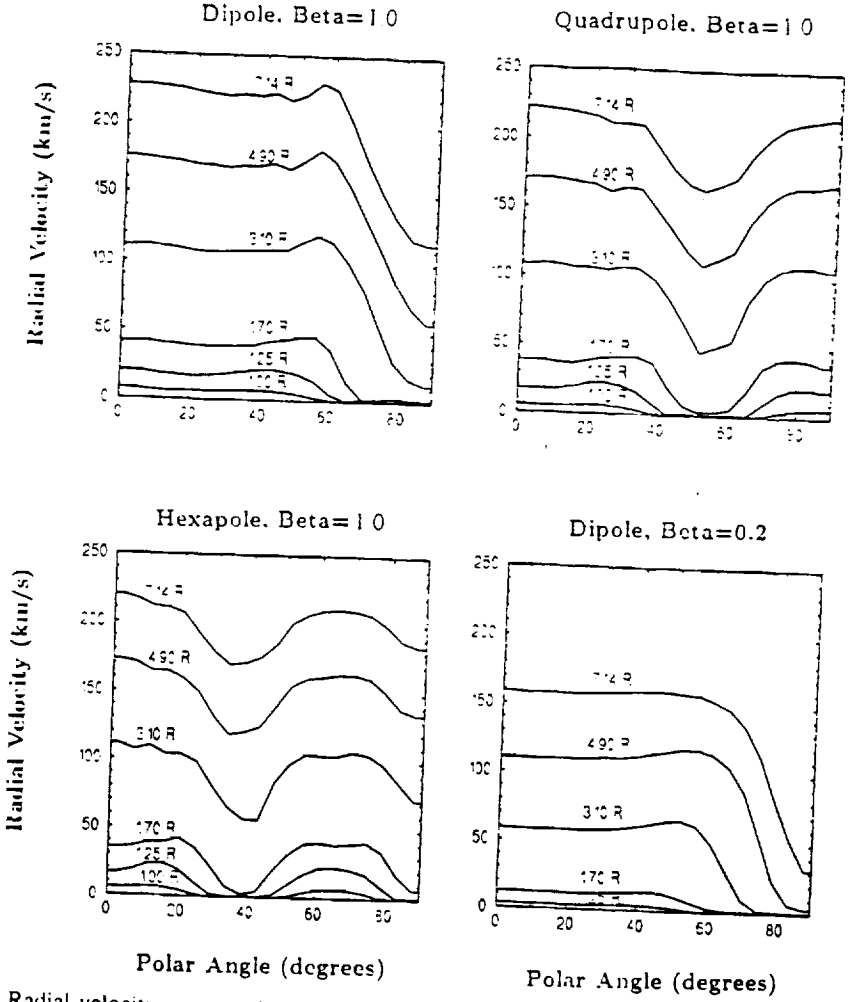

Fig. 6. Radial velocity versus polar angle, between the pole and the equator. Each curve, plotted for different heliocentric distance, is labelled in the same manner as in Figure 5. The velocity in the magnetically closed regions is essentially zero. The reason it is not identically zero is that there is a small amount of numerical diffusion – quite small as indicated by the velocity being less than 10 km s^{-1} inside the $\beta = 1.0$ dipole streamer at 2.30 $R_\odot$.

at all times. The condition is maintained here through accurate differencing rather than a self-correcting scheme. No anomalous acceleration due to errors in flux conservation is apparent in the results. The numerical scheme is pressure-based so it is limited by stability to large and moderate β values (e.g., $\beta \geq 0.1$) – which turns out to be the same restriction for maintaining $\nabla \cdot \mathbf{B} = 0$ to the required degree.

Finally, the energy equation

ORIGINAL PAGE IS
OF POOR QUALITY

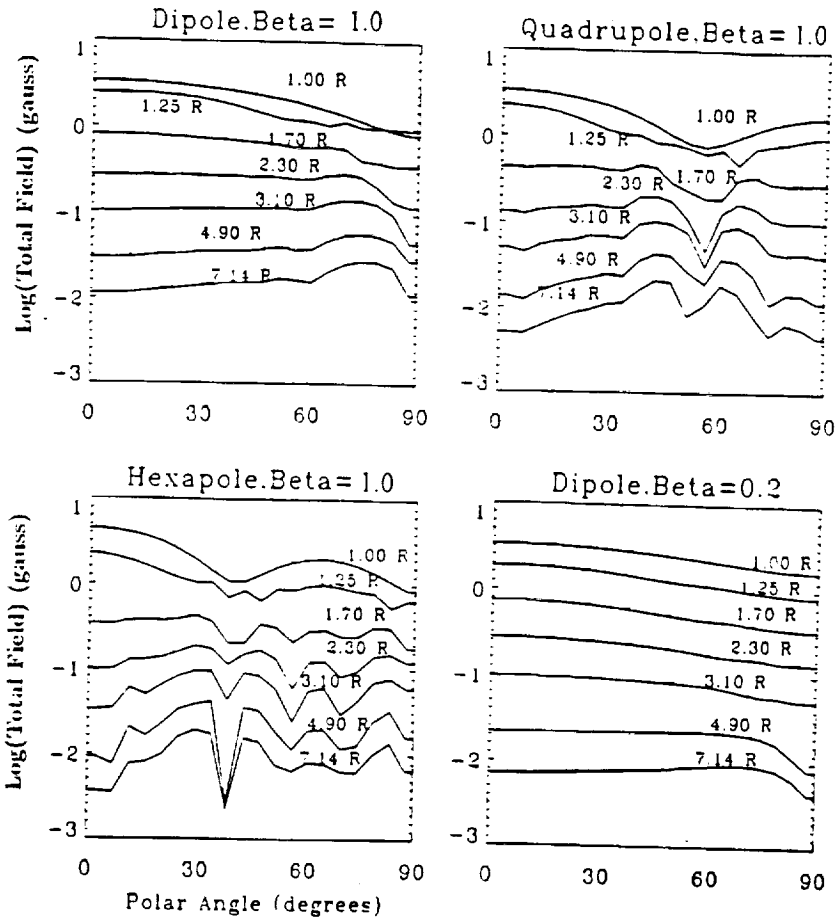

Fig. 7. The total magnetic field, $(B_r^2 + B_\theta^2)^{1/2}$, versus polar angle, between the pole and the equator. Each curve, plotted for different heliocentric distance, is labelled in the same manner as in Figure 5. The field in the vicinity of the current sheet above the cusp in the streamers has a greatly reduced amplitude, as would be expected. The effect is amplified above the mid-latitude streamers.

$$\left(\frac{\partial}{\partial t} + \mathbf{v} \cdot \nabla\right)\left(\frac{p}{\rho^\gamma}\right) = 0$$

reduces to $\mathbf{v} \cdot \nabla(p/\rho^\gamma) = 0$ when a steady state is reached, which means that (p/ρ^γ) is then a streamline constant. This becomes an analytic test of the achievement of a steady-state solution in our case. The boundary values of p and ρ are the same at all latitudes. Therefore, $(p/\rho^\gamma) = 0$ has the same value everywhere in the computation regime as it has on the boundary if a steady state has been reached. We have checked this for the cases shown in Figure 2 and find that for the dipole and quadrupole it is constant to within a maximum of 1% and for the hexapole it is constant to within a maximum of 4% (average values over the whole grid are less than 1% in all cases).

ORIGINAL PAGE IS
OF POOR QUALITY

5. Discussion

The new feature of this model, with respect to analogous simulations, is the extension of the outer boundary to 15 $R_\odot$. This is not a conceptual advance, but this and the stability and ruggedness of the code make it very useful for simulating realistic coronal conditions. We present new results for quadrupole and hexapole fields, with their accompanying mid-latitude streamers and open magnetic field regions. The Alfvén speed ranged between 800 km s^{-1} and a few tens of km s^{-1}. This is lower than is believed appropriate for the corona (Suess, 1988), but we expect our model will now enable simulations with higher Alfvén speeds.

When comparing our results to those of Steinolfson, Suess, and Wu (1982; henceforth referred to as SSW), an interesting and important difference becomes apparent. In the present calculation, we have held the density and temperature constant at the base, allowing the velocity (and, hence, the mass flux) to 'float' with time in accordance with the compatbility relations determining the velocity from the solution inside the computational domain. In contrast, SSW hold the temperature and velocity constant at the base and allow the density to change according to the compatibility relationships. SSW determine the location of the streamer by locating closed field lines and allowing the velocity to decrease to zero at the feet of these field lines. A consequence is that inside the streamer, the final density is considerably higher than the initial density and this is the primary reason for the quantitative differences between their results and ours.

There is an important consequence of this difference in boundary conditions between SSW and the present calculation: the plasma β is computed using the temperature, density, and magnetic field at the equator and at 1 $R_\odot$. This is invariant in the present calculation, but in SSW this number is different in the final, steady state than at the beginning: there β was computed using the initial values. Therefore, in SSW in the steady-state solution is actually larger than stated for each example they did. Thus, our calculation for a dipole with $\beta = 0.2$ (case (d)) corresponds to cases for $\beta \leq 0.1$ in SSW. We feel that the way we have done the analysis more closely corresponds to what occurs and what is physically known for the Sun and therefore leads to a more precise definition of the problem. So, we conclude that the present study has demonstrated a preferable treatment of the boundary conditions in comparison to earlier calculations.

A consequence of the precise examples we have done in cases (a) through (d), with constant temperature and density, is the flow speed and high density in the magnetically open regions – in comparison to what is believed to be the case in solar coronal holes. This is a natural consequence of using a polytropic gas in which the flow speed is strongly dependent on base temperature. It also does not reflect suggestions from analysis of Skylab data that densities at the base of coronal holes may be a factor of two smaller than at the base of streamers (G. Noci, private communication). In a continuation of this study, we will produce models with varying temperature and density at the base. The variation in temperature

ORIGINAL PAGE IS
OF POOR QUALITY

will, because it is an 'effective temperature', reflect a difference in energy balance and distribution between the base of coronal holes and streamers instead of a true temperature difference.

Acknowledgements

AHW and STW are supported by NASA Grant NAGW-9. STS has been supported by a grant from the Cosmic and Heliospheric Physics of NASA. GP acknowledges support from ASI (Italian Space Agency) and the University of Alabama in Huntsville.

Appendix. The Inner Boundary Conditions According to the Projected Normal Characteristic Method: a 2D Case

The inner boundary conditions are obtained according to the method of projected characteristics (Nakagawa, Hu, and Wu, 1987) with the FICE algorithm (Hu and Wu, 1984). For the two-dimensional case, the Alfvénic mode does not exist, therefore, there are six eigenvalues. These six eigenvalues lead to six projected normal characteristics and to six compatibility equations (see Wang, 1992; for derivation). At the inner boundary, since $v_r \geq 0$ and $v_r < V_s, V_f$, the characteristics $dr/dt = v_r - V_s$ and $dr/dt = v_r - V_f$ are towards the lower boundary from interior (i.e., outgoing) and need to be considered. There are four incoming characteristics (v_r, $v_r + V_s$, $v_r + V_f$, and one that is degenerate because of the model symmetries), so four variables can be specified at the boundary. Two other variables need to be calculated from related compatibility equations. We choose the values of B_r, B_θ, ρ, and T to be specified, leaving two quantities (i.e., v_r and v_θ) to be computed according to following compatibility equations:

$$\frac{\partial v_r}{\partial t} = \frac{V_s B_- + V_f C_-}{\rho V_s V_f (V_s^2 - V_f^2)}, \tag{A.1}$$

$$\frac{\partial v_\theta}{\partial t} = \frac{V_s (v_A^2 - V_s^2) B_- - V_f (V_f^2 - V_A^2) C_-}{V_s V_f (V_f^2 - V_s^2) B_r B_\theta}. \tag{A.2}$$

with the corresponding variables simplified in two dimensions as follows:

$$v_A^2 = b_r^2 = \frac{B_r^2}{\rho}, \tag{A.3}$$

$$a^2 = \gamma R T, \tag{A.4}$$

$$b^2 = \frac{(B_r^2 + B_\theta^2)}{\rho}, \tag{A.5}$$

$$V_f^2 = \frac{1}{2} a^2 + b^2 + [(a^2 + b^2)^2 - 4 a^2 b_r^2]^{1/2}, \tag{A.6}$$

$$V_s^2 = \frac{1}{2}a^2 + b^2 + [(a^2 + b^2)^2 - 4a^2 b_r^2]^{1/2} . \tag{A.7}$$

$$\begin{aligned} B_- = {} & \rho(V_f^2 - V_A^2)V_f(v_r - V_f)\frac{\partial v_r}{\partial r} - B_r B_\theta V_f(v_r - V_f)\frac{\partial v_\theta}{\partial r} - \\ & -(V_f^2 - V_A^2)(v_r - V_f)\frac{\partial p}{\partial r} - B_\theta V_f^2(v_r - V_f)\frac{\partial B_\theta}{\partial r} + \\ & +\rho(V_f^2 - V_A^2)V_f V_\theta \frac{1}{r}\frac{\partial v_r}{\partial \theta} - \frac{B_\theta v_\theta V_f^2}{r}\frac{\partial B_\theta}{\partial \theta} - \\ & -[\rho a^2(V_f^2 - V_A^2) + B_\phi^2) + B_r B_\theta V_f v_\theta]\frac{1}{r}\frac{\partial v_\theta}{\partial \theta} - \\ & -\left[v_\theta(V_f^2 - V_A^2) + \frac{B_r B_\theta V_f}{\rho}\right]\frac{1}{r}\frac{\partial p}{\partial \theta} - \frac{B_\theta v_f^3}{r}\frac{\partial B_r}{\partial \theta} - \\ & -\frac{v_r V_f^2}{r}[2\rho(V_f^2 - V_A^2) - B_\theta^2] - \frac{V_f^2 B_\theta v_\theta}{r}(B_r + B_\theta \operatorname{ctg}\theta) - \\ & -\frac{v_\theta V_f^2}{r}[\rho(V_f^2 - V_A^2) - B_\theta^2]\operatorname{ctg}\theta - \frac{v_r v_\theta B_\theta B_r V_f}{r} - \\ & -\frac{\rho V_f V_\theta^2}{r}(V_f^2 - V_A^2) + \frac{V_f^3 B_\theta^2}{r} + \rho g(V_f^2 - V_A^2)V_f . \end{aligned} \tag{A.8}$$

$$\begin{aligned} C_- = {} & \rho(V_A^2 - V_s^2)V_s(v_r - V_s)\frac{\partial v_r}{\partial r} - B_r B_\theta V_f(v_r - V_s)\frac{\partial v_\theta}{\partial r} - \\ & -(V_A^2 - V_s^2)(v_r - V_s)\frac{\partial p}{\partial r} + B_\theta V_s^2(v_r - V_s)\frac{\partial B_\theta}{\partial r} + \\ & +\rho(V_A^2 - V_s^2)V_s V_\theta \frac{1}{r}\frac{\partial v_r}{\partial \theta} - \frac{B_\theta v_\theta V_s^2}{r}\frac{\partial B_\theta}{\partial \theta} - \\ & -[\rho a^2(V_A^2 - V_s^2) - B_\phi^2) + B_r B_\theta V_s v_\theta]\frac{1}{r}\frac{\partial v_\theta}{\partial \theta} - \\ & -\left[v_\theta(V_A^2 - V_s^2) + \frac{B_r B_\theta V_f}{\rho}\right]\frac{1}{r}\frac{\partial p}{\partial \theta} + \frac{B_\theta v_s^3}{r}\frac{\partial B_r}{\partial \theta} + \\ & +\frac{v_r V_s^2}{r}[2\rho(V_s^2 - V_A^2) + B_\theta^2] - \frac{V_s^2 B_\theta v_\theta}{r}(B_r + B_\theta \operatorname{ctg}\theta) + \\ & +\frac{v_\theta V_s^2}{r}[\rho(V_s^2 - V_A^2) - B_\theta^2]\operatorname{ctg}\theta + \frac{v_r v_\theta B_\theta B_r V_s}{r} - \\ & -\frac{\rho V_s V_\theta^2}{r}(V_A^2 - V_s^2) - \frac{V_s^3 B_\theta^2}{r} + \rho g(V_A^2 - V_s^2)V_s g . \end{aligned} \tag{A.9}$$

Since the ideal MHD equations have been used, flow is parallel to the magnetic field lines. Thus we determine B_θ from the relation $B_r v_\theta = v_r B_\theta$.

ORIGINAL PAGE IS
OF POOR QUALITY

References

Allen, C. W.: 1955, *Astrophysical Quantities*, Cambridge University Press, London.

Guo, W. P., Wang, J. F., Liang, B. X., and Wu, S. T.: 1992, in Z. Švestka, B. V. Jackson, and M. E. Machado (eds.), 'Eruptive Solar Flares', *IAU Symp.* **133**, 381.

Hu, Y. Q. and Wu, S. T.: 1984, *J. Comput. Phys.* **55**(1), 33.

Munro, R. J. and Jackson, B. V.: 1977, *Astrophys. J.* **213**, 874.

Nakagawa, Y., Hu, Y. Q., and Wu, S. T.: 1987, *Astron. Astrophys.* **179**, 354.

Parker, E. N.: 1963, *Interplanetary Dynamical Processes*, Interscience, New York.

Pneuman, G. and Kopp, R. A.: 1971, *Solar Phys.* **18**, 258.

Steinolfson, R. S.: 1989, in J. H. Waite, Jr., J. L. Burch, and R. L. Moore (eds.), *Geophys. Monograph* **54**, 269, American Geophysical Union, Washington, D.C.

Steinolfson, R. S.: 1991, *Astrophys. J.* **382**, 677.

Steinolfson, R. S., Suess, S. T., and Wu, S. T.: 1982, *Astrophys. J.* **255**, 730.

Suess, S. T.: 1979, *Space Sci. Rev.* **23**, 159.

Suess, S. T.: 1988, in R. C. Altrock (ed.), *Solar and Stellar Coronal Structure and Dynamics. Proceedings of the 9th Sacramento Peak Summer Symp.*, Sunspot, New Mexico, p. 130.

Suess, S. T., Richter, A. K., Winge, C. R., Jr., and Nerney, S.: 1977, *Astrophys. J.* **217**, 296.

Sun, M. T.: 1991, Ph.Dissertation, University of Alabama in Huntsville.

Wang, A.-H.: 1992, Ph.Dissertation, University of Alabama in Huntsville.

SEE ALSO
93N31360

Lα INTENSITY IN CORONAL STREAMERS

G. NOCI
Dipartimento di Astronomia e Scienza dello Spazio, Università di Firenze, Italy

G. POLETTO
Osservatorio Astrofisico di Arcetri, Largo Enrico Fermi, 5, 50125 Firenze, Italy

S. T. SUESS
NASA Marshall Space Flight Center, SSL/ES52, Huntsville, AL 35812, U.S.A.

and

A.-H. WANG and S. T. WU
Center for Space Plasma and Aeronomic Research,
The University of Alabama in Huntsville, Huntsville, AL 35899, U.S.A.

(Received 21 August, 1992; in revised form 5 February, 1993)

Abstract. White-light images are presently the primary source of information on physical conditions in the solar corona at distances greater than a few tenths of a solar radius above the limb. As a consequence, we still only have an incomplete description of structures extending beyond the solar limb. In particular, streamers, although observed for decades, represent a poorly known phenomenon. SOHO, to be launched in 1995, will be able to make long-term observations of these features up to heights of a few $R_\odot$, both in white light and UV. In this paper we present simulations of Lα intensity in coronal streamers, based on the two-dimensional (2-D) model developed by Wang *et al.* (1992, 1993) via a time-dependent numerical relaxation approach. Because the model is 2-D, we make an *a priori* hypothesis about the extension of streamers in the third dimension. Lα data, obtained from a rocket (Kohl *et al.*, 1983), allowed us to identify a shape which fits the observations. We consider streamers with different magnetic field configurations and at different position angles with respect to the plane of the sky to illustrate how different regions along the line of sight contribute to the emergent intensity. Our purpose is twofold: to provide guidelines for UVCS observational operations and to explore the parameter space in order to understand the role of geometric factors and of the physical state of the corona in determining the overall streamer brightness. We conclude by showing how the results guide the future development of streamer models.

1. Introduction

Before the advent of coronagraphs, eclipses offered the only means to observe the solar corona. In spite of the short time over which coronal structures were visible, their basic characteristics have been reproduced in beautiful drawings (see, e.g., Foukal, 1990), which prove that streamers – the most prominent white-light coronal features – had been known and observed for decades. Following earlier balloon-borne coronagraph experiments (Newkirk and Bohlin, 1965; Dollfus, Fort, and Morel, 1968), different techniques have become available, and radio telescopes (see, e.g., Gopalswamy, Kundu, and Szabo, 1987) and space experiments (see, e.g., for Skylab, Hildner *et al.*, 1975; Poland, 1978; for SMM, Illing and Hundhausen, 1986; Kahler, 1991) collected a wealth of data on these large-scale features, which, nevertheless, remain poorly known. We know that streamers, at the time of solar activity minimum, are concentrated along the solar equator in a belt, which broadens

Solar Physics **147:** 73–96, 1993.
© 1993 *Kluwer Academic Publishers. Printed in Belgium.*

PRECEDING PAGE BLANK NOT FILMED

to cover a wider range of latitudes, at other epochs. We know that streamers are stable structures, which may last for several rotations (see, e.g., Poland, 1978). However, we know little about the formation, or the disruption, of streamers: we have only a few observations, for instance, of the contraction of a post/mass ejection structure to form a streamer (see, e.g., Illing and Hundhausen, 1986). As to the physical properties of streamers, our knowledge is limited, as we will discuss later on, to an incomplete understanding of their density structure. This situation may in part be ascribed to the fact that spectroscopic instruments were unable to operate at the large heights reached by streamers, which therefore have been observed mainly in white light. On the other hand, the solar community seemed to have little interest in streamers: no review article has been dedicated to these structures for years, notwithstanding the steady proliferation of scientific papers.

However, streamers are relevant to a number of problems. They represent the ideal structures to investigate the differences in temperature, density, flow velocities, and magnetic field structure between magnetically closed and open areas and to gain some insight into the physical conditions of current sheet regions, which purportedly occur in streamers. Koutchmy (1988) pointing out how tangential discontinuities are almost systematically parts of large streamers, noticed how their analysis would offer the best estimate of the magnetic field value in the corona, provided that the temperature keeps constant across the discontinuity. The capabilities of streamers in providing data crucial to the solution of these questions have hardly been exploited.

In solar wind physics streamers play an ambiguous role. It has been claimed (see, e.g., Feldman *et al.*, 1981) that they constitute the major source of the interstream and low speed solar wind, but we know neither how large is the contribution of streamers to the solar wind mass flux, nor the geometry of the open field lines associated with streamers, along which the wind purportedly propagates. The reason for the depletion of helium, which seems to accompany the slow wind from streamers (see, e.g., Gosling *et al.*, 1981), is not well understood.

In the future, SOHO instrumentation will offer us a means to learn more about these structures. In particular, UVCS will be able to make EUV observations of streamers, up to $\leq 10\, R_\odot$, over an extended period of time, thus allowing us to get a new kind of data whose capabilities have not yet been explored. In order to provide guidelines to be used in devising UVCS observational sequences, we present, in this paper, a variety of simulated, typical Lα observations of streamers. As a basis for our simulations, we adopt the two-dimensional streamer model, developed by Wang *et al.* (1992, 1993), which is summarized in Section 2. After comparing, in Section 3, the model predictions with observations of densities in streamers, we calculate, in Section 4, the Lα emission from different streamer configurations and, in Section 5, we simulate Lα observations of a streamer carried around by solar rotation. Finally, in the Discussion, we illustrate some future development of our work.

2. The Streamer Model

The physical streamer models that we use for calculating Lα intensities are the result of a numerical simulation of global coronal structure. The simulation is a solution of the magnetohydrodynamic equations for two-dimensional, axisymmetric, single fluid, polytropic, time-dependent flow. The steady state is found by starting with an essentially arbitrary initial state having the desired boundary conditions and allowing a relaxation in time until the solution is no longer changing. The resulting model is therefore assured both of being a self-consistent solution for the specified physical boundary conditons and of being stable. The model, since axisymmetric, describes a single continuous streamer that extends all the way around the Sun at a specific latitude. The simulation is further described by Wang *et al.* (1992, 1993).

The boundary conditions at 1 $R_\odot$ are that the temperature and density are constant in latitude and that the vector magnetic field is a potential magnetic field. Three magnetic field geometries are used: a dipole, a quadrupole, and a hexapole; the scalar potentials are proportional to $P_2(\cos\theta)$, $P_3(\cos\theta)$, and $P_4(\cos\theta)$, respectively. There are two dimensionless numbers: the polytropic index, γ, and the ratio of internal to magnetic energy densities, β. We use $\gamma = 1.05$ in all cases, $\beta = 1.0$ for all three field geometries, and, in addition, do a dipole calculation for $\beta = 0.2$. In these cases, β is evaluated at 1.0 $R_\odot$ at the equator, where the field strength is 1.67 G for both $\beta = 1.0$ and $\beta = 0.2$. For the high β case, the base temperature and density are 1.8×10^6 K and 2.25×10^8 cm^{-3}. For the low β case, they are 1.44×10^6 K and 5.61×10^7 cm^{-3}. The three magnetic field geometries naturally lead to a single equatorial streamer, a mid-latitude streamer, and both an equatorial and a mid-latitude streamer for the dipole, quadrupole, and hexapole, respectively.

The simulation extends from 1.0 $R_\odot$ to 15.0 $R_\odot$ and from pole to equator. The boundary conditions are symmetric about the equator, so a solution in the opposite hemisphere is not necessary. In this paper, we only quote results inside 7.0 $R_\odot$ because this covers the range over which closed streamer structures most frequently are observed. There are 20 grid points between the pole and equator, 27 gridpoints between 1.0 $R_\odot$ and 7.0 $R_\odot$. The initial state consists of a potential field and the solution for a spherically-symmetric wind for the given base temperature, density, and polytropic index. The initial temperature, density, and velocity profiles are shown in Figure 1. The temperature curves appear irregular due to the small change in temperature over the relatively large radial range – a consequence of the polytropic index being near unity. Only three significant figures were retained after the calculation so what is seen here is essentially roundoff error.

Results for the steady-state solutions, given the above initial conditions, are ordered according to the four cases treated: (a) dipole, $\beta = 1.0$, (b) quadrupole, $\beta = 1.0$, (c) hexapole, $\beta = 1.0$, and (d) dipole, $\beta = 0.2$. The steady-state magnetic field geometries are shown in Figure 2. Here is seen the well-known property that the flow is nearly radial beyond 3–4 $R_\odot$. The streamers are those volumes which are

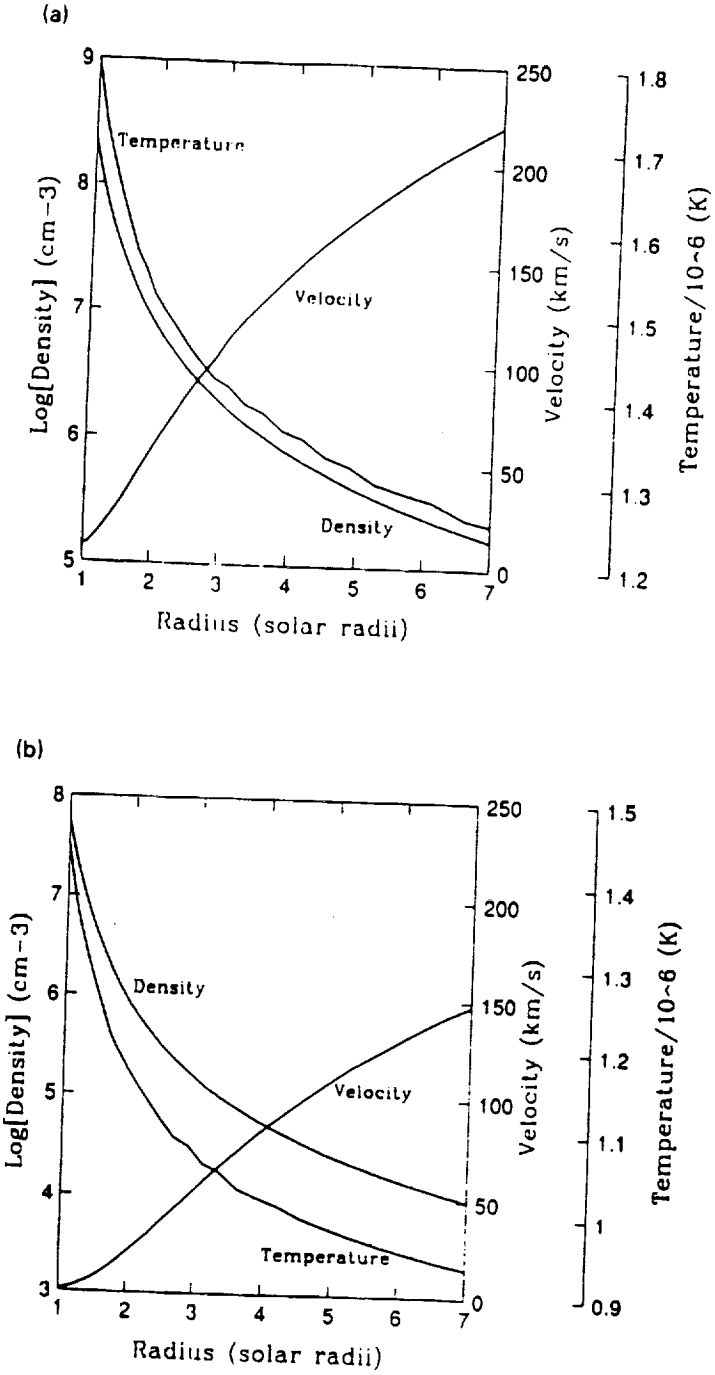

Fig. 1a–b. Density, temperature, and velocity profiles in radius of the initial ($t = 0$) state in the relaxation. (a) Profiles for the $\beta = 1.0$ cases. (b) Profiles for the $\beta = 0.2$ case. Note that, except for the velocity scales, the scales differ between the two panels. The irregularities in the temperature profiles are roundoff errors.

magnetically closed, and it is evident that relatively small volumes in the streamers remain magnetically closed in comparison to the initial states. These volumes are surrounded by a low-density shell but, as will be shown below, the densities in the large coronal hole-like open regions are otherwise only slightly lower than in the streamers. In each panel of Figure 2, four dotted lines are shown and labelled A, B, C, or D. These lines indicate the positions used to plot variables versus radius in Figures 3 and 4 below.

In displaying results for the physical variables, we will concentrate on the density and the velocity, these being the two variables that determine the Lα intensity. Other variables will only be shown when necessary for physical understanding. Figure 3 shows the density variation in the radial directions labelled in Figure 2. These plots show the relative density – the density divided by the density plotted in Figure 1. Thus, it measures the change in density with respect to a spherical flow profile. Curves D in Figures 3(a), 3(c), and 3(d), and curve C in Figure 3(b) are all profiles cutting through the cores of streamers. It is seen that there is a density enhancement in the core ranging from ≈75% for the low β dipole down to 20% for the equatorial streamer in the hexapole. On the flanks of streamers, for example as shown by curve C in Figure 1(a), there is a density deficit. Nevertheless, in the centers of open regions, the density deficit is always less than ≈20%. This is an important point to note in applying this specific model to computing Lα intensities, and we will return to it later. Also apparent in this figure, and the ones that follow showing variation of other variables with radius, is a rapid fluctuation from one grid point to the next for the first two or three points above the base. This is a consequence of the type of extrapolation used to determine those variables at the boundary which are calculated from the interior solution instead of fixed by the boundary conditions (Wang *et al.*, 1992, 1993; Steinolfson, Suess, and Wu, 1982). The phenomenon has no significant effect on the solution above the fourth grid point and, in particular, no effect above 1.2 $R_\odot$ – the minimum radius UVCS can observe.

Figure 4 shows the radial velocity along the directions labelled in Figure 2. In addition, the initial state profile is plotted as a dashed line – the same profile as shown in Figure 1. The flow speed is, except for numerical diffusion, identically zero in the streamers. This is obvious from curves D in Figures 4(a), 4(c), and 4(d), and curve C in Figure 4(b). Above the streamers, the velocity is greatly reduced. However, away from the streamers, whether in the center or at the edges of open regions, the flow speed differs little from the initial state.

Taken together, the density and flow speed illustrate that this is not a constant mass flux model – the flow speed at the base varies with polar angle. Therefore, these results appear somewhat different than might be anticipated based on intuition gained from, for example, the calculation by Kopp and Holzer (1976). A rapidly diverging magnetic field does not necessarily lead to a low density and high velocity flow – depending also on whether the rapid divergence occurs below or above the sonic critical point. So, on the flanks of streamers, where rapid field line divergence

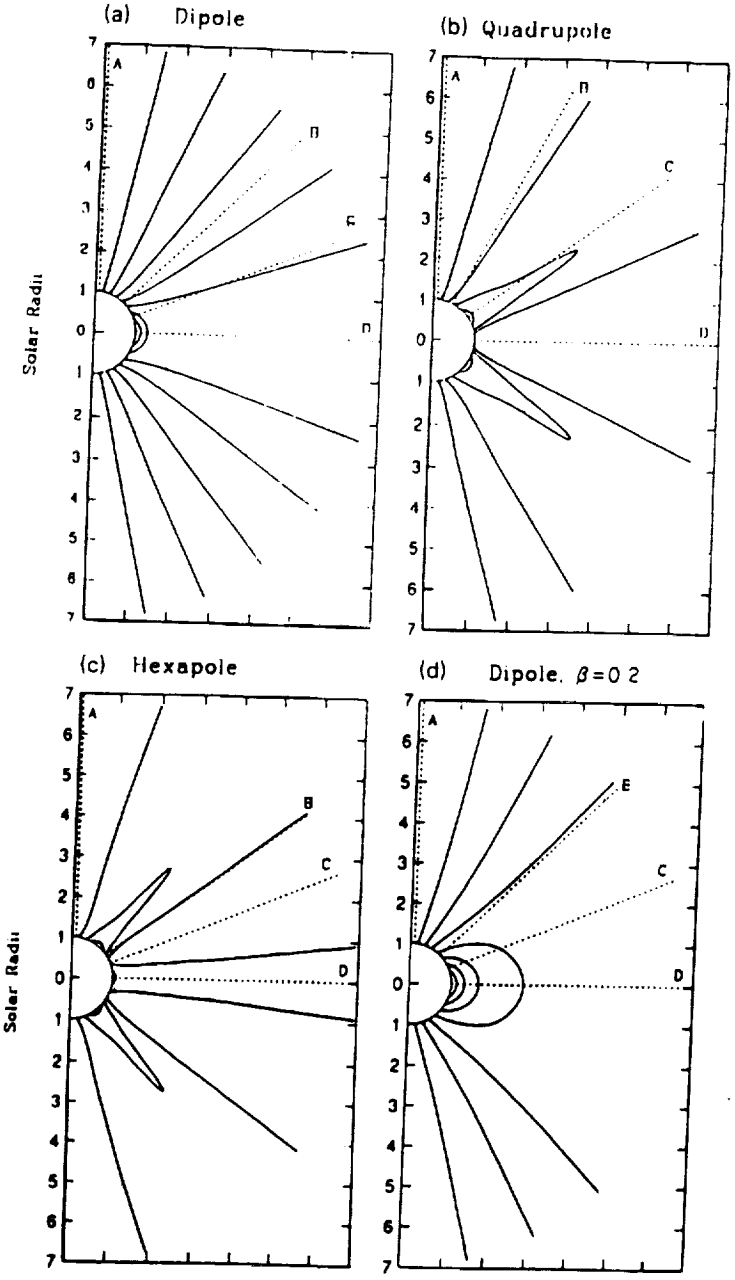

Fig. 2a–d. Magnetic field line plots for the four cases: (a) dipole, $\beta = 1.0$, (b) quadrupole, $\beta = 1.0$, (c) hexapole, $\beta = 1.0$, and (d) dipole, $\beta = 0.2$. The relaxation times allowed to reach these equilibria are: (a) 22.22 hours, (b) 16.67 hours, (c) 18.06 hours, (d) 19.44 hours. In each panel, four dotted lines are labelled 'A, B, C, or D'. These show the radial directions used for plotting certain variables vs radius in succeeding figures. Thus, the quadrupole in plot (b) will have these variables plotted vs radius at the pole (A), at the edge of the polar open region (B), through the mid-latitude streamer (C), and along the middle of the equatorial open region (D).

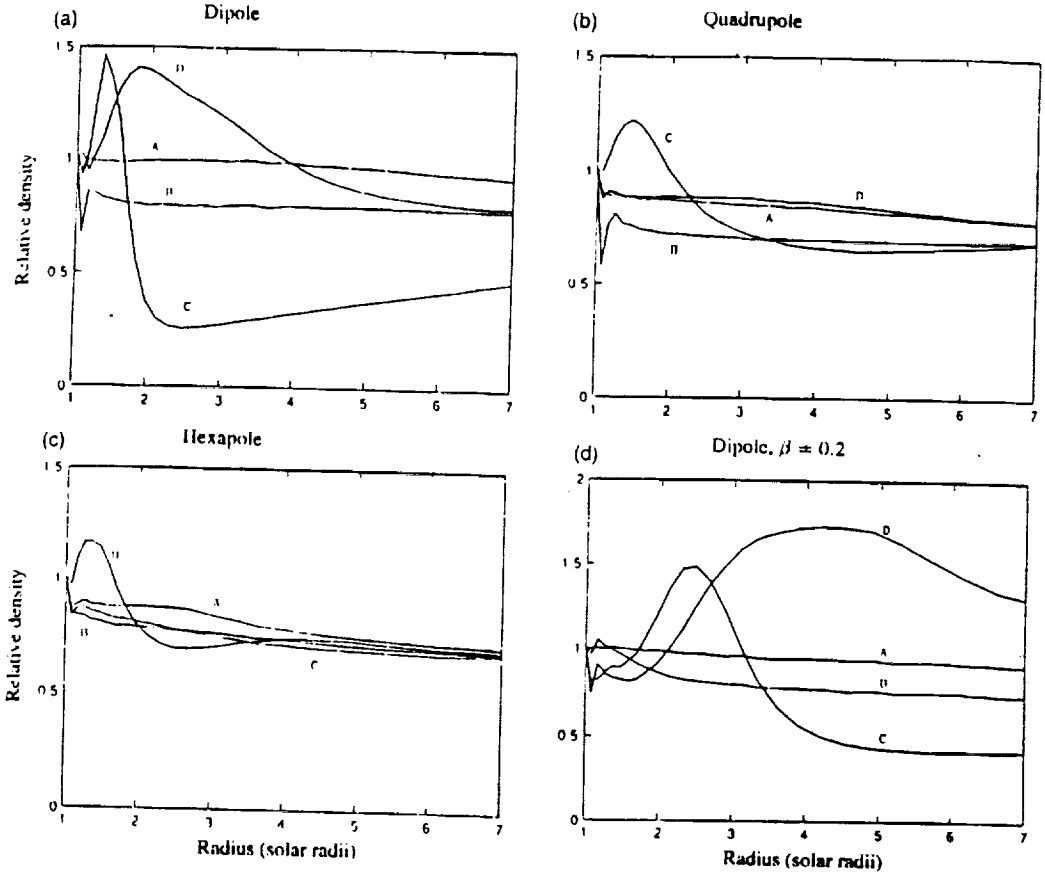

Fig. 3a–d. Density as a function of radius. Each panel is for the corresponding case in Figure 2. The curves are plotted along the directions shown in Figure 2. For example, the four curves in (c), labelled 'A, B, C, D', are along the four directions shown in Figure 2(c) and labelled in the same manner. Densities in each curve have been normalized to their values in the initial profile (Figure 1(a) for (a–c), and Figure 1(b) for case (d)). Hence, a density enhancement is indicated by values greater than unity, and *vice versa*. The density concentrations in the streamers are clearly visible, generally being on the order of 25% to 50% above the initial state.

occurs over a narrow range, the density does become small (as in Figure 3(a), curve C) but the flow speed never gets large (as in Figure 4(a), curve C). The other important thing to note is that the cusp (top of the streamer) in the $\beta = 0.2$ dipole lies at about 6 $R_\odot$. This seems large enough to cover the range of streamer heights expected in the solar corona and therefore we will not concern ourselves with computing models for smaller β-values.

A more complete picture of the behavior of the density can be gained by also considering plots of the density versus polar angle at different heights. These are shown in Figure 5, where each curve is labelled with the heliocentric distance it represents (e.g., 2.30 $R_\odot$ is at 2.30 $R_\odot$). Figure 5(a), the $\beta = 1.0$ dipole, shows the density enhancement in the streamer (polar angle of 90°), the deficit in the adjacent

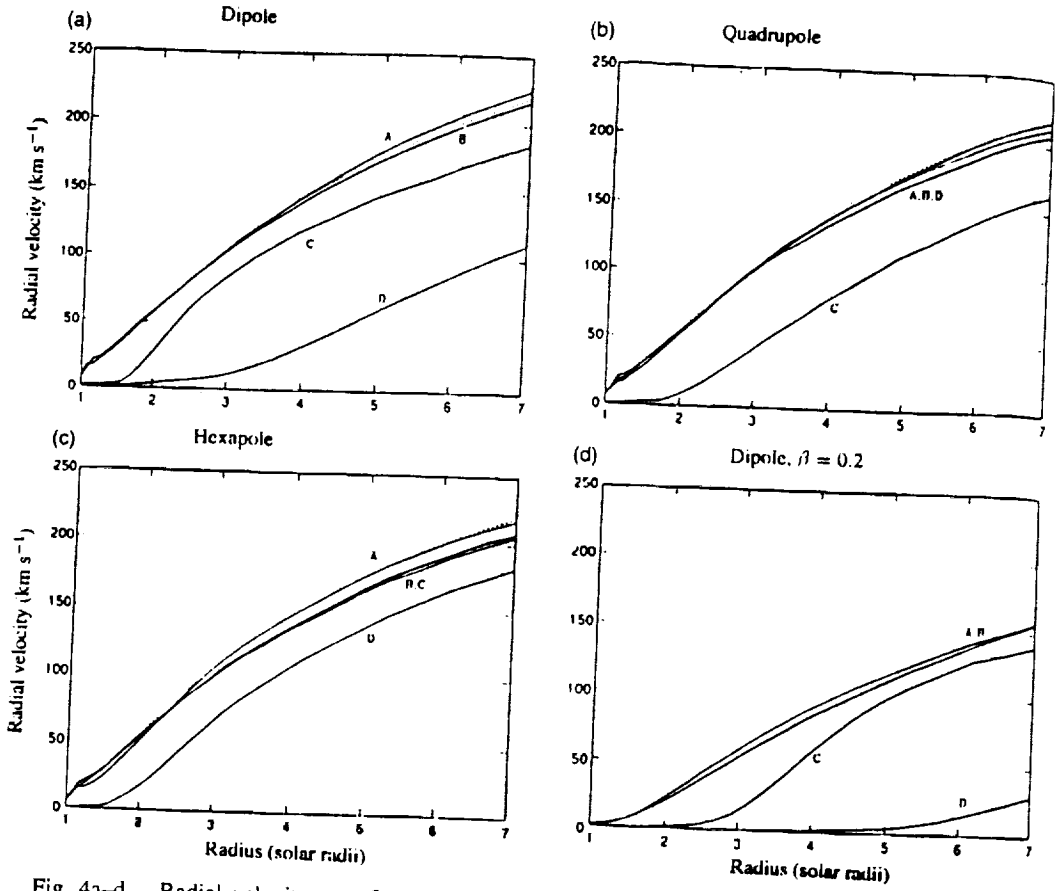

Fig. 4a–d. Radial velocity as a function of radius. Each panel is for the corresponding case in Figure 2. The curves are plotted along the directions shown in Figure 2. For example, the four curves in (c), labelled 'A, B, C, D', are along the four directions shown in Figure 2(c) and labelled in the same manner. The dotted line in these plots is the $t = 0$ profile, the same as shown in Figures 1(a) and 1(b).

trough, and the large plateau of density that is only a small amount less than in the streamer and extending throughout the open region beyond the trough. The behavior of the density around the mid-latitude streamer in the quadrupole, and around the mid-latitude and equatorial streamers in the hexapole is very similar. The only difference for the $\beta = 0.2$ dipole is that the troughs are considerably broader.

The broad, high density plateau in the open region is distinctly unlike a coronal hole. The reason for this is that in this model no effort has been made to generate the high coronal hole flow speeds that lead to low densities. Suess *et al.* (1977) have shown in a similar model that a temperature increase of 50% or more at the center of the open region is necessary in a polytropic model such as this to produce densities like those that are observed in coronal holes.

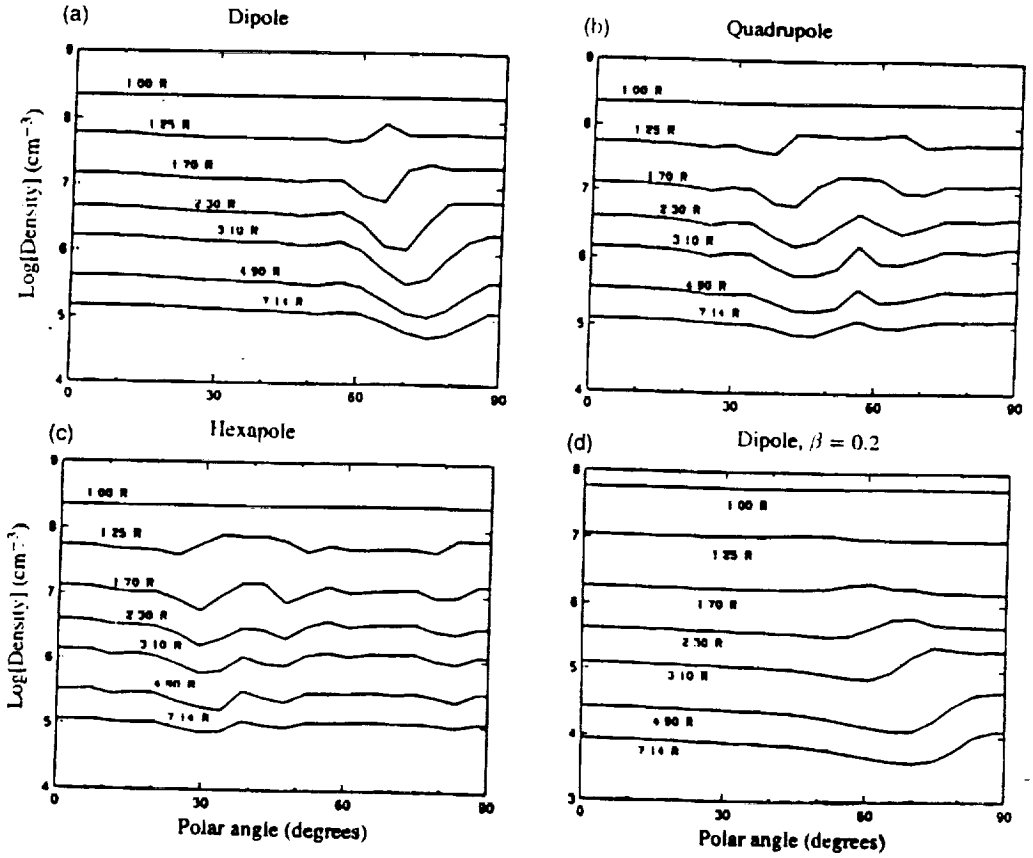

Fig. 5a–d. Density vs polar angle, between the pole (0°) and the equator (90°). Each of the curves is labelled according to the heliocentric distance it refers to. Thus, the curve labelled 1.70 R indicates the density at 1.70 $R_\odot$ heliocentric radius. The density at the base is constant and so the curves there are flat. Above the base, there is a small density enhancement in the streamer (ca. 5% to 50%) and a trough in density at the edge of the streamer. In the middle of the open region, the density is very close to what it was in the initial state (see also Figures 3(a–d)). The reason it is not an order of magnitude smaller, as in an observed coronal hole, is that we have used constant temperature and density at the base. To produce a true coronal-hole-like profile in a polytropic model such as this would have required an increase in the temperature at the base of the open region (Suess *et al.*, 1977). Unless otherwise stated $\beta = 1.0$.

Figure 6 shows the radial velocity plotted in the same manner as the density in Figure 5. The velocity is again seen to be essentially zero inside the streamer(s), whose height decreases rapidly with increasing magnetic field complexity. Thus, while the $\beta = 1.0$ dipole streamer extends to 3 $R_\odot$, neither of the $\beta = 1.0$ hexapole streamers reaches beyond 1.70 $R_\odot$. As indicated above, the flow speed throughout the open region is very similar to the initial state flow speed, excepting for small humps on the flanks of the streamers.

These four models constitute the basis for the calculation of Lα intensities.

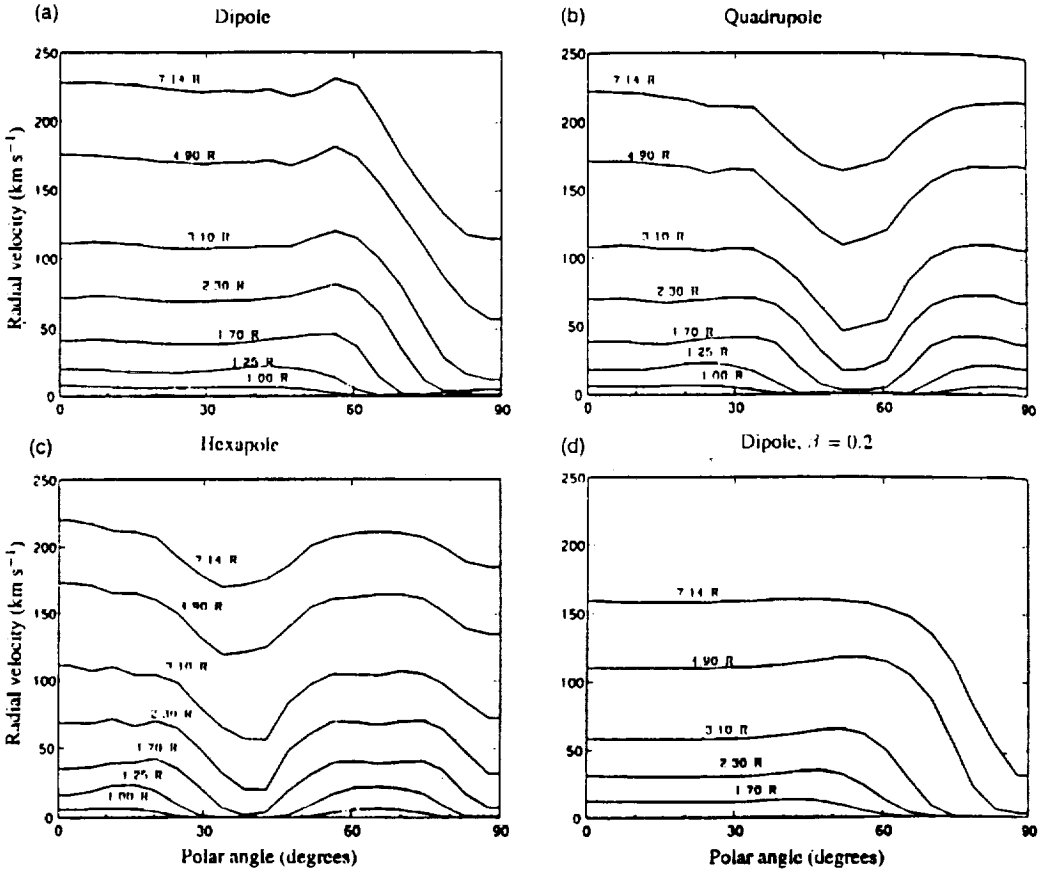

Fig. 6a–d. Radial velocity versus polar angle, between the pole and the equator. Each curve, plotted for different heliocentric distance, is labelled in the same manner as in Figures 5(a–d). The velocity in the magnetically closed regions is essentially zero. The reason it is not identically zero is that there is a small amount of numerical diffusion – quite small, as indicated by the velocity less than 10 km s^{-1} inside the $\beta = 1.0$ dipole streamer at 2.30 $R_\odot$ (top left panel).

In using them, we progress from a straightforward calculation of the intensity measured when viewing the streamer as seen in Figure 2 (i.e., from a position in the magnetic equatorial plane) to other viewing positions and to approximations based on the models. A comparison with intensities from observed streamers is used to guide suggestions for further development of the model by illustrating specific weaknesses in the present four models. We will conclude that a satisfactory physical model of streamers, for the purpose of computing expected UVCS Lα intensities, can be constructed through the application of the present simulation with an appropriate choice of boundary conditions to better represent the dynamics of the solar wind in the open magnetic field regions. This is well within the capabilities of the simulation and will constitute the next stage of this project.

3. Predicted vs Observed Densities

As mentioned in the Introduction, density is the only physical quantity in streamers to be even partially measured. Coronagraph images usually are polarization brightness (pB) images. Because pB is proportional to the line-of-sight integral of the density times a scattering function (Billings, 1966), it is possible from pB images to derive density maps. Usually, this procedure is performed with the Van de Hulst method (1950): that is, the density distribution is supposed to be cylindrically symmetric.

This technique has been used to derive densities from eclipse observations of streamers. Dollfus, Laffineur, and Mouradian (1974) derived densities for a number of streamers observed in the eclipse of February 15, 1961, and compared their values with those pertaining to 13 different streamers, which represent all results published between 1952 and 1972. From this, as well as from a comparison between values derived by different authors for the same streamer, these authors conclude that different determinations for the same structure agree only within a factor 2 and different structures may have densities which differ, at the same altitude, by a factor 10, even in streamers observed at the same eclipse, that is, independently of the epoch of the solar cycle. All densities refer to the streamer axis; Dollfus *et al.* assumed that streamers are axially symmetric and that the distribution of density, in the direction normal to the streamer's axis, is somehow intermediate between being uniform and having a gaussian distribution. Different assumptions on the streamer geometry, or on the distribution of density across a streamer, may possibly explain some of the discrepancies in the values derived for the same structure.

Densities predicted by a theoretical model have to comply with this rather loose observational constraint. Figure 7 gives, on the left panel, the behavior of the density predicted by our model along the axis of equatorial streamers, for dipolar and hexapolar configurations in the case of $\beta = 1.0$, and for dipolar geometry only in the low β ($\beta = 0.2$) case. Densities along the axis of off-equator streamers, both in the quadrupolar and hexapolar geometries, are approximately equal to those along the axis of equatorial streamers and are not shown. In the right panel, we present a figure made up from Figures 16(a–b) of Dollfus *et al.*, which shows, besides all density determinations in streamers between 1952 and 1972, the values derived by Dollfus *et al.* for four different streamers observed in the eclipse of 1961.

The $\beta = 1.0$ curves, cutting through the bundles of curves shown in the right panel, represent correctly the observed densities. As we said, it is not possible to establish, from the data published so far, any trend in the different behavior of individual streamers. For instance, contrary to expectations, the streamer closest to the equator in Dollfus *et al.*'s data (position angle 95°), has lower densities than a mid-latitude streamer (position angle 55°) and the highest densities among those from published results 1952–1972 pertain to a streamer observed close to

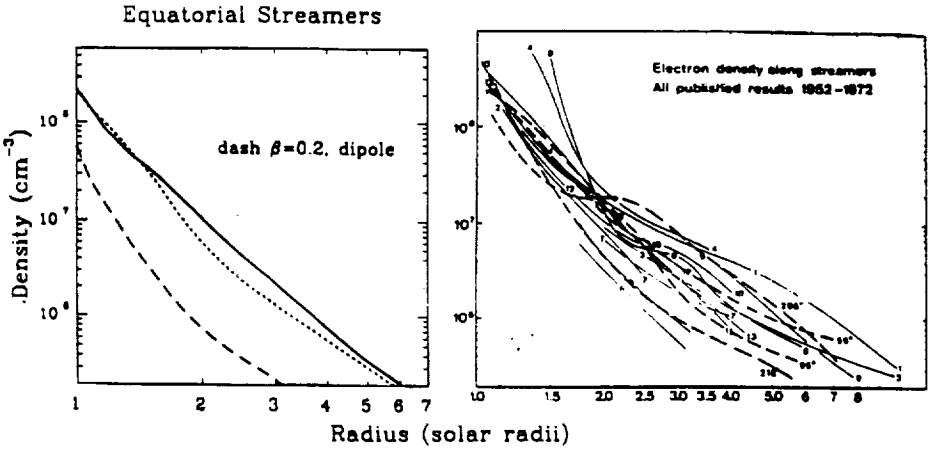

Fig. 7. *Left*: density vs height profiles along the axis of equatorial streamers in dipolar ($\beta = 1.0$ – solid line – and $\beta = 0.2$) and hexapolar geometries as derived from Wang *et al.*'s (1992, 1993) models. *Right*: densities along streamers from all results published between 1952 and 1972 (labels 1–13, solid lines) and along 4 streamers observed at the February 15, 1961 eclipse (dashed lines, labelled by their position angles). See Figures 16(a–b) of Dollfus, Laffineur, and Mouradian (1974) for further information on this panel.

the activity minimum (curve 4, February 5, 1962 eclipse). Hence, we can only conclude that the $\beta = 1.0$ curves are *consistent* with observed density profiles in coronal streamers. This conclusion is confirmed by a comparison of the radial density distribution predicted by our model with densities derived from Clark Lake Radioheliograph streamer observations (Gopalswamy, Kundu, and Szabo, 1987). This comparison is limited to the lower corona, at heights below and near 2 $R_\odot$, and shows (Figure 8) how our predicted density profile lies between densities derived from fundamental and harmonic plasma hypotheses. Finally, we notice that the lack of a definite observational difference between low and high latitude streamers, agrees with predictions from our model.

On the other hand, by comparing the two panels of Figure 7, we conclude that our $\beta = 0.2$ case is not realistic because densities are too low and the cusp is far too high. Nevertheless, the $\beta = 0.2$ curve shows a marked change in its slope that is not so evident in the $\beta = 1.0$ hexapole streamer, and is altogether absent in the $\beta = 1.0$ dipole streamer, which may reproduce the behavior shown by some of the observed structures. To recover this break in the density profile at higher β probably requires changing conditions outside the streamer. A change in the density gradient of the observed profiles has, in fact, been interpreted in terms of a different behavior of this physical parameter in the region of the streamer's helmets (Dollfus *et al.*, 1974). Obviously, the present simulations do not allow us to predict whether the resulting curve will be capable of reproducing some of the observed density profiles more closely than the high β curve. However, it is likely that structures with differing cusp heights correspond to different β values (Steinolfson, Suess,

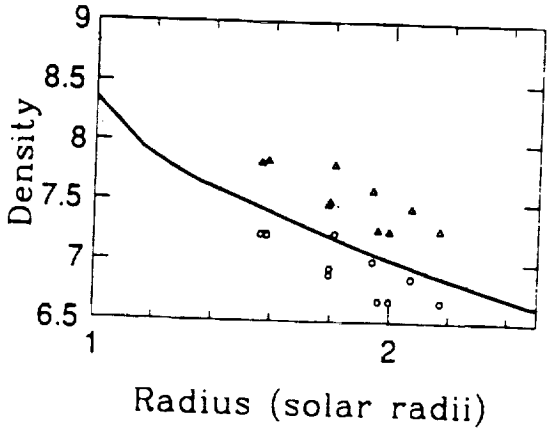

Fig. 8. Predicted density vs height profile along the axis of the equatorial streamer in the case of high β ($\beta = 1.0$) dipolar configuration (solid line) and density determination from radio observations of a streamer obtained on July 27, September 12 and 17, 1985: o represent values of density derived from the hypothesis of fundamental plasma emission. △ represent values of density derived from the hypothesis of harmonic plasma emission.

and Wu, 1982). We conclude that the comparison between model-predicted and observed density profiles points to the need for a thorough analysis of the effect of different boundary conditions in and around streamers on the resulting density profiles.

In the following section we proceed to evaluate the Lα emission in streamers adopting the $\beta = 1.0$ models.

4. Lα Emission from Streamers

The formation of the Lα line in the solar corona has been discussed by a number of authors (Gabriel, 1971; Beckers and Chipman, 1974; Withbroe *et al.*, 1982; Noci, Kohl, and Withbroe, 1987) who showed how coronal Lα observations can be used as a diagnostic tool to determine coronal densities, temperatures, and outflow velocities. Although, at coronal temperatures, only ≈1 proton in 10^7 is tied up in neutral hydrogen, the strongest component of the coronal Lα is due to the scattering of chromospheric Lα photons by neutral hydrogen atoms. An electron scattered component, produced by Thomson scattering of Lα radiation, is about three orders of magnitude weaker than the resonantly scattered component and will be ignored in the following.

The total (i.e., integrated over the line profile) Lα intensity, as observed along the direction **n** is given by

$$I = \frac{hB_{12}\lambda_0}{4\pi} \int_{-\infty}^{\infty} N_1 \, dx \int_{\Omega} p(\varphi) \, d\omega' \int_{0}^{\infty} I_{\text{chrom}}(\lambda, \mathbf{n}')\Phi(\lambda - \lambda_0) \, d\lambda \,, \qquad (1)$$

where h is the Planck constant, B_{12} the Einstein coefficient for the line, λ_0 the rest value for the central wavelength λ of the Lα transition, and N_1 the number density of hydrogen atoms in the ground level; the unit vector $\mathbf{n}$ is along the line of sight x and the unit vector $\mathbf{n}'$ is along the direction of the incident radiation; $p(\varphi)\,\mathrm{d}\omega'$ – where ω' is the solid angle around $\mathbf{n}'$ – is the probability that a photon travelling along the direction $\mathbf{n}$ was travelling, before scattering, along the direction $\mathbf{n}'$; Ω is the solid angle subtended by the chromosphere at the point of scattering; I_{chrom} is the exciting chromospheric radiation and Φ is the coronal absorption profile. In the following we assume that the intensity of the chromospheric Lα radiation is constant across the solar disk and that the velocity distribution of the scattering hydrogen atoms is Maxwellian. The dependence of the Lα scattering process on the angle has been taken from Beckers and Chipman (1974) and we adopted the value given by Gabriel (1971) for the ratio between the neutral hydrogen density and the proton density at different temperatures (because of the low coronal density all hydrogen atoms are assumed to be in the ground level, therefore $N_{\mathrm{H}}/N_p = N_1/N_p$). This is not entirely correct, since temperatures in our model are 'effective' temperatures, resulting from the polytropic index used in the energy equation. We will come back to this point in Section 6.

In order to evaluate the Lα intensity in coronal streamers from Equation (1), we need to know how streamers extend in the third dimension. Because our models are axisymmetric, it is realistic to assume that they give the distribution of physical parameters in a meridional plane, identified with the plane of the sky and normal to the line of sight. If we focus on the dipolar model, we recognize that its geometrical configuration is highly reminiscent of the conditions observed at solar minimum, when streamers are concentrated along the equator. Therefore, as a first hypothesis, we assume that streamers extend all the way around the equator, in a continuous belt, and calculate, on the basis of Equation (1), the radial distribution of Lα intensity in a dipolar geometry. To this end, in the following, densities along the line of sight are considered equal to those given by the model at the same latitude and radial distance. Figure 9 gives the radial profile (solid line) of the Lα intensity, evaluated along the streamer axis (which, in a dipolar geometry, lies in the equatorial plane) up to a height of 4.5 $R_\odot$. Values at larger distances are not given, since, beyond that height, field lines are open and the Lα brightness would no longer originate in the streamer. Moreover, open-field regions are not described realistically in our simulations, their density being definitely overestimated (see Wang *et al.*, 1992, 1993, for further comments on this point). This is apparent also from the slope of the intensity vs distance curve, which keeps constant over all the computational domain as if densities decrease linearly with distance. This is unexpected, as the line of sight, in regions close to the cusp height and beyond it, crosses mostly through the low-density open-field regions. Altogether, the slope of the Lα intensity gradient predicted in the case of a continuous belt of streamers circling the Sun, is open to criticism.

The inaccuracy of the brightness vs distance profile may be ascribed both to

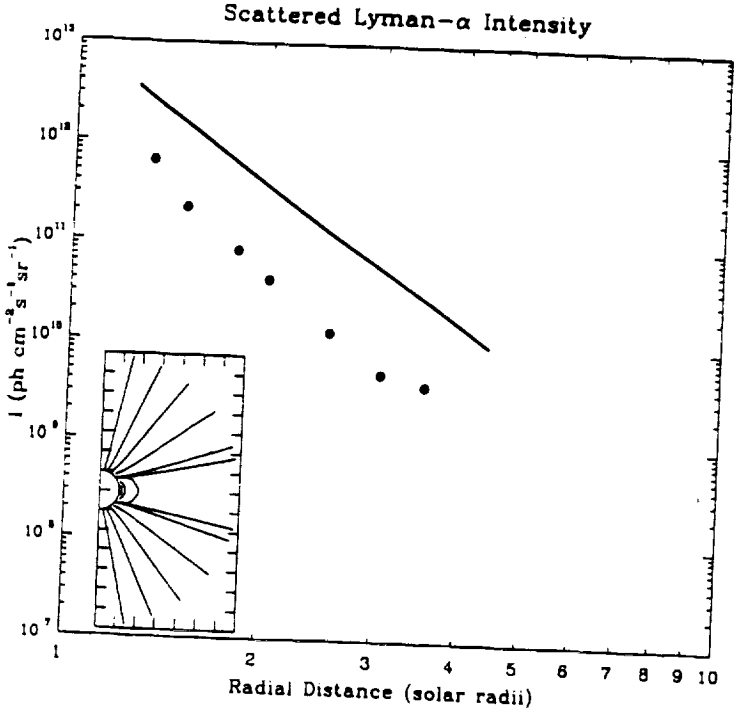

Fig. 9. Predicted Lα intensity vs radial distance along the axis of an equatorial streamer in a dipolar geometry, for a plasma $\beta = 1.0$ (solid line). The streamer is assumed to extend all the way around the equator, and the calculation is performed up to a height of 4 $R_\odot$, as at higher altitudes most of the contribution to Lα intensities will come from open regions. Results from rocket observations of Lα intensities from a quiet coronal region are also shown (dots).

an incorrect treatment of the open field region and to an inappropriate geometry. The latter factor would be influential if only the slope at large distances is wrong. However, the values of the Lα intensity at low heights also look too high, in comparison with the few data points available so far. In Figure 9 we show (dots) the Lα intensities given in Figure 6-1 of the UVCS Science Requirement Document: these data refer to a quiet region and were obtained in 1979 during a rocket flight (Kohl *et al.*, 1980). Because they do not refer to a streamer, they do not provide any information about the change in the slope of the Lα intensity gradient in the cusp region, but we can infer that Lα streamers would be a few times brighter than appears from the rocket data. The Lα brightness predicted from the model is about one order of magnitude larger than observed in quiet regions, which, taking into account that our densities are realistic, is too large a factor. This rules out our initial hypothesis of a continuous belt of streamers circling the solar equator. It is worth pointing out that our conclusion is consistent with observations, as these seem to indicate the presence of several streamers spread, at a given latitude, over different longitudes (Dollfus, private communication).

From this analysis we conclude that we need both a better simulation of open

field regions and a definition of the streamer geometry through a full 3-D model. However, we may still get realistic predictions by adopting *a priori* the streamer configuration and neglecting the contribution from the outer low-density regions. The resulting profiles of intensity vs distance will illustrate the behavior of the Lα brightness for different geometries and UVCS data will eventually allow us to identify the more realistic configurations.

Figure 10 shows the Lα intensity vs distance profiles assuming three different streamer configurations in a direction normal to the streamer axis and parallel to the line of sight (we remind the reader that streamers are supposed to lie in a meridional plane). Either the *angular* width of a streamer is constant with height (fan-shaped streamer) and equal to its base angular width (as seen in the plane of the sky) or its *linear* width is constant with height (constant-thickness streamer) and equal to the distance between the footpoints of the highest closed field lines (as seen in the plane of the sky) or streamers are 'cone-shaped' structures and therefore have a width, initially equal to that of a constant-thickness streamer, which decreases linearly with height up to the cone vertex, identified with the streamer's cusp. Figure 10 shows that, in a dipolar geometry, an equatorial fan-shaped streamer differs negligibly from a continuous belt of streamers circling the Sun. This is due to the large width of the streamer (half width $\approx 38°$): outer regions contribute to the emergent intensities only at great distances where densities are too low to affect significantly the Lα brightness. As a consequence, unless future observations will show streamers to be brighter than assumed so far, we are led to discard the hypothesis of streamers as constant angular width structures. On the contrary, constant thickness and cone-shaped streamer structures lie close enough to the observed data points to be equally plausible.

However, our model locates the cusp only approximately, both because our model does not take diffusive effects into account and because of the coarse resolution of our mesh points. Hence, in order to illustrate, in a cone-shaped geometry, how different cusp altitudes affect the Lα intensity gradient, we have considered the cusp height as a free parameter and evaluated the resulting radial profiles in the usual dipolar geometry and high β plasma. Figure 11 shows the Lα intensity vs distance profiles for a cone-shaped streamer whose vertex – i.e., cusp height – is located at altitudes ranging between 2.5 and 6 $R_\odot$. We point out that such a large variation in the position of the streamer's cusp far exceeds the uncertainty of the model and is shown only for display purposes (although the procedure is not entirely consistent, as different β values would be required to build models with such different cusp heights). We conclude that the Lα intensity and the slope of the Lα intensity gradient initially (i.e., close to the Sun) depend only weakly on the shape of the streamer, but, at large distances, are dictated by the streamer's 3-D structure and, in the case of a cone-shaped feature, by its cusp height.

So far, our examples referred to a global dipolar streamer. However, our results can be extended to the quadrupolar and hexapolar model configurations by taking into account the differences in the streamer geometry. As we have shown in Sec-

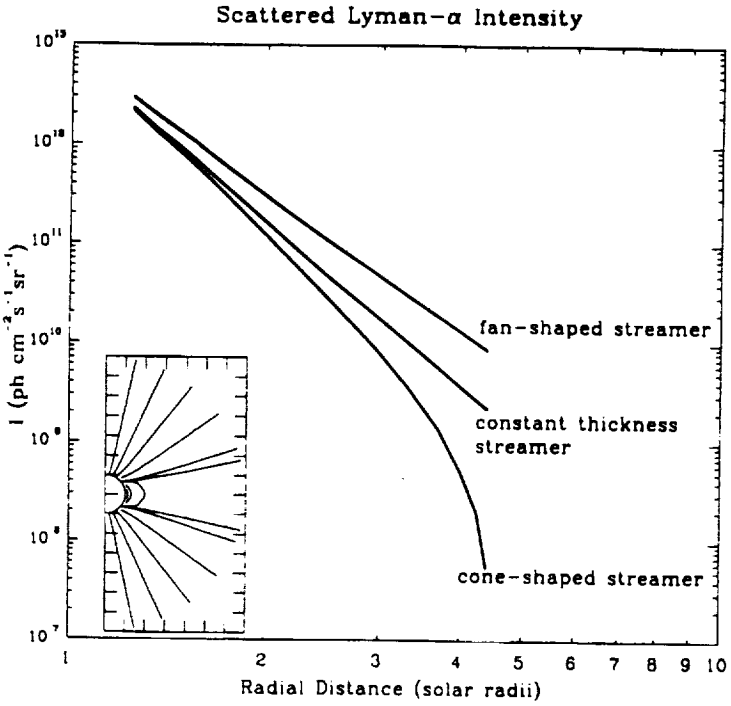

Fig. 10. Predicted Lα intensity vs radial distance along the axis of an equatorial streamer in a dipolar geometry, for a plasma $\beta = 1.0$. The streamer thickness in a direction normal to the plane of the sky is assumed either to have a constant angular width (fan-shaped streamer) equal to its angular base width (≈76°) or to be constant with height (constant thickness streamer) and equal to its base width (≈1 $R_\odot$) or to decrease linearly with height (cone-shaped streamer) up to the cusp height ($R_{cusp} = 4.5\ R_\odot$).

tion 3, densities are about equal in low and high latitude streamers. Therefore, the Lα brightness from these features turns out to scale, with respect to that originating in a dipolar equatorial configuration, in the same proportion as the streamer thickness. The Lα brightness from an equatorial hexapolar streamer, for instance, will be a factor 2–3 smaller than that from an equatorial dipolar streamer and about equal to the brightness from the high-latitude hexapolar streamer.

We did not consider, yet, the case of off-axis observations, which should provide a more comprehensive test of the model by allowing us to determine the physical parameters of the streamer *across* its axis, over a meridional plane. For instance, if SOHO UVCS were to observe an equatorial streamer – symmetrical with respect to a meridional plane through its axis – when its symmetry plane lies in the plane of the sky, it should be possible, via off-equator observations, to check the shape and physical parameters of the streamer in the meridional plane purportedly described by the model.

Figure 12 gives the Lα intensity gradient, measured in the plane of the sky along directions parallel to the axis of the streamer, for the usual dipolar configuration

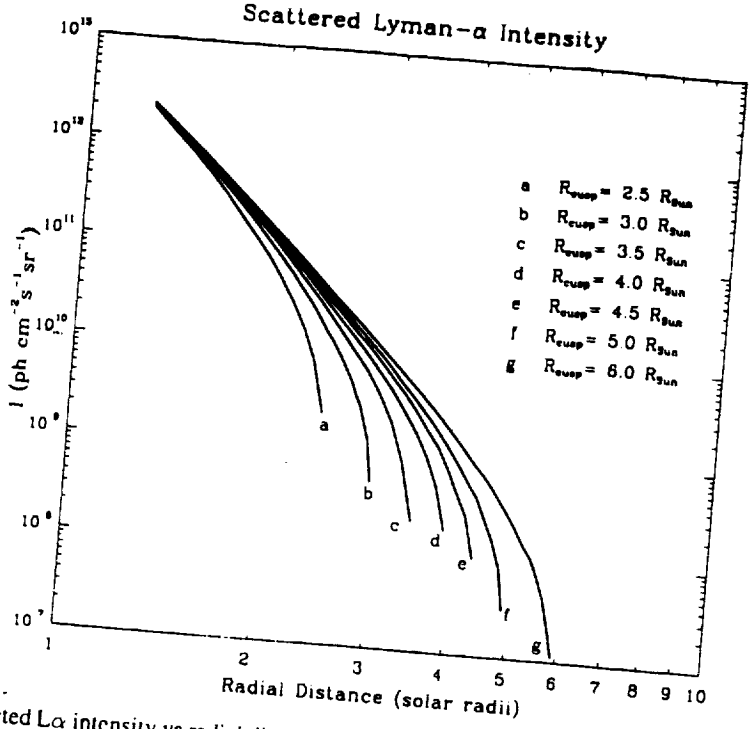

Fig. 11. Predicted Lα intensity vs radial distance along the axis of an equatorial streamer in a dipolar geometry, for a plasma $\beta = 1.0$. The streamer cusp is assumed to be located at different heights ranging from 2.5 to 6 $R_\odot$.

($\beta = 1.0$, $R_{\rm cusp} = 4.5\ R_\odot$), in the hypothesis of a cone-shaped structure. The Lα intensity vs distance gradient is here dictated by the variation of density across the streamer and by the decrease of the integration length along the line of sight, as we move off the equatorial plane. The latter factor is responsible for the intensity drop which occurs at increasingly lower distances, as we move to larger offsets, and mimics the behavior observed in the cusp region in the equatorial plane, also shown in the figure.

If we now move in the plane of the sky, along a direction normal to the streamer axis, and we evaluate the Lα intensity at increasing offsets, we would guess that the Lα brightness decreases proportionally to the decrease in the integration length, and that, as a consequence, the ratio of Lα intensities evaluated at positions corresponding to increasing offsets can never be lower than the ratio between the corresponding integration lengths. For instance, at a distance – measured along the axis of the streamer – of 1.25 $R_\odot$, the intensity ratio $I_R = I_{\rm L\alpha,\ 0.2\ R_\odot}/I_{\rm L\alpha,\ 0.4\ R_\odot}$ is ≈1.5, while the ratio between the integration lengths at those offsets is ≈1.3. The decrease of density, as we move off axis, accounts for a 10% increase in the intensity ratio over the value predicted on the basis of the ratio between integration lengths. However, the intensity ratio is *smaller* than the ratio between integration

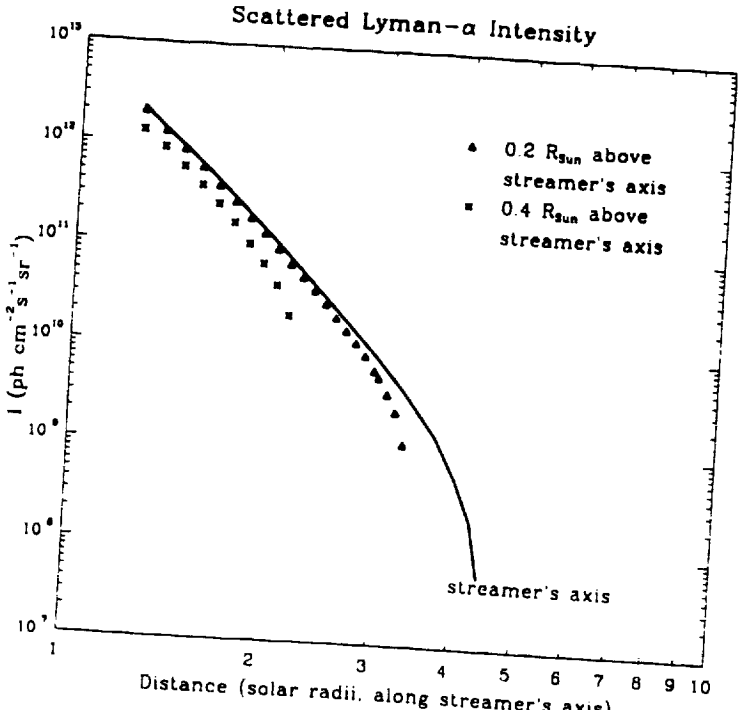

Fig. 12. Predicted Lα intensity vs distance (measured along the axis of an equatorial streamer) for different off-equator offsets in a cone-shaped equatorial streamer: solid line, intensity along the axis of the streamer, zero offset; △, intensity for an offset of 0.2 $R_\odot$; ×, intensity for an offset of 0.4 $R_\odot$. As usual the configuration is dipolar, the base width is ≈38° and the cusp height is 4.5 $R_\odot$.

lengths whenever the shorter integration path, at a larger offset, runs either through the density enhancement at the edge of the streamer (see Figure 5), or through regions with a lower temperature (and, as a consequence, a higher percentage of neutral hydrogen atoms). At a distance of ≈2 $R_\odot$, this effect makes the intensity ratio about 10% *smaller* than the ratio between integration lengths. Thus, from Figure 12, we conclude that the ratio between Lα intensities, evaluated at the same distance (along the streamer's axis) and different offsets, is approximately equal to the ratio of the integration lengths. In the hypothesis of an axially-symmetric density distribution, we conclude that densities play a secondary role, with respect to the streamer's geometry, in determining the value of Lα off-equator intensities. As a consequence, we have to devise a different technique in order to be able to determine the off-axis behavior of densities in streamers. The next section deals with this point.

5. Lα Emission from a Rotating Streamer

The extended lifetime of SOHO makes it possible to observe streamers over a prolonged period of time as they are carried around by solar rotation. Hence, generally, the line of sight will cut through the structure obliquely and the angle between the streamer's axis and the integration path will vary from 0° to 90° as the streamer moves from the central to the limb meridian. When the line of sight cuts normally through the streamer, the region which is closest to the Sun and, therefore, has the highest density, is located at the streamer axis: as a consequence, the highest contribution to the emergent intensity comes from this region. On the contrary, when the line of sight cuts obliquely through the structure it may happen, depending on the angle between the line of sight and the streamer axis and on the axial vs transverse density gradient, that the highest contribution to the emergent intensity originates from a region at some distance from the streamer axis. *If* evolutionary effects are negligible – i.e., *if* streamers are stable throughout a period of time – we may use this effect to get information on the density profile in a direction *normal* to their axis and, through prolonged observations, eventually reconstitute their entire structure. In other words, for stable structures solar rotation allows us to see streamers under different perspectives and use tomographic techniques to obtain their 3-D configurations.

In the previous section, we assumed that the streamers footpoints were rooted at the same longitude. However, if streamers are rooted in active regions, it is likely that their footpoints are rooted at the same latitude – say, along the equator – inasmuch as positive and negative polarities tend to align along the east–west direction. Although our model seems inappropriate to deal with this case – since it is not realistic to have magnetic 'poles' along the solar equator – as long as we do not have a 3-D simulation it is plausible to focus on the streamer sector and adopt the representation provided by the model to describe streamers lying on the equatorial plane. This allows us to explore the capabilities of the tomographic technique, because, in this hypothesis, the model provides a complete description of the behavior of density along the line of sight (at least for on-axis observations). Hence, in the following, contrary to what has been hypothesized so far, the streamer is assumed to lie on the equatorial plane.

Figure 13 shows how individual elements along the line of sight contribute to the total Lα intensity measured in the equatorial plane at a distance of 1.25 $R_\odot$. When the streamer is at the limb (streamer longitude 90°), its axis lies in the plane of the sky and is perpendicular to the line of sight. Therefore, the element lying at 1.25 $R_\odot$ along the axis is the element closest to the observer and provides the highest contribution to the emergent intensity (top left panel of Figure 13). As the streamer is carried around by solar rotation, different elements, at some distance form the axis, become the major contributors to the total intensity. Figure 13 demonstrates the progressive shift of the element which most contributes to the emergent Lα intensity, as the streamer longitude changes by 30°. The bottom right

panel, for instance, shows that, when the streamer has rotated by 30° behind the plane of the sky, the highest contribution to the emergent intensity comes from the element at a distance of $\simeq 0.72\ R_\odot$ along the line of sight (distances along the line of sight are counted from the streamer axis). Thus, by taking an extended set of data, at different locations along the axis of the streamer and at different rotation angles, we eventually get a complete map of the density of the structure.

We do not give any further example of this technique as a more realistic choice of boundary conditions in the open-field regions will modify the distributions of Figure 13. We anticipate that a lower density in open-field areas will result in a steeper decline of the contribution from elements located outside, or at the outer edge of the streamer. This effect may help getting a density map with higher spatial resolution than otherwise possible. Although stable structures may be a minority within the streamer family, the example of Figure 13 shows that it is worth developing this methodology further, as a means for an observational determination of the 3-D streamer's structure.

6. Discussion and Conclusions

Our purpose has been twofold: to provide guidelines for UVCS observational sequences and to compare our simulations with the scanty data available in order to guide further development of the numerical model toward more realistic global configurations.

The first objective has been reached, insofar as we have presented a set of predicted profiles of Lα intensity vs distance, both for on-axis and for off-axis observations and for different rotation angles of the streamer. These profiles can be easily adapted to different magnetic configurations. On the basis of our model for an axially-symmetric structure, we also show that off-axis observations allow an identification of the streamer's dimension along the line of sight. Finally, we have shown that this capability, combined with prolonged observations of a stable streamer at different longitudes, leads to a 3-D map of densities in streamers for comparison with our global simulation.

The model uses a polytropic relationship between density and pressure, rather than a full energy equation. Hence, the temperatures we predict are *effective* temperatures. Observationally, the Lα brightness depends on the electron temperature, via the neutral hydrogen abundance, and on the kinetic temperature, via the coronal absorption profile. As long as we consider integrated Lα brightness, the effect of an incorrect absorption profile is probably negligible. Model temperatures are, however, lower than temperatures derived from streamer observations (Liebenberg, Bessey, and Watson, 1975), so we apparently overestimate the neutral hydrogen abundance. Nevertheless, measured temperatures in streamers have such great uncertainty that we cannot resolve this issue until UVCS provides accurate measurements of the electron temperature.

Ultimately, our second objective is the more relevant. The simulations point

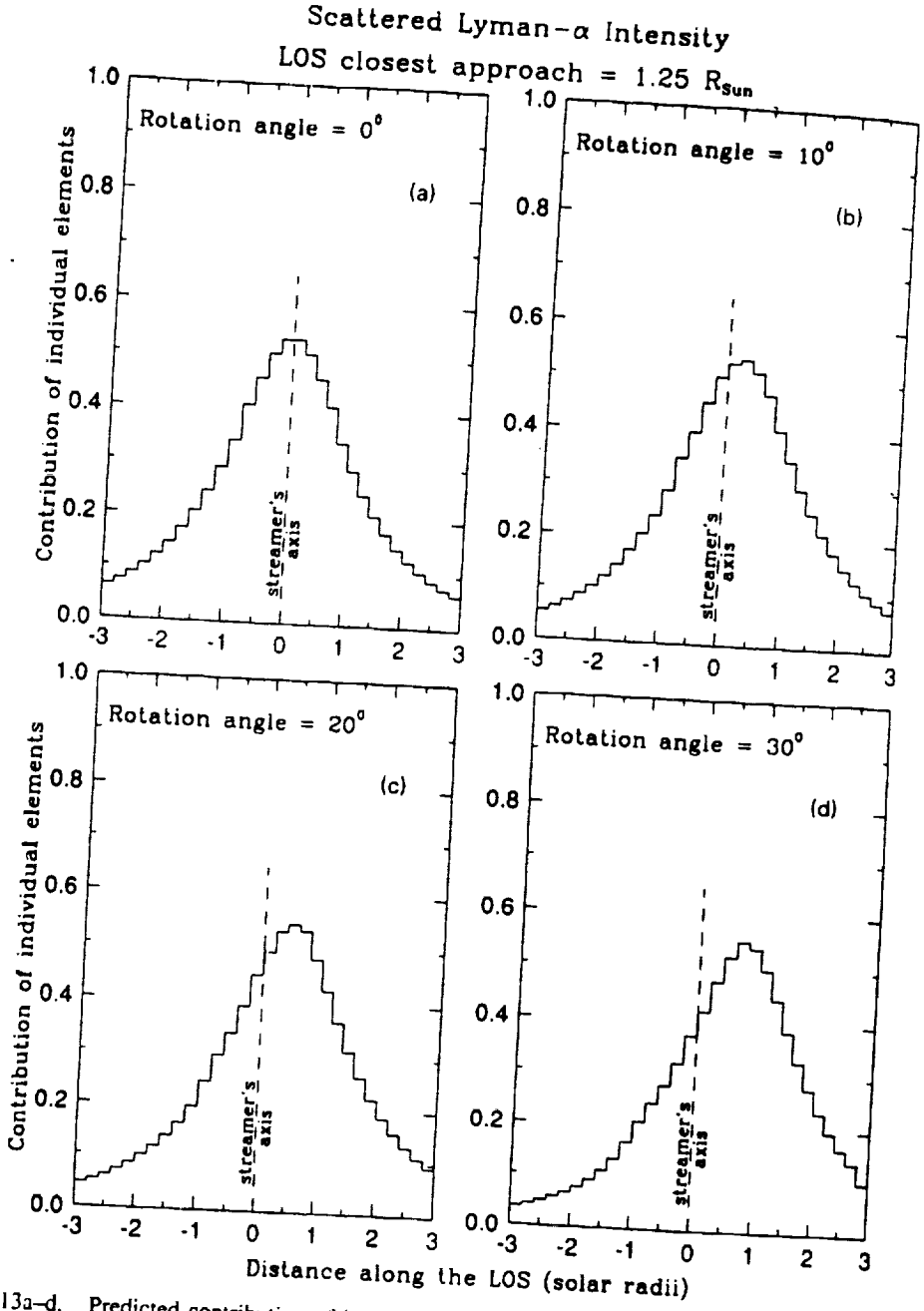

Fig. 13a–d. Predicted contribution of individual elements along the line of sight to the total Lα intensity from the usual dipolar, $\beta = 1.0$ streamer, supposed to lie in the equatorial plane, as a function of their distance along the line of sight. Negative (positive) distances are away from (towards) the observer, as measured with respect to the axis of the streamer. The line of sight intersects the plane of the sky at a distance of 1.25 $R_\odot$ and cuts obliquely through the streamer, unless the streamer axis is in the plane of the sky (streamer longitude: 90°). The contribution of individual elements to the total intensity is shown for: (a) streamer axis in the plane of the sky (rotation angle: 0°), (b) streamer at a longitude of 100° (rotation angle: 10°), (c) streamer at a longitude of 110° (rotation angle: 20°), (d) streamer at a longitude of 120° (rotation angle: 30°).

to the need for (a) a different choice of boundary conditions in open regions than inside the streamer, (b) an extension of the model to different β values, and (c) the development of a 3-D model. We are presently working on these issues and expect to get a realistic simulation of open field regions shortly. Our goal is to attain a reasonable global model that simulates both streamers and coronal holes by achieving agreement between model predictions and existing observations. This is a method to fully determine the 3-D structure of streamers to within the resolution of the model and observations.

Traditionally, three-dimensional mapping of the electron density in coronal structures has been performed via the image reconstruction technique originally developed for X-ray tomography (Altschuler and Perry, 1972; Perry and Altschuler, 1973; Wilson, 1977), or via the already mentioned Van de Hulst's (1950) method. Both procedures have been subject to criticisms (Bagenal and Gibson, 1991) because of their heavy computational requirements. While the ideal method for a 3-D mapping has yet to be found, an alternative approach to devise theoretical models with free parameters that are calibrated against observational data, is being developed (Bagenal and Gibson, 1991). The present work uses this alternative approach and the results achieved so far indicate that it is worth pursuing. We conclude by pointing out that an agreement between model predictions and observations will allow us to determine the magnetic field vector throughout the streamer, thus providing a complete picture of these so far elusive structures.

Acknowledgements

The work of G. Noci and G. Poletto has been partially supported by ASI (Italian Space Agency). S. T. Suess acknowledges support from GNA (Gruppo Nazionale di Astronomia) and MURST (Ministero dell'Università e della Ricerca Scientifica) during his visit to Florence, where this work was initiated. Partial support by a grant from the Cosmic and Heliospheric Physics Branch of NASA is also acknowledged. A.-H. Wang and S. T. Wu are supported by NASA Grant NAGW-9.

References

Altschuler, M. D. and Perry, R. M.: 1972, *Solar Phys.* **23**, 410.
Bagenal, F. and Gibson, S.: 1991, *J. Geophys. Res.* **96**, 17663.
Beckers, J. M. and Chipman, E.: 1974, *Solar Phys.* **34**, 151.
Billings, D. E.: 1966, *A Guide to the Solar Corona*, Academic, San Diego, Ca.
Dollfus, A., Fort, B., and Morel, C.: 1968, *C. R. Acad. Sci. Paris* **266**, 1537.
Dollfus, A., Laffineur, M., and Mouradian, Z.: 1974, *Solar Phys.* **37**, 367.
Feldman, W. C., Asbridge, J. R., Bame, S. J., Fenimore, E. E., and Gosling, J. T.: 1981, *J. Geophys. Res.* **86**, 5408.
Foukal, P. V.: 1990, *Solar Astrophysics*, J. Wiley and Sons, New York, p. 12.
Gabriel, A. H.: 1971, *Solar Phys.* **21**, 392.
Gopalswamy, N., Kundu, M., and Szabo, A.: 1987, *Solar Phys.* **108**, 333.
Gosling, J. T., Borrini, G., Asbridge, J. R., Bame, S. J., Feldman, W. C., and Hansen, R. T.: 1981, *J. Geophys. Res.* **86**, 5438.

Hildner, E., Gosling, J. T., McQueen, R. M., Munro, R. H., Poland, A. J., and Ross, C. L.: 1975, *Solar Phys.* **42**, 163.
Illing, R. M. E. and Hundhausen, A. J.: 1986, *J. Geophys. Res.* **91**, 10951.
Kahler, S.: 1991, *Astrophys. J.* **378**, 398.
Kohl, J. L., Weiser, H., Withbroe, G. L., Noyes, R. W., Parkinson, W. H., Reeves, E. M., Munro, R. H., and MacQueen, R. M.: 1980, *Astrophys. J.* **241**, L117.
Kohl, J. L., Withbroe, G. L., Zapata, C. A., and Noci, G.: 1983, in M. Neugebauer (ed.), *Proc. of Solar Wind 5*, NASA Conf. Publ., CP 2280, p. 47.
Kopp, R. A. and Holzer, T. E.: 1976, *Solar Phys.* **49**, 43.
Koutchmy, S. L.: 1988, in R. C. Altrock (ed.), *Solar and Stellar Coronal Structure and Dynamics*, NSO Publ., p. 208.
Liebenberg, D. H., Bessey, R. J., and Watson, B.: 1975, *Solar Phys.* **40**, 387.
Newkirk, G. and Bohlin, J. D.: 1965, *Ann. Astrophys.* **28**, 234.
Noci, G., Kohl, J. L., and Withbroe, G. L.: 1987, *Astrophys. J.* **315**, 7036.
Perry, R. M. and Altschuler, M. D.: 1973, *Solar Phys.* **28**, 435.
Poland, A. I.: 1978, *Solar Phys.* **57**, 141.
Steinolfson, R. S., Suess, S. T., and Wu, S. T.: 1982, *Astrophys. J.* **255**, 730.
Suess, S. T., Richter, A. K., Winge, C. R., Jr., and Nerney, S.: 1977, *Astrophys. J.* **217**, 296.
Van de Hulst, H. C.: 1950, *Bull. Astron. Inst. Neth.* **11**, 135.
Wang, A.-H., Wu, S. T., Suess, S. T., and Poletto, G.: 1992, in E. Marsch, K. Sauer, and R. Schwenn (eds.), 'Solar Wind Seven', *COSPAR Colloq. 3*, Pergamon Press, Oxford, p. 311.
Wang, A.-H., Wu, S. T., Suess, S. T., and Poletto, G.: 1993, *Solar Phys.* **147**, 55 (this issue).
Wilson, D. C.: 1977, 'The Three-Dimensional Solar Corona: a Coronal Streamer', Ph.D. Thesis, University Colorado, Boulder.
Withbroe, G. L., Kohl, J. L., Weiser, H., Noci, G., and Munro, R. H.: 1982, *Astrophys. J.* **254**, 361.

N15

NUMERICAL SIMULATION OF CME PROPAGATION IN A HELMET STREAMER: EMERGING MAGNETIC FLUX MECHANISM

J. H. ZHANG[1], S. T. WU[1], M. DRYER[2] and F. S. WEI[3]

[1] *Department of Mechanical and Aerospace Engineering and Center for Space Plasma and Aeronomic Research, The University of Alabama in Huntsville*

[2] *Space Environment Laboratory, National Oceanic and Atmospheric Administration, Boulder, Colorado USA*

[3] *Center for Space Sciences and Applied Research, Academia Sinica, Beijing, People's Republic of China*

Abstract. We examine a limited parametric study of time-dependent, numerical MHD simulations of coronal mass ejectsion (CMEs). The physical initiating mechanims (at the base of a helmet-streamer magnetic configuration) is assumed to be magnetic flux that emerges from below the photosphere. The peak flux is taken to be viariable in both magnitude and polarity as well as with/without additional physical mechanisms that include emerging mass and momentum flux. We find that magnetic flux of sufficient magnitude and with polarity opposite to that of the overlying helmet's magnetic field can be a distinct, physically- viable mechanism. We also find: (i) with an appropriate magnetic driver, it is not necessary to add an arbitrary heating function to a pre-event helmet- streamer, as suggested by Steinolfson and Hundhausen (1988) to produce observed CME features; nor (ii) is it necessary to introduce an *ad hoc* accelerating mechanism to a plasmoid as sugested by Linker *et al* (1990). However, we agree with the latter workers that the CME driving mechanism has the same importance as the configuration of the initial ambient corona in the determination of the mass ejection's evolution as detected by coronagraphs.

Key words: Coronal Mass Ejections (CMEs); MHD Modeling of CMEs

1. Introduction

Attention has recently been directed to CMEs that occur in the absence of solar flares but still in association with helmet streamers as indicated in some observations. Several physical mechanisms were proposed. Linker *et al.* (1990) assumed that an *ad hoc* accelerating mechanism, acting continuously on a plasma parcel, would be appropriate to satisfy the three points noted by some observers. They also concluded that the driving mechanism of CMEs has the same importance as the pre- event

IAU Colloquium 144 'Solar Coronal Structures', 1993, 7– 11.
V. Rušin, P. Heinzel & J.-C. Vial (eds.)

PRECEDING PAGE BLANK NOT FILMED

ambient coronal topology. Hu (1989) combined an arbitrary mass efflux from the photosphere with an emerging magnetic flux that had a polarity opposite to the overlying coronal topology. An additional physical mechanism - photospheric shearing of magnetic field lines - has also been proposed (c.f., see review by Dryer, 1994) but will not be considered in this paper.

The purpose of the present paper is restricted to a limited parametric study of the emerging magnetic flux driver. Basic physics are given by Wu *et al* (1978); initial coronal solution, by Zhang and Wei (1991); and the basic numerical techniques and nonreflecting compatibility relations, by Wang *et al.* (1982) and Hu and Wu (1984).

2. Simulation of Coronal Mass Ejection

We will choose a Gaussian spatial distribution (centered at $\theta = 90°$) of the driver(s) within a latitudinal extent: $64.5° \leq \theta \leq 90°$. We also choose a linear, temporal ramp of each driver(s) during the time: $0 < t \leq 500$ sec and then kept constant during the remainder of the computation to t = 15,000 sec (4.2 hr). When B (only) is considered to be the driver, $[(B_r + B_\theta)^{1/2}]$, the other four dependent variables within the ejection region are determined by the nonreflecting conditions. The boundary is treated the same as in the pre-event calculation within the latitudinal range $0 \leq \theta < 64.5°$.

Our study, then, consists of a limited parameteric survey that starts with a magnetic driver alone and considers four other possibilities (including a thermal pressure driver alone). The five cases, with an attempt at peak magnitude adjustment so as to approximate a constant value of peak total pressure (including dynamic pressure), are: (1) Polarity of Emerging Magnetic Flux is Opposite to the Closed Region's Polarity in the Pre-Event Helmet; (2) Same Polarity as Case 1 But with Additional Momentum from Photospheric Mass Flux Outflow; (3) Same Polarity as Case 1, But with Photospheric Mass Addition Having Negligible Momentum; (4) Polarity Opposite to Case 3 - Again with Photospheric Mass Addition having Negligible Momentum; (5) Pressure Pulse to Simulate Flare-like Thermal Energy Input at Photosphere.

3. Results

We will remark on a very limited set of general features. Figure 1 shows contours of fractional density chagnes, $\Delta N = (N - N_o)/N_o$ at several times for Cases 1 and 2. The subscript "o" represents the value at each pre-event condition. Formation and evolution of a looplike ejection with denser legs (implying brighter observations in white light observations) can clearly be seen. The density enhancement in the legs for Case 1 is about 150% that of the loop's top. Also, the legs for this case are stationary. Also we confirm (with smaller contour intervals) that there is a density depletion near the lower boundary between the footpoints of the legs. Thus, all three of the requirements required for some Skylab observations have been satisfied. For Case

2, however, the footpoints move apart because the additional momentum generates sufficient pressure that overwhelms the helmet configuration's pressure gradient. By contrast this gradient tends to keep the legs stationary, as in Case 1. In principle, it is possible that magnetic emerging flux, acting together with the additionally-strong momentum efflux, could be responsible for those CMEs that display continuous lateral expansion of the legs. This lateral expansion appears to alleviate the leading compression wave in comparison with the steepening shock in Case 1. In both cases, numerical reconnection (not shown) occurs at the equator as the emerging flux is forced against the closed helmet configuration.

Figure 2 shows the same parameter at several times for Cases 3, 4 and 5. Note that the leading edge is weaker for the reverse polarity Case 3 (presumably as a result of reconnection-caused depletion of the driving magnetic driver) in comparison with the much stronger (and higher) shock wave for the same-polarity Case 4. The thermal pressure pulse (Case 5) produces a strong leading edge shock. All three cases show the fixed legs and depletions behind the leading edge compressed zones, but only the reverse-polarity Case 3 shows higher density (hence: expected higher white light brightness) in the legs when compared to the loop top.

4. Concluding Remarks

Our limited parametric study indicates the following conclusions:

- Emerging magnetic flux of opposite polarity can be a distinct physical driving mechanism for generating looplike CMEs. However this magnetic flux, when accompanied by substantial momentum efflux will produce greater lateral motion of the ejection. The latter mechanism does not appear to be a viable candidate.

- We demonstrated that, with a magnetic driver, it is not necessary to add an arbitrary heating function to the pre-event helmet-type corona in order to explain the general characteristics of looplike CMEs as suggested by Steinolfson and Hundhausen (1988).

- With respect to the magnetically driven mechanism, it is not necessary to introduce cold inflowing plasma as used in the simulations by Hu (1989) and Linker *et al* (1990); nor is an accelerating mechanism of the initial driver required as presented by the latter workers.

- We are in agreement with Linker *et al* (1990) that the driving mechanism of CMEs has, at least, the same importance as the initial ambient coronal configuration in the determination of the evolution of the mass ejection.

- The comparative thermal pressure pulse provides a faint looplike property in comparison with the sharp structure given by the magnetic driver.

Acknowledgements. STW and MD wish to acknowledge partial support of this work via NASA Grant NAGW-9 and NRL Contract N00173-93-WR30477, respectively.

References

Dryer, M.: 1994, Space Sci. Rev., in press
Hu, Y. Q.: 1989, *J. Comput. Phys.* **84**, 441
Hu, Y. Q. and Wu, S. T.: 1984, *J. Comput. Phys.* **55**, 33
Linker, J. A., Van Hoven, G., and Schnack, D. D.: 1990, *J. Geophys. Res.* **95**, 4229
Steinolfson, R. S. and Hundhausen, A. J.: 1988, *J. Geophys. Res.* **93**, 14269
Wang, S., Hu, Y. Q., and Wu, S. T.: 1982, *Scientia Sinica* **25**, 1305
Wu, S. T., Dryer, M., Nakagawa, Y. and Han, S. M.: 1978, *Astrophys. J.* **219**, 324
Zhang, J. H. and Wei, F. S.: 1991, in *4th International School Space Simulation*, ed.: , , Japan.

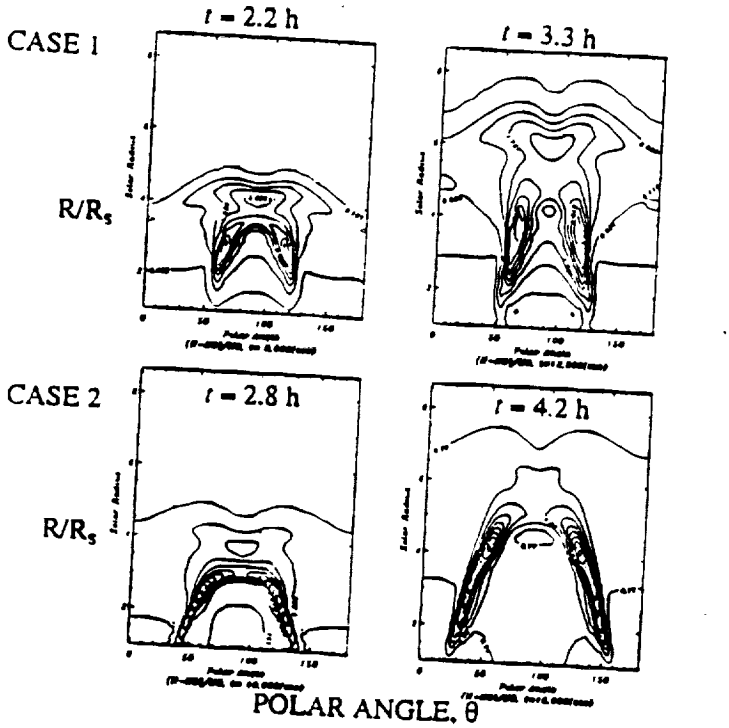

Figure 1. Temporal, fractional density changes, $(N - N_o)/N_o$ in the corona for emerging magnetic driver alone, Case 1 (upper panels) and for a magnetic driver plus emerging momentum flux, Case 2 (lower panels). The emerging magnetic flux has polarity opposite to that in the pre-event helmet magnetic topology.

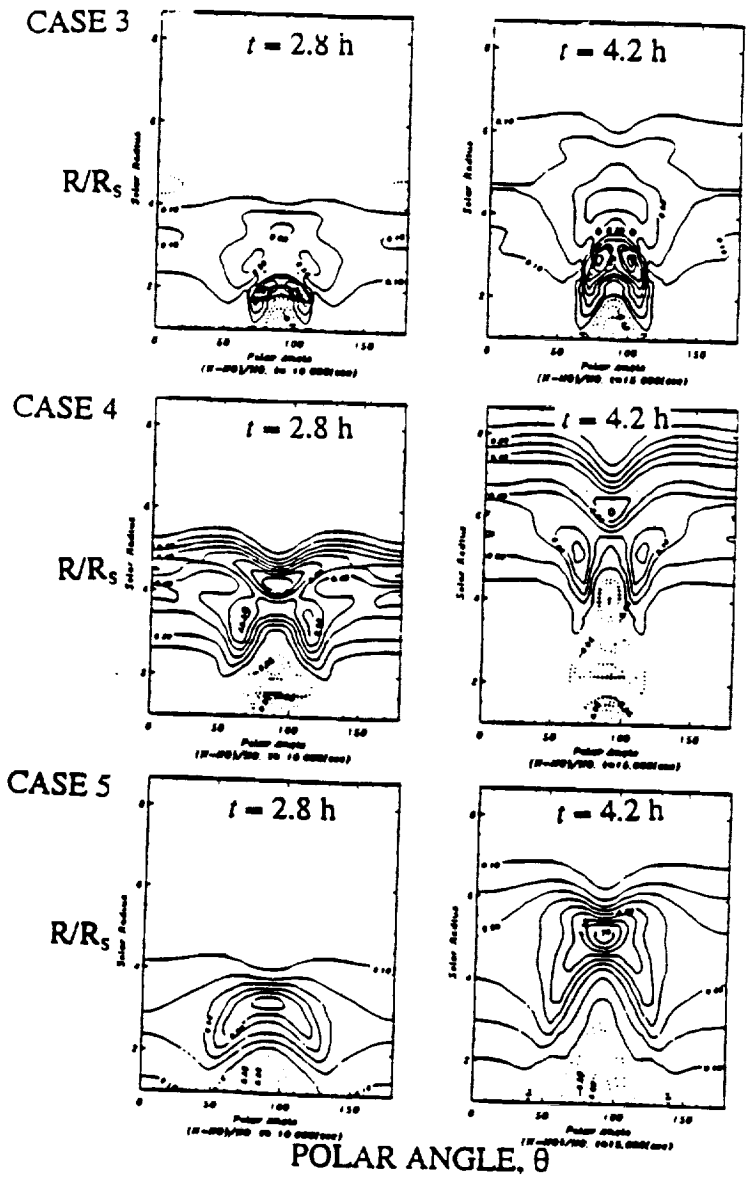

Figure 2. Temporal, fractional density changes, $(N - N_o)/N_o$ in the corona for emerging magnetic driver (again with opposite polarity) and moderate momentum efflux Case 3 (upper panels); same, but with same polarity as in the pre-event helmet, Case 4 (middle panels); and a flare-like thermal pressure pulse for comparison.

Proceedings of SOHO Workshop, Elba, Italy. Sept. 27-Oct 1993.

N15

MAGNETOHYDRODYNAMIC SIMULATION OF A STREAMER BESIDE A REALISTIC CORONAL HOLE

S. T. SUESS
Space Science Laboratory
NASA Marshall Space Flight Center
Huntsville, Alabama 35812 U.S.A.

S. T. WU, A.-H. WANG
Center for Space Plasma and Aeronomic Research
The University of Alabama in Huntsville
Huntsville, Alabama 35899

and

G. POLETTO
Osservatorio di Arcetri
Firenze, Italy

September 1993

Abstract. Coronal streamers have been simulated using numerical solutions to the time-dependent equations for polytropic, magnetohydrodynamic flow. Up to the present time, these models have focused on establishing the credibility of the solutions and on their application as the initial state in simulations of coronal transients. In general, the models have produced satisfactory streamer simulations. The same has not been true for the magnetically open regions simulating coronal holes. This is simply a consequence of the character of the models and the boundary conditions. The models all have higher densities in the magnetically open regions than that reported to occur in coronal holes (Noci, *et al.*, 1993). The impact in using the models to simulate observations is that scattered radiation and radio intensities from the magnetically open regions are too high.

Key words: Streamers - Coronal Holes - MHD Simulations

1. Introduction

An MHD numerical simulation of coronal streamers was described at the last SOHO workshop (Suess, 1992). That model systematically used constant temperature and density at its base. The consequence was that although streamers seemed to be well simulated, the density and flow speed in the magnetically open regions were too large and too small, respectively, compared to what is believed to occur in coronal holes. Here, that problem is addressed by using a varying temperature and density at the base. This is a polytropic model so that the energy equation still produces an 'effective temperature' which bears little relation to true temperatures in coronal holes. However, the reduced density in the coronal hole in this new model will result in a significant improvement in simulation of scattered light in the corona and related analyses of SOHO measurements made both in coronal holes and

in streamers. This article presents the results from the hole-streamer model and compares them with the previous constant boundary value results. The emphasis is on the differences resulting from this different choice of boundary conditions and the more realistic densities which result in the coronal hole.

2. The Physical and Numerical Model

The model is for axisymmetric, single fluid, polytropic, time-dependent, ideal magnetohydrodynamic flow. The solution is computed in a meridional plane defined by the axis of the magnetic field, which is a dipole at the base of the corona in all examples presented here. In these examples, results are shown between 1.0 and 7.0 $R_\odot$, although the solution itself generally is extended to $15.0R_\odot$. There are 20 grid points between the pole and equator and 37 grid points, on a varying grid, between the base and 15 $R_\odot$. A solution is produced by a relaxation in time from an essentially arbitrary initial state - thereby insuring uniqueness and stability. Here, the initial state is a vacuum dipole field superimposed on a Parker-type solar wind solution defined by the prescribed variation in temperature and density at the base. The polytropic index, γ, is 1.05 in all cases. This model is described in detail by Suess (1992), Wang, *et al.* (1992,1993), and Wang (1992).

3. Results

3.1 Initial State

The initial profiles ($t = 0$) of temperature, density, and flow speed versus polar angle are shown in Figure 1, at 1.0, 2.0, 3.9, and 7.1 $R_\odot$. At this time, the plasma beta, β, is 3.5 at the equator and 0.06 at the pole, corresponding to field strengths of 0.833G and 1.67G, respectively. The base density at the equator is 2×10^8 cm^{-3}, and at the pole it is 10^7 cm^{-3}, while the corresponding temperatures are 1.74×10^6 and 2.42×10^6 K, respectively. The boundary values between these points vary linearly with polar angle. The polar density has to be this low to obtain proper densities higher in the coronal hole, while the temperature is required to be higher in the hole than in the streamer to obtain high flow speeds in the hole. No other choice is possible in a polytropic model. However, this 'effective temperature' is not a true temperature; it reflects extended acceleration and heating of the solar wind that is known to exist in coronal holes.

3.2 The Magnetic Field Topology

The magnetic field topology is shown in Figure 2. The three panels show the final state, after 20 hours of relaxation in physical time, in comparison both to the intitial vacuum diopole field (left panel) and the corresponding

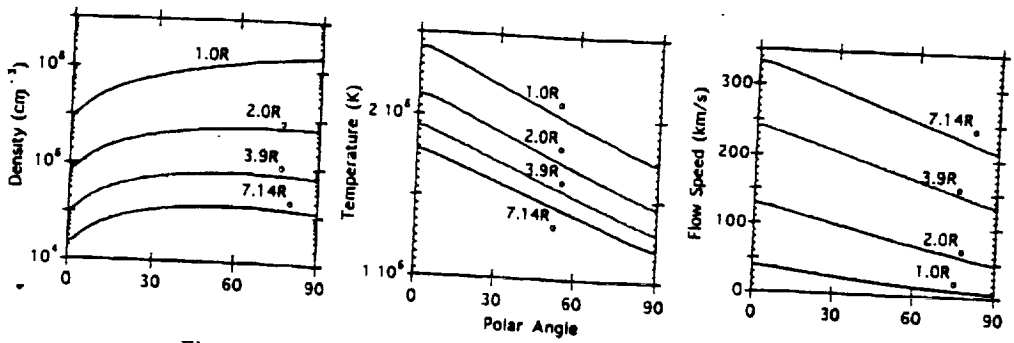

Fig. 1. The density, temperature, and flow speed at $t = 0$.

magnetic field topology with constant temperature and density at the base (center and right panels). The constant temperature and density used for this comparison are 1.8×10^6 degrees and 2.25×10^8 cm^{-3}, respectively (Wang, *et al.*, 1993). The magnetic field strength at the equator was 1.67 G, resulting in $\beta = 0.5$ at that point. In all three panels of Figure 2, field line footpoints lie at 10 degree intervals. Thus, from the left panel it can be seen that fieldlines equatorward of somewhere between 40 and 50 degrees are closed. The center and right panels show that the low density and high flow speeds that occur in the present model lead to fieldlines lying systematically poleward of the case with the constant boundary conditions. This is a natural consequence of the higher energy in the flow field.

3.3 Flow Speed and Density

The dramatic difference introduced by varying the temperature and the density at the base is shown in Figure 3. The density, temperature, and flow speed are shown as a function of polar angle at four different radii ($1.0R_\odot$,$2.0R_\odot$,$3.9R_\odot$, and $7.14R_\odot$). The results for constant boundary values are shown as dashed lines in each panel. The left panel shows that at the important heights of 2.0 and 3.9 $R_\odot$, the density at the center of the coronal hole is $10^5 - 10^6$ cm^{-3}, as opposed to an order of magnitude more with constant boundary values. The flow speed, in the right panel, is correspondingly much larger, reaching almost 250 km/s at the center of the hole at 3.9 $R_\odot$. The temperature varies little with height because of the polytropic index being 1.05, so little can be inferred from the temperature plot. Again, it must be emphasized that this is an 'effective temperature.'

The low density in the coronal hole is obviously mainly due to the lower boundary value for the density below the hole - the increase in flow speed only accounts for about a factor of two reduction, while the boundary condition raises the reduction to an order of magnitude. This is not quite what

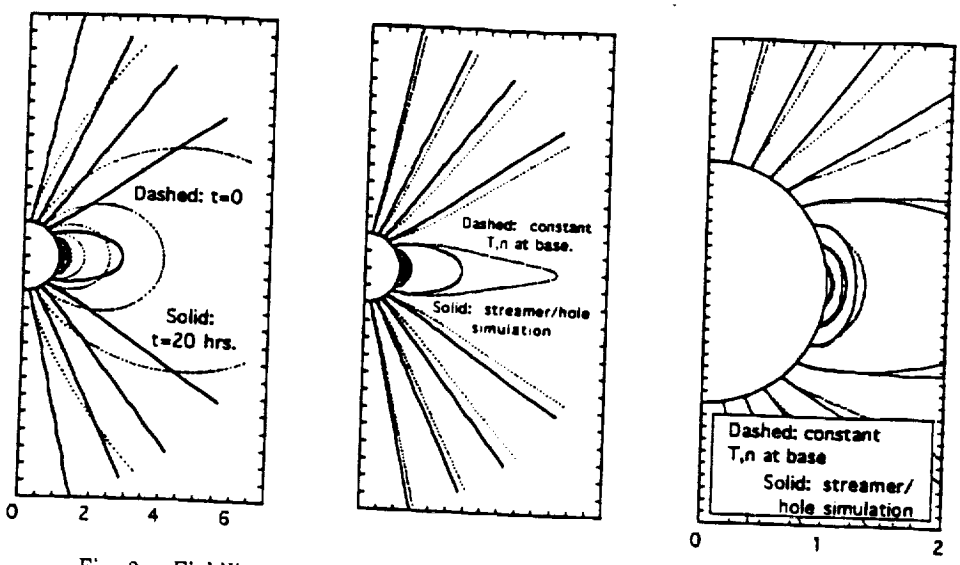

Fig. 2. Fieldline geometry for variable and constant bounary values.

would be most desireable for simulating coronal holes, but is about the most that can be expected from a polytrope. The limitation is that the polytrope has a large flow speed at $1.0R_\odot$ at the base of the coronal hole - 40 km/s. This is perhaps an order of magnitude larger than what really exists at this level. Physically, the solar wind undergoes strong acceleration between the transition zone and a few tens of thousands of kilometers altitude. Such acceleration is not represented in the polytrope model. Therefore, it is impossible to achieve both a low flow speed at the base (and correspondingly high density) and a high flow speed at $1.1 - 1.2R_\odot$. Consequently, the polytrope has a density scale height in this region that is much larger than for the Sun. The only way to achieve more realistic velocity and density profiles at these low heights is to incorporate source terms into the momentum and energy equations. For the present, we make the cautionary note that this model, although representing well the density contrast between streamers and coronal holes above ca. $1.1R_\odot$, does not do the same below that height. It is a limitation inherent in both polytropic models and models that explicitly treat thermal conduction if they do not also have energy and momentum source terms low in the corona.

3.4 Polar Plots

The effect of causing the density and flow speed in the magnetically open region to be more like that expected in coronal holes is large, and modifies

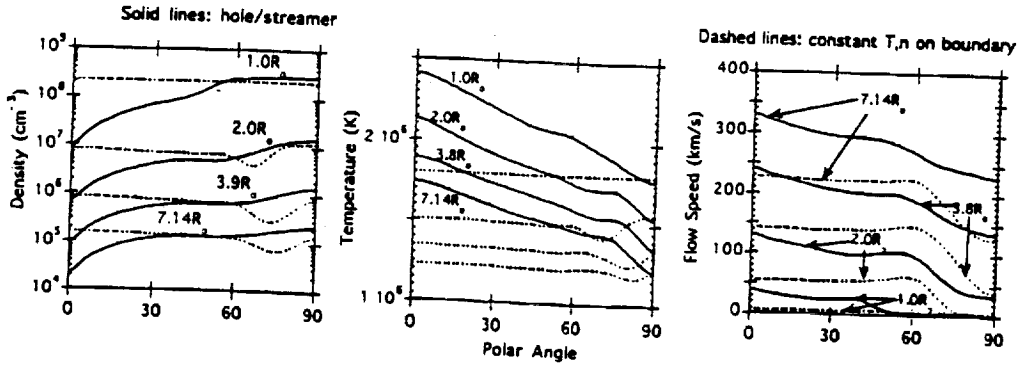

Fig. 3. The density, temperature, and flow speed at $t = 20$hrs.

the structure not only in the open region, but also in the adjacent closed region. It is of order one importance in developing a model appropriate for simulating the scattering of photospheric radiation in the corona because of the line of sight contribution to the scattering (Noci, *et al.*, 1993). An impression of the effect can be seen using a polar gray-scale plot of the density. Here, in the right panel of Figure 4, the logarithm of the number density is plotted in this way, along with overlays of temperature contours, flow speed contours, and magnetic field lines. For comparison, the left panel shows a corresponding plot for constant temperature and density at the base - the case shown by the dashed lines in Figure 3. In these plots, the gray scale shows the logarithm of the density. Overlayed onto the gray scale plots are contours and fieldlines. The solid contours on the left half of the panels are flow speed (Min=0, Max=350 km/s, 50 km/s contour levels). The dashed contours on the right half of the panels are temperature (Min=1×10^6, Max=2×10^6 K. 2×10^5 contour levels). The solid lines on the right sides of the panels are magnetic field lines.

The main difference to be noted between these two panels is that the density distribution on the left is far more spherically symmetric than on the right. However, there are other interesting differences. First, the temperature notch above the streamer (dashed contours, right sides) is much narrower in the hole/streamer simulation. This reflects what is observed in the solar wind. Next, it can be seen that the density follows the contours of velocity (solid contours, left sides) better than the magnetic field lines. This reflects the control flow speed exerts on density in the corona - it is not a hydrostatic medium. Conversely, the magnetic field lines do not seem to closely refelect the background density distribution.

There are many detail differences between normally observed coronal

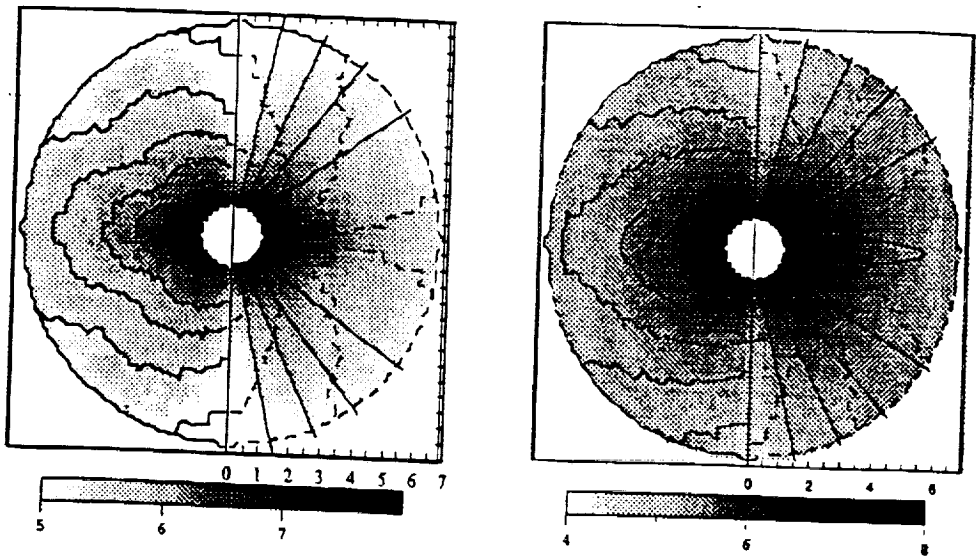

Fig. 4. Left: Constant T,n on boundary. Right: Coronal hole/ streamer simulation.

structure and the structure in this model. The streamer is not so pointed at the cusp as seems to be the case in white light eclipse photos and the edges are not so sharp. Whether this reflects structure in the flow speed or in the magnetic field is not clear. However, these differences will be used to help guide further development of this model.

4. Summary

The objective of this exercise has been to develop a useful global model for simulating coronal observations that will be made using LASCO and UVCS on SOHO. This objective has been met in the sense that an order of magnitude improvement has been made in simulating the density contrast between holes and streamers. Details in the results raise further modeling problems and will be used to guide future studies. In parallel, the experience gained in this axisymmetric coronal model will be used to guide the development of a fully three dimensional global coronal model.

Acknowledgements

STS has been supported by the Cosmic and Heliospheric Physics Branch of NASA. AHW and STW are supported by NASA Grant NAGW-9. GP acknowleges support from the Italian Space Agency.

References

Noci, G., Poletto, G., Suess, S. T., Wang, A.-H., and Wu, S. T.: 1993, 'Ly-α Intensity in Coronal Streamers', *Solar Phys.* **147**, 73

Parker, E. N.: 1963, *Interplanetary Dynamical Processes*, Interscience: New York

Suess, S. T.: 1992, 'Modeling Solar Coronal Streamers' in Domingo, V., Poland, A., and Mariska, J., ed(s)., *Coronal Streamers, Coronal Loops, and Coronal and Solar Wind Composition*, *SP-348*, European Space Agency: Noordwijk, 63

Wang, A.-H.: 1992, *Two-Dimensional and Three-Dimensional Time-Dependent MHD Model of Extended Corona*, Dissertation, The University of Alabama: Huntsville

Wang, A.-H., Wu, S. T., Suess, S. T., and Poletto, G.: 1992, 'A Two-Dimensional MHD Global Coronal Model: Steady-State Streamers' in Marsch, E., and Schwenn, R., ed(s)., *Solar Wind Seven*, Pergamon Press: Oxford, 311

Wang, A.-H., Wu, S. T., Suess, S. T., and Poletto, G.: 1993, 'A Two-Dimensional MHD Global Coronal Model: Steady-State Streamers', *Solar Phys.* **147**, 55

SPACE SCIENCE REVIEWS, 1994 (in press)

N15

CORONAL HEATING DUE TO THE EMERGENCE OF MAGNETIC FLUX

S. T. WU and M. T. SONG*
Center for Space Plasma and Aeronomic Research
and Department of Mechanical Engineering
The University of Alabama in Huntsville
Huntsville, AL 35899 USA

C. C. CHENG
Naval Research Laboratory, Washington, DC 20375 USA

and

M. DRYER
Space Environment Laboratory/ERL
National Oceanic and Atmospheric Administration, Boulder, CO 80303 USA

Abstract. A self-consistent time-dependent, two-dimensional MHD model with a realistic energy equation is developed to understand the origin of bright coronal emission accompanying the occurrence of a new bipolar magnetic region. The motivation for this study is the interpretation of anticipated observations to be made by the SOHO mission.

Key words: Coronal Heating

1. Introduction

It has been shown observationally that the appearance of the emergence of a new bipolar magnetic region (BMR) is always accompanied by bright coronal emissions (Sheeley, 1976; Meyer *et al.* 1979; Chou and Fisher, 1989). Recently, Shibata *et al.* (1989) used a nonlinear, time-dependent, two-dimensional MHD, two-temperature simulation model to represent the transition region (i.e., photosphere, chromosphere and corona) to study the dynamical responses of this part of the solar atmosphere due to emergence of magnetic flux. The purpose of this simulation study is attempt to explain the bright coronal emission associated with the appearance of a BMR. Because the earlier model did not model the realistic features of transition, in this study we use a newly developed numerical technique (Song, Wu, and Dryer, 1993) which enables us to construct a transition region that includes the Harvard-Smithsonian standard atmosphere in the MHD model. We use this model to simulate the atmospheric responses due to the emergence of the magnetic flux across the transition region up to the edge of the corona with the objective to exhibit observed features. The fundamentals of the model are given in Section II. Numerical results are presented in Section III; finally, concluding remarks are given in Section IV.

* Purple Mt. Obser., PRC

PRECEDING PAGE BLANK NOT FILMED

2. Fundamentals of the Model

The fundamentals which describe this physical system contain two parts:

2.1 Mathematical Description

The mathematical model used for this study can be described by the first principle of the MHD theory, but the realistic energy equation was used as follows:

$$\frac{\partial p}{\partial t} + (\mathbf{u}\cdot\nabla)p + \gamma p(\nabla\cdot\mathbf{u}) + (\gamma-1)[\nabla\cdot\mathbf{Q} - (\frac{J^2}{\sigma}) + G_{\text{mech}} + L_{\text{rad}}] = 0(1)$$

where p is the plasma pressure, $\mathbf{u}$ is the velocity vector, γ is specific heat ratio, $\mathbf{Q}$ is the thermal flux, $\mathbf{J}$ is the current, σ is electric conductivity, G_{mech} is the wave heating term and, finally, L_{rad} is the radiation loss term. The terms of $\mathbf{Q}$, G_{mech} and L_{rad} are determined by specific models.

2.2 Boundary and Perturbed Conditions

The boundary conditions set for this calculation are divided into two parts; (i) computational boundary conditions and (ii) physical boundary conditions. It is realized that the left, right and top boundary conditions are computational boundary conditions which are set as non-reflecting boundary conditions at all times. The bottom boundary condition is the physical boundary condition. At the initial time (i.e. $t = 0$), the quiet photospheric conditions (i.e. $\rho_0 = 3.5 \times 10^{-7}\text{gm/cm}^3$, $T_0 = 6.5 \times 10^{4\,\circ}$ K and $B_0 = 500$ gauss) are given. The perturbed boundary conditions are prescribed at the bottom boundary when $t > 0$, which are:

a. $[p + \frac{B^2}{8\pi}]|_{\text{outside}} = 1.5[p + \frac{B^2}{8\pi}]|_{\text{inside}}$

b. In order to make sure that $\nabla\cdot\mathbf{B} = 0$ is satisfied, we set $[B_{\text{n}}]_{\text{outside}} = [B_{\text{n}}]_{\text{inside}}$.

It should be noticed that this is a Lagrangian calculation. Hence, the boundary conditions and perturbed conditions are functions of time.

3. Numerical Results

In this study, three cases of perturbed conditions are employed. These three cases are:

Case I: The strong magnetic flux emergence strength is seven times the background of the field strength. In this case, the magnetic field outside the computational domain is pushed into the region by the pressure difference between the outside and inside of the computation domain.

Case II: The strength of the emergence of the magnetic field is the same as the background field strength but with a vertical velocity of 0.2 km s^{-1}

at the lower boundary. This velocity is required to carry the field into the computational domain.

Case III: The strong magnetic field emergence with isothermal atmosphere case is the same as Case I, but the transition region structure is ignored.

We briefly summarize the results in the following: The velocity vectors and the fractional density, temperature, and pressure contours at various times for Case I are shown in Figures 1 and 2 respectively. Figures 2(b) and 2(c), respectively, show temperature depletions and enhancements relative to the initial temperature profile from the chromosphere, through the transition region and into the corona. The schematic description of the physical results is shown in Figure 3. From these results we notice that the induced plasma flow oscillates at the Brunt-Vaisala frequency with a period of $\sim$ 200 s (see Fig. 1). In general, we observed from density and temperature contours (see Fig. 2) that the cool region surrounded by two hotter regions appeared in the chromosphere and is identified as the arch filament system surrounded by bright coronal emissions (see Fig. 3). Upward movement of the transition region (T.R.) is indicated by a vertical arrow in Figure 3.

Case II, not only induced the "Brunt Vaisala" oscillation, but also induces horizontal plasma flow which may be identified as the source of a Morton wave.

4. Concluding Remarks

We have presented a two-dimensional, time-dependent MHD model with realistic energy equation which not only can be used for interpretation of UVCS/SOHO data analysis, but also could be utilized for planning SOHO observations.

Acknowledgements

The work by STW is supported by NASA grant (NAGW-9) and NOAA (RANR000104). The work by MD is supported by U.S. Naval Research Laboratory Work Order N0017392WR20046.

References

Chou, D. Y. and Fisher, G. H.: 1989, *Ap. J.* **341**, 533.
Meyer, F., *et al.*: 1979, *Astron. and Astrophys.* **76**, 53.
Sheeley, N. R.: 1976, *Solar Phys.* **47**, 173.
Shibata, K., *et al.*: 1989, *Ap. J.* **345**, 584.
Song, M. T., Wu, S. T. , and Dryer, M.: 1993, *AIAA Paper No. 93-3177*, American Institute of Aeronautics and Astronautics: Washington, DC

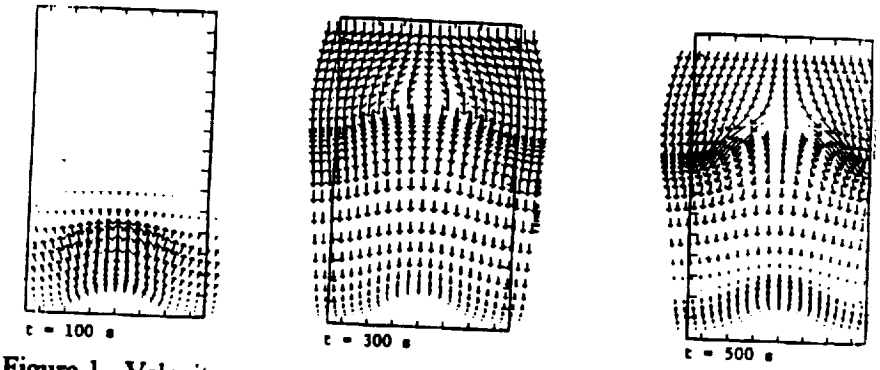

Figure 1. Velocity vectors at various times after appearance of the emerging magnetic flux of Case I.

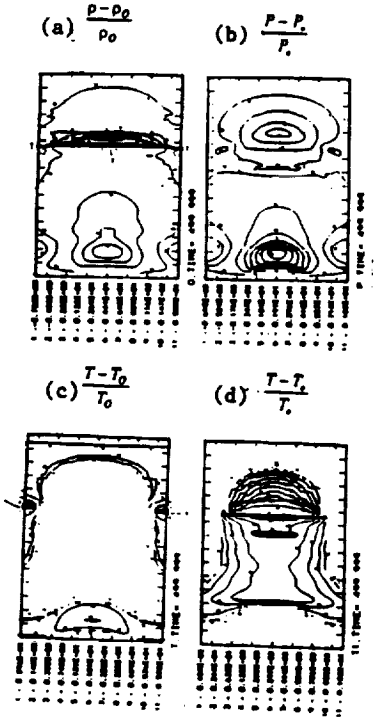

Figure 2. Plasma parameters of Case I at 500 s. Note that (c) represent temperature increases relative to the ambient values and (d), decreases.

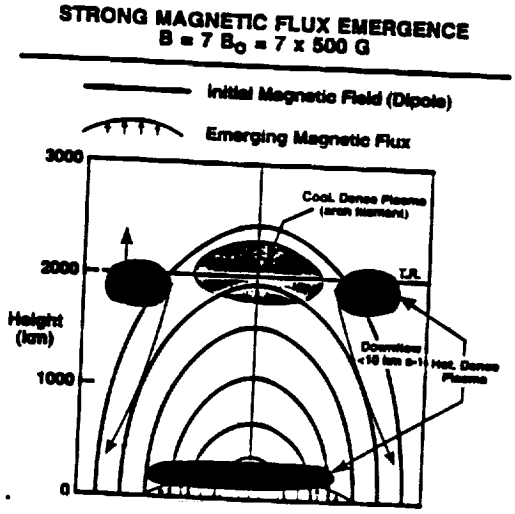

Figure 3. Schematic representation of the physical behavior of the simulation of Case I. Upward movement of the transition region (T.R.) is indicated by the short vertical arrow. Note the regions of cool dense plasma (arch filament) and hot dense plasma as indicated by Figures 2(a) - 2(c).

PRECEDING PAGE BLANK NOT FILMED

SEE ALSO
93N31723

THREE-DIMENSIONAL NUMERICAL SIMULATION OF INTERPLANETARY MAGNETIC FIELD CHANGES AT 1 AU AS A CONSEQUENCE OF SIMULATED SOLAR FLARES

S. T. Wu[1], Chin-Chun Wu[1] and Murray Dryer[2]

[1]Center for Space Plasma and Aeronomic Research, and Department of Mechanical Engineering, The University of Alabama in Huntsville;
[2]Space Environment Laboratory/ERL, National Oceanic and Atmospheric Administration

ABSTRACT

In order to study the relationship between different forms of activity and transient variations of the north-south component, B_z, of the interplanetary magnetic field, IMF, at 1 AU, we employ a three-dimensional numerical simulation code to study several aspects of this problem. We simulate one form of solar activity, the flare, by using a pressure pulse at different locations near the solar surface and observe the simulated IMF evolution of $B_\theta(=-B_z)$ at 1 AU. We found, for a given pressure pulse, that the orientation of the corresponding transient variation of B_z has a strong relationship with the location of the pressure pulse and the initial condition of IMF.

Keywords:

1. Introduction

The configuration of the magnetic field in the disturbed solar wind has become important in magnetospheric physics, since it has been found that the direction of the interplanetary magnetic field (IMF) is an important factor in causing geomagnetic disturbances. The north-south component of the IMF B_z (accurately speaking, in the solar-magnetospheric coordinate system) plays a crucial role in determining the amount of solar wind energy to be transferred to the magnetosphere (Arnold[3]; Tsurutani[8]; Russell[6]; Akasofu[1]; Akasofu[2]). Specifically, when the IMF has a large magnitude ($\geq 10\gamma$) and a large southward component, the amount of the transferred energy becomes very large. On the other hand, the transferred energy becomes very small when the IMF is directed primarily northward. Also, Tang[7] show that a simple relationship between the orientation of the IMF B_z component and the magnetic orientation of the associated flare region does not appear.

In this study we employ a three-dimensional numerical magnetohydrodynamic (MHD) simulation code to study the relationship between the solar activity location and the changes of IMF B_z at 1 AU. We examine one form of solar activity, the flare, by assuming that it can be simulated by a pressure pulse for a period of several hours. Then for a simple three- dimensional IMF configuration (undisturbed), we examine the IMF consequences at 1 AU. Using this procedure, we explain why a simple relationship between the orientation of IMF B_z component at 1 AU and the magnetic orientation of the associated flare region does not appear.

2. Mathematical Methods

In order to understand the correlation of the locations of various forms of solar activity and the changes of IMF B_z at 1 AU, we choose a MHD three- dimensional numerical simulation code (Han[5]) to study this problem. The governing equations represent the conservation of mass, momentum, and energy well as the induction equation for a single-fluid, fully-ionized plasma in the spherical coordinate system.

The basic numerical methodology used for the present modeling is an extension of the Lax-Wendroff finite difference methods. The details of the computation procedures are given by Han[5]. We are not going to repeat these details here.

3. Simulation Results

We consider a unipolar IMF as the initial magnetic field configuration in this study. In this case, there is no current sheet, and the magnetic fields are all of positive polarity, i.e., the IMF is directed outward from the sun. The other case has a current sheet near the equatorial plane which will be discussed by Dryer[4].

To obtain a representative steady state solar wind, we choose a set of plasma conditions at 18 solar radii that, by trial and error in the ecliptic plane, can produce representative solar wind conditions at the earth's orbit. The conditions used at the inner boundary are:

$\rho = 2.35 \times 10^{-9} kg/km^3$, V_r = 250 km/sec, T = $1.1 \times 10^6 K°$, $B_r = 3 \times 10^{-2}$ gauss;

B_θ = - $\sin 2\theta \times 10^{-5}$ gauss; B_ϕ = $-16 \sin\theta \times 10^{-5}$ gauss; $V_\theta = V_r(B_\theta/B_r)$;

$V_\phi = -V_r(B_\phi/Br)$

where the last two expressions are found from the specification of the electric field $E = V \times B = 0$. The computational domain for this steady-state simulation covers $45° \leq \theta \leq 135°$; $0° \leq \phi \leq 90°$; $18R_s \leq r \leq 215R_s$. An open boundary condition at both $\theta = 45°$ and $\theta = 135°$ is used so that there are no reflective disturbances. A constant grid size of $\delta\phi = 3°, \delta r = 3R_s$ and $\delta\theta = 3°$ are used.

Proceedings of the 26th ESLAB Symposium – Study of the Solar-Terrestrial System, held in Killarney, Ireland, 16–19 June 1992 (ESA SP-346, September 1992).

The integration along the radial direction continued until the distance reaches 1.1 AU. We put a high pressure pulse at different locations at 18 solar radii. There is no special significance to this choice of lower boundary other than the fact that it is representative of both a supersonic and super-alfvenic zone where all input pulses will propagate in the anti-sunward direction. We will show three major cases in this paper. The high pressure pulse has $\delta\rho/\rho_o = 4$ and $\delta T/T_o = 7.5$. Temporally, the strength of the perturbation increases from the initial condition to maximum in one hour, then the perturbation lasts for four hours, and then ramps downward to zero during the following hour. We suggest that this initialization procedure may approximate some representative long duration soft x-ray solar flares. Spatially, this input pulse is inserted at the three locations noted below: (i) a northern hemisphere location at $N24°$; (ii) an ecliptic plane location: and (iii) a southern hemisphere location at $S18°$. The first and third locations for this first, simple unipolar case are, of course, nearly mirror image cases.

Figure 1 shows the calculated variations of the B_θ-component of IMF (nearly equal to $-B_z$) due to those three simulated flares for the initial magnetic field configuration being a unipolar IMF. These variations are monitored in various locations such that the effects of the B_θ variations on the locations of the flare are clearly indicated. For example, the variations of B_θ observed at six degrees north of the solar equator behaved differently in comparison to the case observed at six degrees south of the solar equator and in the solar equator. This feature has particular meaning in the practical sense. Because, it gives the characteristic for the prediction of geomagnetic activity. Since, it has been suggested that when the B_θ-component of IMF turned south and its magnitude reaches about 10 nT, it will enhance the ionospheric current system.

Figure 2 shows the same results but with the initial IMF configuration that incorporates a flat equatorial heliospheric current sheet. It is immediately noticed that the arriving time is much ahead $\sim$ 10 *hr.* when the flare location is at the equator (i.e., the location of the current sheet). This point is discussed by Dryer[4].

Figure 3 shows a three-dimensional view of the radial component of solar-wind velocity in the $\phi = 45°$ meridional plane at t = 50 hours, 75 hours, and 100 hours after the introduction of the pressure pulse for initial unipolar IMF configuration at various flare locations; $N24°$ flare (upper row), $S00°$ (mid row) and $S18°$ (lower row). The steep "cliff" at the figures right side represents the outer boundary's dropoff to the background as set by the computer graphics, therefore, should be ignored.

We notice that the $N24°$ flare's fast forward MHD shock can be seen (t = 50 hrs.) at the north-most boundary of the computational domain and $S18°$ flare's forward MHD shock was seen on the opposite direction (i.e. the

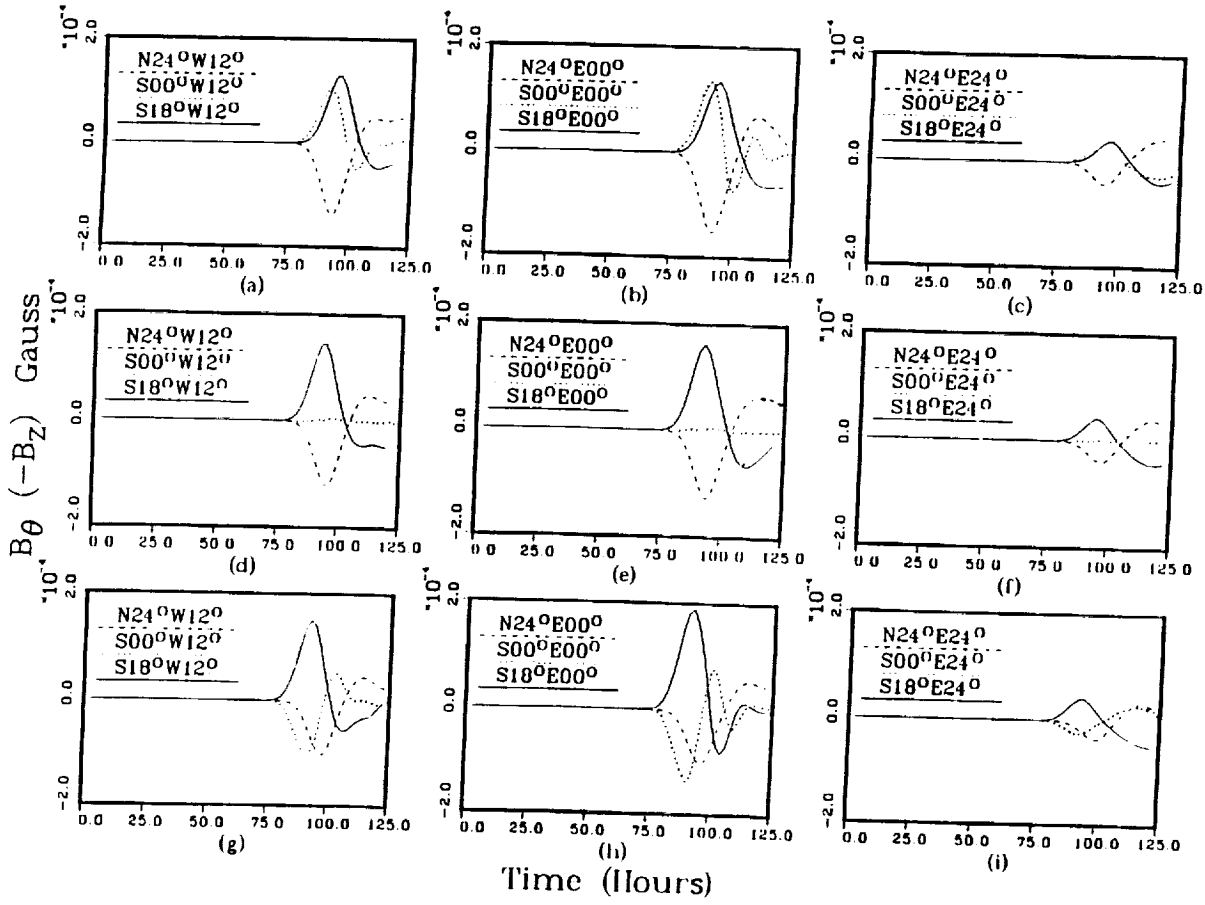

Figure 1. The variations of $B_\theta(-B_z)$ component of IMF at 1 A.U. for the initially unipolar magnetic field configuration and at various locations of the flare.

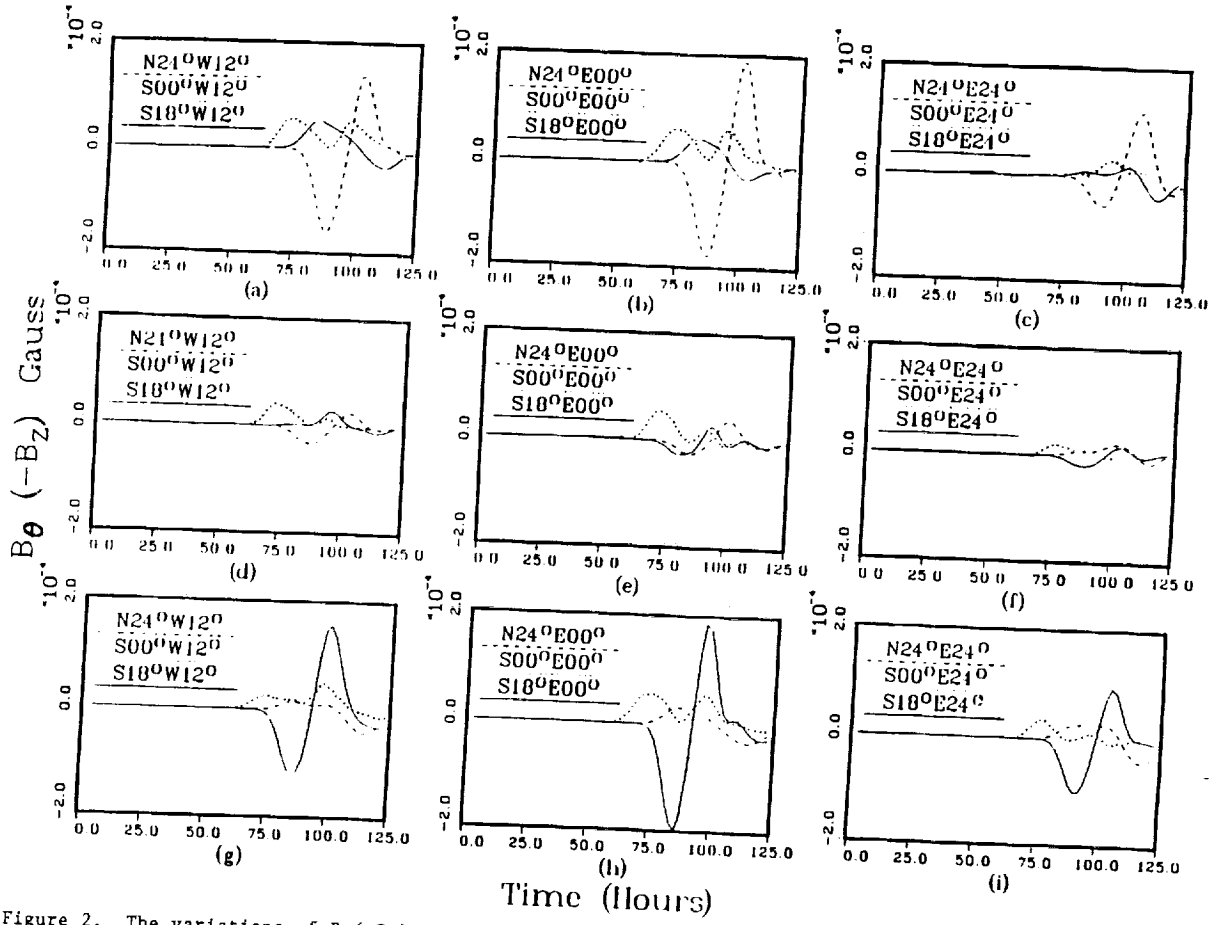

Figure 2. The variations of $B_\theta(-B_z)$ component of IMF at 1 A.U. for the initially magnetic field configuration with current sheet at solar equator and at various locations of the flare.

south- most boundary of the computational domain) from these results. Further, we also see the development of fast reverse MHD shocks. A detailed discussion on the MHD shock interaction will be presented elsewhere.

4. Conclusion and Remarks

We chose two cases of an undisturbed IMF configuration. In one case, it was unipolar (positive outward); in the other, a flat heliospheric current sheet (positive in the northern hemisphere; negative in the southern hemisphere) was used. Then we used the same pressure pulse (to simulate a long duration solar flare) at various positions in these two cases. From the above simulation results, we can point to a simple relationship between the locations of the solar flare, the IMF initial conditions and the north-south components, B_z at 1 AU. We catalog these simulation results into two groups; the first group is the case for the uniform IMF (i.e. without current sheet); the second group is the case for a nonuniform polarity IMF (i.e. with the flat heliospheric current sheet).

For the initial condition of the IMF such that the polarity is everywhere outward from the sun, we found that the orientation of the IMF turns northward ($-B_z$) at 1 AU when the simulated flare is in the northern hemisphere at a time of 75 hours after the perturbation was started. The orientation of IMF turns southward at 1 AU at the same time after the perturbation was launched when the flare is in the southern hemisphere. Therefore, in principle, it would appear that it may be easy to predict the occurrence of a geomagnetic storm from the location of a solar flare if the IMF were everywhere outward from the sun. For example, if there is a flare in the southern hemisphere of the sun, then we might expect a geomagnetic storm at earth three days later. On the other hand, if the location of solar activity is in the northern hemisphere of the sun, we might expect a small amount of solar wind energy transfer to the magnetosphere resulting in only a weak disturbance according to various studies (Arnold[3]; Tsurutani[5]; Russell[6]; Akasofu[1], Akasofu[2])

From the above discussion, it seems easy to predict the occurrence of a geomagnetic storm from the location of the solar flare. Unfortunately, the IMF configuration is quite complicated and substantially different from the simple unipolar example assumed here. A current sheet near the equatorial plane of the solar coordinate system is known to be present at solar minimum. Therefore, it is necessary to study some cases in the second group which has a current sheet in it in order to understand more details about the behaviour of the north-south component, B_z of IMF at 1 AU. We note in passing, that the B_z component of the IMF is always measured in the solar-ecliptic coordinate system that is fixed to the spacecraft. We used, in the model, the spherical coordinate system, fixed at the sun's center, with $\theta = 0°$ at the north pole. Thus, our B_θ is equal to $-B_z$ which, in turn, must eventually be converted to the solar magnetospheric coordinate system for one-to-one comparison.

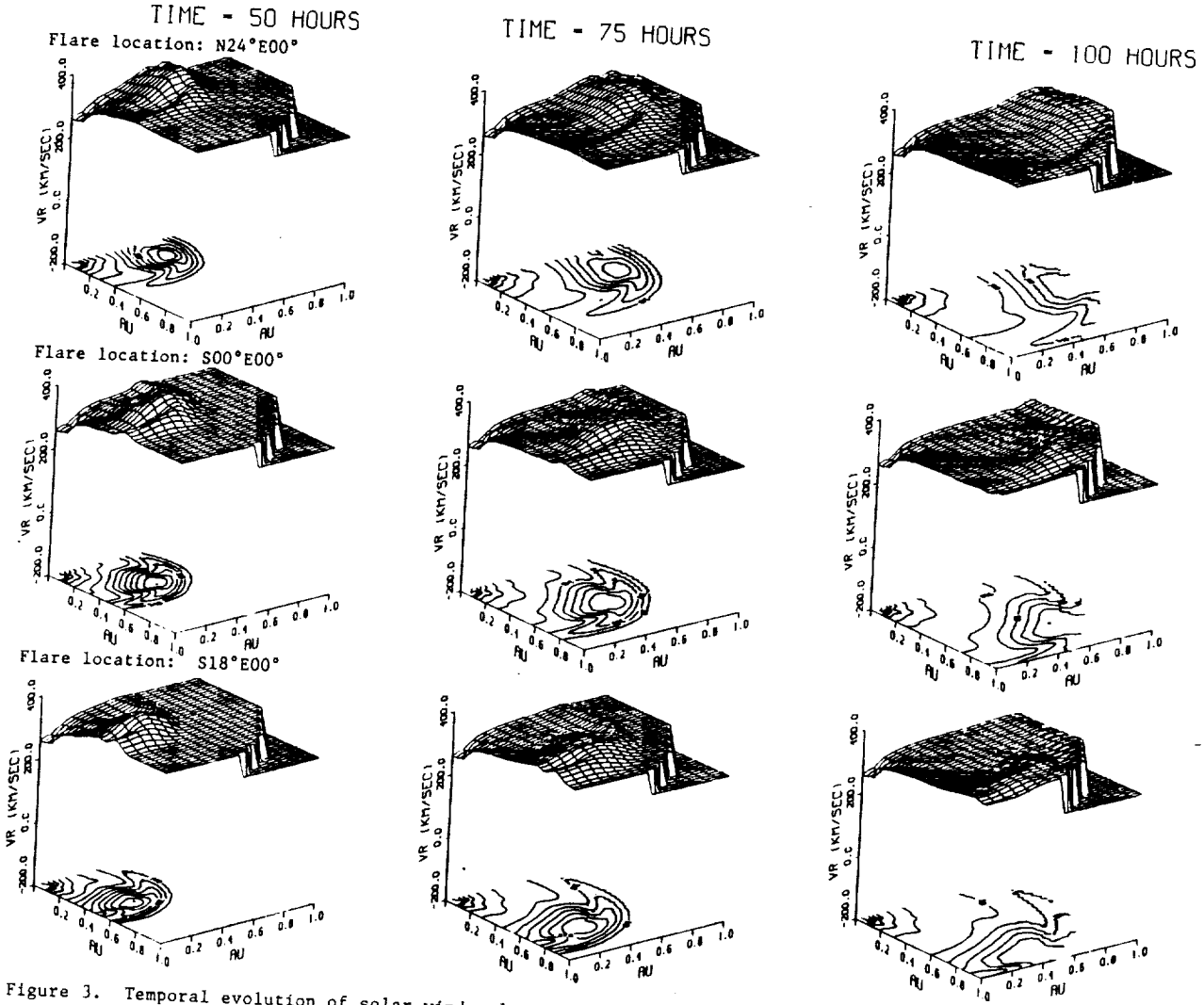

Figure 3. Temporal evolution of solar wind velocity v_r in the $\phi = 45^0$ meridional plane at various flare locations as indicated.

. The objective of this study was to examine the IMF polarity changes at Earth's position, given initial (steady-state) IMF configurations, following simulated solar flares at several representative latitudes. The MHD simulation results provide a basic picture of the IMF changes as a consequence of realistic three-dimensional shock propagation through the solar wind. The change of IMF polarity in the north-to-south (or vice-versa) direction depends on the initial IMF configuration and the location of the solar flare. In principle, if these two factors are known, the likelihood of geomagnetic storm occurrence should be a more-easily-predictable task. In any case, our study supports the study of Tang[7] who noted that there is no simple relationship between the dominant magnetic polarity in the solar flaring active region and the orientation of the IMF B_z component at Earth after the flare.

Acknowledgement

This work is supported by the Solar Physics Branch/-Space Physics Division of a NASA HQ Grant (NAGW-9) and NOAA contract (50RANR000104).

References

1. Akasofu, S.-I., Energy Coupling Between the Solar Wind and the Magentosphere, Space Sci. Rev., 28, 121, 1981.

2. Akasofu, S.-I., C. Olmsted, E. J. Smith, B. Tsurutani, R. Okida, and D. N. Baker, Solar Wind Variations and Geomagentic Storms: A Study of Individual Storms Based on High Time Resolution ISEE 3 Data, J. Geophys. Res., 90, 325, 1985

3. Arnold, R., Signatue in the Interplanetary Medium for Substorms, J. Geophys. Res., 76, 5189, 1971.

4. Dryer, Murray, S. T. Wu, Chin-Chun Wu and S. M. Han, 1992, Proceedings of 26th ESLAB Symposium, this volume.

5. Han, S. M., S. T. Wu and M. Dryer, A Three-Dimensional, Time-Dependent Numerical Modeling of Supersonic, Super Alfvenic MHD Flow, Computers and Fluids, 16, No. 1, 81, 1988.

6. Russell, C. T., and R. L. McPherron, The Magnetotail and Substorms, Space Sci. Rev., 28, 121, 1981.

7. Tang, F., S.-I. Akasofu, E. J. Smith, and B. T. Tsurutani, Magnetic Fields on the Suna nd the North-South Component of Transient Variations of the Interplanetary Magnetic Field at 1 AU, J. Geophys. Res., 90, 2703, 1985.

8. Tsurutani, B. T., C. I. Meng, Interplanetary Magnetic-Field Variations and Substorm Activity, J. Geophys. Res., 77, 2964, 1972.

SEE ALSO
93N31685

PRECEDING PAGE BLANK NOT FILMED

HELIOSPHERIC CURRENT SHEET EFFECTS ON THE PROPAGATION OF SOLAR-GENERATED SHOCK WAVES

M. Dryer[1], S.T. Wu[2], C.C. Wu[2], and S.M. Han[3]

[1]NOAA Space Environment Laboratory
[2]Center for Space Plasma and Aeronomic Research, University of Alabama in Huntsville
[3]Department of Mechanical Engineering, Tennessee Technological University

ABSTRACT

A fully three-dimensional (3D), time-dependent, MHD interplanetary global model (3D IGM) is used to investigate the effect of a flat heliospheric current sheet (HCS) on the propagation of solar flare-generated shock waves and the structures behind them. The time series of the interplanetary magnetic field's meridional component, B_θ ($\equiv -B_z$ in solar-ecliptic coordinates) is examined by Wu et al. (1992, this volume) for a matrix of 27 cases of flare location and observer positions (e.g., Earth). A strong dependence of B_θ phasing and rotation (by the nonlinear, large-amplitude MHD waves that follow the leading shock), as a function of observer position relative to the flare location, was clearly shown. The presence of the HCS compounds this dependence, as is obvious in a comparative examination of the case when the HCS is absent. Interaction of the incident, leading, fast forward MHD shock upon the HCS may produce a plethora of products; we speculate that one of these is a fast rarefaction wave that propagates in the anti-sunward direction, within the HCS, faster than the shock itself.

Keywords: 3D modeling, heliospheric current sheet, shock interaction.

1. INTRODUCTION

The development of a fully three-dimensional (3D), time-dependent MHD model of heliospheric interplanetary magnetic field (IMF) and solar-wind flow (Refs. 4, 6) has made it possible to investigate a number of scientific questions concerning the evolution of solar-generated disturbances and their heliospheric consequences. Kinematic studies, method-of-characteristics schemes, and even numerical 1D and 2D steady-state and time-dependent studies are valuable for early exploration of various questions; however, only a fully 3D numerical model, with sufficient computer and graphics capability, can expand our understanding of the complex phenomena that challenge physicists who study the Sun and the interplanetary medium.

In this spirit, Ref. 12 addressed the question: what is the temporal behavior at a given point (Earth's location would be an obvious choice) when a solar-flare-generated shock propagates past that point? Those authors considered a simple, unipolar, outward-pointing IMF (i.e., with no heliospheric current sheet) and examined the comparative temporal B_θ ($\equiv -B_z$) response following individual flares in both northern and southern solar hemispheres as well as at central meridian and in the eastern and western hemispheres. They also compared the response of B_θ with the more realistic case in which a flat, equatorial, heliospheric current sheet (hereafter HCS) is present in the undisturbed ambient medium—representative of solar minimum conditions. In two arbitrarily chosen examples they found the following interesting situation: An observer located 6° above, within, or 6° below the solar equatorial plane received information of a disturbance from an equatorially located solar flare about 10 hours earlier than reception of the same kind of information when the same representative flares were located either 24° above or 18° below this plane.

This paper is limited to a brief discussion of velocity profiles in the meridional plane; these profiles suggest the presence of a complex sequence of products following the fast, forward interplanetary shock's interaction with the HCS. A fast rarefaction wave may be one of the products of this interaction process (c.f. Ref. 7). This wave may move, anti-sunward, faster than the shock itself, thereby explaining the signal's earlier arrival at the observer's position when compared with the signals arriving from higher-latitude flares. The analysis procedure is summarized in Section 2, results are given in Section 3, and concluding remarks are presented in Section 4.

2. ANALYSIS

The analysis procedure, including the finite differencing solution of the eight fundamental MHD equations, with infinite electrical conductivity and neglect of dissipation except at shocks, is given in detail by Ref. 6. Some results are given by Refs. 2, 3, and 4 for a series of applications that include shock propagation and evolution of solar-generated plasmoids as well as a croissant-shaped plasmoid that may be representative of magnetic clouds. As in these works, we will use a representative, steady-state solar wind and IMF. Other profiles will, of course, change the magnitudes discussed later, but they will not change the basic trends. As in our earlier work, the computational domain is chosen to be a heliolongitudinal sector, $0 \le \phi \le 90°$, where the outward axis in the solar equatorial plane may be considered to be in the $\phi = 45°$ meridional plane. The heliolatitudinal sector is taken to be $45° \le \theta \le 135°$, or, in terms of solar latitude, $45° \ge \theta \le -45°$. The outer boundary is taken to be $R = 238\ R_\odot$; the inner boundary is at $18\ R_\odot$. The grid size is $\Delta R = 3R_\odot$, $\Delta\theta = 3°$, $\Delta\phi = 3°$.

The flat HCS is taken to be representative of solar-minimum conditions. The velocity and density within and near (latitudinally) the HCS are anti-correlated: the velocity at 1 AU rises from about 325 km/s in the equatorial plane to about 400 km/s at $\theta = \pm 45°$. The density was increased to achieve pressure balance within and near the HCS (where the IMF decreases to zero).

The lower boundary is in the supersonic and superalfvénic zone; thus arbitrary values of all eight dependent variables can be chosen for initialization purposes. In this study, a moderate-sized solar flare was simulated by a combined product of density and temperature increases (supported by many X-ray and spectrographic observations from Skylab, SMM, etc.) that peak at $\Delta P/P = 30$ (see Ref. 12) at the domain's lower boundary. This peak, together with a sinusoidal drop-off to the background pressure, is taken at the center of a circular base of 30° angular radius at the lower boundary. It is assumed that a similar profile would have existed at the flare site near $R = 1\ R_\odot$. The temporal duration of this pressure pulse is assumed to be representative of a long-duration X-ray event (LDE); its thermal pressure profile in time is taken to be a 4-hour duration with 1-hour ramps at the start and end.

Three separate computations were made at the $\phi = 45°$ meridional plane at $\theta = 66°$, 90°, and 108°. The temporal profiles for all dependent variables could, of course, be plotted at any of the $31 \times 31 \times 70$ grid points—an enormous task! In this effort it was decided to examine B_θ at $R = 165\ R_\odot$ (0.77 AU—to be considered in another paper) and at 1 AU, at a matrix of nine sets of angular positions, as follows:

- $\theta = (84°, 90°, 96°)$: thereby simulating the observer's point (e.g. Earth) 6° above, within, and 6° below the solar equatorial plane. For Earth, this procedure approximates the seasonal effect.
- $\phi = (33°, 45°, 69°)$: thereby simulating central meridian (CM) positions of the observer (viz Earth) relative to flares in the eastern and western hemispheres as well as at CM ($\phi = 45°$).

Thus, as in Ref. 12, the simulated B_ϕ time-series will be examined at nine observer locations, for a matrix of three solar points considered to be the center of solar flares at the positions shown in Table 1.

The computations were actually performed with the centers of the pressure pulses at three positions in the $\phi = 45°$ meridional plane: $\theta = 66°$, 90°, and 108°, as discussed by Ref. 12. Hence, for these three flares, observed at each of the nine observer locations given above, we have a total of 27 simulated flare disturbances. Section 3 contains a few general remarks about these flares.

Table 1. Flare locations.

Western Hemisphere	CM	Eastern Hemisphere
N24°W12°	N24°E00°	N24°E24°
S00°W12°	S00°E00°	S00°E24°
S18°W12°	S18°E00°	S18°E24°

3. RESULTS

The discussion of results will be limited to the following topics: (1) a remark about the B_ϕ time series, (2) a 3D view of the solar-wind velocity in the $\phi = 45°$ meridional plane at several times after a flare occurred at N24° and S18°, and (3) a schematic discussion of the possible products of the interaction of the flare-generated shock with the HCS.

3.1 B_ϕ Time-Series at 1 AU

Ref. 12 has discussed the B_ϕ response as observed at 6° above and below the solar equatorial plane. Several points should be made here. First, the direction of the polarity response (except for the flares in the equatorial plane) is anticorrelated for flares in the northern and southern hemispheres. Second, the polarity time-series is sinusoidal, reflecting the post-shock, large-amplitude, MHD waves that produce large IMF rotations. Third, the shock (or other disturbance) from flares in the equatorial plane arrives about 10 hours earlier than the other shocks. (An explanation for this phenomenon is offered in Section 3.3, where the velocity in the meridional plane is discussed within the context of shock–HCS interaction.) At $R = 165\ R_\odot$, all profiles returned to background values at $t = 125$ hours, thereby providing a check on the accuracy of the numerical simulation.

3.2 Solar-Wind Velocity Profile: A 3D View

Figure 1 is a 3D view of the radial component of the solar-wind velocity in the $\phi = 45°$ meridional plane at $t = 50$ hours, 75 hours, and 100 hours after the start of the pressure pulse. Shown here are the velocity profiles for the N24° flare (upper row) and for the S18° flare (lower row). The steep "cliff" at each carpet plot's right side represents the outer boundary's drop-off to the background; no information is given here, outside the computational domain, and therefore this area should be ignored.

From the reader's vantage point, the N24° flare's fast forward MHD shock can be seen ($t = 50$ hours) at the northern-most boundary of the computational domain—the velocity profile closest to the reader, between the two vertical dotted lines. At the same boundary, the development of a small, fast reverse MHD shock wave can be seen.

3.3 Interaction of Shock with HCS

A better vantage point, vis-à-vis the HCS, is provided by the view of the S18° flare's fast forward MHD shock. At $t = 50$ hours, we can see what appears to be a precursor "hump" in the velocity profile, where the shock intersects the deepest part of the HCS' velocity minimum in the upstream, steady-state solar wind. This hump persists at $t = 75$ hours, but can no longer be seen at $t = 100$ hours because the 3D view shows only the rear of the shocked structure. The fast forward shock has already moved out of the computational domain at the right side. The $t = 100$ hour perspective does, however, allow a view of the return to the original, undisturbed, steady-state solar wind—thereby indicating another check on the accuracy of the numerical procedure (Ref. 12).

We believe that the hump noted above is produced by interaction of the incident fast forward shock with the HCS. Classical non-linear studies (Ref. 7) of the "splitting of an initial discontinuity" problem (viz shock-on-shock, shock-on-tangential discontinuity, etc.) have been used by Refs. 5, 8–10, and others. Wave-guide studies have been made by Ref. 11, and a linear approximation has been made by Ref. 1. The "shock-on-rotational discontinuity" problem probably comes closest to the case studied here. In this case, the incident shock encounters a current sheet through which the IMF reverses direction by 180°, and the plasma density rises and then drops off. Figure 2 shows a simplified sketch of this suggested interaction of the incident shock, S_f, with the HCS.

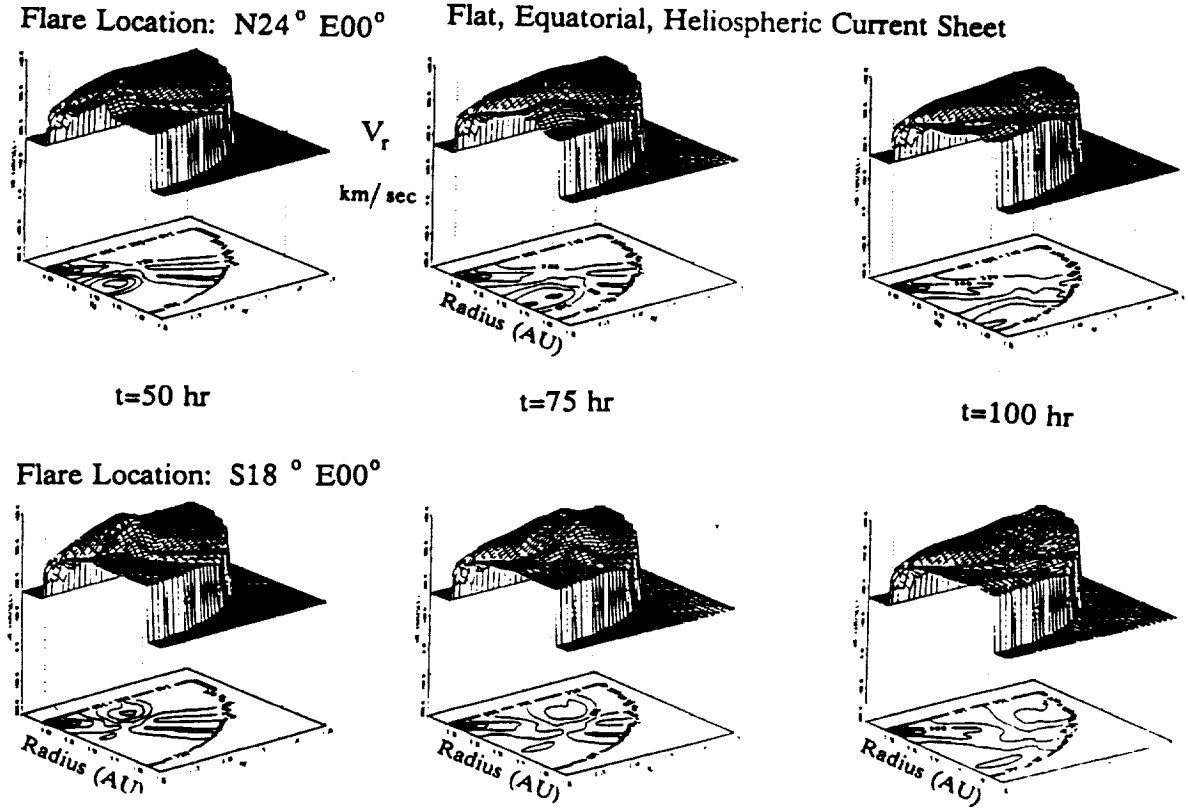

Figure 1. 3D view of the radial solar wind velocity in the $\phi = 45°$ meridional plane at three times following flares at N24° (top row) and at S18° (lower row).

ORIGINAL PAGE IS
OF POOR QUALITY

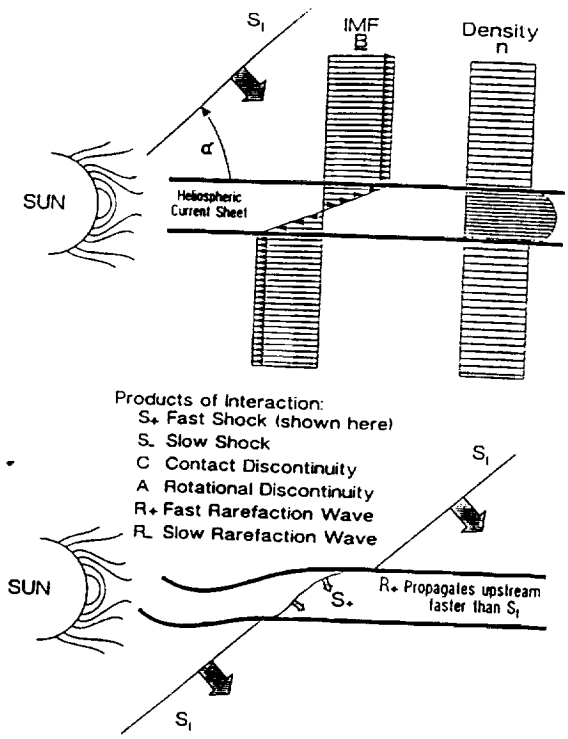

Figure 2. Schematic sketch of the interaction of a fast shock, S_I, with the HCS.

We are not aware of a rigorous study of the oblique shock's interaction with the HCS as described above. Based on related studies of Refs. 5 and 9, however, we know that the impinging shock first decreases its speed as it encounters the denser plasma in the HCS; it then increases its speed as it moves toward the other side of the HCS, and exits at the same speed with which it entered the HCS. Other products of the interaction (in addition to the fast shock just discussed) may include a slow shock, contact discontinuity, rotational discontinuity, a fast rarefaction wave, and a slow rarefaction wave. We believe that a fast rarefaction wave propagates within the HCS "wave guide" in the anti-sunward direction. If correct, this assumption could be an appropriate physical explanation for the early arrival of the disturbances from the equatorial-plane flares, as discussed in Section 3.1.

4. CONCLUDING REMARKS

In this study, the propagation of solar-generated shock waves has been investigated within the context of 3D numerical simulations that included the heliospheric current sheet in an assumed flat configuration, representative of solar-minimum conditions. In a closely related paper (Ref. 12) a simple, unipolar IMF was considered. In the present study we found, for a matrix of 27 simulated flare and observer positions, that the B_θ ($\equiv -B_z$ in solar-ecliptic coordinates used by *in situ* interplanetary experimenters) time series is strongly dependent on the observer's position relative to the flare—as found by Ref. 12. The presence of the HCS compounded this strong dependence. Further studies, particularly with animated, 3D color graphics, will provide further understanding of the complex, nonlinear, large-amplitude MHD waves that follow in the wake of the leading, fast forward MHD shock.

Finally, our 3D simulations yielded some hints concerning the interaction of the HCS with the leading, fast forward interplanetary shock. We speculated as to the products of this interaction and suggested that a fast rarefaction wave, R_+, would propagate upstream (faster than the shock itself) through the effective wave guide provided by the HCS. The speed of R_+ is probably dependent on the angle, α, between the incident fast forward shock (as shown in Figure 2) and the HCS as well as on the profiles of IMF magnitude and plasma density.

ACKNOWLEDGMENTS

STW, CCW, and SMH were supported by NOAA/SEI. Contract 50RANR000104. We thank Dr. T. Yeh and Dr. R. Zwickl for making useful suggestions and Ms. J. Trolinger for preparing the manuscript.

REFERENCES

1. Barton, M.E., G.L. Siscoe, and E.J. Smith, Shapes of strong shock fronts propagating through the coronal streamer belt, *J. Geophys. Res.*, in press, 1992.

2. Detman, T.R., M. Dryer, T. Yeh, S.M. Han, S.T. Wu, and D. McComas, A time-dependent, three-dimensional MHD study of interplanetary magnetic draping around plasmoids in the solar wind, *J. Geophys. Res.*, **96**, 9531, 1991.

3. Dryer, M., S.T. Wu, and T.R. Detman, Numerical simulations of solar disturbances and their interplanetary consequences, *Basic Plasma Processes on the Sun* (E.R. Priest and V. Krishan, Eds.), Proceedings of IAU Symposium 142, Bangalore, Kluwer Publ., Utrecht, 331–340, 1990.

4. Dryer, M., S.T. Wu, and S.M. Han, Three-dimensional, time-dependent MHD model of a solar-generated interplanetary shock wave, *The Sun and the Heliosphere in Three Dimensions* (R. G. Marsden, Ed.), 19th ESLAB Symposium. D. Reidel Publ. Co., Dordrecht, 135–140, 1986.

5. Grib, S.A., B.E. Brunelli, M. Dryer, and W.-W. Shen, Interaction of interplanetary shock waves with the bow shock–magnetopause system, *J. Geophys. Res.*, **84**, 5907, 1979.

6. Han, S.M., S.T. Wu, and M. Dryer, A three-dimensional, time-dependent modeling of super-sonic, super-Alfvénic MHD flow, *Computers and Fluids*, 16, 81, 1988.

7. Jeffrey, A., and T. Taniuti, *Non-Linear Wave Propagation*, Academic Press, New York, Chapter 7, 1964.

8. Neubauer, F.M., Nonlinear interaction of discontinuities in the solar wind and the origin of slow shocks, *J. Geophys. Res.*, **81**, 2248, 1976.

9. Shen, W.-W., Interaction of interplanetary MHD shock waves with the magnetopause, *Astrophys. Space Sci.*, **24**, 51, 1973.

10. Shen, W.-W., and M. Dryer, Magnetohydrodynamic theory for the interaction of an interplanetary double-shock ensemble with the earth's bow shock, *J. Geophys. Res.*, **77**, 4627, 1972.

11. Uralova, S.V., and A.M. Uralov, A numerical calculation of parameters of explosion MHD shock waves from moderate solar flares, *Plasma Astrophysics*, European Space Agency Publ. ESA SP-11, Proc. of joint Varenna–Abastumani–ESA–Nagoya–Potsdam Workshop, Telavi, Georgia, USSR, 4–12 June 1990, 99–101, 1990.

12. Wu, S.T., M. Dryer, and C.C. Wu, Three-dimensional numerical simulation of interplanetary magnetic field changes at 1 AU as a consequence of simulated solar flares, this volume, 1992.

ORIGINAL PAGE IS OF POOR QUALITY

SEE ALSO
93A29759

1992 SPIE Conference Paper

Forecasting the arrival of fast coronal mass ejecta at Earth by the detection of 2 - 20 keV neutral atoms

K. C. Hsieh and K. L. Shih

Department of Physics, University of Arizona
Tucson, AZ 85721

D. J. McComas

Los Alamos National Laboratory
Los Alamos, NM 87545

S. T. Wu and C. C. Wu

Center for Space Plasma and Aeronomic Research, University of Alabama
157-F Engineering Building, Huntsville, AL 35899

ABSTRACT

Studies have shown that Earth passages of fast coronal mass ejections (CMEs) trigger geomagnetic storms. Early identification of fast Earth-directed CME can help provide storm warnings, but detection of such by coronagraphs is extremely difficult. We suggest that energetic hydrogen atoms (EHA) between 2 and 10 keV produced during the transit phase of an Earth-directed CME by recombination between protons and electrons in the CME can travel ahead of the CME and act as harbingers of a magnetic storm. This forecasting scheme should work if enough EHA are produced, because while CMEs decelerate continuously after their ejection, the EHA fluxes produced in the initial phase of fast CMEs propagate at their initial high speeds ($> 1 \times 10^3$ km s^{-1}). Model simulations support this proposed mechanism. A coarse measurement of the CME-produced ENA at 1 AU could provide storm warning hours in advance, and finer measurements could yield detailed information on the likely geomagnetic effectiveness of a CME, as well as the evolution and propagation of CME between the Sun and Earth.

1. INTRODUCTION

Geomagnetic storms, manifested in a decrease in the horizontal component of Earth's magnetic field worldwide, have even more direct consequences on the public in the form of telecommunication and electrical power disruptions. For this reason, storm prediction is of considerable interest.[1]

Thus far, geomagnetic storms have been linked to the arrival at Earth of a compressed southward-pointing interplanetary magnetic field (IMF) and a coronal mass ejection (CME). A scheme to predict the arrival of a CME up to three days in advance by monitoring the space between Sun and Earth with a photometer has been proposed.[2] However, not all CMEs would trigger a major storm that could cause radio and electrical power blackouts. Of all the parameters associated with CMEs and IMF, that are relevant to the

triggering of large storms, the initial speed of a earthward directed CME close to the Sun appears to be most crucial.[3]

To avoid the difficulty of resolving a developing CME from the blinding background of the solar disk. Gosling et al.[3] proposed to place coronalgraphs well ahead and behind Earth in its orbit to monitor earthward directed CMEs in their initial stages near the limb. As an alternative option, we would like to examine the possibility of detecting any other signals that could be emitted by earthward directed CMEs of high initial radial speeds on a more affordable Earth-satellite. The brightness of the solar disk rejects serious considerations of photons as candidates. The spiral shape of the IMF that connects the Sun and Earth rules out charged particles as a medium. What remains are neutral particles. Neutral particles produced in CME in the initial high-speed stage can fly ahead of the CME as the CME slows down in its earthward propagation. If the deceleration of the CME is significant, then the neutrals born in the initial high-speed stage would arrive at Earth sufficiently early to provide warning. Fig. 1 illustrates this basic idea.

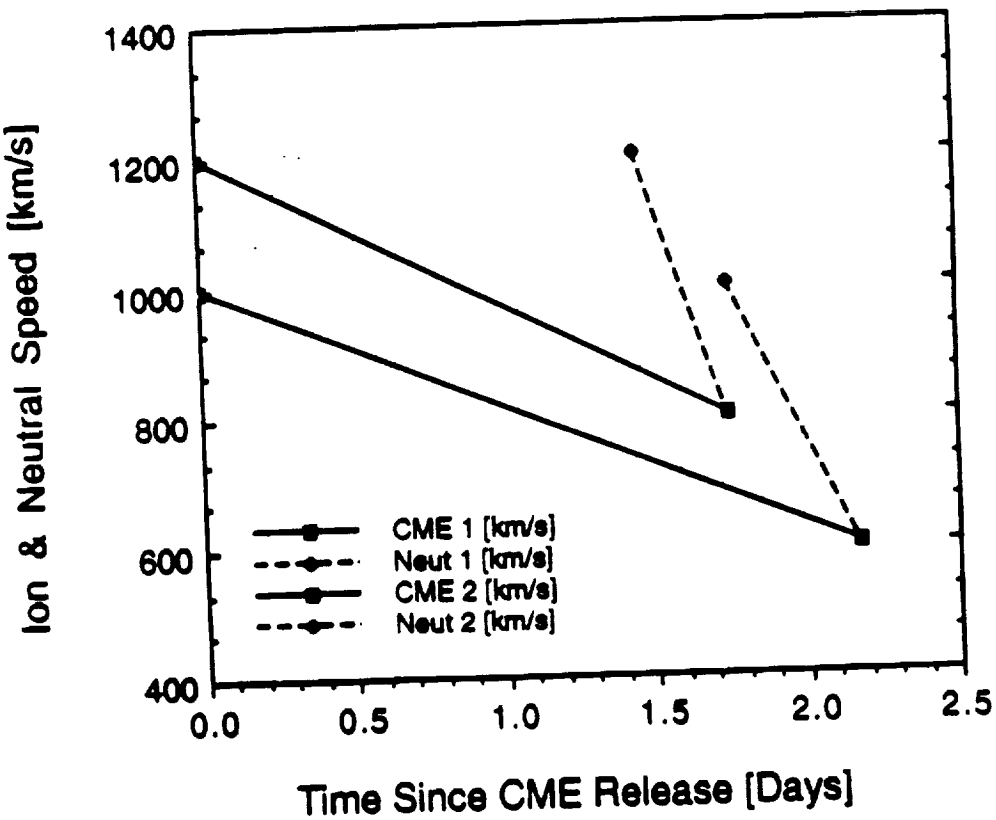

Fig. 1. Comparison of speeds of arriving neutrals (dashed lines) for two CMEs (solid lines) as functions of time after release from the sun. The top (bottom) trace is for a CME which is released at 1,200 (1,000) km/s and slows uniformly to 800 (600) km/s by 1 AU. This illustrates the basic idea of using EHA of CME origin as predictor of geomagnetic storms.

2. PRODUCTION OF H IN CME

The predominance of protons in space plasma allows us to concentrate only on the production of hydrogen atoms in CME. Protons can become neutral hydrogen atoms in a plasma by one of two interactions, provided the necessary ingredients are available.

Charge exchange: $p + H \rightarrow H + p$

Recombination: $p + e \rightarrow H^*$

The p's on the LHS are protons associated with the CME, which after the interactions become the H's on the RHS. The disparity in the proton and electron masses (1836 : 1) entails that the resulting H atom carries essentially the initial energy of the proton. Due to the lack of evidence of significant amount of ions of energies >2 keV in CMEs, let us rely only on the initial high bulk speed and the expansion of the CME to provide the high speed H atoms we need for storm prediction.

Although some CMEs contain large amounts of neutral H in their early stages, as observed in Hα out to ~5 R_s (solar radii),[4] the number density of H, n_H, is only 10^{-5} of that of protons, n_p, for a typical temperature of 10^6 K.[5] Therefore, charge exchange cannot be of significance to the production of neutral H in CMEs. On the other hand, the overall neutrality of plasma demands that within a CME $n_p \approx n_e$, the number density of electrons. Hence, we shall examine only the production of neutral H by recombination.

Along the direction of propagation of a CME, the flux of H in $(cm^2 \quad s)^{-1}$ resulting from recombination in a volume element moving with a bulk speed of v is

$$df = \alpha \, n_p \, n_e \, v \, dt \exp(-D) \qquad (1)$$

where α is the recombination coefficient, which is a function of the temperature of the gas. The exponential term represents extinction of H by impact- and photo-ionization while in flight between the point of recombination and the point of observation, i. e.

$$D = \int \{ \iint [\sigma_1(\varepsilon) + \sigma_2(\varepsilon)] \, n_p(\varepsilon, r') \, d\varepsilon + \int \sigma_3(\varepsilon) \, n_e(\varepsilon, r') \, d\varepsilon + \beta(r')(m/2E)^{1/2} \} \, ds'. \qquad (2)$$

The σ_i's are the cross-sections for the various interactions to remove the EHA before reaching the observer: σ_1 for charge exchange with solar-wind protons, σ_2 for proton impact ionization of hydrogen (σ_2 does not include σ_1) and σ_3 for electron impact ionization of hydrogen are given by Freeman and Jones;[6] β is the solar photoionization rate for H (= 8.8×10^{-8} s^{-1} at 1 AU, and falls off as r^{-2})[5, 7] and m is the rest mass of H. All σ_i's and the differential number densities n_i's (subscript p for proton, e for electron) are expressed in the appropriate relative energy ε between H the respective projectile. For each type of projectile, the kinematic transformation is different; therefore, the integration over relative energy must be done separately. After an H is born inside the CME, it has to go through portions of CME and overtake the CME in order to

reach Earth's orbit earlier than the CME. In such cases, charge exchange with a CME proton may occur, the resulting H will have a speed slightly slower than, but still close to, the original H. Therefore, we drop the effect of charge exchange with any proton of the CME. One may also ignore ionization by electron impact, since σ_3 << both σ_1 and σ_2.[6] Second and third encounters with the solar wind particles and solar photons need not be considered since the local IMF would remove the newly ionized H from its flight towards the observation point.

Since the CME is moving towards Earth with a deceleration as depicted in Fig. 1 and since the CME has a radial spread of several R_S at ~20 R_S and continues to expand as it propagates, H flux produced in one portion of the CME at an earlier time may arrive at the monitor at Earth's orbit simultaneously with those coming from another portion of the CME at a later time. To find the H flux arriving at the observer as a function of time, we integrate Eq. (1) over all elements of the CME, as it evolves and propagates, that would have the same arrival time. For the purpose of prediction of the arrival of a fast CME, we need only consider the activities along the Sun-Earth line.

3. PARAMETRIZED MODEL

To obtain the time profile of the fast H atoms of CME origin, at the observation point at Earth's orbit, R_o, we parametrize (for computational convenience) the evolving and propagating CME produced by a three-dimensional MHD simulation.[8,9] The radial profile of n_e (= n_p) is approximated by a gaussian distribution

$$n_e(r) = n_o \, (R_S / r)^{1.6} \exp [-(r - r_p)^2 / \sigma^2] \qquad (3)$$

where r is heliocentric distance; and the measure of the spread of the density distribution evolves with time as

$$\sigma(t) = (A + B t) \, R_S .$$

The centroid of the distribution propagates with a constant deceleration a

$$r_p = 15 \, R_S + v_o t - a t^2 / 2 ,$$

where v_o is the initial radial velocity. For the lack of knowledge at r < 15 R_S, we take r = 15 R_S as our initial r_p. Consequently, radial velocity of any element away from the centroid has a time dependence

$$r'(t) = v_o - a t + B \, (R_o - r - v_o t + a t^2/2) / (A + B t)$$

which decreases in a nonuniform fashion as compared to that of the centroid, but more like that from the MHD simulation.

4. H OF CME ORIGIN AT EARTH'S ORBIT

Obviously, the fastest H that traveled the least distance will arrive at Earth's orbit first. For a model just described, however, it is not so straight forward. To find the H flux arriving at the observer at Earth's orbit

as a function of time, we integrate Eq. (1) over all elements of the CME that would produce H atoms having the same arrival time. The value of α in Eq. (1) is 1×10^{-14} cm^3 s^{-1} for a gas at 2×10^6 K, temperature of the simulated CME.[10] For each time of arrival at Earth's orbit, t_E, the limits of integration are

$$t_1 = t_E - g(t_E; m = -2.0) \text{ and } t_2 = t_E - g(t_E; m = 2.0) \text{ , where}$$

$$g(t_E; m) = [t_E^2 - 2 (v_o + m B) t_E / a + 2 (R_o - r - m A) / a]^{1/2} , \qquad (4)$$

where m runs from -2.0 to +2.0. Any contribution from within 5 R_S is dropped due to the limitation of this particular model. Neutrals generated by any portion of the CME that has already arrived or passed Earth's orbit are also ignored for obvious reason.

The two CMEs depicted in Fig.1 are tried with the above model with the following pairs of v_o and a: v_o = 1,200 km s^{-1} and a = 2.7×10^{-3} km s^{-2} for CME 1 and v_o = 1,000 km s^{-1} and a = 2.3×10^{-3} km s^{-2} for CME 2. They share the other parameters, based on the MHD simulation mentioned earlier: $n_o = 5.8 \times 10^5$ cm^{-3} $R_S^{1.6}$, corresponding to 5.7×10^3 cm^{-3} at 18 R_S; A = 10; and B = 0.2 hr^{-1}. The results are shown in the two panels of Fig. 2.

In each case, the dotted line represents the CME protons (same for electrons), and the solid line represents the time profile of the neutral H atoms (3.3 - 7.5 keV in the upper panel and 1.9 - 5.2 keV in the lower) produced in the CME by recombination. The sharp cut-offs are due to our limits of integration (m = -2.0 to 2.0 in Eq. (4)). The limits are reasonable, because the proton fluxes are comparable to the quiet-time solar-wind flux of 2×10^8 cm^{-2} s^{-1}.The neutrals do arrive about 2 - 3 hours earlier than the CME. The peak value of the CME proton flux, in both cases, is $<10^2$ that of the quiet-time solar wind. The H atoms do arrive earlier as expected.

5. DISCUSSION AND CONCLUSION

The results shown in Fig. 2 are not surprising. The neutral H atoms produced in the CMEs arrive earlier than the decelerated CMEs. The two cases differ only in their respective initial v_o at 15 R_S and constant deceleration a. We note that the peak ratio, p : H ≈ 10^5, is consistent with that of a plasma at 10^6 K.[5] The loss of H due to ionization by collisions with protons and photons is heaviest for those neutrals produced closer to the Sun, which has a total loss of ~10%.

Since the parametrized CME is based on the results of MHD simulations of a CME starting at 18 R_S, we consider our model realistic. If our model is sufficiently realistic, the question of how we can benefit from the earlier arrival of neutrals of CME origin becomes a question of detection techniques. As Fig. 2 shows, the lead time in prediction depends on the sensitivity of the neutral-particle detector. Obviously, the lead time can be even longer, if the triggering of a geomagnetic storm would require a proton flux more than a few times that of the quiet-time solar wind. If a detector has a sensitivity of 10^2 particles (cm^2 sr s)$^{-1}$, then a prediction of 3 hours or more is possible. One crucial criterion on the sensitivity of these instruments is their ability to reject photons, since they have to detect particles coming directly from the Sun. Techniques for detecting neutrals in the energy range of 2 - 20 keV with the required sensitivity have been developed.[11] and some of them may be presented in this same issue.

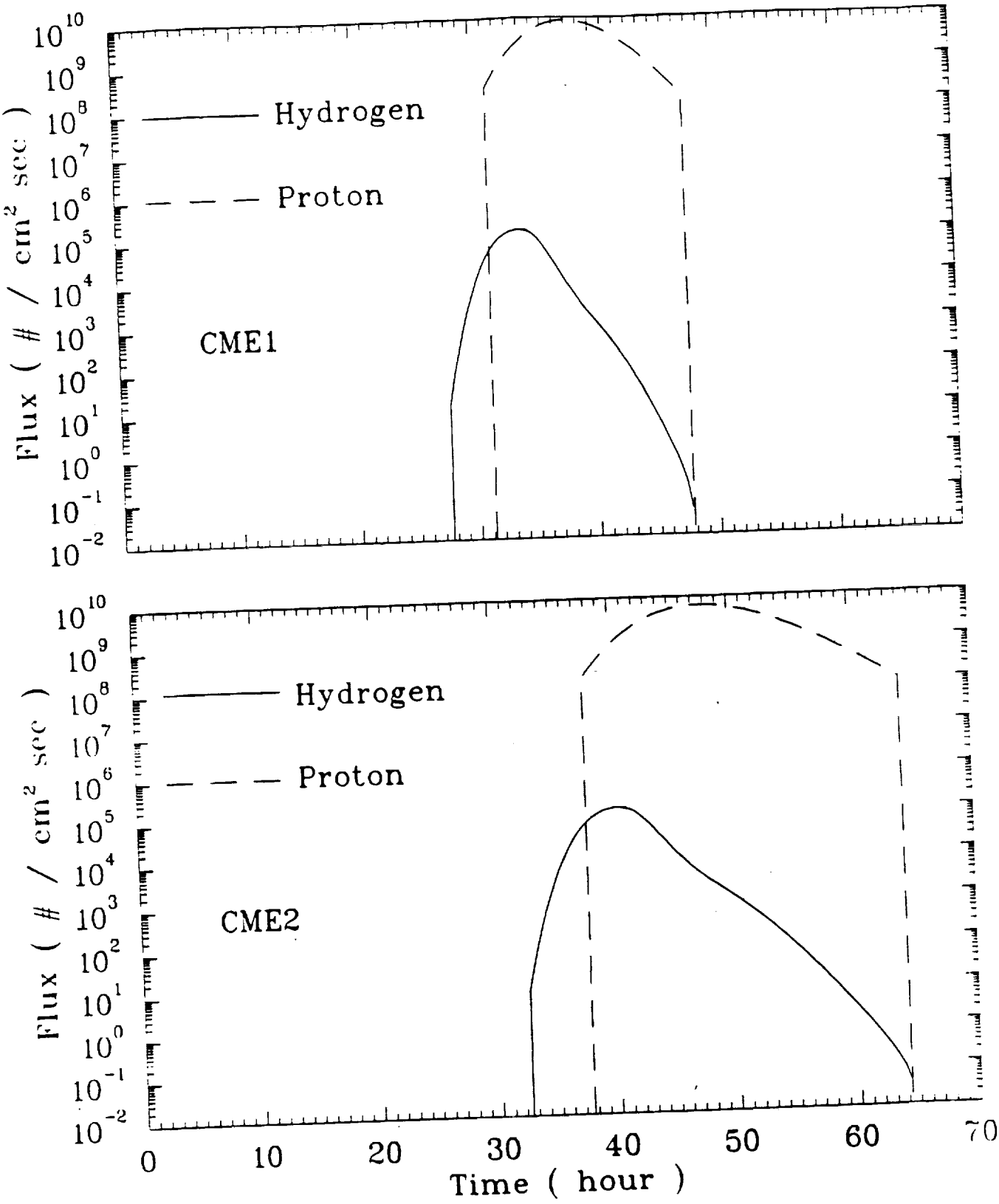
Hydrogen
Proton
CME1
Flux (# / cm^2 sec)
10^{10}
10^{9}
10^{8}
10^{7}
10^{6}
10^{5}
10^{4}
10^{3}
10^{2}
10^{1}
10^{0}
10^{-1}
10^{-2}
Hydrogen
Proton
CME2
Flux (# / cm^2 sec)
0
10
20
30
40
50
60
70
Time (hour)

Figure 2

Although there is no need for energy resolution in such detectors, if their task is limited to storm warning. Detectors with even modest energy resolution, however, can actually provide us information on the evolution and propagation of CME between the Sun and Earth for the first time. Since the fastest neutrals are produced nearest to the Sun, we can even measure the initial high speed of the CME, thus determine the geomagnetic effectiveness of that CME.[3]

We hope the results presented here will lead to immediate actions resulting in early-warning capabilities for geomagnetic storms and first-hand studies of the evolution and propagation of CME.

6. ACKNOWLEDGEMENT

This work is supported in part by NASA grant NAGW-1676 to the University of Arizona, NASA Grant NAGW-9 and NOAA Contract with EII(50RANR000104) to the University of Alabama. The work at Los Alamos National Laboratory was conducted under the auspices of the United States Department of Energy.

7. REFERENCES

1. J. T. Hoeksema, "Solar Sources of Geomagnetic Storms," APSNews, 1(3), 47-48, 1992.
2. B. Jackson, R. Gold, and R. Altrock, "The Solar Mass Ejection Imager," Adv. Space Res. 11(1), 377-381, 1991.
3. J. T. Gosling, D. J. McComas, J. L. Phillips, and S. J. Bame, "Geomagnetic Activities Associated with Earth Passage of Interplanetary Shock Disturbances and Coronal Mass Ejections," J. Geophys. Res. 96(A), 7831- 7839, 1991.
4. R. M. E. Illing and R. G. Athay, "Physical Conditions in Eruptive Prominences at Several Solar Radii," Solar Phys. 105, 173-190, 1986.
5. T. E. Holzer, "Neutral Hydrogen in Interplanetary Space," Rev. Geophys. Space Phys. 15, 467- ,1977.
6. R. L. Freeman and E. M. Jones, "Atomic Collision Processes in Plasma Pysics Experiments: Analytic Expressions for Selected Cross Sections and Maxwellian Rate Coefficients," CLM-R 137, UKAEA Culham Laboratory, 1974)
7. P. M. Banks and G. Kockarts, Aeronomy, Academic Press, New York, 1973.
8. S. T. Wu, S. Wang, M. Dryer, A. I. Poland, D. G. Sime, C. J. Wolfson, L. E. Orwig, and A. Maxwell, "Magnetohydrodynamic Simulation of the Coronal Transient Associated with the Solar Limb Flare of 1980, June 29, 18:21 UT," Solar Phys., 85, 351-373, 1983.
9. S. M. Han, S. T. Wu, and M. Dryer, "A Three-dimensional, Time-dependent Numerical Modeling of Super-sonic, Super-Alfénic MHD Flow," Computers &Fluids, 16 (1), 81-103, 1987
10. H. S. W. Massey and H. B. Gilbody, Electronic and Ionic Impact Phenomena, Chapter 20, IV. Oxford University Press, 1974.
11. D. J. McComas, B. L. Barraclough, R. C. Elphic, H. O. Funsten III, and M. F. Thomsen, "Magnetospheric Imaging with Low-energy Neutral Atoms," Proc. Natl. Acad. Sci. USA, 88, 9598-9602, 1992.

91A43535

AIAA 91-1470

MODIFIED ICED-ALE METHOD FOR ASTROGEOPHYSICAL PLASMA FLOWS

S. T. Wu, M. T. Song
Center for Space Plasma and Aeronomic Research
and Department of Mechanical Engineering
The University of Alabama in Huntsville
Huntsville, AL
and
M. Dryer
NOAA/Space Environment Laboratory
Boulder, CO

AIAA 22nd Fluid Dynamics, Plasma Dynamics & Lasers Conference
June 24-26, 1991 / Honolulu, Hawaii

For permission to copy or republish, contact the American Institute of Aeronautics and Astronautics
370 L'Enfant Promenade, S.W., Washington, D.C. 20024

MODIFIED ICED-ALE METHOD FOR ASTROGEOPHYSICAL PLASMA FLOWS

S. T. Wu* and M. T. Song**
Center for Space Plasma and Aeronomic Research
and Department of Mechanical Engineering
The University of Alabama in Huntsville
Huntsville, Alabama 35899 U.S.A.
and
Murray Dryer***
NOAA/Space Environment Laboratory
Boulder, Colorado, 80303

ABSTRACT

The ICED-ALE (Implicit-Continuous-Eulerian-Difference Mesh - Arbitrary-Lagrangian-Eulerian) algorithm which was originally suggested by Brackbill and Pracht (1973) is modified for the study of astrophysical plasma flows in which dynamical effects are important. In their work, the energy conservation includes only the sum of specific internal and magnetic energy. The kinetic energy of the plasma flow was not considered by these workers. In the present study, we have derived the general energy conservation law based on the Boltzmann equation which is suitable for astrophysical plasma flows. Thus, the total energy density includes three parts; kinetic, specific internal and magnetic energies. Because of this addition, the iteration procedure is modified in the present study in which we have included both total energy density and magnetic field components as the major iterative variables. Thus, the total energy is computed implicitly and the energy equation and magnetic induction equations are satisfied at the end of the iteration procedures to account for convergence.

A numerical example is given for a highly structured astrophysical plasma flow which shows that the convergence speed of the present scheme is better than the original one suggested by Brackbill and Pracht (1973). In addition, we also demonstrated that the rezoning algorithm can be used as a noise suppressor which greatly improves the numerical stability.

1. INTRODUCTION

In solving magnetohydrodynamic (MHD) flow problems the ICED-ALE method (Brackbill and Pracht, 1973 hereafter referred to as BP) has more advantages such as its ability to resolve arbitrary continuing boundaries; to have variable zoning for purposes of obtaining optimum resolution; to be almost Lagrangian for improved accuracy in problems where fully Lagrangian calculations are not possible; and to operate with a time step many times larger than possible with an explicit method. The most important advantage is to avoid the so-called Alfven problem which means that stability conditions severely limit the maximum time step when the Alfven speed is very large compared with the maximum fluid velocity. Thus, this method also allows us to deal with strong magnetic field problems with lower ratios of the gas pressure to magnetic pressure, $\beta = (p/(B^2/8\pi))$. In astrophysics there is often a necessity of disposing of a severely nonhomogeneous boundary interface on both sides of which gas densitites or magnetic fields are quite different. Several examples are the solar prominence in the chromosphere and corona as well as the solar magnetic flux tube in the subphotosphere. The ICED-ALE method (BP) potentially has the ability to solve such problems. In view of this possibility we will apply ICED-ALE to astrophysics problems with some improvement and extension.

First, in BP's extension of ICED-ALE to magnetohydrodynamic flow problems, the iterative variables and equations include only the magnetic induction equations together with the momentum and mass conservation laws. The total energy is computed explicitly. BP substituted the magnetoacoustic speed for the adiabatic sound speed and then introduced the proportionality between variations of augmented pressure and gas density as follows:

$$\delta\bar{p} = \left(c_s^2 + v_a^2\right)\delta\rho. \qquad (1)$$

But the validity of equality (1) was not strictly proved. Later we will demonstrate that, in the case of ordinary fluid flow the

equality $\delta p = c_s^2 \delta\rho$ used in the iteration

process corresponds to the energy conservation law and, thus, the ICED-ALE algorithm (Hirt, et al, 1974) seems to be adequate. In the case of MHD flow, the equality (1) is only an approximation to the energy conservation law.

Therefore, instead of the equality (1), we directly apply the general energy conservation law to the iteration process; thus, the total energy is obtained implicitly at the end of the iteration process. For the purpose of comparison we compute an example in which the convergence speed of the latter method is

*Director, CSPAR; Distinguished Professor, Univ. of Ala. System
Fellow, AIAA
**Permanent Address: Purple Mountain Obsv. Nanjing, People's Republic of China
***Senior Scientist, Interplanetary Phys.

substantially faster than that of the former. In fact, the total energy density is considerably influenced by the adjustments of velocities, positions, and magnetic fields in the iteration process. It is, therefore, reasonable to include both magnetic fields on the one hand and total energy density on the other hand for problems of magnetohydrodynamics. The magnetic field and fluid must be considered equally in such problems.

A full Lagrangian algorithm is very sensitive to variations in velocities and positions of vertices. Therefore, noises in velocity and positions will produce numerical instability and prevent obtaining a numerical solution. In order to remedy this difficulty, we use rezoning to eliminate or alleviate the numerical stability which is caused by velocity noise (and position noise) by adding another negative velocity noise and move the vertices to their original places. Such action is very similar to that in some electronic apparatus in which the feedback inhibition is used to suppress the electric noises.

In this paper we extend the BP method to include three components of $\vec{B}$ and $\vec{V}$ in two-dimensional cylindrical (or Cartesian) coordinates. In section 2, we describe the initializing calculation or explicit phase in which the electric current density, magnetic diffusion of field, energy augmentation due to Joule heating work done by gravity; and the zero-order approximation of the flow velocity are given. In section 3 we discuss the iteration process or implicit phase, from which we obtain the exact Lagrangian solution for energy density, velocity, magnetic field, etc. In section 4 an example is given from the field of solar physics to illustrate the advantage of the present method.

2. INITIALIZING CALCULATION

The basic MHD equations used in astrophysics are as follows (see Boyd et al. 1969):

$$\frac{\partial \rho}{\partial t} + \nabla \cdot (\rho \vec{U}) = 0, \tag{2}$$

$$\frac{\partial}{\partial t}\left(\rho \vec{U} + \frac{1}{4\pi c}\vec{E} \times \vec{B}\right) + \nabla \cdot \Pi - \rho \vec{g} = 0, \tag{3}$$

$$\frac{\partial}{\partial t}(\rho \epsilon) + \nabla \cdot (\rho \epsilon \vec{U}) = -\nabla \cdot \left[\left(p + \frac{B^2 - E^2}{8\pi}\right)\vec{U} - \frac{(\vec{U}\cdot\vec{B})}{4\pi}\vec{B} + \vec{Q}\right] - \nabla \cdot \left(\frac{c}{4\pi\sigma}\vec{j} \times \vec{B}\right) + \rho \vec{g} \cdot \vec{U}, \tag{4}$$

$$\frac{\partial \vec{B}}{\partial t} = \nabla \times (\vec{U} \times \vec{B}) - \nabla \times \left(\frac{c\vec{j}}{\sigma}\right), \tag{5}$$

$$\nabla \times \vec{B} = \frac{4\pi}{c}\vec{j}, \tag{6}$$

$$\vec{E} + \frac{1}{c}\vec{U} \times \vec{B} - \frac{\vec{j}}{\sigma} = 0, \tag{7}$$

where ρ is gas density, $\vec{U}$ flow velocity, $\vec{g}$ gravity acceleration, p gas pressure, c speed of light, σ electric conductivity, $\vec{j}$ electric current density, $\vec{E}$ electric field, B magnetic field. All quantities used here are in c.g.s. and gauss units. $\rho\epsilon$ is the total energy density which is defined as

$$\rho\epsilon = \frac{p}{\gamma - 1} + \frac{1}{2}\rho U^2 + \frac{E^2 + B^2}{8\pi}, \tag{8}$$

where γ is specific heat ratio (γ is often taken to be 5/3 for a fully-ionized plasma in Astrophyics). Q is the thermal energy flux having the formulation

$$\vec{Q} = -\lambda \operatorname{grad} T, \tag{9}$$

where λ is thermal conductivity, T gas temperature. Joule heating is included in the term $-\nabla \cdot \left(\frac{c}{4\pi\sigma}\vec{j} \times \vec{B}\right)$. The tensor π is defined as (in cartesian coordinates)

$$\pi_{ij} = \rho U_i U_j + p_{ij} + \frac{E^2 + B^2}{8\pi}\delta_{ij} - \frac{E_i E_j + B_i B_j}{4\pi}. \tag{10}$$

In magnetohydrodynamics the electric field can be neglected compared with the magnetic field, because E has an order of magnitude $\sim |U|/c\, B \ll B$ from eq. (7). In the same way the electromagnetic momentum $1/4\pi c\ E \times B$ also can be ignored compared with the gas momentum $\rho\vec{U}$. When neglecting the viscosity term the fluid stress tensor p_{ij} is simplified as $p_{ij} = p\,\delta_{ij}$. Therefore the momentum and energy conservation laws take the following form:

$$\frac{\partial}{\partial t}(\rho U_i) + \frac{\partial}{\partial x_j}(\rho U_i U_j) = -\frac{\partial}{\partial x_j}\left(\bar{p}\,\delta_{ij} - \frac{B_i B_j}{4\pi}\right) + \rho g_i, \tag{3a}$$

$$\frac{\partial}{\partial t}(\rho \epsilon) + \nabla \cdot (\rho \epsilon \vec{U}) = -\nabla \cdot \left[\bar{p}\,\vec{U} - \frac{(\vec{U}\cdot\vec{B})}{4\pi}\vec{B} + \vec{Q}\right] - \nabla \cdot \frac{c}{c\pi\sigma}\vec{j} \times \vec{B} + \rho \vec{g} \cdot \vec{U}, \tag{4a}$$

where $\bar{p}$ is augmented pressure defined as

$$\bar{p} = p + (B^2/8\pi). \tag{11}$$

In addition, the $\nabla \cdot \vec{B} = 0$ is used in this derivation.

Our computational mesh is shown in Figure 1 in the plane of which the axes z and r (or x and y) lie, but it must be kept in mind that the computation volume has a thickness $r \cdot \Delta\phi = r$ (taken with a unit azimuthal angle) or a thickness Δz for Cartesian coordinates. Later all formulae are written out in cylindrical coordinates, but they are valid for the Cartesian coordinates when replacing z, r, ϕ by x, y, z respectively and the thickness r is changed to Δz.

Similar to the procedure used by Hirt, et al. (1974) gas pressures p, augmented pressures $\bar{p}$, temperatures T, gas densities ρ, cell volumes V, total energy

ORIGINAL PAGE IS OF POOR QUALITY

densities $\rho\epsilon$, magnetic field components (B_z, B_r, B_ϕ) are assigned to cell centers, marked by A, B, C, D, etc. as shown in Fig. 2, while coordinates (z, r), velocity components (u, v, w) [$u = U_z$, $v = U_r$, $w = U_\phi$], current density components (j_z, j_r, j_ϕ) are assigned to cell vertices, marked by 1, 2, 3, 4 .... etc. as shown in Fig. 2. Notice that in this paper all quantities are independent of the azimuthal angle ϕ. It should be noted, however, that it is not difficult to extend this procedure to the three-dimensional case. Each of the following formulae is an integration approximation of the basic MHD equations either over the cell volume V_A with its surface indicated by the enclosed curve 1234 or over the vertex volume V_4 [$V_4 = 1/2\ (V_A + V_B + V_C + V_D)$] with its surface indicated by enclosed curve 1368.

To advance a solution one step in time, δt, we first need to complete the initializing calculation. This part included computing the current density $(J_4)_z$, $(J_4)_r$, $(J_4)_\phi$ [subscript 4 indicates the current around the vertex 4], magnetic diffusion term $-\nabla \times (c\vec{j}/\sigma)$, Joule heating, and energy gain from thermal conduction. Because of the smallness of these quantities, it is enough to compute them explicitly using the last time-step values (not the update data) only. Furthermore, we have to calculate the first-order approximation of advanced velocity components u_4, v_4, w_4 (here the tilde sign signifies the first-order approximation) in this phase in favor of entering the iteration phase.

Integrating eq (6) (Ampere's law) over the vertex volume V_4 gives

$$(j_4)_\phi \frac{V_A+V_B+V_C+V_D}{2} = \frac{c}{4\pi}\left[\oint_{1368} \bar{r}\cdot B_r dr + \oint_{1368} \bar{r}\cdot B_z dz\right] \quad (12)$$

Similarly, the other physical quantities are expressed by Joule heating contribution

$$= -\frac{\delta t}{V_A}\iiint_{V_A} \nabla\cdot\left(\frac{c}{4\pi\sigma}\cdot\vec{j}\times\vec{B}\right)d\tau \quad (13)$$

$$\text{thermal conduction} = -\frac{\delta t}{V_A}\iiint_{V_A}\nabla\cdot\vec{Q}\,d\tau$$

$$= -\frac{\delta t}{V_4}\left[\iint_{12\ \text{surface}}\vec{Q}\cdot d\vec{S} + \iint_{23\ \text{surface}}\vec{Q}\cdot d\vec{S} + \iint_{43\ \text{surface}}\vec{Q}\cdot d\vec{S} + \iint_{14\ \text{surface}}\vec{Q}\cdot d\vec{S}\right] \quad (14)$$

For example where the integration $\iint_{43\ \text{surface}}\vec{Q}\cdot d\vec{S}$ represents the thermal flux across the interface between vertices 4 and 3 which can be calculated as follows:

$$-\frac{\delta t}{V_4}\iint_{43}\vec{Q}\cdot d\vec{S} = \frac{\delta t}{V_4}\bar{\tau}\int_{\text{vertex 3}}^{\text{vertex 4}}\left(\lambda\frac{\partial T}{\partial z}dr - \lambda\frac{\partial T}{\partial r}dz\right), \quad (15)$$

The initializing calculation for the magnetic field and energy density are represented by

$$(\bar{B}_z)_4 = B_{z4}^n + \left[-\nabla\times\left(\frac{c\vec{j}}{\sigma}\right)\right]_{z,4}\cdot\delta t$$

$$(\bar{B}_r)_4 = B_{r4}^n + \left[-\nabla\times\left(\frac{c\vec{j}}{\sigma}\right)\right]_{r,4}\cdot\delta t \quad (16)$$

$$(\bar{B}_\phi)_4 = B_{\phi4}^n + \left[-\nabla\times\left(\frac{c\vec{j}}{\sigma}\right)\right]_{\phi,4}\cdot\delta t$$

$$(\overline{\rho\epsilon})_4 = (\rho\epsilon)_4^n + \frac{M_4}{V_4}\cdot\delta t\cdot\frac{1}{4}\sum_{i=1}^{4}(g_z u_i + g_r v_i + g_\phi w_i) -$$

$$+ \text{thermal contribution} + \text{Joule heating contribution}, \quad (17)$$

where the superscript n indicates the old time-step.

Eq. (3) is integrated over the vertex volume V_4. The integration of the left hand side of Eq. (3) gives the momentum variation with time in Lagrangian coordinates. So Eq. (3) turns out to be in the form:

$$\bar{u}_4 = u_4^n + \delta t\cdot g_z - \frac{\delta t}{2M_4}\left[\bar{P}_A(r_3 - r_1)\frac{r_3+r_1}{2} + \bar{P}_B(r_4 - r_3)\frac{r_4+r_3}{2} + \bar{P}_C(r_B - r_4)\frac{r_B+r_4}{2} + \bar{P}_D(r_1 - r_B)\frac{r_1+r_B}{2}\right]$$
$$+ \frac{\delta t}{2M_4}\cdot\frac{1}{4\pi}\left[(B_zB_z)_A\cdot(r_3 - r_1)\frac{r_1+r_3}{2} + (B_zB_z)_B(r_4 - r_3)\frac{r_4+r_3}{2} + (B_zB_z)_C(r_B - r_4)\frac{r_B+r_4}{2} + (B_zB_r)_D(r_1 - r_B)\frac{r_1+r_B}{2}\right] - \frac{\delta t}{2M_4}\cdot\frac{1}{4\pi}\left[(B_zB_r)_A\cdot(z_3 - z_1)\frac{r_1+r_3}{2} + (B_zB_r)_B(z_4 - z_3)\frac{r_4+r_3}{2} + (B_zB_r)_C\cdot(z_B - z_4)\frac{r_B+r_4}{2} + (B_zB_r)_D(z_1 - z_B)\frac{r_1+r_B}{2}\right]$$

$$\bar{v}_4 = v_4^n + \delta t\cdot g_r + \frac{\delta t}{2M_4}\left[\bar{P}_A\cdot r_4(z_3 - z_1) + \bar{P}_B r_4(z_4 - z_3) + \bar{P}_C\cdot r_4(z_B - z_4) + \bar{P}_D\cdot r_4(z_1 - z_B)\right] + \frac{\delta t}{2M_4}\cdot\frac{1}{4\pi}$$
$$\left[(B_rB_z)_A\cdot(r_3 - r_1)\frac{r_1+r_3}{2} + (B_rB_z)_B(r_4 - r_3)\frac{r_4+r_3}{2} + (B_rB_z)_C(r_B - r_4)\frac{r_B+r_4}{2} + (B_rB_z)_D(r_1 - r_B)\frac{r_1+r_B}{2}\right]$$
$$- \frac{\delta}{2M_4}\cdot\frac{1}{4\pi}\left[(B_rB_z)_A\cdot(z_3 - z_1)\frac{r_1+r_3}{2} + (B_rB_r)_B(z_4 - z_3)\frac{r_4+r_3}{2} + (B_rB_r)_C(z_B - z_4)\frac{r_B+r_4}{2} + (B_rB_r)_D(z_1 - z_B)\frac{r_1+r_B}{2}\right]$$

ORIGINAL PAGE IS
OF POOR QUALITY

ORIGINAL PAGE IS
OF POOR QUALITY

$$\bar{v}_4 = \bar{w}_4 + \delta t \cdot g_0 + \frac{\delta t}{2M_4} \cdot \frac{1}{4\pi} \{ (B_3B_2)_A (r_3 - r_2) \frac{r_2 + r_3}{2} + (B_3B_2)_B (r_4 - r_3) \frac{r_4 + r_3}{2} + (B_3B_2)_C (r_2 - r_4) \frac{r_2 + r_4}{2} + (B_3B_2)(r_1 - r_2) \frac{r_1 + r_2}{2} \} - \frac{\delta t}{2M_4} \cdot \frac{1}{4\pi} \{ (B_3B_2)_B (z_4 - z_3) \frac{r_4 + r_3}{2} + (B_3B_2)_C (z_2 - z_4) \frac{r_2 + r_4}{2} + (B_4B_2)_D \cdot (z_1 - z_2) \frac{r_1 + r_2}{2} \}, \quad (18)$$

where $M_4 = (1/4) \cdot (M_A + M_B + M_C + M_D)$, $M_A = V_A \cdot \rho_A$. The average radius in the $\bar{p}$ term in $\bar{v}_4$-representation is taken to be r_4 in order to keep $\bar{U}$ constant in the steady state, if we suppose $g_r = 0$, $g_\phi = 0$, $g_z = g$. Of course, other choices for $\bar{r}$ are allowed. Using Eq. (18) we start from the values at the last time-step and obtain the first-order appoximation of time-advanced velocity components before commencing the iteration procedure.

3. ITERATION PROCESS

The objective of this section is to obtain new velocities that have been accelerated with time-advanced augmented pressure gradients and new magnetic stress tensors. Since the new magnetic fields depend on the new velocities, and the time-advanced p is based on the densities as well as energies obtained when vertices are moved with their new velocities, which in turn, are functions of the new B and p, these fields and augmented pressures are defined implicitly and must be found by iteration. The major iterated variables we choose are B_z, B_r, B_ϕ, $\rho\epsilon$ in order to satisfy the induction equation (5) and energy conservation law (4) exactly. Because we have included the magnetic diffusion term and Joule heating as well as thermal conduction term, in the initialization phase as described in section 2, it is reasonable to leave the dynamic terms (i.e. the terms associated with $\bar{U}$) in Eqs. (5) and (4) only during this process. Therefore, the equations which must be obeyed in the iteration are:

$$\frac{\partial \vec{B}}{\partial t} - (\vec{U} \cdot \nabla)\vec{B} = (\vec{B} \cdot \nabla)\vec{U} - \vec{B}(\nabla \cdot \vec{U}), \quad (19)$$

$$\frac{\partial}{\partial t}(\rho\epsilon) + \nabla \cdot (\rho\epsilon\vec{U}) = -\nabla \cdot (\bar{p}\vec{U}) - \frac{(\vec{U} \cdot \vec{B})}{4\pi} \vec{B}, \quad (20)$$

$$\frac{\partial \rho}{\partial t} + \nabla \cdot (\rho\vec{U}) = 0 \quad (2)$$

Integrating Eq. (2) over the cell volume V_A gives

$$M_A = \text{const. or } \frac{\delta \rho_A}{\rho_A} - \frac{\delta V_A}{V_A} = 0 \quad (21)$$

which means that the mass remains constant in Lagrangian coordinates. The integrations of the left hand sides of Eqs. (19) and (20) are none other than the time-derivatives in Lagrangian Coordinates. Considering that Eqs. (19) and (20) are only satisfied gradually during the iteration, we introduce some new functions called "unsatisfactory" quantities, s_z, s_r, s_ϕ, $s_{\rho\epsilon}$ which are defined as the differences between the integrations of left and right hand sides of Eqs. (19) - (20). Thus, we get (after integrating Eqs. (19) - (20) over the cell volume V_A).

$$S_z \equiv \frac{({}^L B_z - B_z^N)}{\delta t} - {}^L B_z \, DU_z DZ - {}^L B_r DU_z DR + {}^L B_z D, \quad (22)$$

$$S_r \equiv \frac{({}^L B_r - B_r^N)}{\delta t} - {}^L B_z DU_r DZ - {}^L B_r DU_r DR + {}^L B_r \frac{v_1+v_2+v_3+v_4}{r_1+r_2+r_3+r_4} + {}^L B_r D, \quad (23)$$

$$S_r \equiv \frac{({}^L B_r - B_r^N)}{\delta t} - {}^L B_z DU_z DZ - {}^L B_r DU_r DR + {}^L B_r \frac{v_1+v_2+v_3+v_4}{r_1+r_2+r_3+r_4} + {}^L B_r D, \quad (24)$$

$$S_\epsilon \equiv \frac{({}^L(\rho\epsilon) - (\rho\epsilon)^N)}{\delta t} + {}^L\bar{p} \cdot (DU_z DZ + DU_r DR) - ({}^L B_z)^2 \cdot DU_z DZ - ({}^L B_r)^2 DU_r DR - {}^L B_z {}^L B_r DU_z DZ - {}^L B_z {}^L B_r \cdot (DU_r DZ + DU_z DR), \quad (25)$$

where superscript L denotes time-advanced values and N denotes first order approximations coming from initializing calculations and,

$$D = \frac{1}{V_A} \iiint \text{div } \vec{U} \, dr = DU_z DZ + DU_r DR + \frac{v_1+v_2+v_3+v_4}{r_1+r_2+r_3+r_4}, \quad (26)$$

$$DU_z DZ = \frac{1}{V_A} \iiint \frac{\partial V_z}{\partial z} dr = \frac{(r_4-r_2)(u_3-u_1) - (u_4-u_2)(r_3-r_1)}{2 \cdot ARE}, \quad (27)$$

$$DU_z DR = \frac{1}{V_A} \iiint \frac{\partial V_z}{\partial r} dr = -\frac{(z_4-z_2)(u_3-u_1) - (u_4-u_2)(z_3-z_1)}{2 \cdot ARE}, \quad (28)$$

$$DU_r DZ = \frac{1}{V_A} \iiint \frac{\partial V_r}{\partial z} dr = \frac{(r_4-r_2)(v_3-v_1) - (v_4-v_2)(r_3-r_1)}{2 \cdot ARE}, \quad (29)$$

$$DU_r DZ = \frac{1}{V_A} \iiint \frac{\partial V_z}{\partial r} dr = -\frac{(z_4-z_2)(v_3-v_1) - (v_4-v_2)(z_3-z_1)}{2 \cdot ARE}, \quad (30)$$

$$ARE = \frac{1}{2}[(z_3-z_1)(r_4-r_2) - (r_3-r_1)(z_4-z_2)],$$

$$V_A = \frac{v_1+v_2+v_3+v_4}{4} \cdot (\Delta RE), \quad (31)$$

$$DU_\phi DZ = \frac{1}{V_A} \iiint \frac{\partial V_\phi}{\partial z} dr = \frac{(r_4-r_2)(w_3-w_1) - (w_4-w_2)(r_3-r_1)}{2 \cdot ARE}, \quad (32)$$

$$DU_\phi DZ = \frac{1}{V_A} \iiint \frac{\partial V_\phi}{\partial z} dr = \frac{(z_4-z_2)(w_3-w_1) - (w_4-w_2)(z_3-z_1)}{2 \cdot ARE}. \quad (33)$$

Notice that the terms $(v_1+v_2+v_3+v_4)/(r_1+r_2+r_3+r_4)$, $(w_1+w_2+w_3+w_4)/(r_1+r_2+r_3+r_4)$ will disappear when these equations are written in Cartesian coordinates.

The iteration convergence process is achieved by computing the adjustments of $\rho\epsilon$, B as well as p, $\bar{U}$ which make the magnitudes of S_z, S_r, S_ϕ, $S_{\rho\epsilon}$ diminsh. When they all go to zero, the exact Lagrangian solutions for MHD equations have been obtained. In order to find out such adjustment for various quantities let us have a look at what the independent iterative variables are. From Eq. (18) it seems that they are B_z, B_r, B_ϕ, and p.

ORIGINAL PAGE IS
OF POOR QUALITY

But the definition of augmented pressure and energy density gives the exact relationship between them:

$$\bar{P} = (\gamma-1)(\rho\epsilon) + (2-\gamma)\frac{B^2}{8\pi} - (\gamma-1)\frac{\rho U^2}{2} \qquad (34)$$

Recalling Eq. (18) it can be seen that the independent iterative variables are either $(B_z, B_r, B_\phi, \rho\epsilon)$ or $(B_z, B_r, B_\phi, \bar{P})$. But the former is better than the latter, because we have the energy conservation law Eq. (20) which determines the variation of $\rho\epsilon$. On the other hand, if the set of variables $(B_z, B_r, B_\phi, \bar{P})$ is chosen, we do not know how to get the adjustment for $\bar{P}$ appropriately. It was for this reason that BP introduced another relation $\delta\bar{p} = (C_s^2 + V_A^2)\,\delta\rho$ which expresses an extension of the adiabatic sound speed to the magnetoacoustic speed. However, this relation is not fully self-consistent with the energy conservation law.

Now let us find the adjustments to B_z, B_r and B_ϕ. From Eqs. (22) - (24) it can be seen that S_z, S_r, S_ϕ are essentially based on B_z, B_r, B_ϕ and only weakly depend on $(\rho\epsilon)$ through the derivatives of velocity DU_z/DZ etc. Because we only need the approximate values of such adjustments, it is enough to compute the variations of S_z, S_r, S_ϕ, associated with B_z, B_r, B_ϕ. Therefore, the total variation of S_z can be written as (expanded to include first-order terms in Taylor series):

$$\Delta S_z = \frac{\partial S_z}{\partial B_z}\delta B_z + \frac{\partial S_r}{\partial B_r}\delta B_r + \frac{\partial S_z}{\partial B_\phi}\delta B_\phi .$$

If we put ΔS_z equal to the negative unsatisfactory quantity S_z computed at each iteration cycle, then at the next iteration S_z would turn out to be zero or very small. In this way, we are able to diminish unsatisfactory quantities very quickly.

4. NUMERICAL RESULTS

In order to illustate the present improved ICED-ALE algorithm, we will apply it to an astrophysical problem concerning the compression of a slender magnetic flux tube beneath the solar photosphere. The flux tube is assumed to be surrounded by a gravity-stratified ionized gas without magnetic field (Parker, 1977; Sweet, 1972). First, let us present a mathematical model to describe the physical situation of this problem. Due to the small depth (~10^9 cm, i.e. one seventh of solar radius ($R_\odot$)) of the layer we will study, it is reasonably assumed that the temperature varies linearly, and that the gas obeys the ideal state equation $p = R\rho T$ with a gas-constant R having a slow, linear (beta-dependence) variation. Thus, from the basic equations:

$$T = T_0 - \alpha(z-z_0),\quad R = R_0 - \beta(z-z_0)$$

$$p = R\rho T,\quad \frac{dp}{dz} + \rho g = 0 \qquad (35)$$

we obtain the pressure and density distribution in the sub-photosphere:

$$p = p_0 F,$$

$$\rho = F\cdot(p_0/R_0T_0)\cdot\left(1-\frac{\beta}{R_0}(z-z_0)\right)^{-1}\cdot\left(1-\frac{\alpha}{T_0}(z-z_0)\right)^{-1}$$

$$F = \left(1-\frac{\alpha}{T_0}(z-z_0)\right)^{g/R_0\alpha-\beta/R_0-1}\Big/\left(1-\frac{\beta}{R_0}(z-z_0)\right)^{g/R_0\alpha-\beta/R_0-1} \qquad (36)$$

Using the following parameters as the boundary conditions

$p_0 = 2.15 \times 10^4$ dyne/cm^2, $\quad g = 2.7 \times 10^4$ cm/s^2

$\rho_0 = 4 \times 10^{-5}$ gm/cm^3, $\quad \alpha = 5.2 \times 10^{-3}$ °K/cm

$T_0 = 4.9 \times 10^4$ °K, $\quad \beta = 4 \times 10^{-4}$ erg/K gm-cm

$z_0 = 3 \times 10^8$ cm,

the computation of (35) and (36) gives the respresentative mathematical model for the flux tube which is assumed to be perpendicular to the subphotosphere. This model is in good agreement with solar physical data (Allen, 1973; Stromgren 1965).

Next, a magnetic flux tube whose length is 10^9 cm and radius 1×10^8 cm is investigated. In particular, we study the propagation of physical disturbances along its lower half-part. Inside the tube we assume that there is a constant magnetic field parallel to the tube's vertical axis. For the reason of simplicity, suppose that the gravitational force is parallel to its axis, too. We divide the lower half-part of the tube into 15 zones axially and 10 radially. These 10 radial zones are homogeneous but the axial 15 zones are nonhomogeneous whose lengths are in a geometric sequence with the common factor 1.2 (in response to the gravity-stratification), as shown in Fig. 2. According to the demand of discrete mathematics we will compute the steady state of the subphotosphere (outside the tube). Static equilibrium demands that the pressure is independent of radius r (see Fig. 2):

$$p_A = p_D,\ p_B = p_C, \qquad (37)$$

and that the pressure only depends on z:

$$p_A = p_B\left(1+g\cdot(ARE)_i\cdot(2\Delta r\cdot R_BT_B)^{-1}\right)\cdot\left(1-g(ARE)_{i+1}\cdot(2\Delta r R_iT_i)^{-1}\right)^{-1} \qquad (38)$$

where the discrete temperature and gas-constants are computed by means of the following formula:

$$T_i = 6.4\times10^4 - 5.2\times10^{-3}\,(z_i+z_{i+1})/2,$$

$$R_i = 1.09814\times10^8 - 4\times10^{-4}\,(z_i+z_{i+1})/2, \qquad (39)$$

$$= 1.9317\times10^8 + 7.6923\,T_i,$$

(Notice that T and R depend on z (on index i) only). When the magnetic field is present inside the tube, we have to make the alternative choices: i) the temperature inside the tube is the same as that outside, and there is a difference of gas

densities between the inside and outside or ; ii) the densities are all the same but the temperature is different between the inside and outside of the tube. For the purpose of simplification, we choose the latter assumption, that is, we suppose that the gas density and pressure (or augumented pressure) depends only on z regardless of whether the point of interest is inside or outside of the tube. Numerical results are given in Fig. 3 which represent the steady state of the present model, where the gas-constant inside the tube is chosen to be 1.0944 x 10^8 considering the dynamic effect and the gas pressure as well as temperature are calculated as $p_i = p_i - B^2/8\pi$, $T_i = (p_i/\rho_i)/1.0944 \times 10^8$. After obtaining the steady state. We turn to study the convergence property of our improved ICED-ALE algorithm in comparison with that of BP. As a first test, we apply the following physical disturbance to part of the tube's lower section; $p = 2p_{initial}$. Thus, this disturbed part will be put forward, and the rest remains still; then, as a result, the intersection region between the two parts will develop a strong shear motion. In Fig. 4 the configuration of mesh and the distributions of velocity and magnetic field after a 20 sec. - evolution (δt = 1 sec.) are given. Fig. 5 shows the comparison of speeds of convergence for two methods at the first time advance, $t = 0 + \delta t$. From this result; it can be seen that in the present method the relative error $|\delta p/p|$ drops to less than 10^{-3} only after iterating for three times. On the other hand, when taking δt = 1 sec. the method of BP failed to converge. When lowering δt to 0.1 sec their method began to converge, but the speed of convergence is very slow and may attain saturation after 3 or 4 iterations. Therefore, the present method has a more rapid convergence speed. Furthermore, this convergence hardly reaches its saturation. Sometimes iteration can still achieve convergence for more than 40 iterations.

As another example, we will calculate the case in which a flux tube with a magnetic field of 6000 Gauss has a lateral force applied to part of the tube's length as indicated in Fig. 2 (without increasing the temperature) by an enhanced lateral pressure. The boundary conditions are as follows:

i) At r = 0 (cylindrical axis):
ρ, $\rho\epsilon$, p, T, Bz, Uz are symmetical
B_r, U_r are anti-symmetrical

ii) At lateral boundary (cylinder surface):
B = 0,
p, ρ, $\rho\epsilon$, T remain the same as those in the subphotosphere with the exception at z-direction-index i = 11, 12, 13
$p_{i,11} = p_{subphotosphere} \cdot (1+10\cdot|\cos(4\pi z_i/L)|)$
$\rho_{i,11} = p_{i,11}/(T\cdot R)_{subphotosphere}$,

iii) At the top and bottom:
free-propagation boundary,

that is, the enhanced pressure (= 11 $p_{subphotosphere}$) is added to the middle part (i = 11,12,13) of the tube. This means that such enhanced pressures tend to cut off the tube and divide it into two parts. When t is between 0 and 96 sec, δt is taken to be 0.2 sec. When 96 < t < 108 sec., δt = 0.4 sec., when t > 108 sec., δt = 0.5 sec. The numerical results are shown in Fig. 6 and 7. In this case the mesh configuration is almost Eulerian, i.e., the mesh nearly does not move. From Fig. 6 it can be seen that the magnetic field in the middle part of the tube increases as the pressure application continues. When t ~ 500 sec. the intensities of magnetic field near the axis reach about 8 x 10^4 Gauss where the magnetic pressure has the same order of magnitude as the gas pressure. On the other hand, with continuation of the force application on the tube's boundary, the high pressure and high density gradually invade the tube and, about t ~ 500 sec. occupy the middle of the tube's lower part. Futhermore, as shown in Fig. 7 the distribution of temperature inside as well as outside the tube, more or less, remains unchanged at first (t = 6 sec.) So the property of this kind of "squeeze" is basically isothermal compression at first. However, after 500 sec. evolution of the temperature in the middle of the tube reaches 1.85 x 10^5 °K which is about 4 times larger than the original one. Note, also, that, the density at this location (i = 11) decreases dramatically, thereby indicating that the "squeeze" is effective in cutting the tube into two parts, a lower and a higher portion. One may speculate that the upper part may eventually be expelled as a plasmoidal "melon seed".

ACKNOWLEDGEMENT

The work performed is supported by a NAGA Grant (NAGW-9) and NOAA Contract (5ORANR-000104).

REFERENCES

Allen, C. W., 1973, Astrophysical Quantities, Third Edition, Athlone Press.

Boyd, J. M. and Sanderson, J. J., 1969, Plasma Dynamics, Nelson Publ. Co., London.

Brackbill, J. U. and Pracht, W. E., 1973, J. Comp. Phys., 13, 455.

Engquist, E. and Majda, A., 1977, Math. Comput. 31, 629.

Hirt, C. W., Amsden, A. A., and Cook, J. L., 1974, J. Comp. Phys. 14, 227.

Parker, E. N., 1977, Ann. Rev. Astro. & Astrophys., 15, 45.

Stromgren, B., 1965, Stellar Structure, ed. Aller, Mclaughlin, p. 269, Chicago.

Sweet, P. A., 1972, IAU Sympo. No. 43, 457.

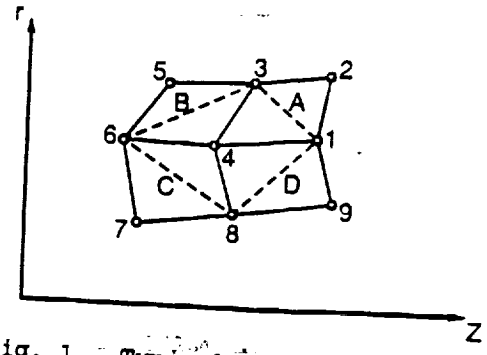

Fig. 1. Typical computation meshes

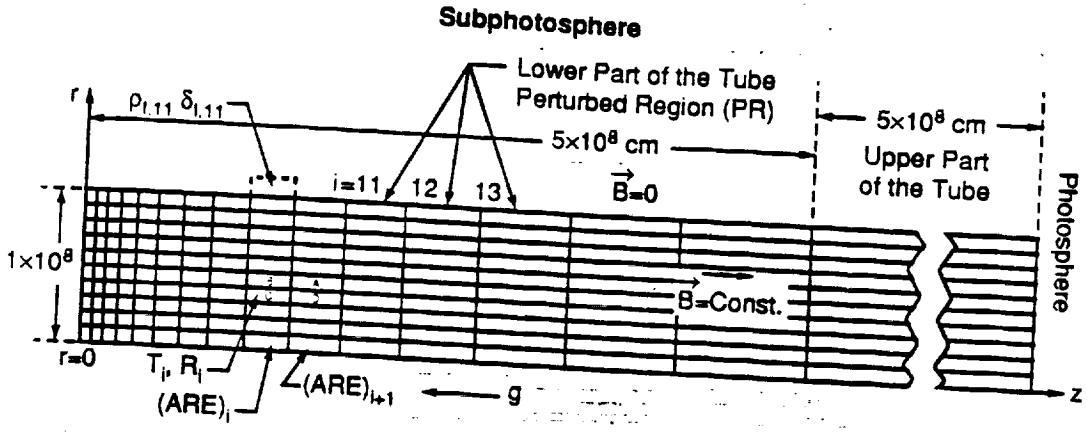

Fig. 2. Configuration of a magnetic flux tube beneath the photosphere, showing the mesh structure, the orientation of $\vec{B}$, $\vec{g}$ and the boundary condition. In one of several dynamical examples is applied to the surface of the cylindrical magnetic flux tube at the three vertical positions shown in the figure. The enhanced pressure is assumed to be equal to eleven times the steady-state subphotospheric pressure at those locations.

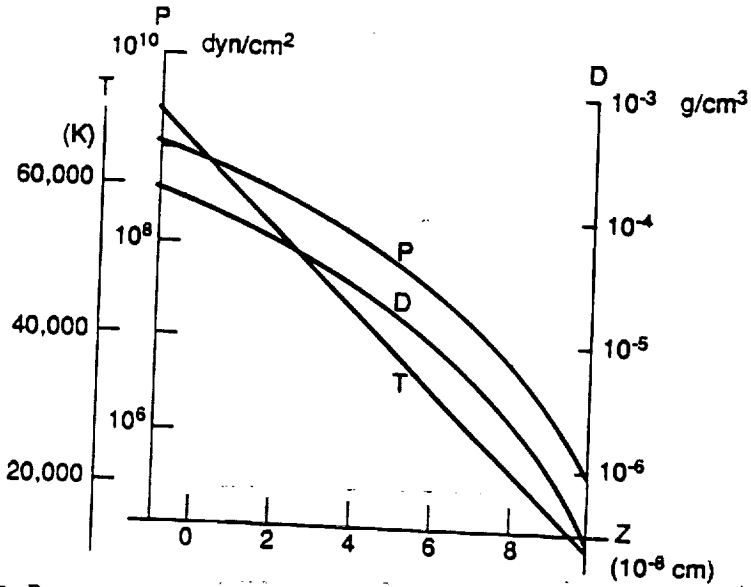

Fig. 3. Plasma Properties of the initial solar atmosphere obtained by the model.

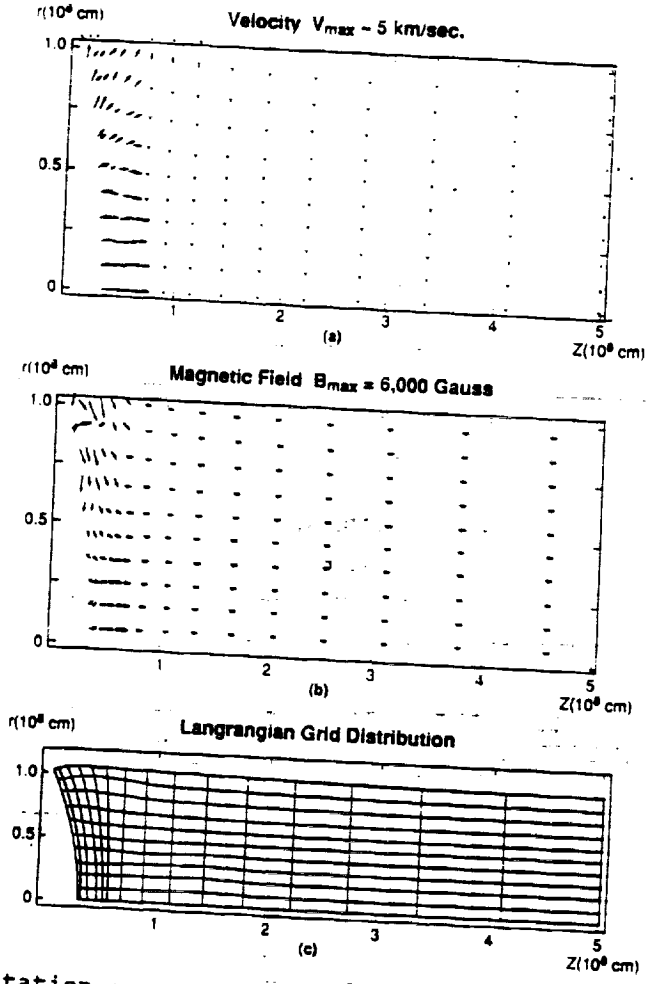

Fig. 4. A computation example. (a) the distribution of flow velocities at t = 20 sec., (b) the distribution of magnetic field at the same time, (c) the configuration of meshes at the same time. For this example, a pressure, $p = 2p_{initial}$, is applied at the bottom of the magnetic flux tube.

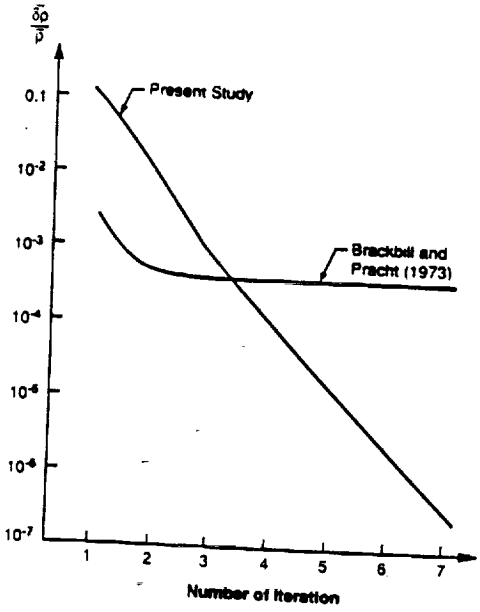

Fig. 5. Relative errors $|\delta\bar{p}/\bar{p}|_{max}$ versus number of iteration steps. Time step is taken to be 0.1 sec. in the method of Brackbill and Pracht (1973). It should be noted that $|\delta p/p|_{max} > |\delta B_z/B|_{max}$, $|dB_r/B|_{max}$, $|\delta(\rho\epsilon)/\rho\epsilon|$ in our case.

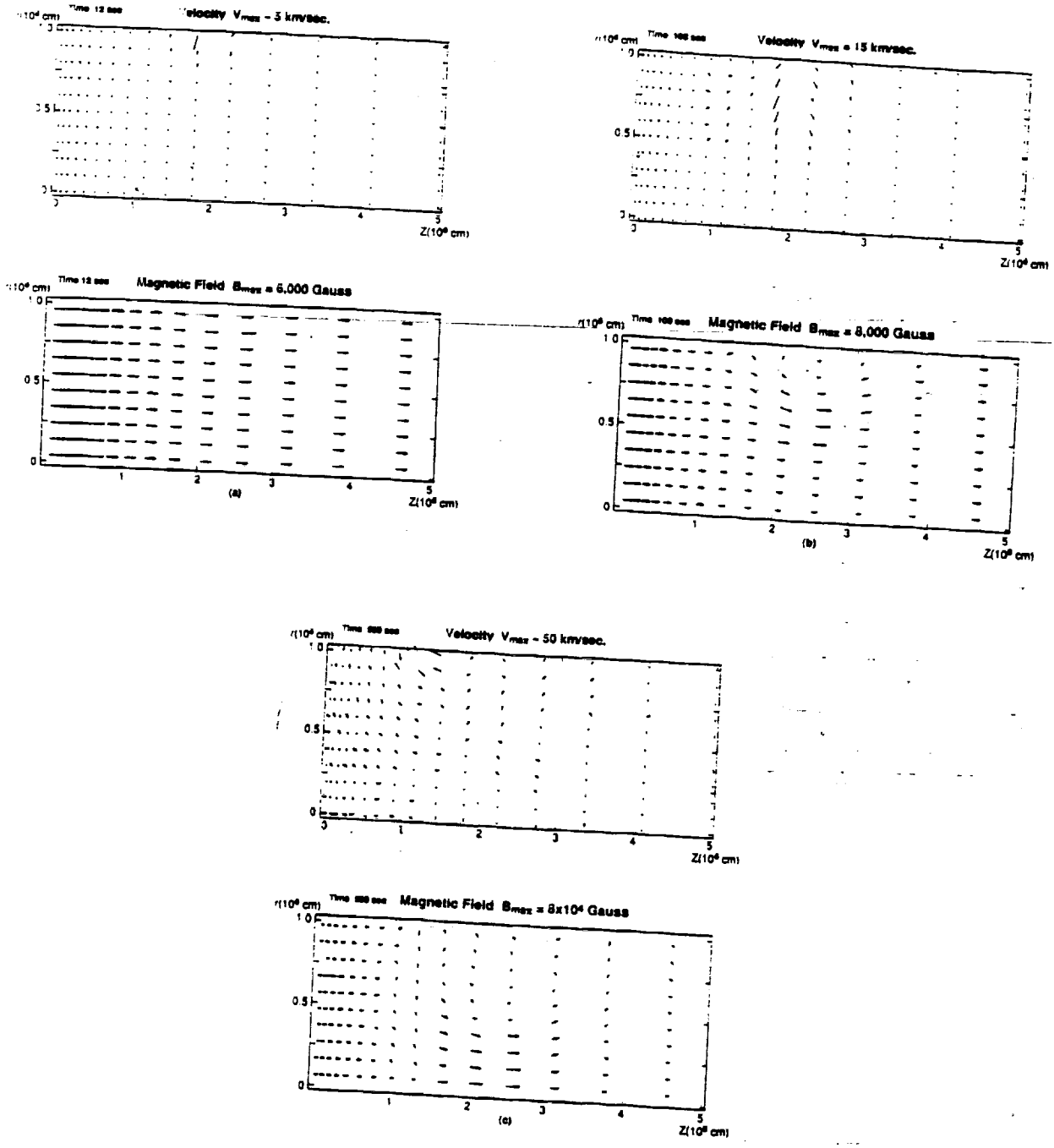

Fig. 6. Evolution of magnetic field and flow velocity of a flux tube following a sudden application of pressure, $p = 11p_{subphotosphere}$, at the positions i = 11, 12, 13, as shown in Figure 2, for an indefinite period of time. (a) at t = 12 sec. (b) at t = 108 sec. and (c) t = 500 sec.

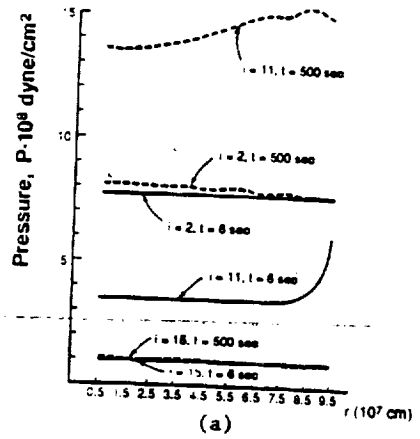

(a)

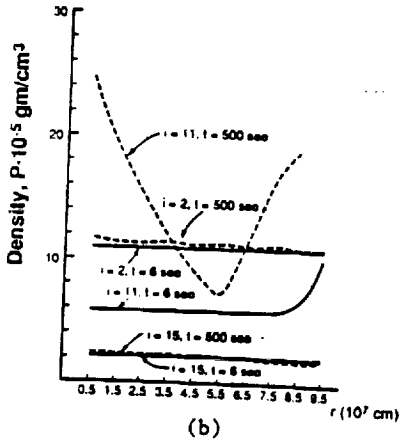

(b)

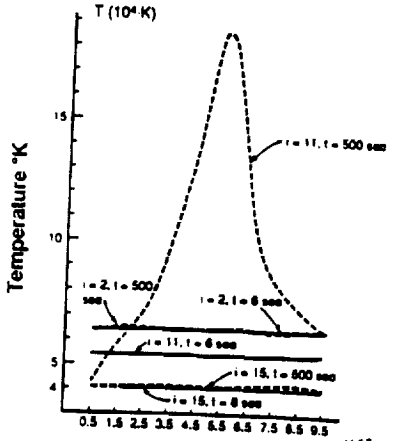

(c)

Fig. 7. $\bar{p}$, ρ, T versus tube's radial distance. These figures show the evolution of augmented pressure, density and temperature of the same tube as in Figure 6. Dashed lines represent the distribution at t = 500 sec while solid lines at t = 6 sec. "i" is z-direction indices (see Figure 2). i = 2 respresents the tube's bottom, i = 11 indicates the middle, and i = 15 the top (i.e., photospheric level).

ORIGINAL PAGE IS
OF POOR QUALITY

93A 46643

AIAA 93-3177
Extension of Rezoned Eulerian-Lagrangian Method to Astrophysical Plasma Applications

M. T. Song, S. T. Wu
The University of Alabama in Huntsville
Huntsville, AL 35899 and
M. Dryer
National Oceanic and Atmospheric Administration
Boulder, CO 80303

AIAA 24th
Plasmadynamics & Lasers Conference
July 6-9, 1993 / Orlando, FL

For permission to copy or republish, contact the American Institute of Aeronautics and Astronautics
370 L'Enfant Promenade, S.W., Washington, D.C. 20024

EXTENSION OF REZONED EULERIAN-LAGRANGIAN METHOD TO ASTROPHYSICAL PLASMA APPLICATIONS

M. T. Song and S. T. Wu*
Center for Space Plasma and Aeronomic Research
and Department of Mechanical Engineering
The University of Alabama in Huntsville
Huntsville, AL 35899
and
Murray Dryer**
Space Environment Laboratory
National Oceanic and Atmospheric Administration
Boulder, CO 80303

Abstract

It is well known that the great advantages of using the pure Lagrangian (or rezoned Eulerian-Lagrangian) scheme developed by Brackbill and Pracht[1] are (i.) dealing with severely nonhomogeneus boundary conditions and (ii.) avoiding numerical diffusion caused by nonlinear convective terms. However, their method is limited to simple configurations of the magnetic fields for which analytical solutions can be found. In astrophysical applications, there are a number of cases in which magnetic field configurations are complex, and for which analytical expressions of magnetic fields are not available. Therefore, numerical procedures are necessary for the temporal determination of magnetic field configurations and their consequences. In order to implement this objective, the rezoned Eulerian-Lagrangian scheme was modified by introducing two specific relaxation techniques to find a discrete solution for a trial analytical expression. These two relaxation techniques are: (i) computing relaxation coefficients and (ii) solving two quadratic equations. A numerical test example is given to illustrate the utilization of the new method.

I. Introduction

It has been recognized that there is a great advantage for using the pure Lagrangian (or rezoned Eulerian-Lagrangian) scheme developed by Brackbill and Pracht[1] to solve magnetohydrodynamic (MHD) flow fields with severely nonhomogeneous boundary conditions to avoid numerical diffusion caused by non-linear convective terms. However, the scheme developed by Brackbill and Pracht does cause some mathematical difficulties in disposing of the complex magnetic field topology. Hence, the original scheme suggested by Brackbill and Pracht[1] is restricted to simple configurations of magnetic topology (i.e. constant magnetic field) for which an analytical expression is required.

In astrophysical plasma applications as well as in engineering applications (MHD generator design), there are numerous cases in which the magnetic field topology is complex. An example is the quadrapolar field with x-type or y-type neutral point; analytical functions of magnetic field expressions are not available for the initial conditions so that numerical procedures may be initiated for their temporal solution. Therefore, we must seek a way to determine an exact numerical solution for the initial field topology in order to proceed. In section II, two methods are proposed to determine the initial field topology for which no analytical expressions are available. Numerical examples to illustrate these methods are given in section III. Finally, the concluding remarks are described in Section IV.

II. Relaxation and Quadratic-Equation Methods

For the purpose of constructing the complex magnetic field topology for the initial state, two techniques are suggested as follows:

Relaxation Methods:

The mathematical model governing the initial state is the magnetohydrostatic momentum equation, such as:

$$-\nabla p_0 + \rho_0 \vec{g} + \frac{1}{4\pi}\left(\nabla x \vec{B}_0\right) x \vec{B}_0 = 0 \qquad (1)$$

where $\vec{g}$ is the gravitational acceleration, p is the pressure, ρ is the density and $\vec{B}$ is the magnetic field induction with subscript "0" representing the initial state.

For very small plasma beta (i.e. $\beta = p_{plasma}/p_B$, the ratio of plasma to magnetic pressure), Equation (1) could be written as,

$$-\nabla p_0 + \rho_0 \vec{g} = 0 \qquad (2)$$

and

$$\left(\nabla x \vec{B}_0\right) x \vec{B}_0 = 0 \qquad (3)$$

---

* Fellow, AIAA
** Associate Fellow, AIAA

Copyright © 1993 by S. T. Wu. Published by the American Institute of Aeronautics and Astronautics, Inc. with permission.

This approximation implies that the initial magnetic field is a force-free magnetic field in which the plasma is confined within the magnetic field and all the currents flow parallel to the magnetic fields. Under the present circumstances, the initial magnetic field would be determined solely by the force-free condition (i.e. Eq.3). The discretization of Eq. (3) in two dimensions (z, x) gives:

$$
\begin{aligned}
&-[\ \left(B_z^2+B_x^2\right)_A\left(x_3-x_1\right)+\left(B_z^2+B_x^2\right)_B\left(x_6-x_3\right)\\
&+\left(B_z^2+B_x^2\right)_C\left(x_8-x_6\right)+\left(B_z^2+B_x^2\right)_D\left(x_1-x_{13}\right)]+\\
&+2[\ \left(B_z^2\right)_A\left(x_3-x_1\right)+\left(B_z^2\right)_B\left(x_6-x_3\right)\\
&+\left(B_z^2\right)_C\left(x_8-x_6\right)+\left(B_z^2\right)_D\left(x_1-x_8\right)\ ]\\
&-2[\left(B_zB_x\right)_A\left(z_3-z_1\right)+\left(B_zB_x\right)_B\left(z_6-z_3\right)\\
&+\left(B_zB_x\right)_C\left(z_8-z_6\right)+\left(B_zB_x\right)_D\left(z_1-z_8\right)]=0
\end{aligned}
\tag{4a}
$$

$$
\begin{aligned}
&[\ \left(B_z^2+B_x^2\right)_A\left(z_3-z_1\right)+\left(B_z^2+B_x^2\right)_B\left(z_6-z_3\right)\\
&+\left(B_z^2+B_x^2\right)_C\left(z_8-z_6\right)+\left(B_z^2+B_x^2\right)_D\left(z_1-z_8\right)]+\\
&+2[\ \left(B_xB_z\right)\left(x_3-x_1\right)+\left(B_xB_z\right)_B\left(x_6-x_3\right)\\
&+\left(B_xB_z\right)_C\left(x_8-x_6\right)+\left(B_xB_z\right)_D\left(x_1-x_8\right)\ ]\\
&-2[\left(B_x^2\right)_A\left(z_3-z_1\right)+\left(B_x^2\right)_B\left(z_6-z_3\right)\\
&+\left(B_x^2\right)_C\left(z_8-z_6\right)+\left(B_x^2\right)_D\left(z_1-z_8\right)]=0
\end{aligned}
\tag{4b}
$$

where B_Z and B_X represent, respectively, the vertical and horizontal components of the two-dimensional magnetic field. The z and x are, respectively, vertical and horizontal coordinates. The A, B, C, and D identify the cell as shown in Figure 1. It is well-known that the initial distribution of the astrophysical plasma parameters (p_0 and ρ_0) is exponential along the vertial coordinate (z-axis) because of the gravitational effect, thus, it is convenient to choose the x-coordinate to be homogeneous and the z-axis to be nonhomogeneous as shown in Figure 1, such as :

$$\left(x_3-x_1\right)=-\left(x_6-x_3\right)=-\left(x_8-x_6\right)=\left(x_1-x_8\right)=\Delta x$$

= Constant ,

and $-\left(z_3-z_1\right)=\left(z_1-z_8\right)\approx\dfrac{z_1-z_6}{2}$;

$\left(z_8-z_6\right)=-\left(z_6-z_3\right)=\dfrac{z_1-z_6}{2}$ with $\left(z_1-z_6\right)$ not a

constant. Using these relations, Eqs.(4a,b) become,

$$
\begin{aligned}
&[\ \left(B_z^2+B_x^2\right)_A-\left(B_z^2-B_x^2\right)_B-\left(B_z^2+B_x^2\right)_C-\left(B_z^2+B_x^2\right)_D\ ]\\
&\cdot\frac{\Delta x}{2}-[-\left(B_zB_x\right)_A-\left(B_zB_x\right)_B+\left(B_zB_x\right)_C+\left(B_zB_x\right)_D\ ]\\
&\cdot\frac{z_1-z_6}{2}=0
\end{aligned}
\tag{5a}
$$

$$
\begin{aligned}
&\left[\left(B_x^2-B_z^2\right)_A+\left(B_x^2-B_z^2\right)_B-\left(B_x^2-B_z^2\right)_C-\left(B_x^2-B_z^2\right)_D\right]\\
&\cdot\frac{z_1-z_6}{4}+\left[\left(B_zB_x\right)_A-\left(B_zB_x\right)_B-\left(B_zB_x\right)_C+\left(B_zB_x\right)_D\right]\\
&\cdot\Delta x=0
\end{aligned}
\tag{5b}
$$

In reference to Fig. 1, it could be noted that point A respresents the cell-A located in the position (z_{i+1}, x_{j+1}), while the cell-B is located in (z_i, x_{j+1}), cell-C located on (z_i, x_j) and cell-D located in (z_{i+1}, x_j). This leads to Eq. (5) becoming an algebraic matrix system which can only be solved by an interation and relaxation technique.

To perform such a computation, the first requirement is to set up the trial functions which are denoted by SSZ and SSX. These two trial functions are obtained by taking the differences between the left and right-hand sides of the Eqs (5a,b) and they become,

$$
\left.
\begin{aligned}
SSZ &= -\left(B_z^2\right)_A+\left(B_x^2\right)_A-\left(B_zB_x\right)_A\cdot a+CTZ\\
SSX &= \left(-B_x^2\right)_A+\left(B_z^2\right)_A-\left(B_zB_x\right)_A\cdot b+CTR
\end{aligned}
\right\}
\tag{6}
$$

where

$$
\left.
\begin{aligned}
&a=(z_1-z_6)/\Delta x\ ,\ b=4\Delta x/(z_1-z_6),\\
&CTZ=A_2+A_3-A_4+a(-B_2+B_3+B_4),\\
&CTR=A_2-A_3-A_4-b(-B_2-B_3+B_4),\\
&\text{with}\\
&A_1=(B_z^2-B_x^2)_A,\quad A_2=(B_z^2-B_x^2)_B\\
&A_3=(B_z^2-B_x^2)_C,\quad A_4=(B_z^2-B_x^2)_D\\
&B_1=(B_xB_z)_A\quad,\quad B_2=(B_xB_z)_B\\
&B_3=(B_xB_z)_C\quad,\quad B_2=(B_xB_z)_D
\end{aligned}
\right\}
\tag{7}
$$

If the magnetic field components B_Z, B_X in cells B, C, and D are known, the relaxation coefficients could be determined from Eq.(6) via the variation principle, thus,

$$\left.\begin{aligned}
\frac{\partial(SSZ)}{\partial(B_z)_A} &= -2(B_z)_A - (B_x)_A \cdot a \\
\frac{\partial(SSZ)}{\partial(B_x)_A} &= 2(B_x)_A - (B_z)_A \cdot a \\
\frac{\partial(SSX)}{\partial(B_z)_A} &= 2(B_z)_A - (B_x)_A \cdot b \\
\frac{\partial(SSX)}{\partial(B_x)_A} &= -2(B_x)_A - (B_z)_A \cdot b
\end{aligned}\right\} \qquad (8)$$

where a and b are arbitrary constants as the measures of vertical and horizontal scale.

From Eq. (8), we noted that SSZ and SSX are dependent on B_{ZA} and B_{XA} which forms the basis to initiate the relaxation procedure for obtaining the true solution according to the governing equations (i.e. Eq.(5)) in. This assures ΔSSZ and ΔSSX as being approximately zero. To implement this relaxation procedure, we adjust the values of B_{ZA} and B_{XA} to $B_{ZA} + \Delta B_{ZA}$ and $B_{XA} + \Delta B_{XA}$ respectively, where ΔB_{ZA} and ΔB_{XA} are estimated according to the values of the first order of the Taylor's expansion. Then, we begin the iteration process to achieve $\Delta(SSZ)$ and $\Delta(SSX)$ as being zero or very small. During the iteration process, we observed significant numerical oscillations for the numerial solution of B_Z and B_X; sometimes this process even caused the solution to be divergent. In order to remedy this deficiency, we introduced a relaxation factor "w", during the iteration process, thus

$$\begin{aligned}
B_{ZA}^{(k+1)} &= (1-w)B_{ZA}^{(k)} + w(B_{ZA}^{(k)} + \Delta B_{ZA}), \\
B_{XA}^{(k+1)} &= (1-w)B_{XA}^{(k)} + w(B_{XA}^{(k)} + \Delta B_{XA})
\end{aligned} \qquad (9)$$

where k indicates the number of iteration steps, and ΔB_{ZA} and ΔB_{XA} are calculated at each iteration step as follows:

$$\left.\begin{aligned}
\Delta B_{ZA} &= \frac{1}{PP}\begin{vmatrix} -SSZ & \frac{\partial}{\partial B_{XA}}(SSZ) \\ -SSX & \frac{\partial}{\partial B_{XA}}(SSX) \end{vmatrix} \\
\Delta B_{XA} &= \frac{1}{PP}\begin{vmatrix} \frac{\partial}{\partial B_{ZA}}(SSZ) & -SSZ \\ \frac{\partial}{\partial B_{ZA}}(SSX) & -SSX \end{vmatrix}
\end{aligned}\right\} \qquad (10)$$

with $PP = 2(a+b)\cdot(B_{ZA}^2 + B_{XA}^2)$.

It should be noted that the above treatment is centered for a particular cell -A. To obtain a true solution in the whole domain, it is necessary to derive a set of similar expressions for cell-B, C and D. The iteration procedure c be summarized as follows:

1. Take an initial guess for B_Z and B_X in the whole computational domain. This initial guess usually could be the approximate solution from the analytica expression.
2. Applying Eq. (10) to all cells in the computation to compute $(SSZ)_{i,j}$ and $(SSX)_{i,j}$ until they reach a desired value such that

$$\left.\begin{aligned}
&\left\{\frac{|SSZ_{i,j}|}{(B_z^2 + B_x^2)_{i,j}^{1/2}}\right\}_{A,B,C,D} < \varepsilon \\
&\left\{\frac{|SSX_{i,j}|}{(B_z^2 + B_x^2)_{i,j}}\right\}_{A,B,C,D} < \varepsilon
\end{aligned}\right\} \qquad (11)$$

Ideally, ε should be zero, but, we have chosen ε to be 10^{-5} for the present calculation. When the iteration reached such a limit, we assume it to mean that the solution had converged to a true solution. The procedure was accomplished.

Quadratic Equations Method

If there should be a null point (or discontinuity) in the domain, the above relaxation method becomes invalid. Therefore, we have derived a quadratic equation for B_{ZA}^2 and B_{XA}^2 from Eq.(6) to assure that the relaxation could go on to reach a converging solution. We call this the "Quadratic Equation" method.

From Eq. (6), we set $SSZ = SSX = 0$. After some mathematical manipulation, we obtained a quadratic equation for magnetic field at a cell.

$$\left(B_A^2\right)^2 - \ell \cdot B_A^2 - C^2 = 0 \qquad (12)$$

where B_A^2 represents B_{ZA}^2 and B_{XA}^2, respectively, and

$$\begin{aligned}
C &= (CTZ + CTR)/(a+b), \\
\ell &= (b\cdot CTZ - a\cdot CTR)/(a+b).
\end{aligned}$$

The solution of Eq. (12) gives

$$\left.\begin{aligned}
B_{ZA}^2 &= \frac{1}{2}\left[\ell + \sqrt{4C^2 + \ell^2}\right] \\
B_{XA}^2 &= \frac{1}{2}\left[-\ell + \sqrt{4C^2 + \ell^2}\right]
\end{aligned}\right\} \qquad (13)$$

It can be shown that solutions of Eq. (12) are unique and that no singular points exist within the domain. With these solutions, we will return to the usual relaxation procedures, namely, we make adjustments for B_{ZA} and B_{XA} according to

$$\left.\begin{aligned} \Delta B_{ZA} &= (B_{ZA})_{NEW} - (B_{ZA})_{OLD} \\ \Delta B_{XA} &= (B_{XA})_{NEW} - (B_{XA})_{OLD} \end{aligned}\right\} (14)$$

where the $(B_{ZA})_{NEW}$ and $(B_{XA})_{NEW}$ are obtained from Eq. (13). Then, using Eq. (9), we get new approximate solutions for the next iteration step. Of course, these procedures will be carried out for cells B, C, and D during a sweep of the whole domain.

III. Numerical Examples

To illustrate the newly developed methods, we have selected an example for the dynamical simulation of the compression of two bipolar magnetic field with a x-type neutral point. The first step in the initialization of this type of simulation is to obtain the initial state which is the configuration of a bipolar magnetic field with x-type neutral points.

To construct such a solution, we need to use the Quadratic Equations method as described in the previous section. To implement this solution procedure, we need to prescribe an initial state and its analytical representation as:

$$\vec{B}_o = \vec{B}_{01} + \vec{B}_{02}$$

with

$$\vec{B}_{0i} = \frac{-\hat{z}\left[2a_1(Z+Z_0)(X-X_{i0})\right] + \hat{x}\left[a\left\{(Z+Z_0)^2 - (X-X_{i0})^2\right\}\right]}{\left[(Z+Z_0)^2 + (X-X_{i0})^2\right]} \qquad (15)$$

with i being 1 and 2 respectively. Where $\vec{B}_{01}$ and $\vec{B}_{02}$ are the usual two-dimensional potential field components. By chosing the computation domain as $0 \le Z \le 2000 km$ and $-1400 km \le X \le 1400 km$, we set Z_0 = 280 *km*, X_{10} = -700 *km*, and X_{20} = 700 *km*. With these prescribed conditions, we will begin our iteration according to the method defined in Section II. In the present calculation, the grid size is chosen in such a way that there are forty uniform grid points in the x-direction (horizontal direction) and 30 exponentially variable grid points in the z-direction (vertical direction). The steady state solution obtained from Eqs. (9), (12) and (14) is given in Figure 2. This result has an accuracy to the order of 10^{-3} after 1000 iterations and then saturates at 4743 iterations which provided an accuracy of ~ 10^{-4}. The accuracy is defined by

$$ACZ = MAX \left| \frac{SSZ}{\sqrt{B_Z^2 + B_X^2}} \right|_{i,j \text{ at } A,B,C,D}$$

$$ACX = MAX \left| \frac{SSX}{\sqrt{B_Z^2 + B_X^2}} \right|_{i,j \text{ at } A,B,C,D}$$

For further testing the numerical code, we performed a time-dependent test, that is by giving a horizontal velocity $(u) = \pm 1\ km/s$ at $j \le 20$ and $i = 0$ where indices j and i represent the horizontal and vertical grid points. These results are shown in Figure 3 for the magnetic field configuration at 500s and 1000s, respectively. The initial plasma parameters (p_o, T_o, ρ_o) for this calculation are taken from the Harvard Smithsonian standard atmosphere model.[2]

IV. Concluding Remarks

In this paper we have demonstrated that the improvement based on the Brackbill and Pracht method could be utilized to construct a highly complex magnetic field configuration for magnetostatic equilibrium state with a discontinuity in the computational domain as shown in Figure 2. It also shows that the method could be used to study the dynamical evolutionary state as shown in Figure 3. Finally, a solution was presented for the structure of the solar atmosphere which includes the thin transition region layer. The plasma parameters within this thin layer possessed several order of magnitude variations. The physics of this study will be discussed in a separate paper by Wu *et al.*[3] .

Acknowledgement

Work performed by STW was supported by a NASA Headquarters grant NAGW-9 and NOAA Contract (50RANR700104).

References

1. Brackbill, J. U. and Pracht, W. E. "An Implicit, Almost-Lagrangian Algorithm for Magnetohydrodynamics" *J. Comp. Phys.*, 13, 455, 1973.
2. Allen, C. W., "Astrophysical Quantities", The Academic Press, New York, 1973.
3. Wu, S. T., M. T. Song, C. C. Cheng and M. Dryer, "Coronal Heating Heating Due to the Emerging of Magnetic Flux" Proceedings of SOHO Workshop, Elba, Italy, Sept. 9 - Oct. 10, 1993.

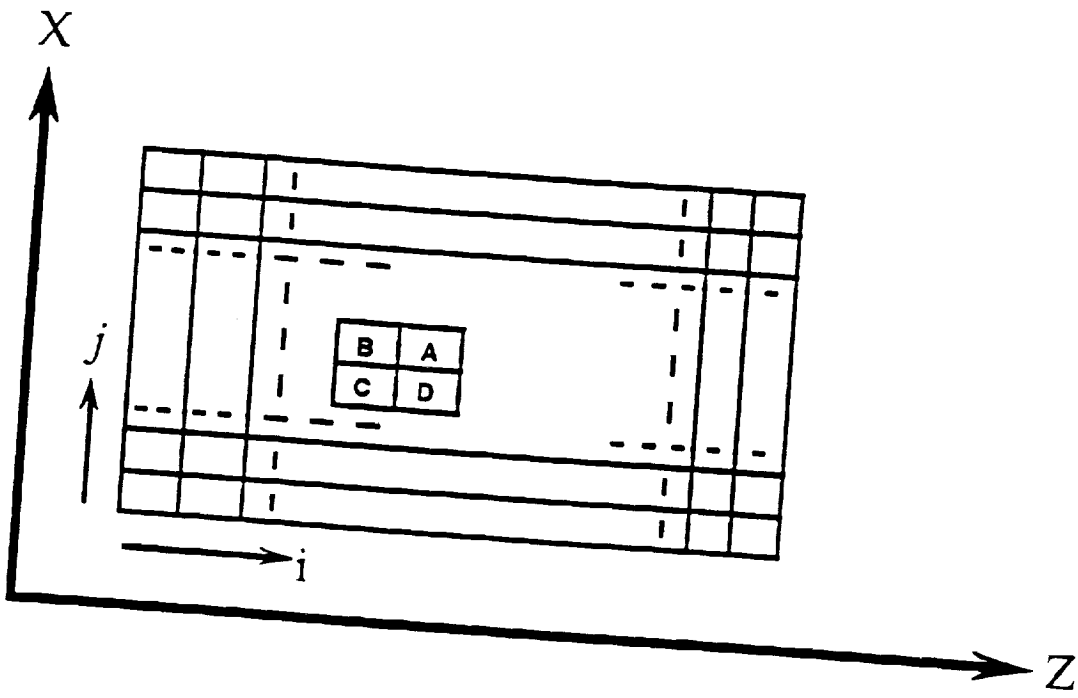

(a)

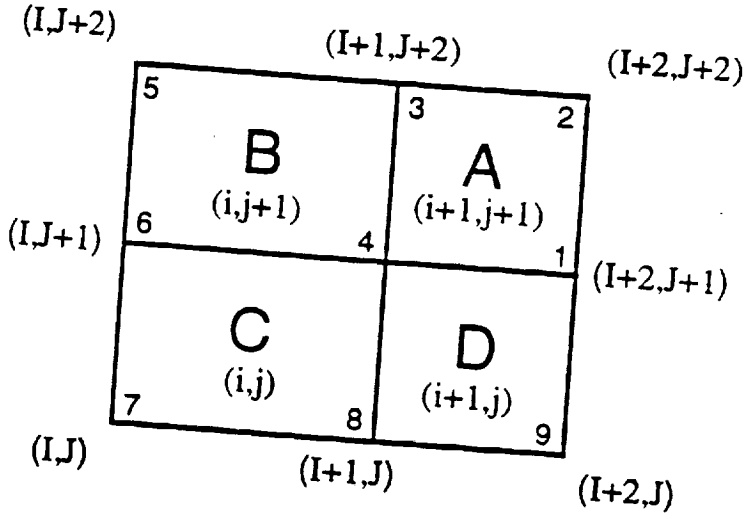

(b)

Fig. 1. Description of the computational network; (a) coordinate system, where z and x represent the vertical and horizontal coordinates respectively and (b) the corrrespondence between the Lagrangian cell and local grid points.

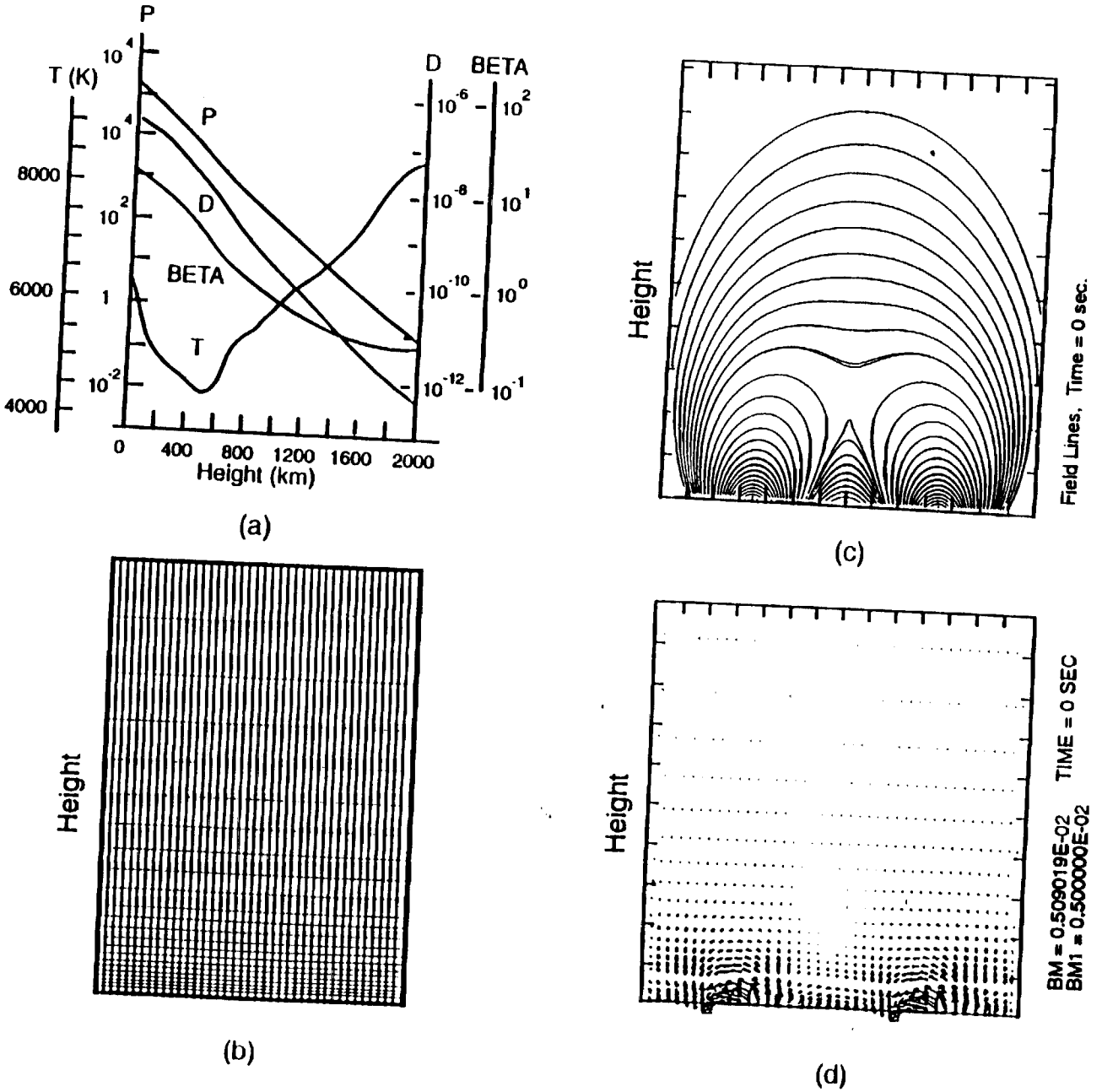

Fig. 2. Steady State solutions and grid point arrangements; (a) the initial distributions for temperature (° K), density (gm/cm^3), pressure (dy/cm^2), and plasma beta as a function of height (km); (b) the grid point distribution for the computational domain; (c) the topology of the magnetic field lines; and (d) the vectoral representation of magnetic field configuration for (c).

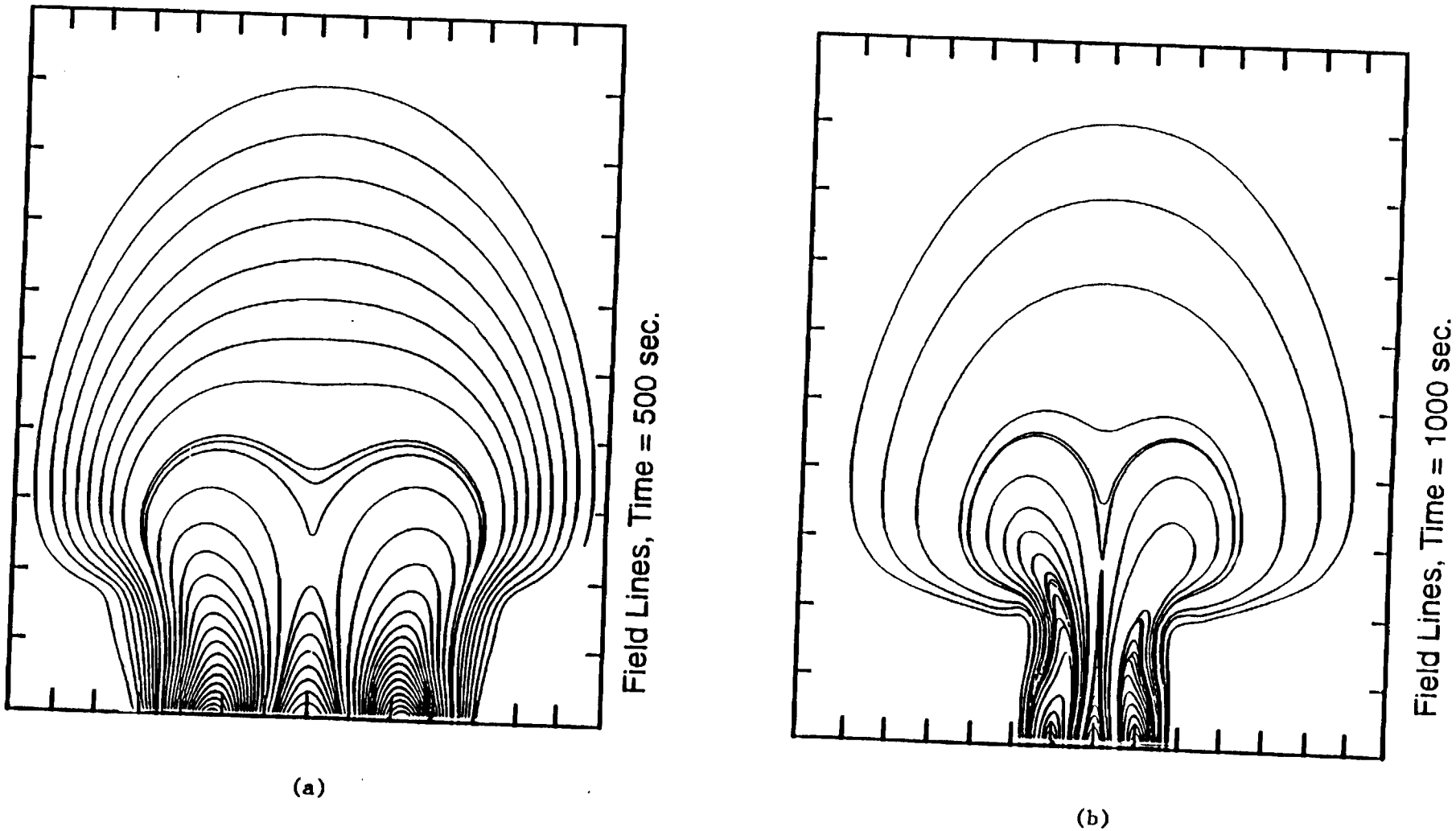

Fig. 3. The dynamical evolution of the magnetic field configuration due to the collision of two dipole fields (i.e. sunspots), (a) at 500 s and (b) at 1000 s.

NLS

On the Time-dependent Numerical Boundary Conditions of Magnetohydrodynamic Flows

M. T. SUN

Department of Physics
National Tsing-Hwa University
Hsinchu, Taiwan

S. T. WU

Center for Space Plasma and Aeronomic Research and
Department of Mechanical and Aerospace Engineering
The University of Alabama in Huntsville
Huntsville, Alabama 35899

MURRAY DRYER

Space Environment Laboratory
National Oceanic and Atmospheric Administration
Boulder, Colorado 80303

The time-dependent numerical boundary conditions for time-dependent magnetodydrodynamic fluid flow simulations have been studied. In this paper, the formulation of the time-dependent numerical boundary conditions are described in a systematic way such that they can be adapted to different applications. In particular, the algorithm presented here could be used to solve both parabolic and hyperbolic systems of partial differential equations. A numerical example for an astrophysical application in the context of photospheric shear induced dynamics was chosen to validate this new formulation.

J. Comptational Physics, 1993 (submitted)

1. INTRODUCTION

Applications of numerical models in the field of astrophysics seek solutions of hyperbolic equations inside a finite domain with boundaries on which no physical boundary conditions can be specified. This approach is called the free boundary value problem. The method of characteristics is often used to specify numerically such boundary conditions in order to keep false physical properties from propagating into the domain as investigated by Wu and Wang [1].

Nakagawa *et al.* [2] developed the method of projected characteristics both to specify the numerical boundary conditions and to solve for the solutions in the computational domain. Hu and Wu [3] used the method for the numerical boundary conditions and developed the *FICE* (Full-Implicit-Continuous-Eulerian) algorithm for the solutions inside the domain. The purpose of the present algorithm is to solve both parabolic and hyperbolic systems of equations. The algorithm used in the test run of this paper is a refined version of the *FICE* algorithm which has been renamed as the *NICE* (Nimble Implicit Continuous-Eulerian) algorithm [4]. However, the method of projected characteristics requires complex formulation which may not be easily modified to suit different applications.

Thompson [5] extended the concept of non-reflecting boundary conditions to the multi-dimensional case in non-rectangular coordinate systems. He later developed a general boundary condition formalism [6] for all type of boundary conditions for first-order hyperbolic systems. However, these boundary conditions are limited to fluid dynamics. Vanajakshi *et al* [7] then applied Thompson's method to solving boundary value problems in magnetohydrodynamics (MHD) particularly for

isothermal plasma. Consequently, for non-isothermal plasma, the semi-analytic approach in solving numerically the eigenvectors of a modified version of the coefficient matrices is no longer valid.

In this paper, a new analytic approach is presented for non-isothermal plasma. In addition, when there are two eigenvectors that are parallel at a boundary, a special treatment is devised. The theoretical approach for this study is the same as that of Thompson's [6], namely, to systematize the formalism. In order to demonstrate the utility and accuracy of the present algorithm, numerical simulation for the dynamical evolution of a force-free magnetic field is presented. These simulation results are compared with a set of quasi-static analytical solutions given by Martens *et al* [8] for the accuracy test.

2. Governing Equations

The normalized MHD equations for a perfectly conducting fluid can be expressed in the following vector form:

$$\frac{\partial \rho}{\partial t} + \nabla \cdot (\rho \mathbf{v}) = 0, \tag{1}$$

$$\rho \frac{\partial \mathbf{v}}{\partial t} + \rho(\mathbf{v} \cdot \nabla)\mathbf{v} = -\frac{1}{\gamma M_o^2}\nabla p - \frac{2}{\beta_o \gamma M_o^2}\mathbf{B} \times (\nabla \times \mathbf{B}) - \nabla \Phi, \tag{2}$$

$$\frac{\partial p}{\partial t} + (\mathbf{v} \cdot \nabla)p = -a^2 \rho \nabla \cdot \mathbf{v} + (\gamma - 1)\triangle Q, \tag{3}$$

$$\frac{\partial \mathbf{B}}{\partial t} = \nabla \times (\mathbf{v} \times \mathbf{B}), \tag{4}$$

where the equation of state $p = \rho T$ is used in the energy equation to replace ρT with pressure p. Φ is the stress tensor or the gravitational potential or both. $\triangle Q$ is the net rate of irreversible energy (heat) gain or loss per unit volume and a is

the speed of sound. The two non-dimensional parameters, Mach number M_o and plasma beta β_o, are expressed, respectively, as following:

$$M_o = \frac{U}{a_o} = \frac{U}{\sqrt{\gamma R T_o}}, \quad \beta_o = \frac{p_o}{B_o^2/8\pi},$$

where the constants subscripted with $()_o$ are scaling factors for normalization purpose. Other scaling factors are $\rho_o = p_o/RT_o$, x_o, v_o, and $t_o = x_o/v_o$.

3. Method of Characteristics

For the convenience of using the method of characteristics on the boundary, the MHD equations need to be expressed as

$$\frac{\partial \mathbf{W}}{\partial t} + \mathbf{A}^{(1)}\frac{\partial \mathbf{W}}{\partial x_1} + \mathbf{A}^{(2)}\frac{\partial \mathbf{W}}{\partial x_2} + \mathbf{A}^{(3)}\frac{\partial \mathbf{W}}{\partial x_3} = \mathbf{E}. \tag{5}$$

The vector of primitive solution variables is

$$\mathbf{W}^{\mathrm{T}} = (\rho,\ u_1,\ u_2,\ u_3,\ p,\ B_1,\ B_2,\ B_3). \tag{6}$$

The 8×8 matrices are

$$\mathbf{A}^{(1)} = \frac{1}{h_1}\begin{pmatrix} u_1 & \rho & 0 & 0 & 0 & 0 & 0 & 0 \\ 0 & u_1 & 0 & 0 & \frac{F_P}{\rho} & 0 & \frac{F_B}{\rho}B_2 & \frac{F_B}{\rho}B_3 \\ 0 & 0 & u_1 & 0 & 0 & 0 & -\frac{F_B}{\rho}B_1 & 0 \\ 0 & 0 & 0 & u_1 & 0 & 0 & 0 & -\frac{F_B}{\rho}B_1 \\ 0 & a^2\rho & 0 & 0 & u_1 & 0 & 0 & 0 \\ 0 & 0 & 0 & 0 & 0 & u_1 & 0 & 0 \\ 0 & B_2 & -B_1 & 0 & 0 & 0 & u_1 & 0 \\ 0 & B_3 & 0 & -B_1 & 0 & 0 & 0 & u_1 \end{pmatrix}, \tag{7}$$

$$\mathbf{A}^{(2)} = \frac{1}{h_2}\begin{pmatrix} u_2 & 0 & \rho & 0 & 0 & 0 & 0 & 0 \\ 0 & u_2 & 0 & 0 & 0 & -\frac{F_B}{\rho}B_2 & 0 & 0 \\ 0 & 0 & u_2 & 0 & \frac{F_P}{\rho} & \frac{F_B}{\rho}B_1 & 0 & \frac{F_B}{\rho}B_3 \\ 0 & 0 & 0 & u_2 & 0 & 0 & 0 & -\frac{F_B}{\rho}B_2 \\ 0 & 0 & a^2\rho & 0 & u_2 & 0 & 0 & 0 \\ 0 & -B_2 & B_1 & 0 & 0 & u_2 & 0 & 0 \\ 0 & 0 & 0 & 0 & 0 & 0 & u_2 & 0 \\ 0 & 0 & B_3 & -B_2 & 0 & 0 & 0 & u_2 \end{pmatrix}, \tag{8}$$

$$\mathbf{A}^{(3)} = \frac{1}{h_3}\begin{pmatrix} u_3 & 0 & 0 & \rho & 0 & 0 & 0 & 0 \\ 0 & u_3 & 0 & 0 & 0 & -\frac{F_B}{\rho}B_3 & 0 & 0 \\ 0 & 0 & u_3 & 0 & 0 & 0 & -\frac{F_B}{\rho}B_3 & 0 \\ 0 & 0 & 0 & u_3 & \frac{F_P}{\rho} & \frac{F_B}{\rho}B_1 & \frac{F_B}{\rho}B_2 & 0 \\ 0 & 0 & 0 & a^2\rho & u_3 & 0 & 0 & 0 \\ 0 & -B_3 & 0 & B_1 & 0 & u_3 & 0 & 0 \\ 0 & 0 & -B_3 & B_2 & 0 & 0 & u_3 & 0 \\ 0 & 0 & 0 & 0 & 0 & 0 & 0 & u_3 \end{pmatrix}. \tag{9}$$

where $a^2 = \gamma T$, $F_P = 1/(\gamma M_\infty^2)$ and $F_B = 2F_P/\beta_\infty$. The factor h_i is the scale length of the coordinate in the ith direction for the orthogonally curvilinear coordinate system. The vector of inhomogeneous terms is

$$\mathbf{E} = \begin{pmatrix} -\rho(\sum_{i=1,3}\sum_{j=1,3} u_i f_{ji} - \sum_{i=1,3} u_i f_{ii}) \\ \sum_{i=1,3}(u_i^2 - c_0 B_i^2) f_{i1} - \sum_{j=1,3}(u_1 u_j - c_0 B_1 B_j) f_{1j} - (\nabla\Phi)_1 \\ \sum_{i=1,3}(u_i^2 - c_0 B_i^2) f_{i2} - \sum_{j=1,3}(u_2 u_j - c_0 B_2 B_j) f_{2j} - (\nabla\Phi)_2 \\ \sum_{i=1,3}(u_i^2 - c_0 B_i^2) f_{i3} - \sum_{j=1,3}(u_3 u_j - c_0 B_3 B_j) f_{3j} - (\nabla\Phi)_3 \\ (\gamma-1)\triangle Q - a^2\rho(\sum_{i=1,3}\sum_{j=1,3} u_i f_{ji} - \sum_{i=1,3} u_i f_{ii}) \\ u_1(B_1 f_{31} + B_2 f_{32} + B_3 f_{23}) + B_1(u_1 f_{21} + u_2 f_{12} + u_3 f_{13}) \\ u_2(B_1 f_{31} + B_2 f_{12} + B_3 f_{13}) + B_2(u_1 f_{21} + u_2 f_{32} + u_3 f_{23}) \\ u_3(B_1 f_{21} + B_2 f_{12} + B_3 f_{23}) + B_3(u_1 f_{31} + u_2 f_{32} + u_3 f_{13}) \end{pmatrix} \tag{10}$$

where $c_0 = 2/(\gamma\rho M_\infty^2 \beta_\infty)$ and

$$f_{ij} = \frac{1}{h_i} h_j \frac{\partial h_i}{\partial x_j}.$$

In the j direction, where $j = 1$, 2, and 3, the eigenvalues of $\mathbf{A}^{(j)}$ are;

$$\begin{aligned} &\lambda_1^j = u_j, \quad \lambda_2^j = u_j, \quad \lambda_3^j = u_j + U_A^j, \quad \lambda_4^j = u_j - U_A^j, \\ &\lambda_5^j = u_j + U_f^j, \quad \lambda_6^j = u_j - U_f^j, \quad \lambda_7^j = u_j + U_s^j, \quad \lambda_8^j = u_j - U_s^j, \end{aligned} \tag{11}$$

where

$$\begin{aligned} U_A^{(j)} &= |b_j| \\ U_f^{(j)^2} &= \frac{1}{2}\left(a^2 + b^2 + \sqrt{(a^2+b^2)^2 - 4a^2 b_j^2}\right), \\ U_s^{(j)^2} &= \frac{1}{2}\left(a^2 + b^2 - \sqrt{(a^2+b^2)^2 - 4a^2 b_j^2}\right). \end{aligned} \tag{12}$$

The definition of b is

$$b_j \equiv \sqrt{\frac{F_B}{\rho}} B_j, \qquad j = 1,\ 2,\ \text{and } 3, \tag{13}$$

and

$$b^2 = \sum_{j=1}^{3} b_j b_j.$$

For simplicity, the following analysis is restrained only in x_1 direction. Details of the formulations in the other two directions are shown in the Appendix.

The inverse matrix $\mathbf{S}_1^{-1}$, whose rows are the left eigenvectors l T_i of $\mathbf{A}$ 1, which gives

$$\mathbf{S}_1^{-1} = \begin{pmatrix} F_P a^2 & 0 & 0 & 0 & -F_P & 0 & 0 & 0 \\ 0 & 0 & 0 & 0 & 0 & c_b & 0 & 0 \\ 0 & 0 & -b_{13} & b_{12} & 0 & 0 & c_3 U_A^1 & -c_2 U_A^1 \\ 0 & 0 & b_{13} & -b_{12} & 0 & 0 & c_3 U_A^1 & -c_2 U_A^1 \\ 0 & U_f^1 u_{ff}^1 & -b_{12} U_f^1 & -b_{13} U_f^1 & F_P \frac{u_{ff}^1}{\rho} & 0 & c_2 u_f^1 & c_3 u_f^1 \\ 0 & -U_f^1 u_{ff}^1 & b_{12} U_f^1 & b_{13} U_f^1 & F_P \frac{u_{ff}^1}{\rho} & 0 & c_2 u_f^1 & c_3 u_f^1 \\ 0 & U_s^1 u_{ss}^1 & b_{12} U_s^1 & b_{13} U_s^1 & F_P \frac{u_{ss}^1}{\rho} & 0 & -c_2 u_s^1 & -c_3 u_s^1 \\ 0 & -U_s^1 u_{ss}^1 & -b_{12} U_s^1 & -b_{13} U_s^1 & F_P \frac{u_{ss}^1}{\rho} & 0 & -c_2 u_s^1 & -c_3 u_s^1 \end{pmatrix}, \quad (14)$$

where $u_f^1 = (U_f^1)^2$, $u_s^1 = (U_s^1)^2$, $u_{ff}^1 = u_f^1 - b_1^2$, $u_{ss}^1 = b_1^2 - u_s^1$, $c_b = \sqrt{F_B/\rho}$, $c_i = c_b b_i$, and $b_{ij} = b_i b_j$. $\mathcal{L}^1$ can be calculated according to the definition

$$\mathcal{L}^1 \equiv \Lambda_1 \mathbf{S}_1^{-1} \frac{\partial \mathbf{W}}{\partial x_1}, \quad (15)$$

and results in

$$\mathcal{L}_i^1 = \lambda_i^1 \sum_{k=1,8} \xi_{ik}^1 \frac{\partial W_k}{\partial x_1}, \quad (16)$$

where ξ_{ik}^1 is the element of $\mathbf{S}_1$ at row i and column k, and W_k is the kth element of $\mathbf{W}$. Then, appropriate boundary conditions are applied to specify the value of $\mathcal{L}_i^1$ for the outwardly pointing eigenvector λ_i^1 with respect to the solution volume.

Now $d^1 = \mathbf{S}_1 \mathcal{L}^1$ can be solved with known $\mathbf{S}_1^{-1}$ and $\mathcal{L}^1$ through the set of equations

$$\mathbf{S}_1^{-1} d^1 = \mathcal{L}^1. \quad (17)$$

Note that the eigenvectors (left or right) of $\mathbf{A}^j$ will always be linearly independent, but they are not orthogonal, and it is possible that any two of them may be nearly parallel. Consequently the matrix $\mathbf{S}^{-1}$ may be ill-conditioned, because it is close to the vicinity of the singularity for which the numerical solution of Eq.(17) is poorly determined. In our case, this means $b_1 \rightarrow 0$. Therefore, Eq.(17) has to be solved analytically and the elements of the solution vector $\boldsymbol{d}^1$, in analytic form, are

$$d_2^1 = \frac{\mathcal{M}_2/U_f^1 + \mathcal{M}_3/U_s^1}{2(u_f^1 - u_s^1)}, \tag{18}$$

$$d_3^1 = \frac{-U_f^1 b_3 \mathcal{M}_1 - b_2(\mathcal{M}_2 - 2\xi_{52}^1 d_2^1)}{2U_f b_1(b_2^2 + b_3^2)}, \tag{19}$$

$$d_4^1 = \frac{U_f^1 b_2 \mathcal{M}_< e < e < e < e1 - b_3(\mathcal{M}_2 - 2\xi_{52}^1 d_2^1)}{2U_f b_1(b_2^2 + b_3^2)}, \tag{20}$$

$$d_5^1 = \frac{\mathcal{N}_2/u_f^1 + \mathcal{N}_3/u_s^1}{2(\xi_{55}^1/u_f^1 + \xi_{75}^1/u_s^1)}, \tag{21}$$

$$d_6^1 = \frac{\mathcal{L}_2^1}{\xi_{26}^1}, \tag{22}$$

$$d_7^1 = \sqrt{\rho}\frac{\mathcal{N}_1 b_3 u_f^1 + b_2 U_A^1(\mathcal{N}_2 - 2\xi_{55}^1 d_5^1)}{2U_A^1 u_f^1(b_2^2 + b_3^2)}, \tag{23}$$

$$d_8^1 = \sqrt{\rho}\frac{-\mathcal{N}_1 b_2 u_f^1 + b_3 U_A^1(\mathcal{N}_2 - 2\xi_{55}^1 d_5^1)}{2U_A^1 u_f^1(b_2^2 + b_3^2)}, \tag{24}$$

$$d_1^1 = \frac{\mathcal{L}_1^1 - \xi_{15}^1 d_5^1}{\xi_{11}^1}, \tag{25}$$

where

$$\mathcal{M}_i = \sqrt{F_B}(\mathcal{L}_{2i+1}^1 - \mathcal{L}_{2i+2}^1), \tag{26}$$

$$\mathcal{N}_i = \mathcal{L}_{2i+1}^1 + \mathcal{L}_{2i+2}^1. \tag{27}$$

Note that d_i^1 are displayed in the solving order in which some of the solved elements may be used for solving the remaining unsolved elements.

In the case of $b_1 = 0_i$, then, this leads to any two eigenvectors being parallel and the analytical solution is not defined. Subconsequently $U_A^1 = 0$ and $U_s^1 = 0$. Physically, this means that the component of the magnetic induction normal to the boundary vanishes or the magnetic lines-of-force are parallel to the boundary. In this situation, a set of new eigenvectors needs to be sought. The determination of these new eigenvectors is described as follows:

Observing closely the original eigenvectors in the rows of $\mathbf{S}_1^{-1}$ in Eq. (14), one can see that l_1^T, l_2^T, l_5^T, and l_6^T still remain linearly independent to each other, i.e., they are still valid eigenvectors, while l_3^T, l_4^T, l_7^T, and l_8^T vanish. To find other valid eigenvectors, the original forms of the vanished eigenvectors are used in cooperation with the linearly combined eigenvectors, and then the limit $b_1 \to 0$ is taken. If l_3^T and l_4^T are summed up and the resulting vector is scaled by $2U_A^1$, from which a valid eigenvector

$$l_3^T = (0, 0, 0, 0, 0, 0, c_b b_3, -c_b b_2) \tag{28}$$

can be derived. Scaling the summation of l_7^T and l_8^T with $2u_s^1$ and taking the limit $b_1 \to 0$, one gets another eigenvector

$$l_7^T = (0, 0, 0, 0, F_P b^2/a^2\rho, 0, -c_b b_2, -c_b b_3). \tag{29}$$

Since the third and fourth components of all the eigenvectors available so far are zero, the most natural selections of the remaining two eigenvectors linearly independent to the other eigenvectors are

$$l_4^T = (0, 0, 1, 0, 0, 0, 0, 0), \text{ and } l_8^T = (0, 0, 0, 1, 0, 0, 0, 0). \tag{30}$$

The new $\mathbf{S}_1^{-1}$ is now

$$\mathbf{S}_1^{-1} = \begin{pmatrix} F_P a^2 & 0 & 0 & 0 & -F_P & 0 & 0 & 0 \\ 0 & 0 & 0 & 0 & 0 & c_b & 0 & 0 \\ 0 & 0 & 0 & 0 & 0 & 0 & c_b b_3 & c_b b_2 \\ 0 & 0 & 1 & 0 & 0 & 0 & 0 & 0 \\ 0 & U_f^1 & 0 & 0 & F_P/\rho & c_b b_2 & c_b b_3 & 0 \\ 0 & -U_f^1 & 0 & 0 & F_P/\rho & c_b b_2 & c_b b_3 & 0 \\ 0 & 0 & 0 & 0 & F_P b^2/a^2\rho & -c_b b_2 & -c_b b_3 & 0 \\ 0 & 0 & 0 & 1 & 0 & 0 & 0 & 0 \end{pmatrix} \tag{31}$$

The solution of Eq.(17) becomes

$$d_2^1 = \frac{\mathcal{L}_5^1 - \mathcal{L}_6^1}{2\xi_{52}^1}, \tag{32}$$

$$d_3^1 = \frac{\mathcal{L}_4^1}{\xi_{43}^1}, \tag{33}$$

$$d_4^1 = \frac{\mathcal{L}_8^1}{\xi_{84}^1}, \tag{34}$$

$$d_5^1 = \rho \frac{\mathcal{L}_5^1 + \mathcal{L}_6^1 + 2\mathcal{L}_7^1}{2F_P(1 + b^2/a^2)}, \tag{35}$$

$$d_6^1 = \frac{\mathcal{L}_2^1}{\xi_{26}^1}, \tag{36}$$

$$d_7^1 = \sqrt{\rho} \frac{b_3 \mathcal{L}_3^1 + b_2(\mathcal{L}_5^1 + \mathcal{L}_6^1 - 2\xi_{55}^1 d_5^1)}{2b^2}, \tag{37}$$

$$d_8^1 = \sqrt{\rho} \frac{-b_2 \mathcal{L}_3^1 + b_3(\mathcal{L}_5^1 + \mathcal{L}_6^1 - 2\xi_{55}^1 d_5^1)}{2b^2}, \tag{38}$$

$$d_1^1 = \frac{\mathcal{L}_1^1 - \xi_{15}^1 d_5^1}{\xi_{11}^1}. \tag{39}$$

After the above procedures are carried out in all three directions, the solutions $\boldsymbol{d}^1$, $\boldsymbol{d}^2$, and $\boldsymbol{d}^3$ are known. The time derivative of the primitive solution variables $\partial \mathbf{W}/\partial t$ can be calculated as

$$\frac{\partial \mathbf{W}}{\partial t} = -\boldsymbol{d}^1 - \boldsymbol{d}^2 - \boldsymbol{d}^3 + \mathbf{E}. \tag{40}$$

The time derivative is integrated through time with

$$\mathbf{W}(t + \triangle t) = \mathbf{W}(t) + \triangle t \frac{\partial \mathbf{W}}{\partial t} \tag{41}$$

to give the boundary values for a new time step.

4. Boundary Conditions of MHD Equations

There are basically two different types of time-dependent boundary conditions that generally need to be treated with the characteristics method in the simulation of space plasma phenomena.

The first type of boundary condition is the *non-reflecting boundary condition* which is commonly used when there is no physical boundary involved. Encountering this type of boundary in the problems of astrophysics is inevitable if the simulation domain is in a finite volume.

The second type of boundary condition is the *coupled boundary condition* which deals with boundaries at which only a portion of the physical properties is known. It is worth noticing that at any time t the boundary conditions contribute only to the determination of $\partial \mathbf{W}/\partial t$ at the boundary, and never define $\mathbf{W}$ itself. For example, a boundary treatment which explicitly sets the normal velocity of a fluid to zero at a wall boundary is not appropriate in the hyperbolic system. Instead one would set the normal velocity to zero in the initial data and then specify boundary conditions which would force the time derivative of the normal velocity to be zero at all times. One advantage of this approach is that it decouples the boundary treatment from the time integration of the differential equations, so that the integration may be performed without reference to any special time behavior at the boundaries.

4.1 *Non-reflecting Boundary Conditions*

At the boundary $x_j = x_{j_{max}}$, wave modes for which $\lambda_i^j > 0$ are propagating out of the computational and physical domain, and $\mathcal{L}_i^j$ may be computed from its definition in Eq. (15) using one-sided finite difference approximation to $\partial \mathbf{W}/\partial x_j$, using only interior data. (Similarly, at $x_j = x_{j_{min}}$ we may compute $\mathcal{L}_i^j$ from its definition in Eq. (15) when $\lambda_i^j < 0$, using one-sided differences, as this case also corresponds to an outgoing wave.)

However, if $\lambda_i^j \leq 0$, then those waves are propagating into the computational and physical domain and generally may not be computed from interior data. In this case we make use of the non-reflecting boundary condition of Reference [4] and set $\mathcal{L}_i^j = 0$ (and set $\mathcal{L}_i^j = 0$ at the inner boundary if $\lambda_i^j \geq 0$), which may be done conveniently by replacing λ_i^j by 0 or letting $\partial \mathbf{W}/\partial x_j$ be 0 in the definition of $\mathcal{L}_i^j$.

In the practical applications, two spatial derivatives denoted by $\mathbf{W}_j^1$ and $\mathbf{W}_j^2$ in each of the three directions (j = 1, 2, and 3) are calculated at each boundary point. Both spatial derivatives are calculated using one-sided differencing: $\mathbf{W}_j^1$, backward differencing; $\mathbf{W}_j^2$, forward differencing. $\mathbf{W}_j^1$ is set equal to zero at the boundary points $x_j = x_{j_{min}}$, evaluated with two point differencing at the points $x_j = x_{j_{min}} + \Delta x_j$, and evaluated with three point differencing elsewhere. Likewise, $\mathbf{W}_j^2$ is set equal to zero at the boundary points $x_j = x_{j_{max}}$, evaluated with two point differencing at the points $x_j = x_{j_{max}} - \Delta x_j$, and evaluated with three point differencing elsewhere. The differencing scheme for these two spatial derivatives at different positions is summarized in Table 1.

Then in Eq. (15), $\mathbf{W}_j^1$ is used in place of $\partial \mathbf{W}/\partial x_j$ when $\lambda_i^j \geq 0$, and $\mathbf{W}_j^2$ is

Table 1: The differencing scheme for $\mathbf{W}_j^1$ and $\mathbf{W}_j^2$.

Position	Value or Differencing Scheme	
x_j	$\mathbf{W}_j^1$ (backward)	$\mathbf{W}_j^2$ (forward)
$x_j = x_j^{\min}$	0	three point
$x_j = x_j^{\min} + \triangle x_j$	two point	three point
$x_j^{\min} + \triangle x_j < x_j < x_j^{\max} - \triangle x_j$	three point	three point
$x_j = x_j^{\max} - \triangle x_j$	three point	two point
$x_j = x_j^{\max}$	three point	0

used when $\lambda_i^j < 0$. This approach has one advantage over replacing λ_i^j with 0: because the stability and accuracy of the upwind scheme in hyperbolic systems can be obtained.

4.2 *Coupled Boundary Conditions*

It is very difficult to give a general description of the boundary treatment for the coupled boundary conditions. Therefore, we have selected an example to illustrate the procedures of the treatment of the coupling boundary condition. In this numerical experiment, the normal direction of the boundary is in the x_3 direction which is z in the Cartesian coordinates. The experiment is done with symmetric conditions in the x_2 direction such that $\partial/\partial x_2 = 0$. The boundary conditions at $z = 0$ are $u_1 = u_3 = 0$, $u_2 = u_2(x_1, t)$, $\rho = \rho_o$, and $B_3 = B_3(x_1)$. Since the normal velocity $u_3 = 0$, the number of outgoing wave modes is three, which is the number of variables on the boundary needed to be determined. These variables are p, B_1, and B_2 for this particular example.

Eq. (40) with $\boldsymbol{d}^2 = 0$ becomes

$$\frac{\partial \mathbf{W}}{\partial t} = -\boldsymbol{d}^1 - \boldsymbol{d}^3 + \mathbf{E}. \tag{42}$$

The known $\partial W_i/\partial t$ denoted by $(W_i)_t = 0$ are $(\rho)_t = 0$, $(u_1)_t = 0$, $(u_2)_t$, $(u_3)_t = 0$, and $(B_3)_t = 0$, whose indices are $i = 1$, 2, 3, 4, and 8 respectively. In the equation, d^1 can be evaluated using Eq. (15) and the vector of inhomogeneous terms $\mathbf{E}$ can also be evaluated assuming that the dissipation terms are either known or equal to zero at the boundary. Now $\mathcal{L}_i^3$, corresponding to the in-coming wave mode for which $\lambda_i^3 \geq 0$, must be evaluated such that the time derivatives can be treated as the known values.

We began with the solutions d^3 of Eq. (42), such as

$$d_4^3 = \frac{\mathcal{M}_2/U_f^3 + \mathcal{M}_3/U_s^3}{2(u_f^3 - u_s^3)}, \tag{43}$$

$$d_2^3 = \frac{-U_f^3 b_2 \mathcal{M}_1 - b_1(\mathcal{M}_2 - 2\xi_{54}^3 d_4^3)}{2U_f b_3(b_1^2 + b_2^2)}, \tag{44}$$

$$d_3^3 = \frac{U_f^3 b_1 \mathcal{M}_1 - b_2(\mathcal{M}_2 - 2\xi_{54}^3 d_4^3)}{2U_f b_3(b_1^2 + b_2^2)}, \tag{45}$$

$$d_5^3 = \frac{\mathcal{N}_2/u_f^3 + \mathcal{N}_3/u_s^3}{2(\xi_{55}^3/u_f^3 + \xi_{75}^3/u_s^3)}, \tag{46}$$

$$d_8^3 = \frac{\mathcal{L}_2^3}{\xi_{28}^3}, \tag{47}$$

$$d_6^3 = \sqrt{\rho}\frac{\mathcal{N}_1 b_2 u_f^3 + b_1 U_A^3(\mathcal{N}_2 - 2\xi_{55}^3 d_5^3)}{2U_A^3 u_f^3(b_1^2 + b_2^2)}, \tag{48}$$

$$d_7^3 = \sqrt{\rho}\frac{-\mathcal{N}_1 b_1 u_f^3 + b_2 U_A^3(\mathcal{N}_2 - 2\xi_{55}^3 d_5^3)}{2U_A^3 u_f^3(b_1^2 + b_2^2)}, \tag{49}$$

$$d_1^3 = \frac{\mathcal{L}_1^3 - \xi_{15}^3 d_5^3}{\xi_{11}^3}. \tag{50}$$

and the eigenvalues are:

$$\lambda_1^3 = 0, \quad \lambda_2^3 = 0, \quad \lambda_3^3 = U_A^3, \quad \lambda_4^3 = -U_A^3,$$
$$\lambda_5^3 = U_f^3, \quad \lambda_6^3 = -U_f^3, \quad \lambda_7^3 = U_s^3, \quad \lambda_8^3 = -U_s^3. \tag{51}$$

The components of $\mathcal{L}_i^3$ that need to be specified are $\mathcal{L}_1^3$, $\mathcal{L}_2^3$, $\mathcal{L}_3^3$, $\mathcal{L}_5^3$, and $\mathcal{L}_7^3$. From

observation, one immediately noticed that, by setting $(\rho)_t$ and $(B_3)_t = 0$, this procedure automatically determined $\mathcal{L}_1^3$ and $\mathcal{L}_2^3$ respectively. To determine the other three $\mathcal{L}_i^3$'s, $\mathcal{M}_1$, $\mathcal{M}_2$, and $\mathcal{M}_3$ have to be solved from the simultaneous Eqs. (44), (45), and (43). The results are

$$\mathcal{M}_1 = 2b_3(b_1 d_3^3 - b_2 d_2^3), \tag{52}$$

$$\mathcal{M}_2 = -2U_f^3 b_3(b_1 d_2^3 + b_2 d_3^3) + 2U_f^3 d_4^3(U_f^2 - b_3^2), \tag{53}$$

$$\mathcal{M}_3 = U_s^3\left[2d_4^3(u_f^3 - u_s^3) - \frac{\mathcal{M}_2}{U_f^3}\right]. \tag{54}$$

where d_2^3, d_3^3, and d_4^3 can be obtained from

$$d_2^3 = e_2 - d_2^1 - (u_1)_t, \tag{55}$$

$$d_3^3 = e_3 - d_3^1 - (u_2)_t, \tag{56}$$

$$d_4^3 = e_4 - d_4^1 - (u_3)_t. \tag{57}$$

where e_i is the ith component of the vector of source terms $\mathbf{E}$. Finally, we have

$$\mathcal{L}_3^3 = \mathcal{L}_4^3 + \frac{1}{\sqrt{F_B}}\mathcal{M}_1, \tag{58}$$

$$\mathcal{L}_5^3 = \mathcal{L}_6^3 + \frac{1}{\sqrt{F_B}}\mathcal{M}_2, \tag{59}$$

$$\mathcal{L}_7^3 = \mathcal{L}_8^3 + \frac{1}{\sqrt{F_B}}\mathcal{M}_3. \tag{60}$$

Now d_5^3, d_6^3, and d_7^3 can be determined from Eqs. (46), (48), and (49) respectively. Consequently, $(p)_t$, $(B_1)_t$, and $(B_2)_t$ are obtained from Eq. (42).

5. Numerical Experiments

The experiments are done to verify the validity of the coupled and non-reflecting boundary conditions separately. The physical problem of interest is the dynamic

evolution of a magnetic force-free field driven by the shear motion of the foot points of the magnetic field lines.

In this scenario, we consider a force-free magnetic arcade straddling a photospheric neutral line. The arcade has translational symmetry along the neutral line, and rotational symmetry about an axis below the surface. In this Cartesian coordinate system, z denotes the height above the photosphere, x the projected distance from the neutral line, and y the coordinate normal to the x-z plane along the neutral line. A parameter t denotes the depth of the symmetry axis below the photosphere ($z < 0$).

One of the closed form analytical solutions for the physical scenario described above for the nonlinear force-free equation

$$\nabla \times \mathbf{B} = \alpha \mathbf{B} \tag{61}$$

obtained by Martens *et al.* (1992) is

$$B_x = - B_o z' \exp(\frac{t^2 - r^2}{2}) \tag{62}$$

$$B_y = - B_o \sqrt{(1 - r^2)\exp(t^2 - r^2) + C^2} \tag{63}$$

$$B_z = B_o x \exp(\frac{t^2 - r^2}{2}) \tag{64}$$

$$\alpha = \frac{(2 - r^2)\exp(\frac{t^2 - r^2}{2})}{\sqrt{(1 - r^2)\exp(t^2 - r^2) + C^2}} \tag{65}$$

where $z' = z + t$ and $r^2 = x^2 + z'^2$. The foot point of a magnetic line-of-force has a shear displacement along a direction parallel to the neutral line given by

$$\Delta y(x, y, z = 0, t) = \tan^{-1}(\frac{x}{t})\sqrt{1 - t^2 - x^2 + C^2\ exp(x^2)}. \tag{66}$$

Velocity of the shear motion on the lower boundary of the computational domain

can easily be obtained by taking time derivative of the displacement in the above expression, Eq (66) such that

$$v = \frac{-x}{t^2+x^2}\sqrt{1-t^2-x^2+C^2\ exp\ (x^2)} - \tan^{-1}\left(\frac{x}{t}\right)\frac{t}{\sqrt{1-t^2-x^2+C^2\ exp\ x^2}}. \tag{67}$$

The time scale used in this numerical experiment is merely a parameter to describe the displacement of the foot points. The magnetic arcades and the displacement profiles on the photosphere are shown in Figure 1 with the the parameters $C = 0.4$ and in (a) $t = 0$ and in (b) $t = t_{\max} \equiv \sqrt{2 + 2\log C}$.

5.1 Test One: Verification of the Coupled Boundary Condition

To test the validity of the coupled boundary condition, two runs are carried out by using mathematical model Eq. (5) with the same initial and upper and side boundary conditions except that the boundary conditions at the lower boundary in each run are different. In run one, the lower boundary is specified with the known physical quantities. In run two, the coupled boundary condition in the previous section is used to calculate the physical quantities at the lower boundary. The results of the two runs are then compared to validate the coupled boundary condition.

In both runs, density, gas pressure, and temperature are kept constant at the lower boundary. The non-reflecting boundary conditions are used at the upper boundary and the two side boundaries since these are the arbitrarily chosen boundaries and no physical boundary conditions can be specified on them. In run one, the lower boundary is specified with all of the magnetic induction components evaluated from

the analytical solutions with $z = 0$ using Eqs. (62) - (65).

Initially, the atmosphere is isothermal and hydrostatic. The velocity field is described by

$$u = \frac{-zx}{x^2 + (z+t)^2} \tag{68}$$

$$v = \left[\frac{-x'}{t^2 + x'^2}\sqrt{1 - t^2 - x'^2 + C^2\, exp\, x'^2} - \arctan^{-1}\left(\frac{x'}{t}\right)\frac{t}{\sqrt{1 - t^2 - x'^2 + C^2\, exp\, x'^2}}\right] \times \times \frac{\left|\arctan\frac{z+t}{x}\right| - \frac{\pi}{2}}{\left|\arctan\frac{t}{x'}\right| - \frac{\pi}{2}} \tag{69}$$

$$w = \frac{-z(z+t)}{x^2 + (z+t)^2} \tag{70}$$

where $x' = \sqrt{(t+z)^2 + x^2 - t^2}$.

In this test, the simulation time period is equal to one tenth of the maximum time and starts from zero, i.e., $0 \leq t \leq 0.041$ with $C = 0.4$. The physical parameters are listed in Table 2. The domain size is 36 grid points by 25 grid points with the grid

Table 2: Physical parameters

Parameters	Numerical Value	Unit
t_o	5000	sec
L	5.0×10^8	cm
U	1.0×10^5	cm/sec
γ	1.67	Dimensionless
R	1.653×10^8	erg/g-K
ρ_o	1.67×10^{-14}	g/cm^3
T_o	3.0×10^6	K
B_o	45	gauss

size $\triangle x = 4/25$ and $\triangle z = 1/6$. This makes the computational domain physical size 28,000 km in the x direction and 12,500 km in the z direction (height).

There are four monitored stations located at the grid points (19,10), (19,20), (30,10), and (30,20) as shown in Fig. 2. The first two stations are close to the neutral line and away from the lower boundary at which the analytical solutions are specified as the boundary conditions. The second station is twice as far as the first station away from the lower boundary. The third and fourth stations are in the region away from the neutral line.

At these four monitored stations, the magnitude of the vector magnetic induction obtained from the numerical simulation is compared with that of the analytical solution. The relative errors of the comparison versus the time normalized with the simulation period are shown in Fig. 3 for run one and Fig. 4 for run two where the four frames show the comparisons at four different grid points as (a): point (19,10), (b): point (19,20), (c): point (30,10), and (d): point (30,20). Also in each frame, the results of three runs with different time step are shown for the purpose of asymptotic analysis. The results from run one with 1000, 2000, and 5000 time steps in the simulation period are expressed in dash-dotted line, dashed line, and solid line respectively. The reason for recording results with different time steps is to investiage the asymptotic behaviour of the solution, i.e., the time accuracy of the algorithm that solve the physical quantities in the computational domain. Since the results with 1000 time steps are close enough to the asymptotic solution with 5000 time steps, thus, the 1000 time steps are used as the number of time step in run two. The dotted line is the two-degree polynomial least square fitting of the curves of the error in each frame. These dotted lines indicate the center lines of the oscillating numerical results which deviate from the analytical solution by less than

2% for run one and 6% for run two.

From these results, it is easy to notice that the waves propagating outward from the lower boundary in run two are eliminated. This indicates that the forced boundary condition at the lower boundary in run one creates spurious waves while the coupled boundary condition eliminates the spurious wave generation as demonstrated by run two. We may conclude that the coupled boundary condition is superior than the fixed boundary condtions.

At the region of monitored station (a), the deviation of the numerical results from the analytical solution becomes larger as time progresses. The excessive decrease of the magnetic induction is caused by the convective effect of the dynamic system that brings in lower magnetic flux from a higher elevation through the convection process of a slightly over-predicted down-flowing velocity field in comparison with analytical solutions. As for the other three monitored points, the gradients of the magnetic induction in the vicinity of these points are not as large as at station (a). Therefore an over-predicted velocity field affects the magnetic flux very little through the convection process. However, this reflects the deviation of the dynamic simulation from the quasi-static solution, and the maximum deviation of the magnitude of the magnetic induction at monitored station (a) is only around 6% at the end of the simulation.

5.2 Test Two: Verification of the Non-reflecting Boundary Condition

The non-reflecting boundary conditions are used in run one and run two of test one without verification because the test one emphasizes the accuracy of the lower

boundary. In test two the non-reflecting boundary conditions will be investigated. To carry out this test, all the parameters are the same as in run one of test one except that the domain size is larger so that the boundary grid points imposed with the non-reflecting boundary condition in run one of test one become interior grid points in this test. Then the physical variables at these grid points resulting from run one of test one are compared with those resulting from this test (i.e. test two) in order to verify the performance of the non-reflecting boundary conditions applied especially in the two-dimensional case. The reason for using this setup for run one of test one instead of that of run two of test one is that run one of test one creates waves which are considered to be undesired in a real simulation but are useful for this test.

Since the positions of interest in this case are the intersections of non-reflecting boundaries, three monitored grid points are selected. The grid point (36,25) shown in Fig. 2, will be referred to as station (a) which is an intersecting point of two non-reflecting boundaries. The other two grid points (35,24) and (34,23) will be referred to as station (b) and station (c) respectively. These two stations are used to monitor the influence of the non-reflecting boundary condition on the interior grid points. The comparison of the results from run one of test one shown by dotted lines and the results from this test in dashed lines are shown in Fig. 5 and Fig. 6 with three monitored stations in each figure. The two physical quantities compared are the normalized velocity component u in Fig. 5 and the normalized magnetic induction component B_y in Fig. 6. From these figures, the non-reflecting boundary condition is proven to work well in the multi-dimensional problem.

6. Conclusion

A new analytic approach of solving the time-dependent boundary conditions of MHD flow is developed for multi-dimensional non-isothermal plasma. In addition, for the situation when two of the eigenvectors are parallel, the solutions of the boundary conditions are shown to be achievable. Numerical experiments to test this formalism of the coupled boundary condition and the non-reflecting boundary condition are presented.

The test results of the coupled boundary condition show that the determination of $\partial \mathbf{W}/\partial t$ at the boundary which is indeed outrange the artificially defined $\mathbf{W}$(cf.[4]). This is especially true when the defined $\mathbf{W}$ is the solution of a set of steady state equations.

For the non-reflecting boundary condition, the test results demonstrate that the solutions on the upper and side boundaries in run one of test one act just like the solutions at the interior points in test two. The most troublesome point is the intersection of two non-reflecting boundaries which is one of the monitored points in the numerical experiment. This test proves the validity of the non-reflecting boundary condition in the multi-dimensional problem.

An application of this newly developed time-dependent boundary conditions, can be found in the work of Martens *et al.* (1992).

Appendix: Solutions of the Boundary Equations

In the x_2 direction, the inverse matrix $\mathbf{S}_2^{-1}$, whose rows are the left eigenvectors

l T_i of $\mathbf{A}^2$, is

$$\mathbf{S}_2^{-1} = \begin{pmatrix} F_P a^2 & 0 & 0 & 0 & -F_P & 0 & 0 & 0 \\ 0 & 0 & 0 & 0 & 0 & 0 & c_b & 0 \\ 0 & -b_{23} & 0 & b_{12} & 0 & c_3 U_A^2 & 0 & -c_1 U_A^2 \\ 0 & b_{23} & 0 & -b_{12} & 0 & c_3 U_A^2 & 0 & -c_1 U_A^2 \\ 0 & -b_{12} U_f^2 & U_f^2 u_{ff}^2 & -b_{23} U_f^2 & F_P \frac{u_{ff}^2}{\rho} & c_1 u_f^2 & 0 & c_3 u_f^2 \\ 0 & b_{12} U_f^2 & -U_f^2 u_{ff}^2 & b_{23} U_f^2 & F_P \frac{u_{ff}^2}{\rho} & c_1 u_f^2 & 0 & c_3 u_f^2 \\ 0 & b_{12} U_s^2 & U_s^2 u_{ss}^2 & b_{23} U_s^2 & F_P \frac{u_{ss}^2}{\rho} & -c_1 u_s^2 & 0 & -c_3 u_s^2 \\ 0 & -b_{12} U_s^2 & -U_s^2 u_{ss}^2 & -b_{23} U_s^2 & F_P \frac{u_{ss}^2}{\rho} & -c_1 u_s^2 & 0 & -c_3 u_s^2 \end{pmatrix}, \quad (71)$$

where $u_f^2 = (U_f^2)^2$, $u_s^2 = (U_s^2)^2$, $u_{ff}^2 = u_f^2 - b_2^2$, $u_{ss}^2 = b_2^2 - u_s^2$, $c_b = \sqrt{F_B/\rho}$, $c_i = c_b b_i$, and $b_{ij} = b_i b_j$. The elements of the solution vector d^2 are

$$d_3^2 = \frac{\mathcal{M}_2/U_f^2 + \mathcal{M}_3/U_s^2}{2(u_f^2 - u_s^2)}, \quad (72)$$

$$d_2^2 = \frac{-U_f^2 b_3 \mathcal{M}_1 - b_1(\mathcal{M}_2 - 2\xi_{53}^2 d_3^1)}{2U_f^2 b_2(b_1^2 + b_3^2)}, \quad (73)$$

$$d_4^2 = \frac{U_f^2 b_1 \mathcal{M}_1 - b_3(\mathcal{M}_2 - 2\xi_{53}^2 d_3^1)}{2U_f^2 b_2(b_1^2 + b_3^2)}, \quad (74)$$

$$d_5^2 = \frac{\mathcal{N}_2/u_f^2 + \mathcal{N}_3/u_s^2}{2(\xi_{55}^2/u_f^2 + \xi_{75}^2/u_s^2)}, \quad (75)$$

$$d_7^2 = \frac{\mathcal{L}_2^2 \xi_{27}}{\xi_{27}^2} \quad (76)$$

$$d_6^2 = \sqrt{\rho}\frac{\mathcal{N}_1 b_3 u_f^2 + b_1 U_A^2(\mathcal{N}_2 - 2\xi_{55}^2 d_5^2)}{2U_A^2 u_f^2(b_1^2 + b_3^2)}, \quad (77)$$

$$d_8^2 = \sqrt{\rho}\frac{-\mathcal{N}_1 b_1 u_f^2 + b_3 U_A^2(\mathcal{N}_2 - 2\xi_{55}^2 d_5^2)}{2U_A^2 u_f^2(b_1^2 + b_3^2)}, \quad (78)$$

$$d_1^2 = \frac{\mathcal{L}_1^2 - \xi_{15}^2 d_5^2}{\xi_{11}^2}, \quad (79)$$

where

$$\mathcal{M}_i = \sqrt{F_B}(\mathcal{L}_{2i+1}^2 - \mathcal{L}_{2i+2}^2), \quad (80)$$

$$\mathcal{N}_i = \mathcal{L}_{2i+1}^2 + \mathcal{L}_{2i+2}^2. \quad (81)$$

In the x_3 direction, the inverse matrix $\mathbf{S}_3^{-1}$, whose rows are the left eigenvectors

l T_i of $\mathbf{A}^3$, is

$$\mathbf{S}_3^{-1} = \begin{pmatrix} F_P a^2 & 0 & 0 & 0 & -F_P & 0 & 0 & 0 \\ 0 & 0 & 0 & 0 & 0 & 0 & 0 & c_b \\ 0 & -b_{23} & b_{13} & 0 & 0 & c_2 U_A^3 & -c_1 U_A^3 & 0 \\ 0 & b_{23} & -b_{13} & 0 & 0 & c_2 U_A^3 & -c_1 U_A^3 & 0 \\ 0 & -b_{13} U_f^3 & -b_{23} U_f^3 & U_f^3 u_{ff}^3 & F_P \frac{u_{ff}^3}{\rho} & c_1 u_f^3 & c_2 u_f^3 & 0 \\ 0 & b_{13} U_f^3 & b_{23} U_f^3 & -U_f^3 u_{ff}^3 & F_P \frac{u_{ff}^3}{\rho} & c_1 u_f^3 & c_2 u_f^3 & 0 \\ 0 & b_{13} U_s^3 & b_{23} U_s^3 & U_s^3 u_{ss}^3 & F_P \frac{u_{ss}^3}{\rho} & -c_1 u_s^3 & -c_2 u_s^3 & 0 \\ 0 & -b_{13} U_s^3 & -b_{23} U_s^3 & -U_s^3 u_{ss}^3 & F_P \frac{u_{ss}^3}{\rho} & -c_1 u_s^3 & -c_2 u_s^3 & 0 \end{pmatrix}, \quad (82)$$

where $u_f^3 = (U_f^3)^2$, $u_s^3 = (U_s^3)^2$, $u_{ff}^3 = u_f^3 - b_3^2$, and $u_{ss}^3 = b_3^2 - u_s^3$. The solution vector d^3 is given in Section 4.2.

ACKNOWLEDGMENTS

The authors would like to thank Dr. P.E. Martens for his invaluable comments and ideas. Thanks are due to Dr. K.W. Thompson for giving instructive suggestions during the period of this work. It is also our pleasure to acknowledge that this work was supported in part by NASA Headquarters under grant NAGW-9 and NOAA (50RANR000104) In addition, partial support from NSPO/Taiwan/ROC is also acknowledged.

REFERENCE

1. Wu, S. T., and J. F. Wang, Computer Methods in Applied Mechanics and Engineering, **64**, 267, (1987).

2. Y. Nakagawa, Y. Q. Hu and S. T. Wu, *Astron. Astrophys.* **179**, 354 (1987)

3. Y. Q. Hu and S. T. Wu, *J. Comput. Phys.* **55**, 33 (1984)

4. M. T. Sun, *Ph.D. Dissertation*, Univ. Alabama in Huntsville (1991)

5. K. W. Thompson, *J. Comput. Phys.* **68**, 1 (1987)

6. K. W. Thompson, *J. Comput. Phys.* **89**, 439 (1990)

7. T. C. Vanajakshi, K. W. Thompson, and D. C. Black, *J. Comput. Phys.* **84**, 343 (1989)

8. Martens, Piet, M. T. Sun and S. T. Wu, *Eruptive Solar Flares* (Z. Svestka, B. V. Jackson and M. Machado, eds.) IAU Symposium 133, Iguazu, Argentina, August 2-6, 1991, Springer Verlag, pp 65-68, 1992.

FIGURE CAPTIONS

Figure 1. Magnetic field configurations and displacement profiles for the photosphere with the parameters $C = 0.4$ and $t = 0$ in (a) and $t = t_{max}$ in (b).

Figure 2 . The coordinate system and the locations of the monitored grid points for the experiments of the plasma shear flow.

Figure 3 . The relative error of the magnitude of magnetic induction between numerical simulations and analytical solutions in run one (i.e. specified lower boundary conditions with known physical quantities) of test I at four monitored stations; (a) at (19, 10), (b) at (19,20), (c) at (30,10) and (d) at (30, 20) respectively as shown in Figure 2.

Figure 4. The relative error of the magnitude of magnetic induction between numerical simulations and analytical solutions in run two (i.e., the quantities at lower boundary are calculated according to the conditions discussed in (4.2)) of test I at four monitored stations; (a) at (19, 10), (b) at (19,20), (c) at (30,10) and (d) at (30,20) respectivelyf as shown in Figure 2.

Figure 5. Comparison between the coupled boundary conditions with specified lower boundary condition (Run one of Test I) and non-reflecting boundary condition (Test II) for the results of the normalized u from E_{SG} and E_{SN} at three monitored grid points ; (a) at (36,25), (b) at (35, 24) and (c) at (34, 23) respectively.

Figure 6. Comparison between the coupled boundary conditions with specified lower boundary conditions (Run one of Test I) and non-reflection boundary conditions (Test II) for the results of the normalized B_y from E_{SG} and E_{SN} at three monitored grid points; (a) at (36, 25), (b) at (35,24) and (c) at (34, 23) respectively.

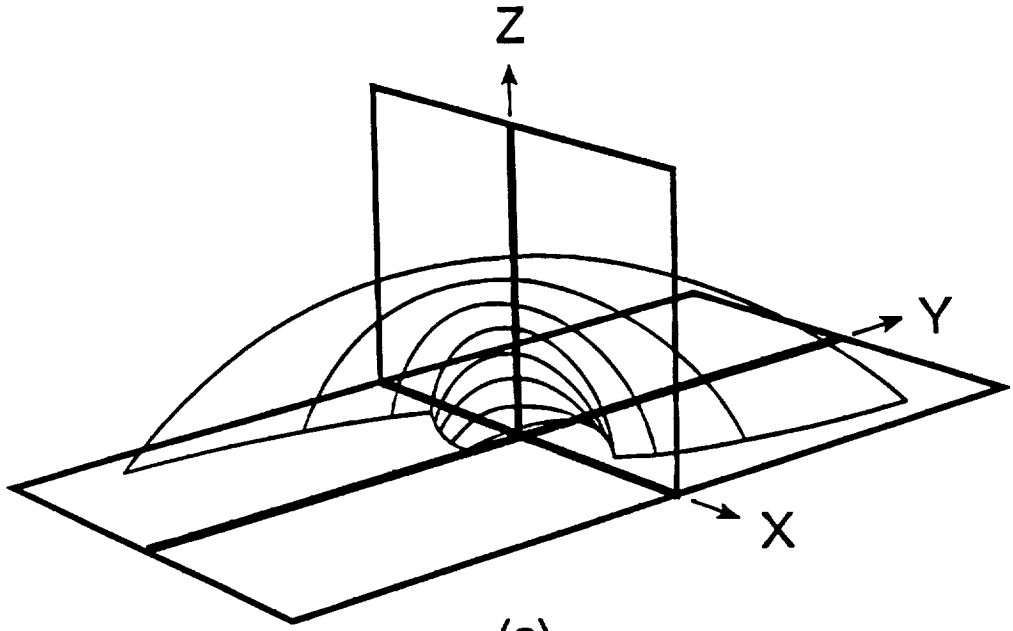

(a)

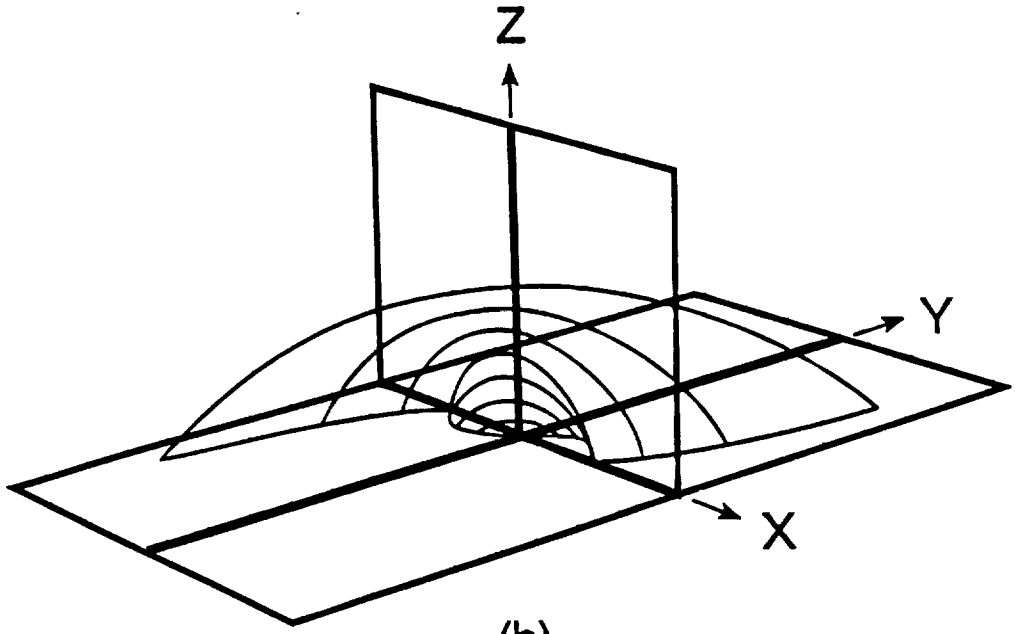

(b)

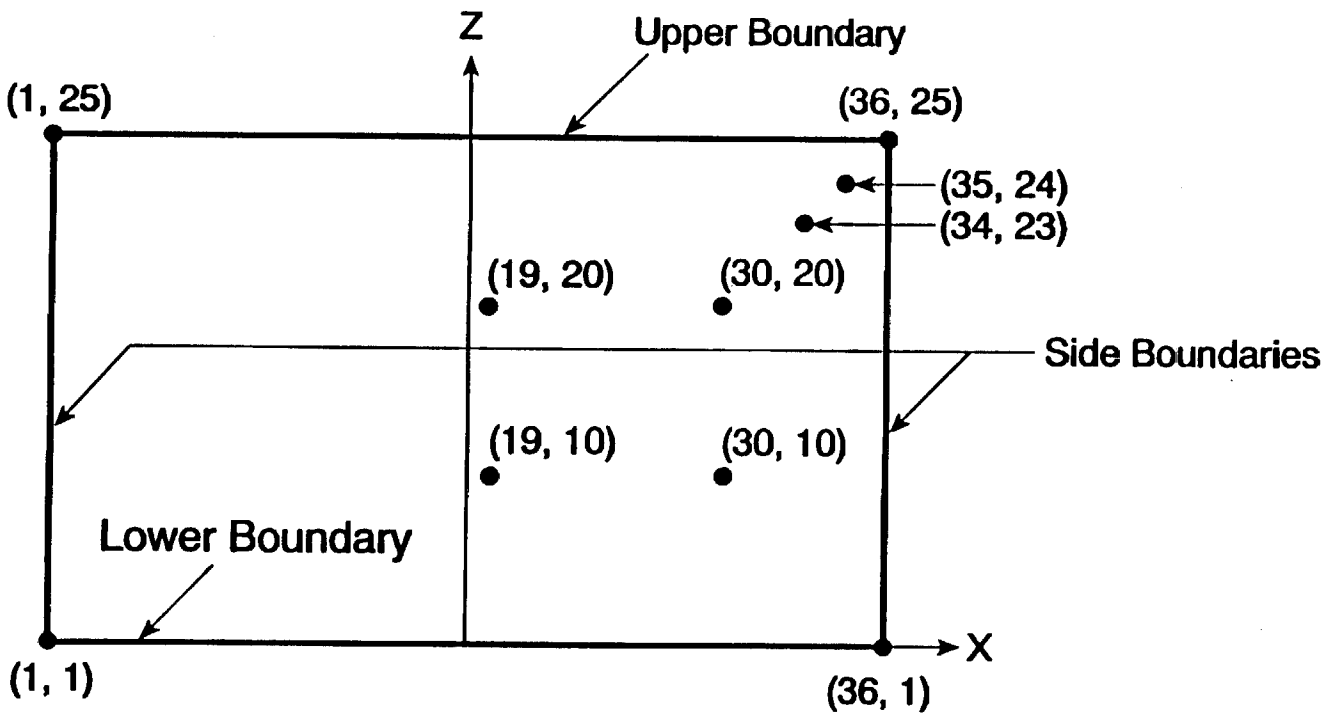
Z
Upper Boundary
(1, 25)
(36, 25)
(35, 24)
(34, 23)
(19, 20)
(30, 20)
Side Boundaries
(19, 10)
(30, 10)
Lower Boundary
X
(1, 1)
(36, 1)

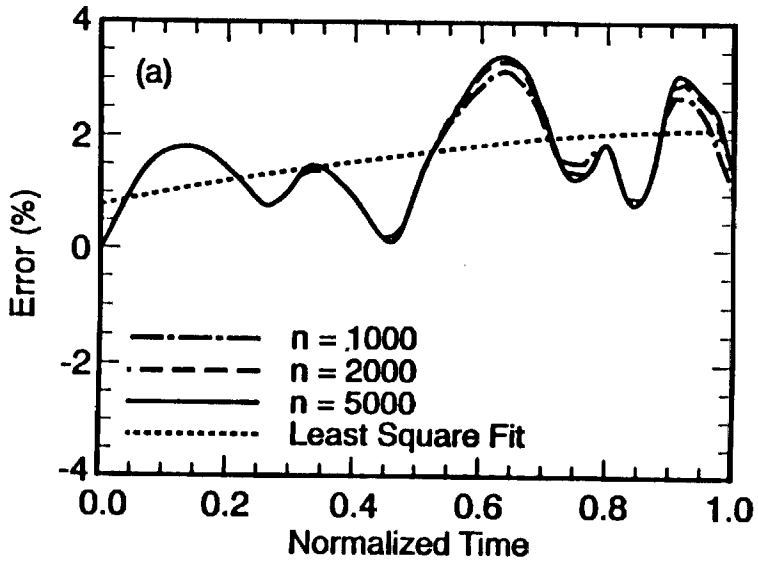
(a)
Error (%)
4
2
0
-2
-4
0.0
0.2
0.4
0.6
0.8
1.0
Normalized Time
n = 1000
n = 2000
n = 5000
Least Square Fit

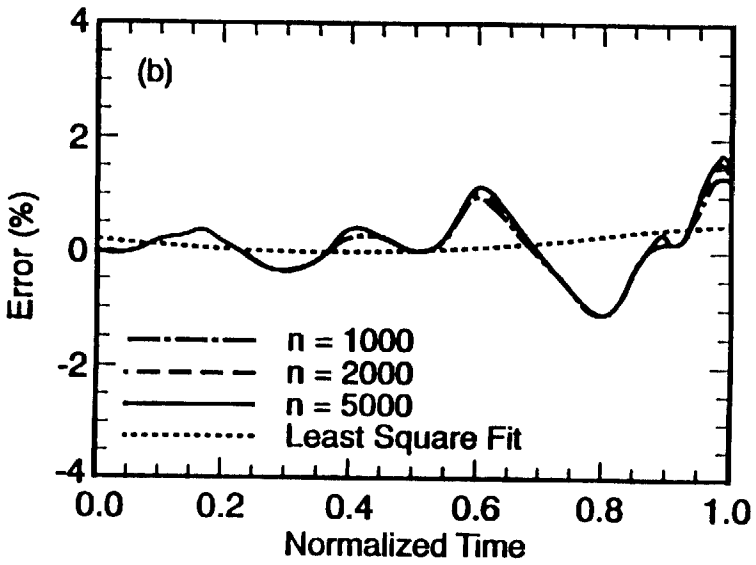
(b)
Error (%)
4
2
0
-2
-4
0.0
0.2
0.4
0.6
0.8
1.0
Normalized Time
n = 1000
n = 2000
n = 5000
Least Square Fit

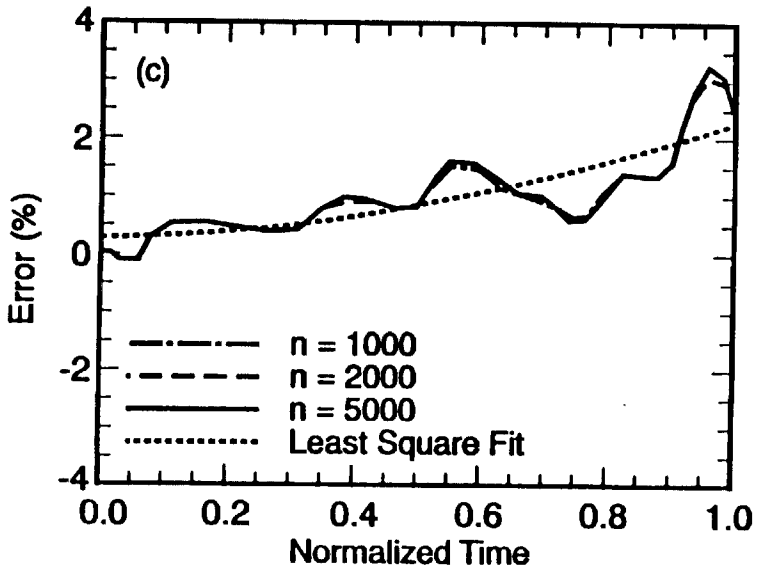
(c)
Error (%)
4
2
0
-2
-4
0.0
0.2
0.4
0.6
0.8
1.0
Normalized Time
n = 1000
n = 2000
n = 5000
Least Square Fit

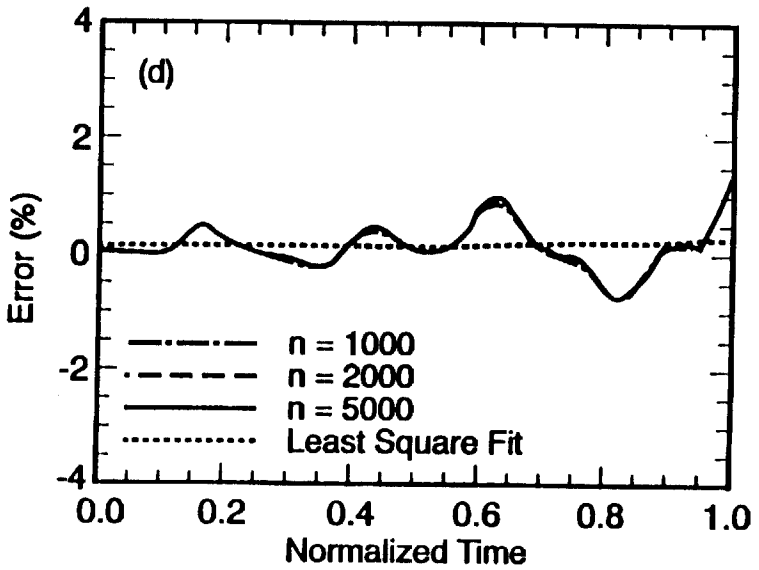
(d)
Error (%)
4
2
0
-2
-4
0.0
0.2
0.4
0.6
0.8
1.0
Normalized Time
n = 1000
n = 2000
n = 5000
Least Square Fit

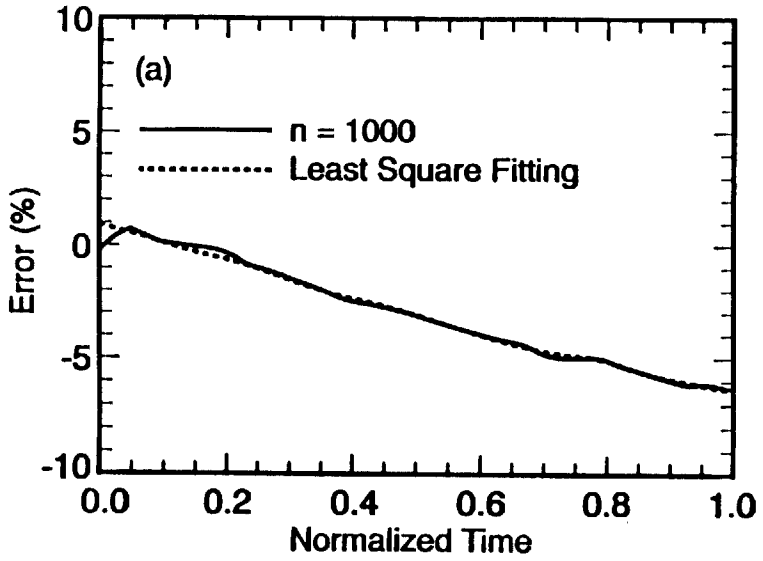
(a)
n = 1000
Least Square Fitting
Error (%)
Normalized Time
10
5
0
-5
-10
0.0
0.2
0.4
0.6
0.8
1.0

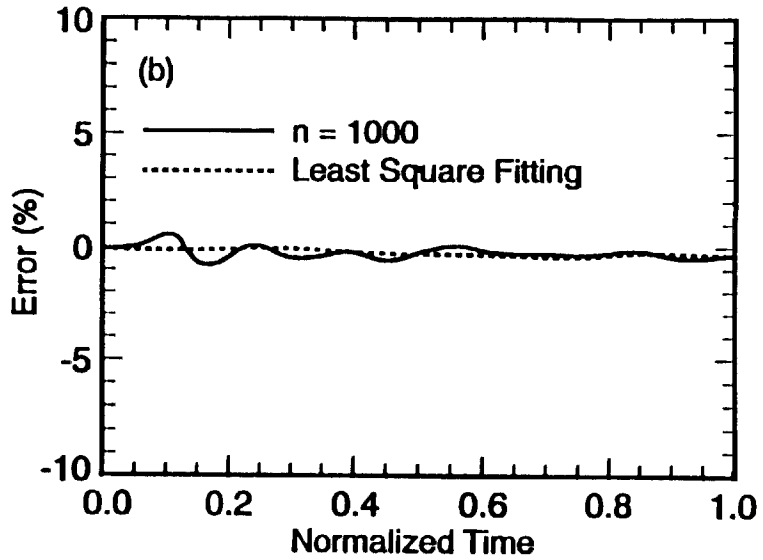
(b)
n = 1000
Least Square Fitting
Error (%)
Normalized Time
10
5
0
-5
-10
0.0
0.2
0.4
0.6
0.8
1.0

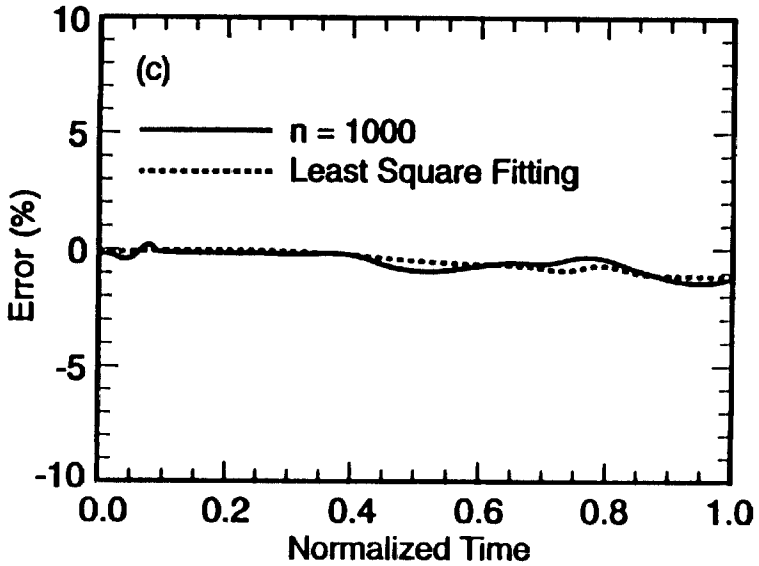
(c)
n = 1000
Least Square Fitting
Error (%)
Normalized Time
10
5
0
-5
-10
0.0
0.2
0.4
0.6
0.8
1.0

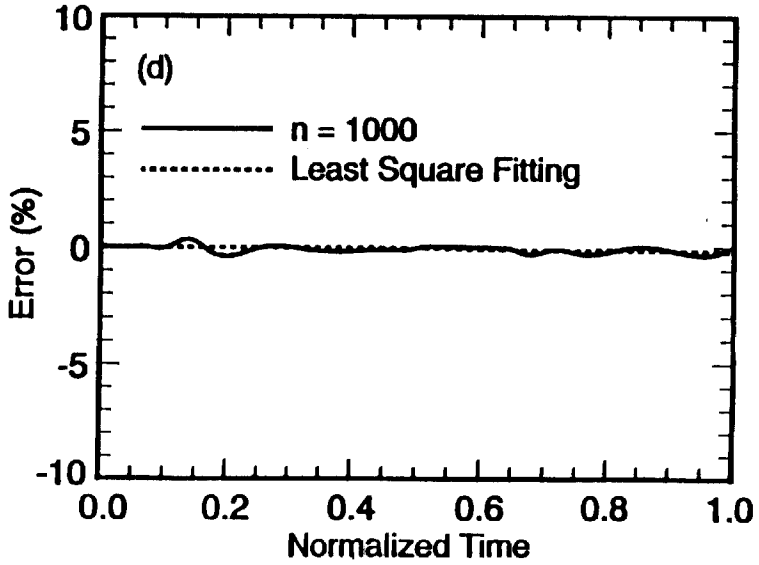
(d)
n = 1000
Least Square Fitting
Error (%)
Normalized Time
10
5
0
-5
-10
0.0
0.2
0.4
0.6
0.8
1.0

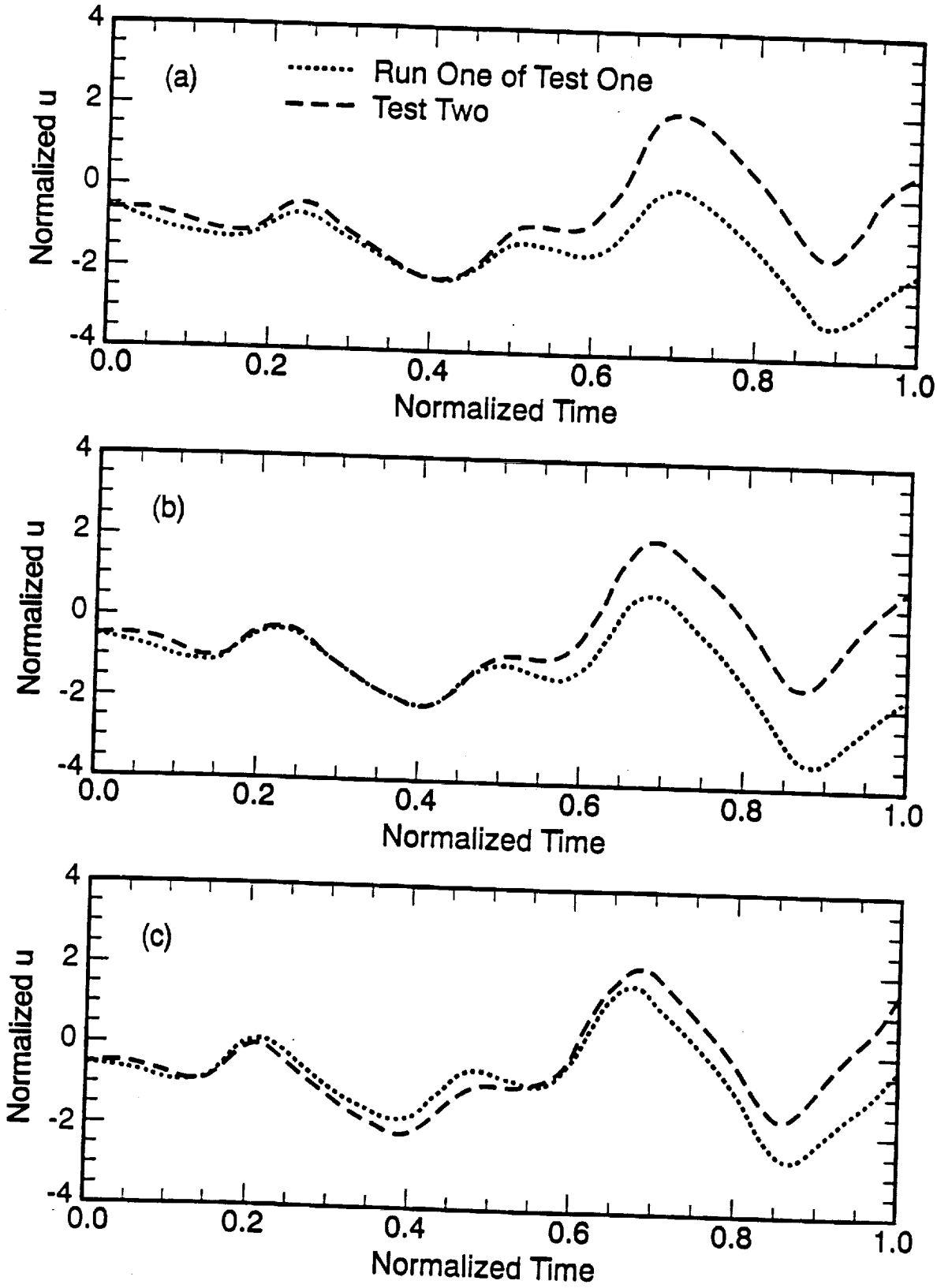
(a)
Run One of Test One
Test Two
Normalized u
Normalized Time
(b)
Normalized u
Normalized Time
(c)
Normalized u
Normalized Time
4
2
0
-2
-4
0.0
0.2
0.4
0.6
0.8
1.0

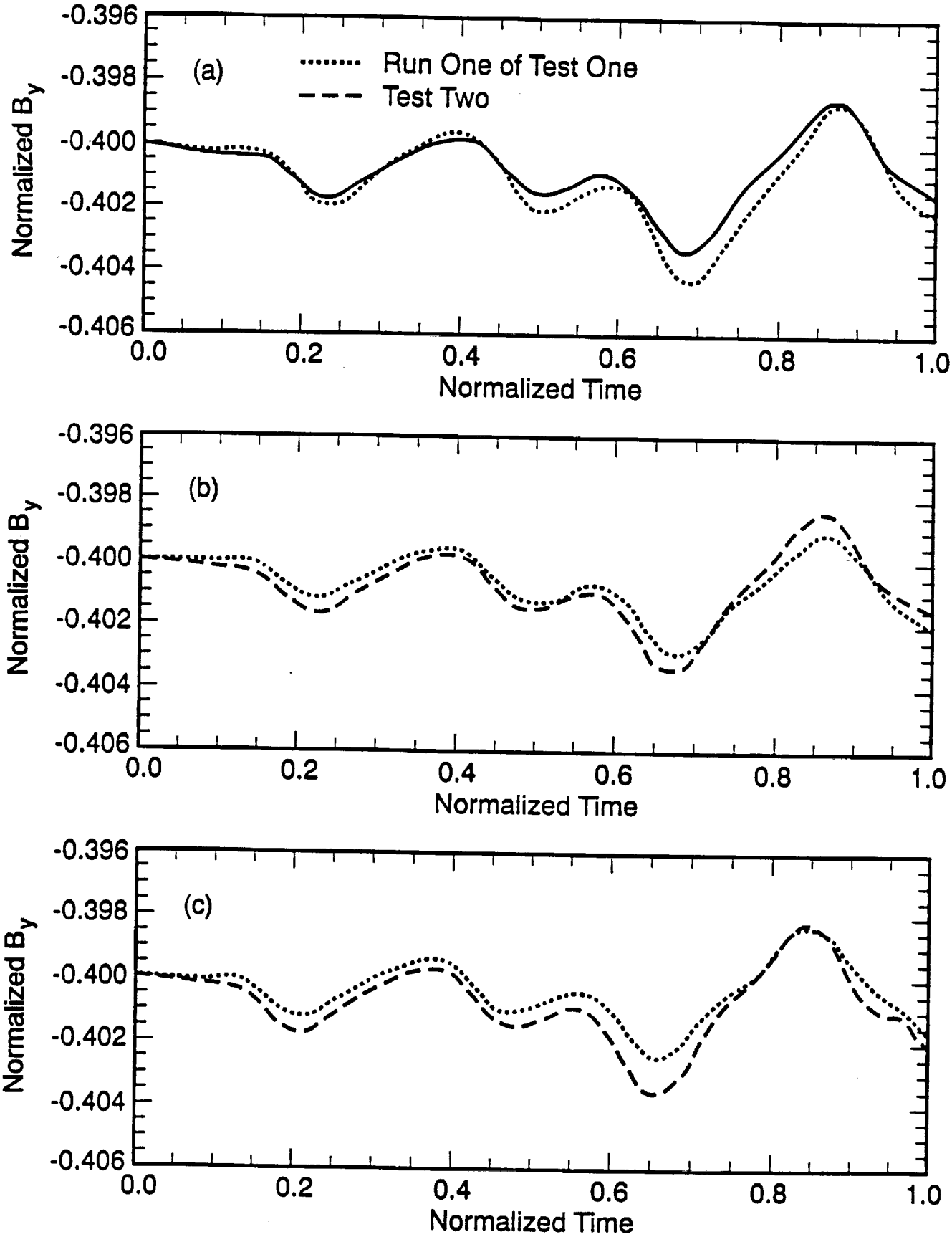
(a)
Run One of Test One
Test Two
Normalized B_y
-0.396
-0.398
-0.400
-0.402
-0.404
-0.406
0.0
0.2
0.4
0.6
0.8
1.0
Normalized Time
(b)
Normalized B_y
Normalized Time
(c)
Normalized B_y
Normalized Time

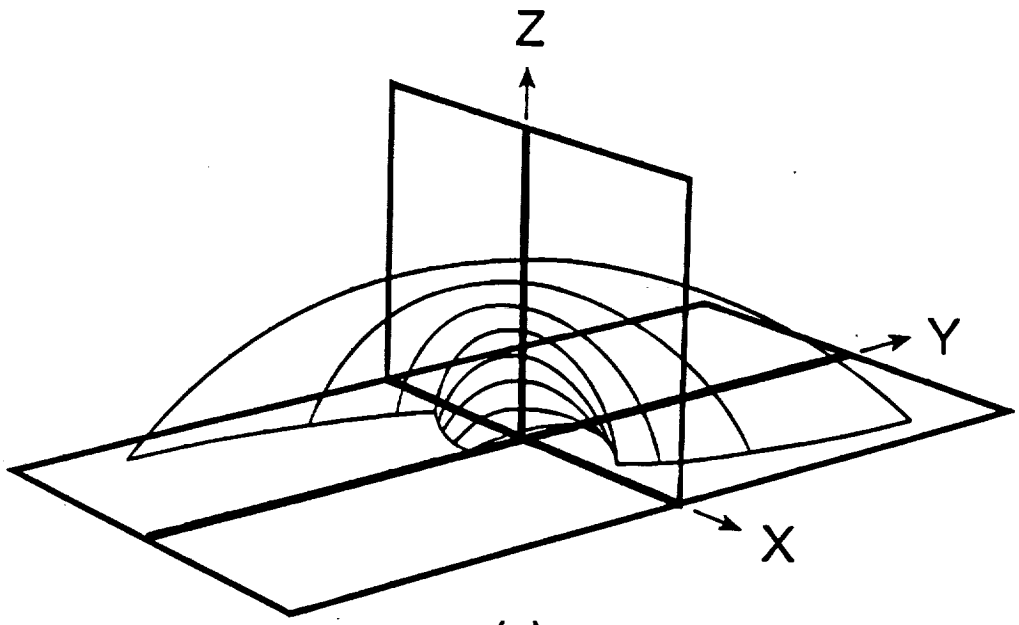

(a)

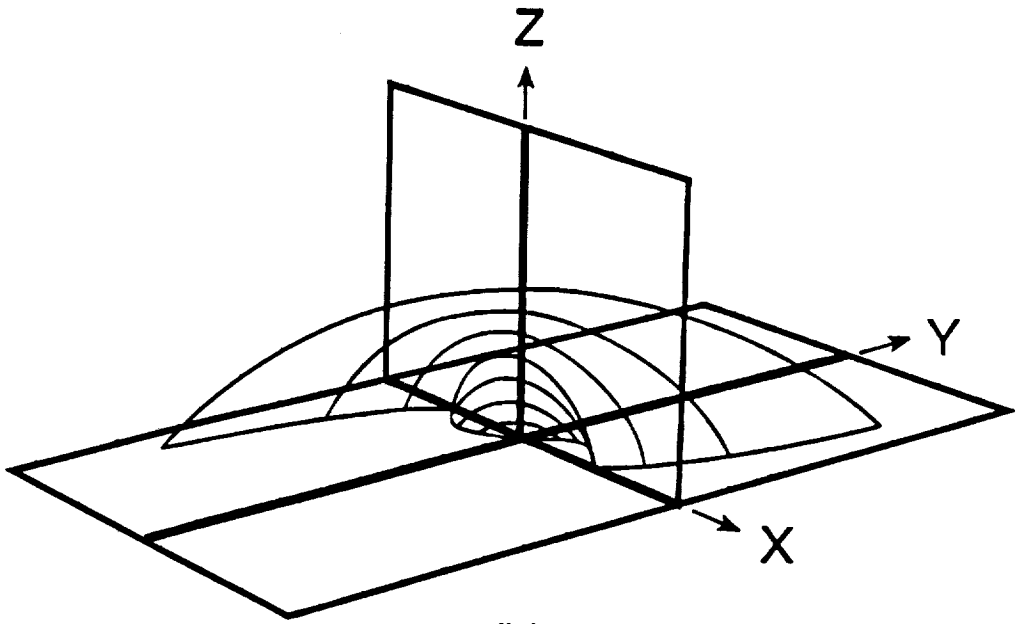

(b)

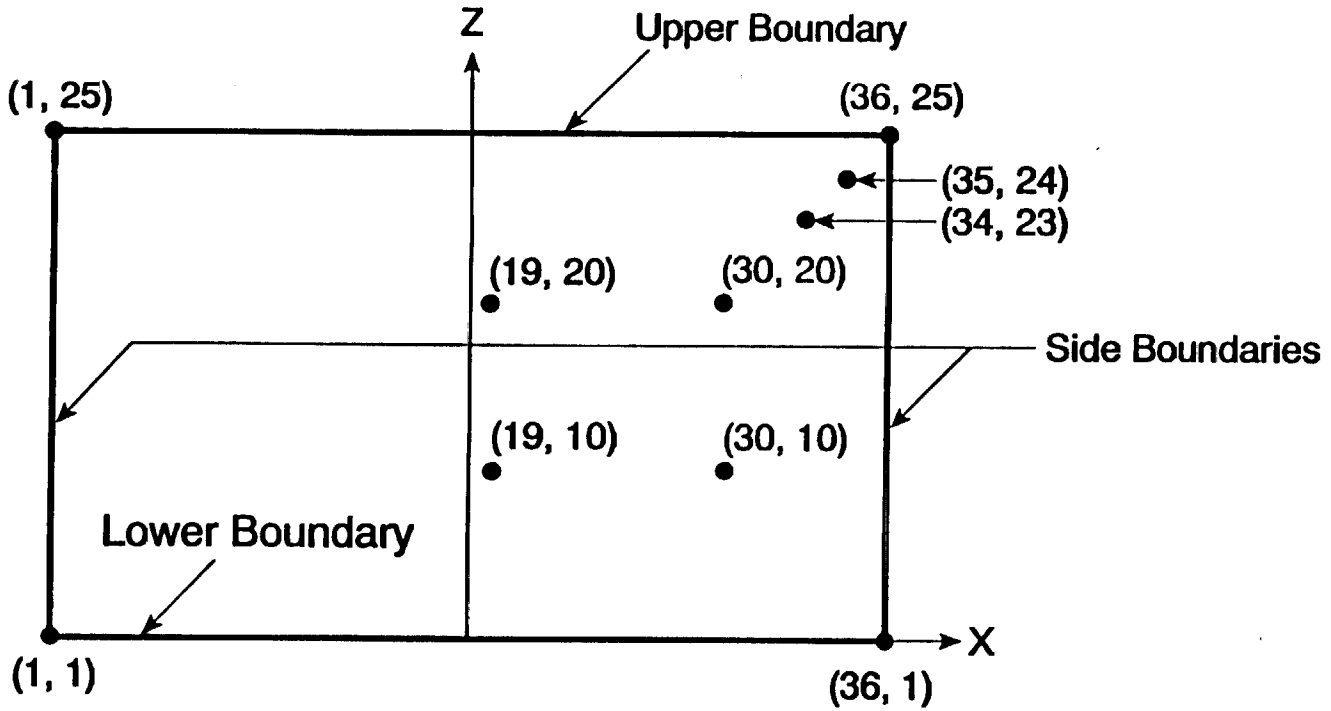
Z
Upper Boundary
(1, 25)
(36, 25)
(35, 24)
(34, 23)
(19, 20)
(30, 20)
Side Boundaries
(19, 10)
(30, 10)
Lower Boundary
X
(1, 1)
(36, 1)

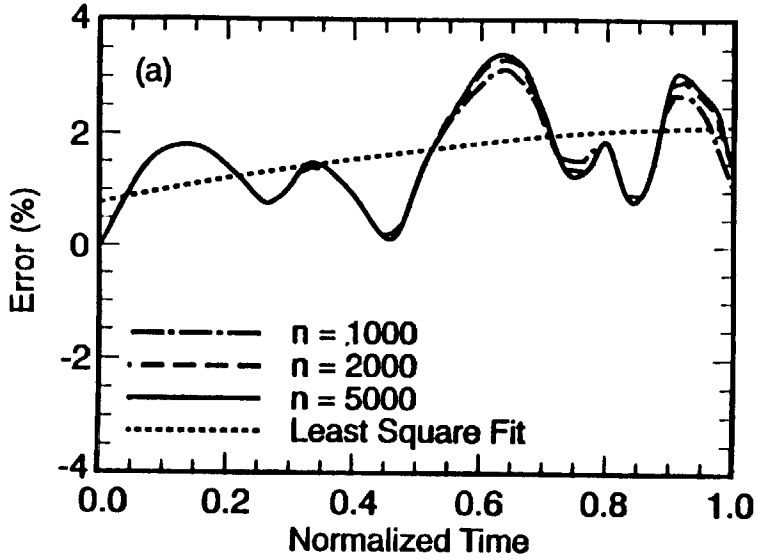
(a)
Error (%)
4
2
0
-2
-4
0.0
0.2
0.4
0.6
0.8
1.0
Normalized Time
n = 1000
n = 2000
n = 5000
Least Square Fit

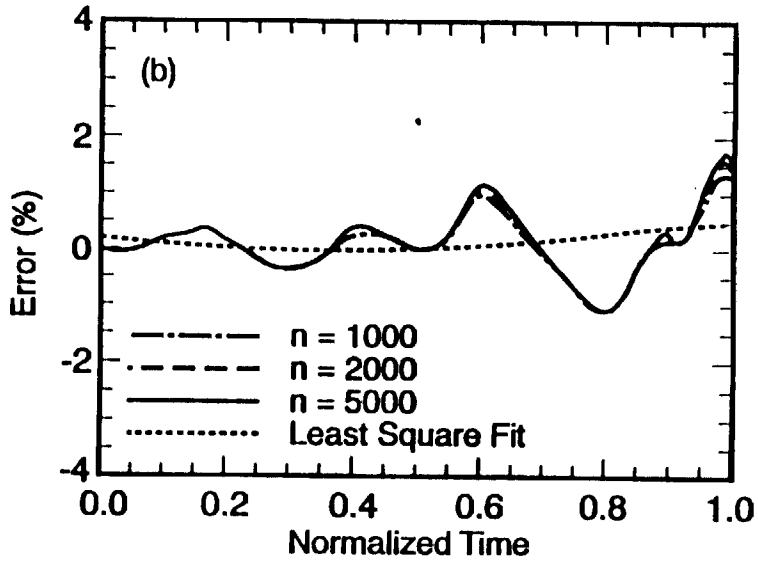
(b)
Error (%)
4
2
0
-2
-4
0.0
0.2
0.4
0.6
0.8
1.0
Normalized Time
n = 1000
n = 2000
n = 5000
Least Square Fit

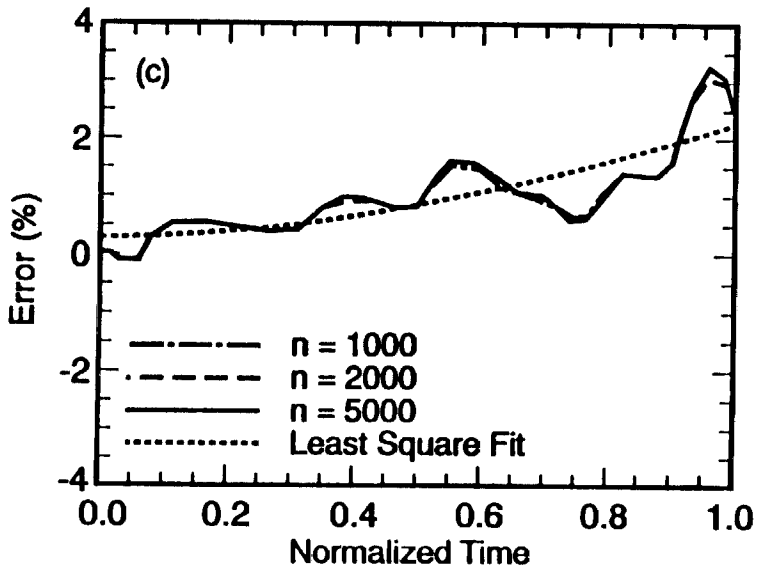
(c)
Error (%)
4
2
0
-2
-4
0.0
0.2
0.4
0.6
0.8
1.0
Normalized Time
n = 1000
n = 2000
n = 5000
Least Square Fit

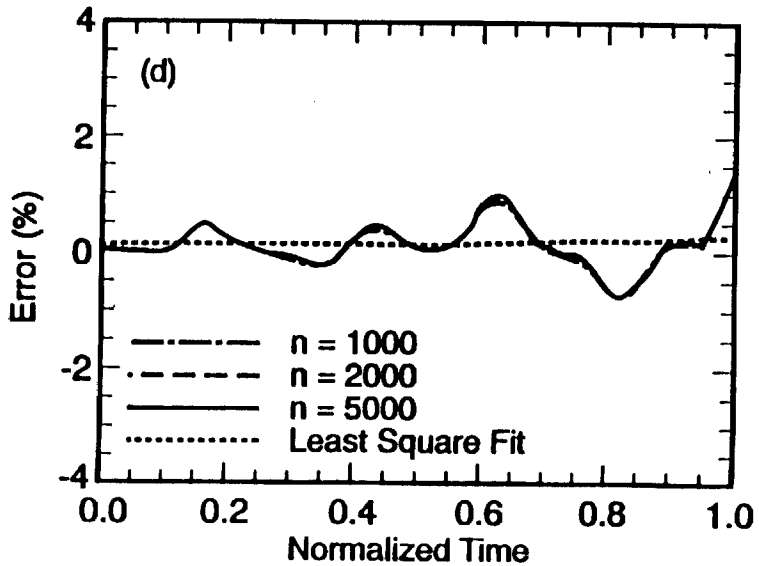
(d)
Error (%)
4
2
0
-2
-4
0.0
0.2
0.4
0.6
0.8
1.0
Normalized Time
n = 1000
n = 2000
n = 5000
Least Square Fit

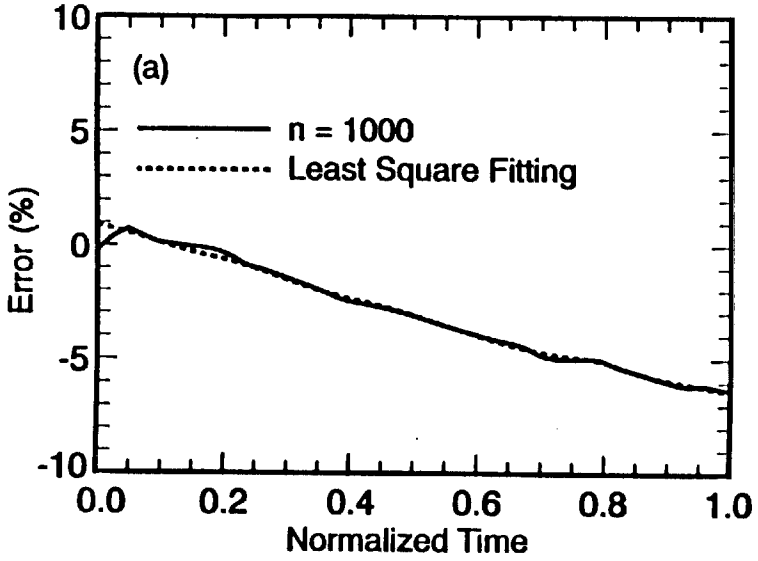
(a)
n = 1000
Least Square Fitting
Error (%)
Normalized Time
10
5
0
-5
-10
0.0
0.2
0.4
0.6
0.8
1.0

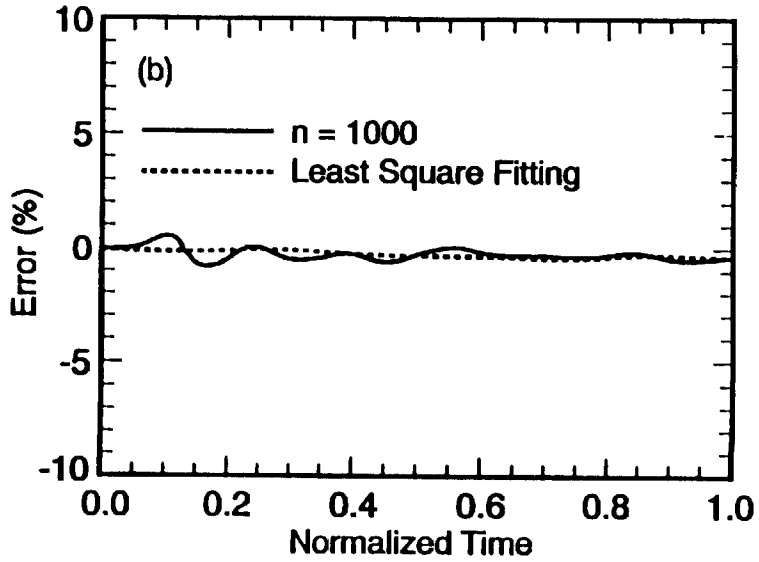
(b)
n = 1000
Least Square Fitting
Error (%)
Normalized Time
10
5
0
-5
-10
0.0
0.2
0.4
0.6
0.8
1.0

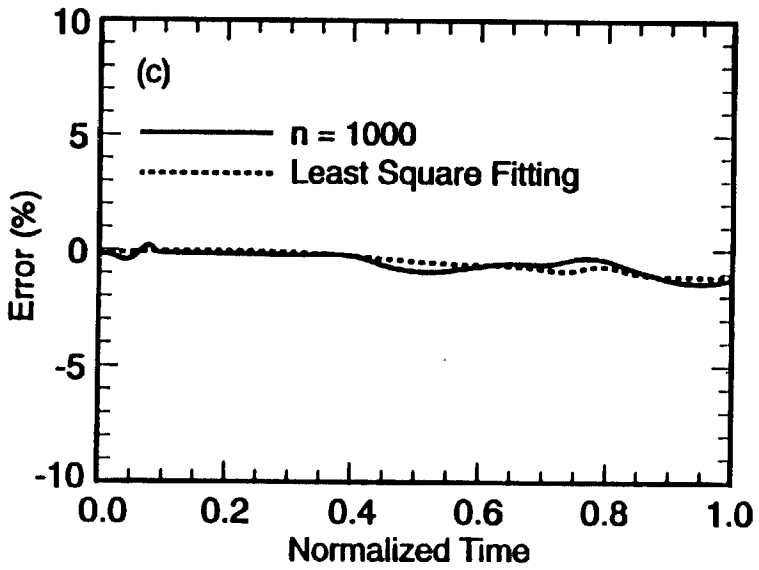
(c)
n = 1000
Least Square Fitting
Error (%)
Normalized Time
10
5
0
-5
-10
0.0
0.2
0.4
0.6
0.8
1.0

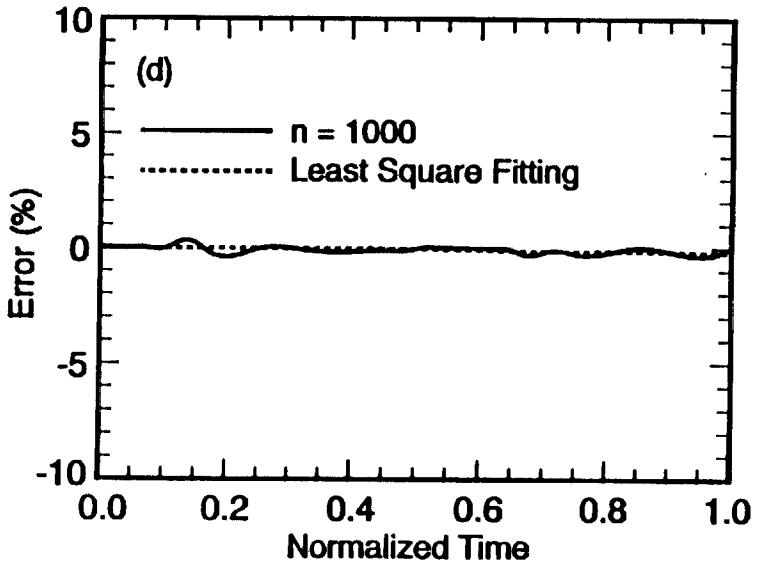
(d)
n = 1000
Least Square Fitting
Error (%)
Normalized Time
10
5
0
-5
-10
0.0
0.2
0.4
0.6
0.8
1.0

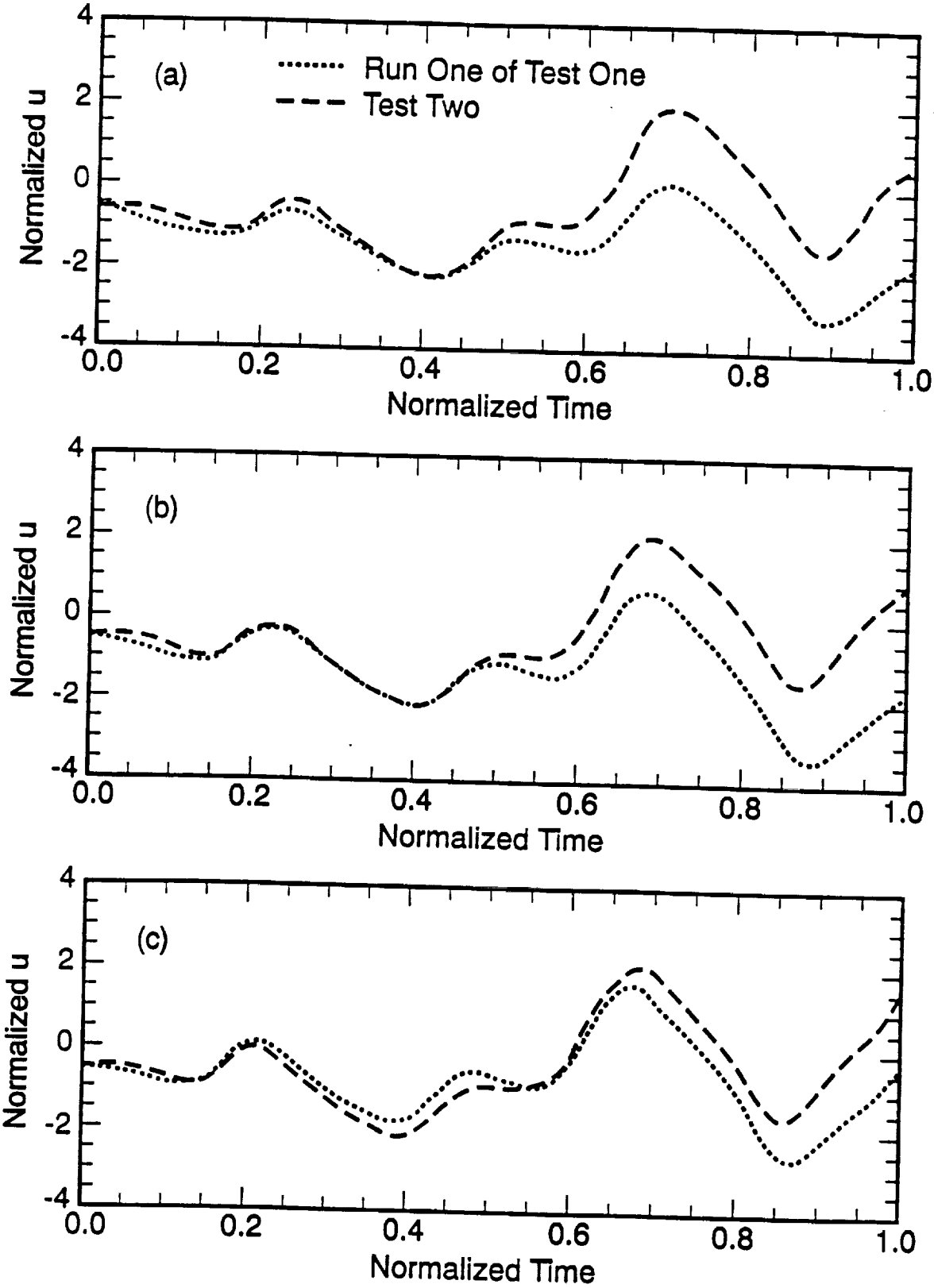
(a)
Run One of Test One
Test Two
Normalized u
Normalized Time
(b)
Normalized u
Normalized Time
(c)
Normalized u
Normalized Time

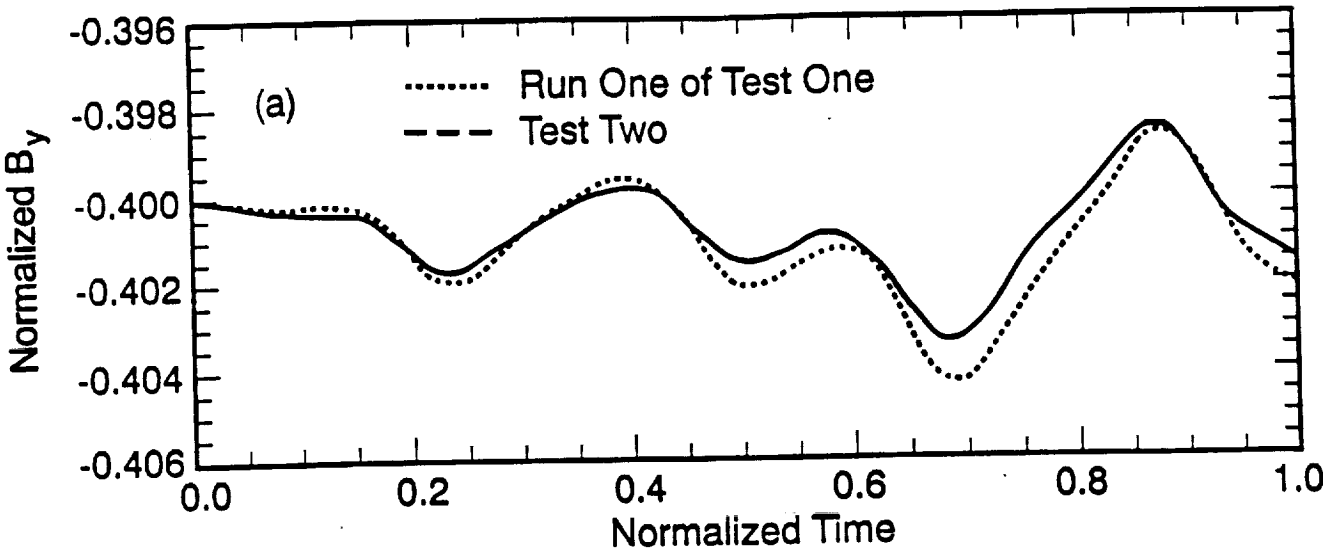
(a)
Run One of Test One
Test Two
Normalized B_y
-0.396
-0.398
-0.400
-0.402
-0.404
-0.406
0.0
0.2
0.4
0.6
0.8
1.0
Normalized Time

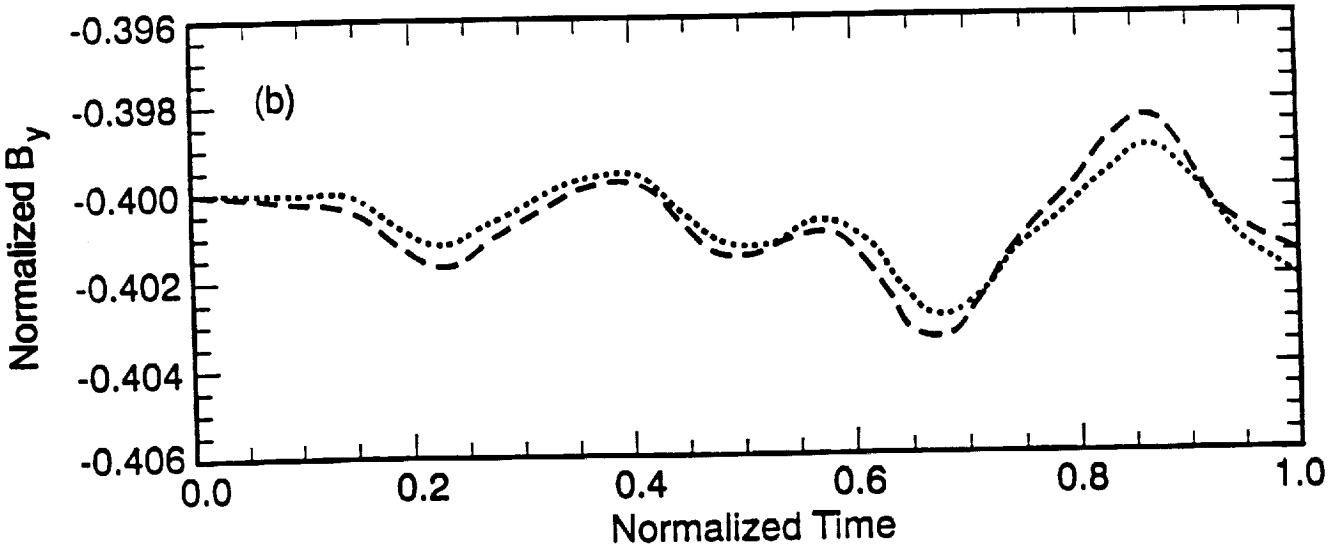
(b)
Normalized B_y
-0.396
-0.398
-0.400
-0.402
-0.404
-0.406
0.0
0.2
0.4
0.6
0.8
1.0
Normalized Time

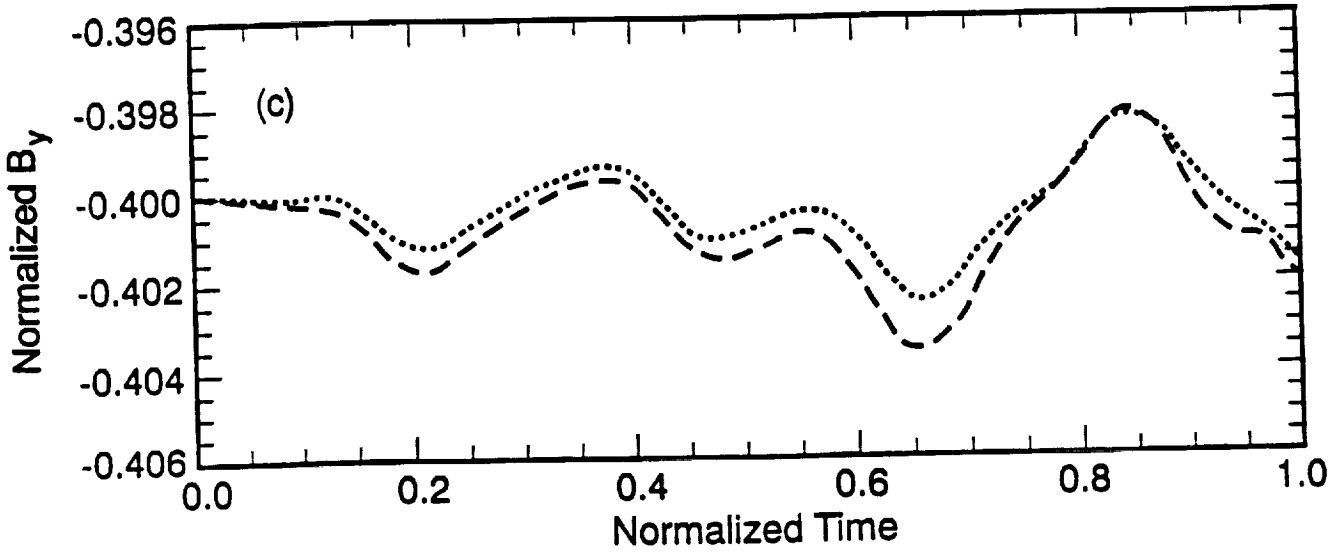
(c)
Normalized B_y
-0.396
-0.398
-0.400
-0.402
-0.404
-0.406
0.0
0.2
0.4
0.6
0.8
1.0
Normalized Time